

Sheffield Hallam University

An Investigation of Aerodynamic Noise from Standard Ground Vehicles using Computational Aeroacoustics

CHODE, Kushal Kumar

Available from the Sheffield Hallam University Research Archive (SHURA) at:

<https://shura.shu.ac.uk/33761/>

A Sheffield Hallam University thesis

This thesis is protected by copyright which belongs to the author.

The content must not be changed in any way or sold commercially in any format or medium without the formal permission of the author.

When referring to this work, full bibliographic details including the author, title, awarding institution and date of the thesis must be given.

Please visit <https://shura.shu.ac.uk/33761/> and <http://shura.shu.ac.uk/information.html> for further details about copyright and re-use permissions.

An Investigation of Aerodynamic Noise from Standard Ground Vehicles using Computational Aeroacoustics

Kushal Kumar Chode

A thesis submitted in partial fulfilment of the requirements of
Sheffield Hallam University
for degree of Doctor of Philosophy

In Collaboration with HORIBA MIRA

July 2023

Candidate Declaration

I hereby declare that:

1. I have not been enrolled for another award of the University, or other academic or professional organisation, whilst undertaking my research degree.
2. None of the material contained in the thesis has been used in any other submission for an academic award.
3. I am aware of and understand the University's policy on plagiarism and certify that this thesis is my own work. The use of all published or other sources of material consulted has been properly and fully acknowledged.
4. The work undertaken towards the thesis has been conducted in accordance with the SHU Principles of integrity in Research and the SHU Research Ethics Policy.
5. The word count of the thesis is **39131**.

Name	Kushal Kumar Chode
Award	Doctor of Philosophy
Date of Submission	19 July 2023
Research Institute	Materials and Engineering Research Institute
Director(s) of Studies	Dr Harish Viswanathan

The noise radiating from ground vehicles and its detrimental effects on occupants, pedestrians, and the environment have spurred vehicle manufacturers to seek effective noise prediction methods and mitigation strategies. This thesis focuses on predicting aerodynamically generated noise from vehicles using a hybrid Computational Aeroacoustics (CAA) method. This study aims to explore how geometrical features influence noise generation and provide valuable insights for noise reduction. A hybrid CAA approach is proposed, employing Stress Blended Eddy Simulation (SBES), and Ffowcs-Williams and Hawkings (FW-H) acoustic analogy to predict noise radiation from standardised vehicle geometries. Initially, SBES is validated against experimental data for scaled notchback geometry, followed by assessing SBES coupled with FW-H to predict noise radiated by half-round mirrors. Subsequently, the methodology is applied to full-scale vehicle geometry with a bluff mirror mounted on one side.

The SBES predictions indicate that the flow behaviour behind the backlight of notchback becomes increasingly asymmetric with a higher backlight angle, which is consistent with the experimental findings. As the backlight angle increased, the strength of the vortex generated from the lateral edges of the backlight decreased on one side and increased on the other side, leading to an asymmetrical flow. The hybrid CAA approach predicts the flow and noise radiated from the half-round mirror in agreement with experiments and reveals increased noise radiation with higher aspect ratios but reduced noise when the mirror is inclined towards the mounting plate. Notably, the radiated noise from the half-round mirror exhibited a dipole-like structure near the plate and a monopole-like structure away from it. This observation is consistent for both variations introduced into the half-round mirror. For the full-scale vehicle model, the absence of the A-pillar is identified as the primary contributor to overall noise radiation. However, in the presence of a side-view mirror, the side window becomes a significant contributor to noise. Additionally, when the mirror is inclined, a linear reduction in the radiated noise is observed, although the vehicle's overall drag becomes nonlinear and highly dependent on the flow behaviour past the mirror.

The proposed hybrid CAA approach provides valuable insights into noise prediction for ground vehicles. By considering the impact of mirror inclination and geometric factors on noise radiation, this research contributes to the development of quieter and more aerodynamically efficient vehicles, thus fostering a comfortable and sustainable transportation environment.

To my parents

Acknowledgement

First and foremost, I would like to express my heartfelt gratitude to my Principal Supervisor (Director of Studies), Dr. Harish Viswanathan, for providing me with the opportunity to work on this subject and for his unwavering support, guidance, and encouragement throughout my PhD journey.

I extend my thanks to my first supervisor, Dr. Kevin Chow, for his encouragement, support, and advice throughout the course. Our discussions on F1 and shared interests always helped me reconnect with my passions. I would also like to thank Dr. Jonathan Potts (Second supervisor) for his invaluable feedback on presentation skills and writing.

This work would not have been possible without the financial support of Sheffield Hallam University and HORIBA MIRA. I am grateful to Dr. Osoko Shonda and Dr. Anthony Baxendale from HORIBA MIRA for his extended support.

I would like to express my appreciation to Dr. Hauke Reese for his support and advice on aeroacoustics concepts and simulations. I am also grateful to Dr. Florian Menter, Dr. Yuri Egorov, and the technical support team at ANSYS for their valuable suggestions, and in-depth discussions on the methodologies used, and the MATLAB support team for assisting me in debugging my MATLAB codes.

I extend my thanks to the researchers at Loughborough University, Chalmers University of Technology, and Friedrich-Alexander University Erlangen-Nürnberg for sharing the experimental data in an open-source format. Without their contribution, validating my simulations would have been impossible.

I would also like to thank the PGR team, especially Dr. Francis Clegg, for their assistance in navigating the administrative procedures smoothly. Additionally, I am grateful to all my colleagues at MERI for their continuous support and enjoyable discussions during coffee breaks.

Lastly, I want to express my sincere gratitude to my family and friends for always being there when I needed them and reminding me that there is life beyond the university. I am particularly thankful to my father and brothers-in-law, whose support has made it possible for me to pursue my PhD and turn my dreams into reality.

Part of the work reported in this thesis has been published in the following:

- Chode, K. K., Viswanathan, H., Chow, K., H. Reese. (2023). Investigating the Aerodynamic Drag and Noise Characteristics of a Standard Squareback Vehicle with Inclined Side-View Mirror configurations using a Hybrid Computational Aeroacoustics (CAA) Approach. *Physics of Fluids*, 35(7), 075148. <https://doi.org/10.1063/5.0156111>
- Chode, K. K., Viswanathan, H., and Chow, K. (2021). Noise emitted from a generic side-view mirror with different aspect ratios and inclinations. *Physics of Fluids*, 33(8), 084105. <https://doi.org/10.1063/5.0057166>
- Chode, K. K., Viswanathan, H., and Chow, K. (2020). Computational aeroacoustics of a generic side view mirror using stress blended eddy simulation. arXiv:2007.12783. <https://doi.org/10.48550/arXiv.2007.12783>
- Chode, K. K., Viswanathan, H., and Chow, K. (2020). Numerical investigation on the salient features of flow over standard notchback configurations using scale resolving simulations. *Computers and Fluids*, 210, 104666. <https://doi.org/10.1016/j.compfluid.2020.104666>

Part of the work reported in this thesis has been presented in the following:

- Chode K.K., Viswanathan, H., Chow, K. A comparison of numerical simulations with experimental results for flow around 20deg SAE Notchback Model, poster presentation, MERI SYMPOSIUM, March 2018.
- Chode K.K., Viswanathan, H., Chow, K. An investigation of Asymmetry in the shear-separated layer of a standard SAE notchback body using Scale Resolving Simulations, poster presentation, MERI SYMPOSIUM, December 2019.
- Chode K.K., Viswanathan, H., Chow, K. Assessment of Scale Resolving Simulations on a standard Notchback Reference model, presentation, MIRA ANNUAL PhD Seminar Series, January 2019.
- Chode K.K., Viswanathan, H., Chow, K. Numerical Investigation of SRS Simulations: Aerodynamics and Aeroacoustics, presentation, MIRA ANNUAL PhD Seminar Series, January 2020.

Abstract.....	i
Acknowledgement	ii
List of Publications	iii
List of Figures	1
List of Tables	7
Nomenclature	9
Acronyms.....	11
Chapter 1 Introduction.....	12
1.1. Background	12
1.2. Aims and Objectives	14
1.3. Thesis Outline	15
Chapter 2 Literature Review.....	18
2.1. Fundamentals of Flow	18
2.1.2. Conservation Equations	18
2.2. Turbulent flows.....	20
2.3. Turbulence Modelling	22
2.3.1. Reynolds-Averaged Navier-Stokes (RANS)	22
2.3.2. Large Eddy Simulation (LES)	23
2.3.3. Hybrid RANS-LES approach	26
2.4. Type of noise sources in ground vehicles	35
2.5. Computational Aeroacoustics (CAA) methods for road vehicles.....	38
2.5.1. Hybrid methods.....	42
2.6. Mesh for the aerodynamic and aeroacoustics studies	46
2.7. Numerical Methods	50
2.7.1. Numerical Errors.....	53
2.8. Standard Geometries	54

2.8.1. Simplified Vehicle Geometries.....	55
2.8.2. Summary of numerical simulations performed using standard vehicle geometries.	60
2.8.3. Standard Mirror Geometry.....	63
2.9. Noise Mitigation.....	65
Summary.....	68
Chapter 3 Computational Modelling Methodology.....	69
3.1. Turbulence Modelling.....	69
3.2. Acoustic Methods	71
3.3. Numerical schemes	73
3.4. Grid Size estimates	74
3.5. Simulation methodology.....	75
3.6. Methodology verification and validation.....	76
3.7. Computational resources.....	76
Summary.....	77
Chapter 4 Assessment of hybrid RANS - LES approaches using standard notchback configurations	78
4.1. Experimental data.....	79
4.2. Numerical Setup.....	79
4.2.1. Model and computational domain description.....	80
4.2.2. Length scale estimations and grid generation.....	81
4.2.3. Boundary conditions and numerical setup.....	83
4.3. Grid evaluation study	84
4.4. Verification and Validation of SAE T20.....	85
4.4.1. Aerodynamic force coefficients:.....	85
4.4.2. Pressure Coefficient (Cp) on midplane and base of the model.....	86
4.4.3. Near wake structure	88
4.4.4. Streamwise velocity profiles.....	89

4.4.5.	Streamwise velocity contours	90
4.4.6.	Assessment of flow resolution:	91
4.5.	Influence of backlight angle on the flow	94
4.5.1.	Flow behaviour on the surface of the backlight	94
4.5.2.	Pressure footprint on the backlight	98
4.5.3.	Trailing vortex structures	100
	Summary	101
Chapter 5	Investigation of Aspect Ratios and Inclinations of mirror on noise radiated ..	102
5.1.	Model and computational domain description:	103
5.2.	Grid generation and solution setup	104
5.3.	Grid Evaluation study	106
5.4.	Validation and Verification of standard HRM	107
5.5.	Effect of Aspect Ratio on Flow and noise radiated by HRM	112
5.6.	Effect of sweep angle (θ) on the flow and noise radiated by HRM	118
	Summary	124
Chapter 6	Noise radiation from a standard vehicle and its mitigation	126
6.1.	Geometry description and computational domain	126
6.2.	Grid generation and Numerical Setup	128
6.3.	Comparison of current results against previously published results	129
6.4.	Side-view mirror and its influence on Drag Coefficient and Hydrodynamic pressure fluctuations	133
6.5.	Effects of Inclining the Mirror on the aerodynamic characteristics of SAE T4	137
6.6.	Effects of inclining the mirror on the acoustic characteristics of SAE T4	143
	Summary	151
Chapter 7	Discussion	153
7.1.	The relevance of SBES turbulence model for ground vehicle aerodynamics and aeroacoustics	153
7.2.	Accuracy of the adopted methodology	154

7.3. Critical parameters affecting both drag and noise and their relationships	155
7.4. Limitations of the work	157
7.5. Recommendations	158
Chapter 8 Conclusions.....	159
Appendix – A Location of Surface Probes and Microphones	161
Appendix – B List of programs	164
B.1. Access to Cluster and File Management	164
B.2. Fluent Activation files	166
B.2.1. Fluent in GUI mode.....	166
B.2.2. Fluent in batch Mode.....	166
B.3. User Defined Functions and Scalars	170
B.3.1. User-Defined Function.....	170
B.3.2. User-Defined Scalar	172
B.4. Data Processing using MATLAB	174
B.4.1. Surface Plots from Experimental Data.....	174
B.4.2. Surface plots for CFD data.....	178
B.4.3. Script for calculating pressure drag.....	180
References.....	183

List of Figures

Fig. 1.1. Contribution of various noise sources to the overall noise in both conventional and electric vehicles (Goetchius, 2011).....	12
Fig. 2.1. A depiction of the observed energy and its cascade. The above graph is also referred to as the energy spectrum.....	21
Fig. 2.2. Comparison of mesh resolution for a) full RANS, b) full LES, and c) Hybrid based on a flat plate boundary layer.....	27
Fig. 2.3. Illustration of the switch between RANS and LES in the DES approach.....	28
Fig. 2.4. Aeroacoustics sources in the side glass region (Oettle and Sims-Williams, 2017) ..	36
Fig. 2.5. Identification of type of noise source a) Monopole, b) Dipole, and c) Quadrapole (Russell et al., 1999). ..	38
Fig. 2.6. Comparison of direct and hybrid methods used for evaluating aeroacoustics. Here $(.)_h$ and $(.)_a$ represents the hydrodynamic and acoustic components.	39
Fig. 2.7. Type of meshes: a) Structured Mesh, b) Unstructured mesh, c) Hybrid Mesh, and d) Generalised Mesh (Koomullil et al., 2008).....	48
Fig. 2.8. Cut sections of a) hexcore and b) poly-hexcore generated for an aircraft wing with flaps (Karkoulis et al., 2022).....	49
Fig. 2.9. Overview of transition layer generated in unstructured polyhedral–dominant hex mesh (Zore et al., 2019).....	49
Fig. 2.10. Schematic representation of the DrivAer model in three configurations (Heft et al., 2012). ..	55
Fig. 2.11. Schematic representation of the wake topology behind (a) square-back, (b) fastback and (c) notchback geometries (Pavia, 2019).....	56
Fig. 3.1. Flow chart presenting the simulation procedure for performing an aeroacoustics study	75
Fig. 4.1. The dimensions of the SAE notchback geometry are in mm, and the backlight angle θ^* in degrees ranges from 20° - 40°	79
Fig. 4.2. Layout of the computational domain with normalised dimensions and the specified boundary conditions.....	80
Fig. 4.3. Grid used in assessing turbulence models a) Cut in the xz plane showing the grid distribution around the body. b) Detailed view of the mesh with highlighted zones TB – Taylor	

Box, DR 1,2 – Domain Refinement, and FR – Focus Region. c) a detailed view of the boundary layer, and d) a detailed view of refinements behind the model.	82
Fig. 4.4. Time-averaged Streamwise velocity profiles (right) over the backlight and in the wake (left) of SAE T20 body compared against the grids used in this study.	84
Fig. 4.5. Time-averaged pressure coefficient (C_p) obtained from turbulence model predictions on the midplane of the SAE T20 body compared against the experimental data (Wood et al., 2014).	86
Fig. 4.6. Numerical predictions of the time-averaged pressure coefficients (C_p) obtained at the base of the SAE T20 compared against the experimental data (Wood et al., 2014).	88
Fig. 4.7. Wake structure comparison of turbulence models used in the present study against experimental data (Wood et al., 2014). The centres of the upper and the lower recirculation bubbles are indicated by e'' and e' , respectively.	89
Fig. 4.8. Predictions of the normalised, time-averaged streamwise velocity profiles from different turbulence models at several locations compared against the experimental data (Wood et al., 2014). In the zoomed image indicate the axis for the velocity profiles presented.	90
Fig. 4.9. Normalised time-averaged velocity magnitude contours compared with the experimental data (Wood et al., 2014). From top to bottom, each row corresponds to the locations $x = -190$ mm, -240 mm, -290 mm, -340 mm, -380 mm and -420 mm, respectively.	91
Fig. 4.10. Iso-surface of the instantaneous Q-criterion generated at $0.014 s^2$ for all turbulence models and coloured by Turbulent Viscosity Ratio.	92
Fig. 4.11. The turbulence energy spectrum ($E(k)$) of SDES and SBES in the near wake of the model at point ($x = 440$ mm, $y = -180$ mm, $z = 0$).	93
Fig. 4.12. Assessment of flow resolution a), c) Shielding function of SBES and SDES in streamwise and spanwise direction at $z = 0$ mm and $x = 380$ mm respectively, b), d) TVR of all the turbulence models in streamwise and spanwise direction at $z = 0$ mm and $x = 380$ mm respectively.	94
Fig. 4.13. Time-averaged values of a) Wall shear stresses (Friction lines) and b) Experimental results (Oil flow) presented by (Wood, 2015) plotted on the rear of the model for all the backlight angles used in this current study.	97
Fig. 4.14. Time-averaged values of a) pressure coefficient predicted by numerical simulation and b) Experimental pressure coefficient results presented by (Wood, 2015), plotted on the rear of the model for all the backlight angles used in this current study.	99
Fig. 4.15. Iso surface of time-averaged velocity magnitude ($30 ms^{-1}$) coloured with normalised time-averaged x vorticity for all the backlight angles investigated.	100

Fig. 5.1. Geometrical representation of a) Half-Round Mirror as proposed by Höld et al.(1999) and Siegert et al.(1999), b) Half-Round Mirror with an Aspect Ratio (AR) of 2.5D and c) Half-Round Mirror with sweep angle represented by θ	103
Fig. 5.2. a) Geometrical representation of the domain with normalised dimensions and boundary conditions used in the simulation, b) Layout of the sensor position in the wake of the mirror, and c) Layout of the microphones around the mirror.	104
Fig. 5.3. Grid used for validation study a) Overview of the grid generated for the grid 3 with local refinement, b) Detailed view of the mesh on the mirror and its vicinity, and c) Isometric view of the cells on the surface of the mirror and the plate.	105
Fig. 5.4. a) time-averaged Pressure Coefficient (c_p) on the surface of the mirror, b) Hydrodynamic pressure fluctuations (HPF) extracted at two different sensor positions, s112 on the mirror and s120 on the plate. Solid vertical lines represent the mesh cut-off frequencies, and c) a schematic of the sensor placed for extracting pressure on the mirror.	107
Fig. 5.5. a) Comparing the time-averaged Pressure Coefficient (c_p) on the mirror's surface generated at several sensors is compared against experimental data and published Numerical Results. b) schematic of the sensor layout on the mirror for measuring the pressure coefficients.	108
Fig. 5.6. Dominant Flow patterns around the HRM generated on the plane $y = 0.01D$ and coloured with Mean Pressure Coefficient. L_{hx} , L_{hz} and L_{ws} represent the normalised length of the horseshoe vortex from the mirror in the streamwise direction, the normalised height of the horseshoe vortex from the lateral edge of the mirror, and the normalised length of the wake structure measured from the rear face of the mirror, respectively.	109
Fig. 5.7. HPF extracted at two locations on the mirror, s111 and s113, are compared between the grids used in the study against a) experimental data and b) numerical data. The legends in both s111 and s113 are same.	110
Fig. 5.8. HPF extracted at four locations on the plate, s119 and s121-s123, are compared between the grids used in the study against a) experimental data and b) numerical data. The legends are same for s119 and s121-s123.	111
Fig. 5.9. SPL extracted at five locations around the mirror, M1, M4, M10, M11 and M14, are compared between the grids used in the study against a) experimental data and b) numerical data. The legends shown in M1 are same for all the plots.	112
Fig. 5.10. Comparison of time-averaged velocity magnitude contour plots superimposed with velocity streamlines on midplane for a) AR = 1, b) AR = 1.25, c) AR = 1.5, d) AR = 2, and e) AR = 2.5. e and e' represent the centre of recirculation bubbles formed behind the mirror..	113

Fig. 5.11. Comparison of vortical structures of an instantaneous flow field visualised by iso-surfaces of $Q = Q = 10^3 \text{ s}^{-2}$ coloured with instantaneous x-velocity for all the investigated for a) AR = 1, b) AR = 1.25, c) AR = 1.5, d) AR = 2 and e) AR = 2.5..... 114

Fig. 5.12. Comparison of normalised pressure fluctuations on the plate between a) AR = 1, b) AR = 1.25, c) AR = 1.5, d) AR = 2, and e) AR = 2.5. Here Pu and Pd indicate the pressure zone formed due to the interaction of the lateral vortices with the plate. 115

Fig. 5.13. Comparison of HPF extracted on the mirror at a) s112 and b) s113 between AR = 1, 1.25, 1.5, 2 and 2.5. The sensor's location is represented by a black dot in the schematic shown in the plots..... 116

Fig. 5.14. Comparison of HPF extracted on the mirror at a) s119, b) s121, c) s122, and d) s123 between AR = 1, 1.25, 1.5, 2 and 2.5. The sensor's location is represented by a black dot in the schematic shown in the plots. 116

Fig. 5.15. Comparison of SPL extracted at four microphone positions: a) M1, b) M4, c) M10, and d) M14 between AR = 1, 1.25, 1.5, 2 and 2.5..... 117

Fig. 5.16. The overall sound pressure level extracted at several microphones placed in a circular array at planes a) $y = 0.25D$ and b) $y = 2D$ plate are compared for AR = 1, 1.25, 1.5, 2 and 2.5 investigated, and c) illustrates the planes at which the directivity are plotted..... 117

Fig. 5.17. Comparison of the flow separation between a) $\theta = 0^\circ$, b) $\theta = 8^\circ$, c) $\theta = 16^\circ$, d) $\theta = 24^\circ$, and $\theta = 32^\circ$ represented by friction lines superimposed on the contours of time-averaged pressure coefficient. 118

Fig. 5.18. Comparison of time-averaged velocity magnitude contour plots superimposed with velocity streamlines on midplane for a) $\theta = 0^\circ$, b) $\theta = 8^\circ$, c) $\theta = 16^\circ$, d) $\theta = 24^\circ$, and e) $\theta = 32^\circ$. e and e' represent the centre of recirculation bubbles formed behind the mirror..... 119

Fig. 5.19. Comparison of time-averaged velocity magnitude streamlines superimposed on pressure coefficient generated on a plane at $y = 0.01D$ between all the sweep angles investigated: a) $\theta = 0^\circ$, b) $\theta = 8^\circ$, c) $\theta = 16^\circ$, d) $\theta = 24^\circ$, and e) $\theta = 32^\circ$ 120

Fig. 5.20. Comparison of vortical structures of an instantaneous flow field visualised by iso-surfaces of $Q = 10^3 \text{ s}^{-2}$ coloured with instantaneous x-velocity between all the sweep angles investigated: a) $\theta = 0^\circ$, b) $\theta = 8^\circ$, c) $\theta = 16^\circ$, d) $\theta = 24^\circ$, and e) $\theta = 32^\circ$ 121

Fig. 5.21. Comparison of time-averaged normalised pressure fluctuations on the plate for all the sweep angles investigated: a) $\theta = 0^\circ$, b) $\theta = 8^\circ$, c) $\theta = 16^\circ$, d) $\theta = 24^\circ$, and e) $\theta = 32^\circ$. Pu and Pd represent the pressure regions formed due to the lateral vortex, and P_m represents the pressure region formed due to the impingement of the flow. 122

Fig. 5.22. Comparison of HPF extracted on the mirror at a) s111 and b) s114 for all the sweep angles investigated: 0° , 8° , 16° , 24° and 32° 123

Fig. 5.23. Comparison of HPF extracted on the plate at a) s119, b) s120, c) s122 and d) s123 for all the sweep angles investigated: 0°, 8°, 16°, 24° and 32°	123
Fig. 5.24. Comparison of SPL at four microphone positions a) M1, b) M4, c) M10, and d) M14 for all the sweep angles investigated: 0°, 8°, 16°, 24° and 32°	123
Fig. 5.25. Comparison of overall sound pressure level extracted at 36 microphones placed in a circular array at planes a) $y = 0.25D$ and b) $y = 2D$ for all the sweep angles investigated: 0°, 8°, 16°, 24° and 32°, and c) illustrates the layout of the sensors located.	124
Fig. 6.1. a) SAE Reference squareback (SAET4) model with a bluff mirror mounted in the positive spanwise direction; b) naming conventions used for SAE T4 design features; c) schematic representation of surface pressure probe locations on the side window.	127
Fig. 6.2. Overview of computational domain with boundary conditions used in this study.	128
Fig. 6.3. a) Overview of a medium grid with local refinement zones used for validation study, b) grid generated closer to forebody, side window (zoom plane), and spanwise cut plane...	129
Fig. 6.4. Comparison of flow patterns on the side of SAET4 a) experimental data (Müller et al., 2014) and b) numerical prediction obtained from the SBES.	130
Fig. 6.5. Comparison of amplitude of pressure fluctuations in dB on the side window between experiment (Nusser, 2019) and numerical results for a) p'_{RMS} , b) 150 Hz, and c) 500 Hz. A reference pressure of 2×10^{-5} pa.	132
Fig. 6.6. Comparison of HPF between experiment (Nusser, 2019) and numerical (SBES) prediction for sensors a) pos1 and b) pos15. The locations of the sensors are marked with red dots in the schematic of the graph. Refer to Fig. 6.1(c) shows the number labelling of the sensors on the side window.....	133
Fig. 6.7. Comparison between the predictions made by SBES and LES (Nusser, 2019) at four different positions in the side view, as illustrated by the red dots in the schematic: a) pos1, b) pos2, c) pos20, and d) pos32. Refer to Fig. 6.1(c) shows the number labelling of the sensors on the side window.	133
Fig. 6.8. Comparison of vortical structures of an instantaneous flow field visualised by iso-surfaces of $Q = 1100 \text{ s}^{-2}$ coloured with instantaneous x-velocity for SAE T4 a) with mirror and b) without mirror, while c) and d) represent the zoomed image of the flow structures around the A-pillar and side window.....	135
Fig. 6.9. Comparison of normalised p'_{rms} (Np'_{rms}) (defined as $Np'_{rms} = p'_{rms}/\text{max.}p'_{rms}$) where $\text{max.}p'_{rms} = 142.73 \text{ dB}$ (predicted from the case with mirror) between a) with mirror and b) without mirror cases. The scales presented are intentionally different due to the level of intensity predicted in both cases. The changes in the pressure fluctuations are highlighted using a dotted oval shape.....	136

Fig. 6.10. Comparison of HPF between experiment SAET4 with and without a mirror at sensors a) pos1 and b) pos15. The locations of the sensors are marked with red dots in the schematic of the graph (see Fig.1(c) for the number labelling of the sensors on the side window)..... 137

Fig. 6.11. Schematic of inclination of the mirror. Here, θ was varied from 0° to 32° in intervals of 8° . w_m and w'_m represent the sides with and without a mirror, respectively. 137

Fig. 6.12. Comparison of the coefficient of pressure at the base of SAE T4 (top) and the wake structure near the base visualised by the generated isosurface of the mean total pressure $C_{p, \text{tot}} = -0.2$ (bottom) between all the cases investigated. 139

Fig. 6.13. Relationship between % difference in side forces and drag coefficient of vehicle ($C_{d_{\text{vehicle}}}$) with respect to inclination angle (θ)..... 141

Fig. 6.14. Comparison of time-averaged vorticity contours superimposed with velocity streamlines on the midplane of the side-view mirror at $y/H = 0.68$ between a) 0° , b) 8° , c) 16° , d) 24° , and e) 32° 141

Fig. 6.15. Time-averaged velocity magnitude plotted in the wake of the mirror and SAE T4 for $\theta =$ a) 0° , b) 8° , c) 16° , d) 24° , and e) 32° . V_1 and V_2 represent mirror-induced vortices emerging from the top and bottom faces of the mirror, respectively..... 143

Fig. 6.16. Comparison of time-averaged wall shear stresses on the forebody of SAE T4 with varying sweep angles: a) 0° , b) 8° , c) 16° , d) 24° , and e) 32° . f) shows a schematic of obtaining a tangent for the streamline..... 145

Fig. 6.17. Comparison of RMS of pressure fluctuations in dB on the side window for all sweep cases investigated for a) 0° , b) 8° , c) 16° , d) 24° , and e) 32° 146

Fig. 6.18. Comparison of the HPF between all sweep angles investigated at specific sensor locations is illustrated by the red dot in the schematic for a) pos1 and b) pos15. Refer to Fig.6.1(c) shows the number labelling of the sensors on the side window. 147

Fig. 6.19. Component-wise comparison of SPL evaluation at two probes positioned away from SAE T4. a) Side-view mirror, b) side window, c) frame and d) A-pillar. 148

Fig. 6.20. Directivity plot comparison among all sweep angles investigated at a) $z = 0.56 W$ and $0.62 W$. On the left, a single source is used to evaluate directivity, while on the right, all the sources are selected. 150

Fig. 6.21. Directivity plot comparison amongst all the sweep angles investigated at a) $z = 1.13 W$ and $2.5 W$. On the left, a single source is used to evaluate directivity, while on the right, all the sources are selected. 151

Fig. 7.1. Relationship between θ , α , and L_{ws} 156

Table 2.1 Overview of turbulence modelling approaches for road vehicles.....	31
Table 2.2 Classification of noise sources and their generation mechanisms	37
Table 2.3 Detail comparison between DNC and Hybrid methods.....	40
Table 2.4 Merits and demerits of various meshes used in CFD.....	47
Table 2.5 Summary of the numerical schemes	51
Table 2.6 Aerodynamic characteristics of the standard fastback geometries	57
Table 2.7 Aerodynamic characteristics of the standard notchback geometries	58
Table 2.8 List of previous studies conducted using simplified geometries.	61
Table 2.9 A review of studies using geometrical features to mitigate noise.....	67
Table 3.1 Review of case studies - accuracy of SBES predictions.....	71
Table 3.2 Mesh resolution recommendations for LES and DDES cases	75
Table 3.3 HPC specifications used for computing both aerodynamic and aeroacoustics simulations.....	76
Table 4.1 Characteristic length scales of SAE T20.....	81
Table 4.2 Comparison of grids generated for obtained SAE T20 with WRLES recommendations	82
Table 4.3 Numerical methods used for SAE notchback	83
Table 4.4 Aerodynamic force coefficients assessed from the grid resolution study.....	84
Table 4.5 Time-averaged Aerodynamic Force Coefficients for SAE T20	85
Table 4.6 Contribution of each body part to the total time-averaged pressure drag coefficient	86
Table 4.7 The time-averaged drag coefficient predicted by the numerical models for various backlight angles (θ) compared with experimental data (Wood, 2015).....	96
Table 5.1 Comparison of mesh resolution used in the current study	104
Table 5.2 Numerical methods used for HRM cases.....	105
Table 5.3 Comparison of Drag Coefficient against previously published numerical results	106
Table 5.4 Normalised lengths of the time-averaged flow features compared against published numerical results.	108
Table 5.5 Comparison of the change in the centre of recirculation bubble (e) and normalised lengths of time-averaged flow features with change in AR.....	113
Table 6.1 Comparison of frontal area (F_A) and drag coefficient ($Cd_{vehicle}$) between SAET4 with and without mirror	135

Table 6.2 Comparison of noise radiated from SAE T4 with mirror and without mirror. The units for the values presented are in dB	136
Table 6.3 Comparison of force coefficients and pressure coefficients on the base between all the inclination angles (θ) investigated in this study.....	138
Table 6.4 Comparison of difference obtained for the CsA evaluated at the mirror side (w_m) and no mirror side (w'_m) between all the angles investigated.	140
Table 6.5 Comparison of the vortex strength evaluated at streamwise planes between all the sweep angles investigated. All the values presented for vortex strength have units of '1/s'.142	142
Table 6.6 Comparison of the change in the angle made between A-pillar and streamline (α) and the normalised lengths of time-averaged flow feature with the change in θ	144
Table 6.7 Comparison of noise radiated OASPL (dB) in the vicinity of SAE T4 for all the sweep angles investigated.	147

Nomenclature

x, y, z	3D Cartesian coordinates (Streamwise, normal, spanwise)	m
p^a	Acoustic Pressure	Pa
CdA	Area weighted Drag Coefficient	-
θ^*	Backlight Angle	Deg
C_{Db}	Base Drag Coefficient	-
e'	Center of Lower Recirculation bubble	m
e''	Center of Upper Recirculation bubble	m
C_p	Coefficient of Pressure	-
p_{ij}	Compressive Stress tensor	-
ρ	Density	Kg/m ³
D	Diameter of the Half Round Mirror	m
$\Delta x^+, \Delta y^+, \Delta z^+$	Dimensionless wall units	-
$\delta(f)$	Dirac Delta function	-
C_D	Drag Coefficient	-
$Cd_{vehicle}$	Drag Coefficient of the whole vehicle	-
v_t	Eddy/Turbulent Viscosity Ratio	-
\tilde{S}	Filtered Strain rate	-
$\tilde{\Omega}$	Filtered Vorticity	-
ν	Fluid viscosity	Pa.s
U_∞	Freestream velocity	m/s
C_{Df}	Front Slant Drag Coefficient	-
F_A	Frontal area	m ²
$H(f)$	Heaviside function	-
h	Height of the Half Round Mirror	m
H	Height of the Vehicle	m
η	Kolmogorov length scale	m
L_{hz}	Length of horseshoe vortex in spanwise	m
L_{hx}	Length of horseshoe vortex in streamwise	m
L_{ws}	Length of the mirror wake	m
L	Length of the Vehicle	m
C_L	Lift Coefficient of the model	-
$Cl_{vehicle}$	Lift Coefficient of the whole vehicle	-
T_{ij}	Lighthill Stress tensor	-
p'_L	Loading Term	-
M	Mach Number	-
f_{mc}	Mesh cut-off frequency	Hz
V_1, V_2	Mirror induced vorticity	-
C_p	Pressure coefficient	-
C_{Dp}	Pressure Drag Coefficient	-
p'	Pressure fluctuations	Pa

p'	Pressure Perturbations	Pa
C_{Dr}	Rear Slant Drag Coefficient	-
Re	Reynolds Number	-
Re_L	Reynolds Number based on Length of the Vehicle	-
τ_{ij}	Shear stress tensor	-
f_s	Shielding function	-
w_m	Side of the vehicle with mirror	-
w'_m	Side of the vehicle without a mirror	-
Ω	Specific Dissipation Rate	1/s
c	Speed of sound	m/s
S	Strain Rate magnitude	-
S_{ij}	Strain rate tensor	-
St	Strouhal number	-
λ_t	Taylor microscale	m
α	The angle between the A-pillar and the flow interaction line	degree
θ	The angle of mirror inclination	Deg
L_c	The characteristic length of the Mirror	m
l_{DI}	The dissipative range	m
l_{EI}	The inertial subrange	m
Δ_c	The length scale of the cell	m
L_{hx}	The thickness of the horseshoe vortex	m
p'_t	Thickness Term	-
t	Time	s
k	Turbulence Kinetic Energy	m^2/s^2
L_t	Turbulent Length Scale	m
η_{mw}	Viscous boundary sublayer	m
τ_w	Wall-Shear Stress	
L_{hy-}	Width of the horseshoe vortex in the negative normal direction	m
L_{hy+}	Width of the horseshoe vortex in the positive normal direction	m
W	Width of the Vehicle	m

APE	Acoustic Perturbation Equation
AR	Aspect Ratio
CAA	Computational Aeroacoustics
CBC	Convective Boundedness Criterion
CFL	Courant-Friedrichs-Lewy
DDES	Detached Delayed Eddy Simulation
DES	Detached Eddy Simulation
DM	Direct Method
FW-H	Ffowcs-Williams and Hawkings
GIS	Grid Induced Separation
HPF	Hydrodynamic Pressure Fluctuations
HM	Hybrid Method
IDDES	Improved DDES
IDDES	Improved Detached Delayed Eddy Simulation
KI	Kirchhoff Integral
LES	Large Eddy Simulation
NS	Navier-Stokes
NVD	Normalised variable diagram
OASPL	Overall Sound Pressure level
PPW	Points per wave
RANS	Reynolds Averaged Navier Stokes
RMS	Root Mean Square
SA	Spalart Allmaras
SBES	Stress-Blended Eddy Simulation
SDES	Shielded Detached Eddy Simulation
SPL	Sound Pressure Level
SRS	Scale Resolving Simulations
SSL	Separated Shear Layer
SST	Shear Stress Transport
TVD	Total Variation diminishing
TKE	Turbulence Kinetic Energy
TVR	Turbulent Viscosity Ratio
UD	Upwind Differencing
URANS	Unsteady Reynolds Average Navier Stokes
WALE	Wall-Adapting Local Eddy-Viscosity

1.1. Background

Noise perceived inside and outside a vehicle is a combination of various sources that contribute to the overall noise. Each noise source has its own noise generation mechanism: a rolling noise source generated by the interaction of the tire with the road (Li et al., 2018; Molisani et al., 2003), powertrain noise sources generated by the engine and powertrain (Qatu, 2012), aerodynamic noise from the airflow around the vehicle (Hartmann et al., 2012), other noise sources such as sloshing noise resulting from the interaction of liquids with solid surfaces (mainly from fuel tanks)(Ganuga et al., 2014; Jadon et al., 2014), and noise sources generated from the vibrations of the vehicle structure (Elliott, 1994; Pang, 2018). The contribution of these noise sources to the overall noise for both conventional and electric vehicles is illustrated in Fig. 1.1.

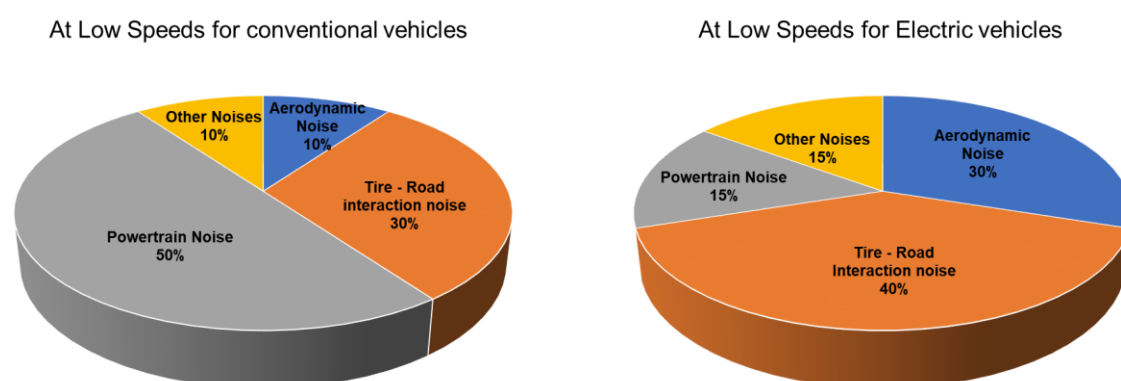


Fig. 1.1. Contribution of various noise sources to the overall noise in both conventional and electric vehicles (Goetchius, 2011).

Typically, aerodynamic noise becomes dominant at higher driving speeds (> 100 km/h) in conventional vehicles (Helfer, 2005) and can even mask other noise sources. For electric vehicles, aerodynamic noise dominates even at lower speeds due to significant reduction in power train noise. The primary source of aerodynamic noise is the turbulence present around vehicle body and its external fixtures such as windscreen wipers, roof-mounted racks, a-pillars, and side-view mirrors and turbulence interaction with solid surfaces. Different mechanisms can generate aerodynamic noise; for instance, aerodynamic noise is generated by flow separation, leading to turbulent flow at the exterior fixtures of the vehicle, such as side-view mirrors. Turbulent flow generates noise because turbulence is stochastic by nature, and when it interacts with the vehicle surface, it tends to induce pressure fluctuations which generate noise. As a result, the side window experiences both hydrodynamic pressure fluctuations due

to the interaction of separated flow with the vehicle surfaces and acoustic pressure fluctuations due to the turbulent flow field caused by flow separation.

Several numerical and experimental techniques can be employed to evaluate exterior noise generated by pressure fluctuations. At an early stage in the development process, vehicle manufacturers prefer numerical methods such as Computational Aeroacoustics (CAA) to predict sound sources and radiated noise levels. Experimental techniques can only be employed in the late phases of the vehicle development process, as the details present on the prototypes are sufficiently high in this phase. Component-based acoustic evaluations and isolated studies can be performed quickly using numerical techniques, which are challenging to perform using experimental techniques. In numerical techniques, the noise generated and radiated outside and transmitted inside the vehicle is obtained by combining CAA approaches with Computational Fluid Dynamics (CFD) simulations.

The accuracy of the predicted sound field depends on the accurate prediction of the turbulent flow field and level of flow resolution obtained. In CFD, numerous turbulence modelling approaches are derived from NS equations to resolve the different length scales present in turbulent flow, and the most widely used turbulence approach to resolve the flow field around the vehicle is the Reynolds-averaged Navier–Stokes (RANS) equations. RANS approaches are less complicated to model and require fewer computational resources but include several assumptions about turbulent flow behaviour. For example, assuming that a single length and time scale characterise the turbulent flow limits the accuracy of resolving the flow field, resulting in an inaccurate acoustic solution. Large-eddy simulation (LES) is employed to achieve higher accuracy in resolving the flow field and is the preferred approach for aeroacoustics studies (Wagner et al., 2007). LES uses a spatial filter to separate the resolved turbulence from the modelled turbulence, and this filter width should ideally be the same as that of the smallest turbulent eddy of interest. In addition, the grid generated should be capable of resolving the flow up to 80% of turbulence (Pope, 2001); as a result, denser grids are needed closer to the walls where smaller length scales are present, resulting in a significant increase in the overall computational costs.

Hybrid RANS-LES models, such as Detached Eddy Simulation (DES), have been developed to overcome LES computational challenges, but DES tends to over-predict the flow separation under heavy refinement grids. Thus, several improvements have been proposed to DES approaches by introducing different shielding functions such as Delayed DES (DDES), Improved DDES (IDDES), Shielded Detached Eddy Simulation (SDES) and Stress Blended

Eddy Simulation (SBES). Despite the advantages of hybrid RANS-LES models over LES in terms of computational requirements, the accuracy of each hybrid RANS-LES in predicting flow features that are adequate for evaluating the acoustic field is yet to be determined. Once the flow field is determined, acoustic models such as the acoustic perturbation wave equation (APE) and Ffowcs-Williams and Hawkings (FW-H) can be used to obtain the noise propagation and intensity of the radiated noise at a distance, respectively.

From a vehicle perspective, the primary sound sources are the side-view mirror and a-pillar, and the turbulent flow past these noise sources induces hydrodynamic pressure fluctuations in the side window. The noise radiated from these components, their intensity, and the structure of the radiated noise from the sources are essential to comprehend before investigating approaches to mitigate noise; therefore, state-of-the-art numerical methods must be sought in the vehicle development phase. Nevertheless, several outstanding questions and challenges are not yet well understood, such as *a)* what approaches can be employed to predict surface pressure fluctuations? *b)* What level of resolution is required to resolve aerodynamic noise adequately? *c)* How computationally feasible are such approaches in predicting the changes in vehicle geometries that may lead to changes in both aerodynamic drag and noise?

Hypothesis:

In this thesis, a systematic approach was followed to address the questions mentioned above, and the hypotheses were as follows:

The application of hybrid RANS-LES approaches, such as the SBES, can be effective in analysing the aerodynamics and aeroacoustics of idealised vehicle and mirror geometries, especially when coupled with acoustic analogies. Geometrical modifications, such as altering aspect ratios, rounding corners, and inclining the geometry away from the flow, are used to mitigate noise radiation from bluff bodies, such as cubes and cylinders. The same modifications can be applied to mirror geometries, including half-round mirrors, to reduce the overall noise levels while maintaining the optimal aerodynamic performance when mounted on a vehicle body. Nevertheless, this raises the question of whether similar geometrical changes can be made to idealised mirror geometries mounted on a vehicle body to achieve noise mitigation, and would they reduce overall noise levels without negatively affecting aerodynamic performance?

1.2. Aims and Objectives

The numerical prediction of noise generated by vehicles is an inherently complex task. While hybrid Computational Aeroacoustics (CAA) methods have shown promise in this

regard, the challenge lies in obtaining a computationally feasible approach that is both reliable and robust. Therefore, this thesis aims to establish "A computationally feasible methodology for aeroacoustics analysis to investigate drag and noise emanating from standard ground vehicles." To achieve this overarching goal, the following sub-aims have been formulated, each designed to address various facets of the hypothesis stated above:

Sub-Aims:

- a) Assess a fleet of hybrid turbulence models based on the recently developed hybrid RANS-LES formulation to predict salient aerodynamic features of standard notchback vehicle configurations.
- b) Identify suitable CAA approaches that work together with approaches assessed *a)* to predict aerodynamically generated noise. A subsystem that is as simple as a standard mirror configuration is considered, so a thorough understanding of the CAA approaches can be obtained.
- c) The next step is to apply the knowledge gained from *a)* and *b)* to a different vehicle geometry, such as a standard square-back model embedded with a simple mirror, to predict and identify the influence of the a-pillar, side window, and mirror on aerodynamically generated noise.
- d) Finally, this thesis aims to examine the crucial geometrical features that contribute to both *a)* the aerodynamic drag and *b)* the noise emitted from the vehicle.

Objectives:

1. To validate a hybrid RANS-LES methodology and assess its robustness by examining flow structures sensitive to geometric variations in standard vehicle design, presenting both qualitative and quantitative changes in flow features and aerodynamic characteristics.
2. To validate and assess the methodology developed in the aerodynamic study with acoustic analogies for obtaining noise generated by standard side-view mirror geometry identified in the literature.
3. To obtain geometrical features that influence the noise radiated from side-view mirror and performing a comparative analysis of noise intensity and radiation structure between various geometrical features introduced to idealised mirrors, aiming to ascertain a CAA methodology for aeroacoustics study and optimal noise mitigation strategy.

4. Leveraging the previously used CAA methodology, the research evaluates noise generated by a full-scale standard vehicle geometry commonly used in aeroacoustics investigations, refining the methodology to suit full-scale geometry and validating it against available experimental data.
5. Investigating the influence of side-view mirrors on both aerodynamic characteristics and noise generation using the validated CAA methodology, the study also assesses the contribution of other geometric features, such as the A-pillar, and conducts a qualitative analysis of flow structures around the forebody of the vehicle to determine mirrors impact.
6. By introducing idealistic side-view mirror geometrical configurations, the study identifies critical geometric features responsible for noise generation and attempts to investigate the relationship between drag and noise of a full-scale vehicle, thereby providing valuable insights into aeroacoustics investigations.

1.3. Thesis Outline

This thesis is organised as follows.

- **Chapter 2** presents a literature review of the fundamental flow fields around vehicles and noise generation resulting from these flow fields. In addition, this chapter introduces different turbulence modelling approaches and acoustic methodologies used to evaluate noise generation and its limitations. A detailed overview of aerodynamic and aeroacoustics studies of several generic vehicle bodies is also presented.
- **Chapter 3** describes the methodologies adopted in this thesis for turbulence modelling and CAA. It also introduces various meshing strategies and discretisation schemes used in this study.
- **Chapter 4** presents an aerodynamic analysis of a scaled generic notchback vehicle using hybrid RANS-LES turbulence models. The behaviour of pressure and velocity over the notchback model was analysed and validated against previously published experimental results. The complex interaction of the flow structures at the rear of the notchback model was analysed using different rear slant angles. The grid generated in this study was based on wall-normalised units and the estimated characteristic lengths. Furthermore, the predicted flow topologies for various backlight angles were compared with previously published data to assess the robustness of the proposed methodology.
- **Chapter 5** implements the hybrid RANS-LES methodology used in Chapter 4 with acoustic methods for predicting the radiated noise. Chapter 5 presents a suitable approach for predicting noise based on hybrid RANS-LES models and an acoustic

analogy. Two different meshing methodologies were employed based on hybrid and structured meshes. The radiated noise is predicted for standard mirror geometry using different acoustic analogies to obtain a suitable strategy for noise prediction. Realistic configurations of the mirror were employed in the standard mirror geometry to evaluate the structure and quality of the radiated noise.

- **Chapter 6** presents an investigation of a full-scale standard vehicle geometry with a bluff mirror mounted on the surface closer to the side window, using the knowledge gained from Chapter 5. The validation and verification of the study were conducted using published experimental and numerical data. The surface pressure fluctuations exerted by the turbulent flow were quantified by obtaining pressure fluctuation data from the surface probes, and the critical flow features responsible for the generated pressure fluctuations on the surfaces were identified. Furthermore, the influence of geometrical variation on *a*) critical flow features, *b*) radiated noise and its structure, and *c*) aerodynamic characteristics of the mirror and overall vehicle are analysed.
- **Chapter 7** discusses the quality and accuracy of the results obtained from previous chapters. The relevance of the results in the context of academia and industry are discussed highlighting potential questions yet to be answered and alternative methods and techniques that may be implemented. Additionally, this chapter presents the limitations of the work carried along with the recommendations.
- **Chapter 8** presents concluding remarks for the thesis. Finally, the thesis is supplemented with appendices that include the following. Appendix A contains the location of surface probes and microphones used and Appendix B contains the scripts to use SHU cluster and file management systems, Fluent activation files and MATLAB codes used for several calculations and postprocessing results.

This chapter introduces the fundamentals of flow and the governing equations, assumptions, and techniques used to evaluate turbulent flow fields around ground vehicles. The noise generation mechanism due to turbulent flow is introduced, along with the classification of noise sources observed from the flow past a ground vehicle and its components. A review of feasible approaches for predicting the aeroacoustics performance of ground vehicles is presented. Due to the incompressible flow assumption, an overview of acoustic analogies coupled with recently developed turbulence modelling approaches, such as hybrid RANS-LES for ground vehicles, is also presented. In addition, the choice of grids available for aeroacoustics studies is presented in this chapter. Furthermore, an overview of generic and standard vehicle configurations is provided, and in the end, the choice of grids, turbulence models, and standard geometries used in this study are summarised.

2.1. Fundamentals of Flow

In fluids, the flow motion can be described by the governing equations of fluid mechanics. The variables that describe the fluid, such as air, are density ρ , pressure p , velocity u , and temperature T , which are linked by fundamental physical laws, such as the conservation of mass, momentum, and energy. This set of equations is often referred to as Navier-Stokes (NS) equations in numerical fluid mechanics.

The conservation equations are presented in generic form in the following sections. The derivations of these conservation equations are not presented here but are available in standard textbooks.

2.1.2. Conservation Equations

The continuity equation can be derived from the physical law of mass conservation inside a closed system and is presented below for compressible flows.

$$\frac{\partial \rho}{\partial t} + \frac{\partial(\rho u_i)}{\partial x_i} = 0 \quad (2.1)$$

Here, time is defined as t and u_i as a velocity component in the x -direction, and the derivation of the momentum conservation equations is based on Newton's second law of motion. It is assumed that the change in impulse with respect to time in one direction is equal to the sum of forces acting in the same direction. The forces acting on a fluid element can be divided into

pressure, body, and viscous forces. From this assumption, the general form of the conservation of momentum equation is derived and shown below.

$$\underbrace{\rho \left(\frac{\partial u_j}{\partial t} + U_i \frac{\partial (u_j)}{\partial x_i} \right)}_{\text{Change in momentum in time}} = - \frac{\partial p}{\partial x_j} - \frac{\partial \tau_{ij}}{\partial x_i} + f_j \quad \text{for } j = 1,2,3. \quad (2.2)$$

Here, τ_{ij} defines the viscous stress and f_j defines all volume forces. The viscous stress tensor can be derived to be.

$$\tau_{ij} = -\mu \left(\frac{\partial u_i}{\partial x_j} + \frac{\partial u_j}{\partial x_i} \right) + \frac{2}{3} \delta_{ij} \mu \frac{\partial u_k}{\partial x_k} \quad (2.3)$$

where μ is defined as the dynamic viscosity of the fluid and δ_{ij} is the Kronecker delta.

The resulting system of equations formed by Eqs. 2.2, and 2.3, are incomplete because only four equations are available to solve for the five unknown values ρ , p , and u_i . Assuming that the flow is incompressible with a constant density, Eqs. 2.2, and 2.3, reduce to

$$\frac{\partial u_i}{\partial x_i} = 0 \quad (2.4)$$

$$\rho \frac{\partial u_i}{\partial t} + \rho u_j \frac{\partial u_i}{\partial x_j} = - \frac{\partial p}{\partial x_i} + \frac{\partial \tau_{ij}}{\partial x_j} \quad (2.5)$$

And the viscous stress for incompressible flow can be simplified using the continuity equation (See Eq. 2.4)

$$\tau_{ij} = -\mu \left(\frac{\partial u_i}{\partial x_j} + \frac{\partial u_j}{\partial x_i} \right) \quad (2.6)$$

Because this system of equations is closed, the most common fluid mechanical problems can be solved by employing the appropriate boundaries and initial conditions. The incompressible flow assumption is common when investigating the ground vehicle, as the maximum speed that can be achieved is less than Mach Number (M) 0.3. The density and temperature variations at $M < 0.3$ are negligible; thus, the change in the flow variables past a vehicle is assumed to be an isentropic process. In addition, the assumptions of incompressible flow imply that no acoustical information can be derived directly from the system of equations because density variations are neglected.

2.2. Turbulent flows

The flow past a road vehicle and its external fixtures is generally considered turbulent. A stronger mixing behaviour characterises a turbulent flow owing to the vortical structures of different length scales present in the flow. The nature of the flow can be determined using the ratio between the inertial and viscous forces in the flow, known as the Reynolds Number Re .

$$Re = \frac{UL}{\nu} \quad (2.7)$$

Where U and L are the characteristic velocity and length, respectively; and $\nu = \mu/\rho$ is the kinematic viscosity of the fluid. Generally, if the flow $Re > 5 \times 10^5$, then the flow is considered to be fully turbulent in aerodynamic applications.

2.2.1. Characteristic length scales

The turbulent flow contains eddies with different characteristic length scales that exist in a turbulent flow field. These length scales were represented using the energy spectrum of a turbulent flow field as a function of wavenumber k , as illustrated in Fig. 2.1. According to Pope (2001), the energy spectrum can be divided into two parts: the energy-containing range and universal equilibrium range. In the first range, turbulence is generated, which contains eddies defined by the flow over the geometry and boundary conditions. The largest eddies (l_o) with the highest turbulent kinetic energy decay and break down into smaller eddies (η) until the eddies become sufficiently small to dissipate thermal energy in the universal equilibrium range. l_o is also referred to as the integral length scale and is determined by the flow, whereas the smallest eddies start dissipating at the Kolmogorov scale. The length, velocity and time scales for the smallest eddies are defined as shown in Eq. 2.8, as determined by the viscosity ν and the dissipation rate (ϵ). For a high mean flow Re , the smallest scales in the turbulent flow are characterised by an isotropic nature according to the Kolmogorov hypothesis (Versteeg and Malalaskera, 2007); therefore, the geometry or boundary condition information is lost (Pope, 2001).

The length scales associated with the integral length scale and Taylor microscale are determined by considering the ratios between the largest and the smallest eddies in the subranges of the spectrum. The intermediate-length scale splits the energy spectrum into two subranges, l_{DI} and l_{EI} (See Fig. 2.1), which are functions of both the Kolmogorov scale and integral length scale, as shown in Eq. 2.9.

$$\begin{aligned}
\text{Length Scale:} \quad & \eta = \left(\frac{\nu^3}{\varepsilon}\right)^{\frac{1}{4}} \\
\text{Velocity Scale:} \quad & u_n = (\varepsilon\nu)^{\frac{1}{4}} \\
\text{Time Scale:} \quad & \tau_n = \left(\frac{\nu}{\varepsilon}\right)^{\frac{1}{2}}
\end{aligned} \tag{2.8}$$

$$\begin{aligned}
\text{Integral length scale: } l_o &= \eta Re^{3/4} \\
\text{Taylor microscale: } \lambda &= 15^{1/2} Re^{-1/2} l_o \\
\text{Inertial range: } l_{EI} &= l_o/6 \\
\text{Dissipation range: } l_{DI} &= 60\eta
\end{aligned} \tag{2.9}$$

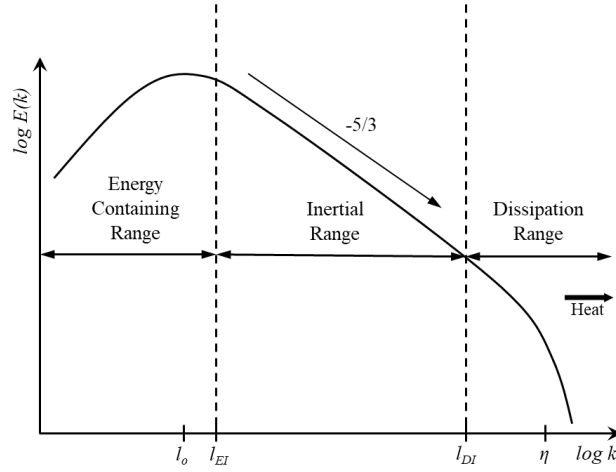


Fig. 2.1. A depiction of the observed energy and its cascade. The above graph is also referred to as the energy spectrum.

2.2.2. Time Scales

The time scale associated with the largest eddy within the energy-containing range is referred to as the large eddy turnover time (t_L) and is defined as shown in Eq. 2.10. The smallest time scale for the small eddies can be defined using the viscosity of the fluid and dissipation rate, as shown in Eq. 2.11. The ratio of the timescales between the largest and the smallest scales is defined in Eq. 2.12.

$$t_L = \frac{L}{U} \tag{2.10}$$

$$t_n = \left(\frac{\nu}{\varepsilon}\right)^{1/2} \tag{2.11}$$

$$\frac{t_L}{t_n} = \left(\frac{UL}{\nu}\right)^{1/2} = Re_L^{1/2} \tag{2.12}$$

The estimate of the time taken by the integral scale eddy to reduce to the Kolmogorov scale is given by Eq. 2.13

$$\frac{t_l}{t_L} = 1 - \left(\frac{\eta}{L}\right)^{\frac{2}{3}} = 1 - Re^{-1/2} \quad (2.13)$$

The grid size and time step must be sufficiently small to resolve the time scales of the small-scale motion to resolve both the length and time-accurate solutions. The grid sizes can be estimated based on the characteristics, lengths and wall-normalised units, while the time step is estimated based on the Courant-Friedrichs-Lewy (CFL) number, which is defined as follows

$$CFL = U \frac{\Delta t}{\Delta x} \quad (2.14)$$

The NS equations can fully describe turbulence by resolving all scales in space and time using Direct Numerical Simulation (DNS). The computational costs to resolve all the turbulence scales were estimated to be approximately Re^3 . However, DNS is still far too computationally expensive for many engineering flows of interest and is restricted to low Re flows and simple shapes (Alam and Sandham, 2000; Endo and Himeno, 2002; Leonardi et al., 2003). Therefore, spatial filters are introduced to the N- S equations to resolve larger eddies in turbulent flow, while smaller eddies are modelled. Spatial filters based on local grid sizing are used to obtain resolved and modelled turbulent scales, where at least 80% of the turbulence is resolved to capture all eddies in the inertial subrange, as shown in Fig. 2.1, which implies that the production and cascading behaviour (-5/3 slope) of turbulence are well captured (Pope 2001). In addition, the eddies are resolved at least up to the Taylor microscale (below which the turbulent motion is subjected to strong viscous forces and kinetic energy is dissipated into heat). Several equations were formulated to resolve the turbulent flow based on the turbulence modelling approach and are presented in the following section.

2.3. Turbulence Modelling

Turbulence modelling approaches and their accuracy in resolving turbulent scales are discussed in the following sections.

2.3.1. Reynolds-Averaged Navier-Stokes (RANS)

RANS methods are widely used turbulence models to resolve flows in which time-averaged flow features are necessary. In RANS models, the mean flow characteristics are obtained using the Reynolds decompositions (Wilcox, 1997)

$$\phi(x_i, t) = \bar{\phi}(x_i) + \phi'(x_i, t) \quad (2.15)$$

Where ϕ is a flow variable, $\bar{\phi}$ represent means variable, and ϕ' is the perturbations quantity. After substituting Reynolds decomposition into Eq. (2.4 and 2.5) and the time-averaging process, the RANS equations are obtained.

$$\frac{\partial \bar{u}_i}{\partial x_i} = 0 \quad (2.16)$$

$$\rho \bar{u}_j \frac{\partial \bar{u}_i}{\partial x_j} = -\frac{\partial \bar{p}}{\partial x_i} + \frac{\partial}{\partial x_j} (2\mu \bar{S}_{ij} - \overline{\rho u'_j u'_i}) \quad (2.17)$$

Here, (2.18)

$$\bar{S}_{ij} = \frac{1}{2} \left(\frac{\partial \bar{u}_i}{\partial x_j} + \frac{\partial \bar{u}_j}{\partial x_i} \right)$$

The obtained equations are similar to the NS equations, but the variables represent time-averaged values. The additional fluctuating unknown term ($-\overline{\rho u'_j u'_i} = \tau_{ij}^t$) is named the Reynolds-stress tensor introduced τ_{ij}^t representing the turbulent fluctuations in the mean flow which results in a symmetric tensor with six components and requires modelling due to the nonlinearity. Therefore, a closure technique is required to address the ten unknowns in the system of four equations, as shown in Eq. 2.16 and 2.17 respectively, which are achieved by introducing transport equations to close the system of equations.

Among the models introduced for the turbulence closure problem, the widely used two-equation models are the $k - \varepsilon$ (Launder and Spalding, 1974), $k - \omega$ (Wilcox, 1997), and shear stress transport (SST) model (Menter, 1994). The formulations of these models are detailed in the Appendix for the reader's reference. Most RANS approaches can predict force coefficients and large flow features, as shown by Ashton et al. (2016), Ashton and Revell (2014, 2015), Guilmineau (2008), Guilmineau et al. (2018), Li et al. (2022), Read and Viswanathan (2020), and Viswanathan (2021). However, for specific cases, the accuracy decreases for the RANS approach when predicting aerodynamic characteristics, such as drag and lift, when adverse pressure gradients and separated flows are present. This decrease is attributed to the underestimation of the turbulent stresses where massively separated flow regions are present (Guilmineau, 2008; Han, 1989; Khalighi et al., 2001; Rodi, 1997).

2.3.2. Large Eddy Simulation (LES)

The LES approach is adopted to overcome the limitations of RANS, where the largest scales of the flow are resolved, while the smallest scales are modelled using subgrid-scale (SGS) models, thus capturing all flow features. The spilt is achieved by employing a filter in

space to divide the flow into resolved and subgrid parts. The most commonly used filter is based on a local grid size, which is larger than the Kolmogorov length scale. The small scales filtered out are governed by the viscosity, which dissipates the energy in the turbulent flow. When the filter is introduced into the conservation of the mass and momentum equations (Eq. 2.16 and 2.17), an unknown SGS stress tensor is obtained, representing the SGS motions in the resolved field of the LES, which results in a closure problem arises that needs to be modelled. Therefore, SGS models were introduced to model the SGS stresses.

The spatial filter used in LES is defined as

$$\bar{\phi}(x_i, t) = \int_{\Omega} G(x_i, x'_i, \Delta) \phi(x'_i, t) dx'_i \quad (2.19)$$

Where, x'_i the integration variable in space in three dimensions, x and x' represents each mesh point and the region near x , respectively. $\bar{\phi}(x, t)$ denotes the filtered parameter while $\phi(x', t)$ is the original parameter. Δ is the cutoff width used to separate large and small eddies. Generally, the filter width is equal to the grid size because no smaller scales can be resolved (Rogallo and Moin, 1984), as the grid sizes generated are larger than the Kolmogorov length η .

The NS equations become, as shown in Eq. 2.20 and 2.21 after the filtering operation.

$$\frac{\partial \bar{u}_i}{\partial x_i} = 0 \quad (2.20)$$

$$\frac{\partial \bar{u}_i}{\partial t} + \frac{\partial \bar{u}_i \bar{u}_j}{\partial x_j} = -\frac{1}{\rho} \frac{\partial \bar{p}}{\partial x_j} - \frac{1}{\rho} \frac{\partial \tau_{ij}^R}{\partial x_j} + \nu \nabla^2 \bar{u}_i \quad (2.21)$$

where ν is the kinematic viscosity and τ_{ij}^R denotes the SGS stress (Eq. 2.22) required to be modelled. An over-prediction in the energy dissipation can lead to instability in the computation owing to improper modelling of the SGS stresses, although only a small part of the turbulent energy is contained in the small scales. SGS stresses can be modelled based on the Boussinesq hypothesis (Wilcox, 1997), similar to Reynolds Stresses

$$\tau_{ij}^R = \overline{u_i u_j} - \bar{u}_i \bar{u}_j \quad (2.22)$$

$$\tau_{ij}^R = -2\rho \nu_{SGS} \bar{S}_{ij} + \frac{2}{3} \delta_{ij} k \quad (2.23)$$

where $\nu_{SGS} = \mu_{SGS}/\rho$ and μ_{SGS} represents the SGS eddy viscosity.

Smagorinsky-Lilly Model (SL)

The Smagorinsky-Lilly Model is one of the most widely used SGS models for LES. In this model, the viscosity determines the level of energy dissipation and is given as follows

$$v_{SGS(SL)} = L_s^2 |\overline{S}| \quad (2.24)$$

where $|\overline{S}| = \sqrt{2\overline{S_{ij}}\overline{S_{ij}}}$ and L_s is the mixing length for the SGS and is defined as

$$L_s = \min(\kappa d, C_s \Delta) \quad (2.25)$$

where κ is the von Karman constant, d is the distance to the closest wall, C_s is the SL-SGS constant, and Δ is the grid filter length. The SL-SGS model constant was taken as 0.1, and the grid filter length was calculated as the cubic root of the cell volume. Ideally, the cell should be defined as a cube (structured grid) to increase the accuracy of the SGS. The wall damping function κd ensures that the mixing length approaches zero at the wall.

Dynamic Smagorinsky-Lilly Model (DSL)

The dynamic Smagorinsky-Lilly model (Germano et al., 1991; Lilly, 1992) modifies the model constant defined in the Smagorinsky-Lilly model. The model constant is dynamically calculated as a function of space and time. This was achieved by introducing a test filter ($\hat{\Delta}$) equal to twice the standard grid filter used in the SL model. The test filter is applied to the NS equation, which results in the subtest-scale stress defined as shown below

$$T_{ij} = \widehat{u_i u_j} - \widehat{\widehat{u_i} \widehat{u_j}} \quad (2.26)$$

Here, $\hat{\Delta}$ denotes the test filter variable. Assuming the scale similarity between T_{ij} and τ_{ij}^R and the difference between resolved stress of the smaller scale between the grid and test filter is given by L_{ij} , also referred to as Leonard stresses.

$$L_{ij} = T_{ij} - \tau_{ij}^R \quad (2.27)$$

The model constant in the DSL is defined as shown in Eq. 2.28.

$$C_{ds} = \left(\frac{L_{ij} M_{ij}}{M_{ij} M_{ij}} \right)^{1/2} \quad (2.28)$$

Where, $M_{ij} = -2(\hat{\Delta}^2 |\widehat{S}| \widehat{S_{ij}} - \widetilde{\Delta}^2 |\widetilde{S}| \widetilde{S_{ij}})$. C_{ds} vary in space and time and range from 0 to 0.23 to avoid numerical instabilities, if the value of C_{ds} is too large, it overestimates the subgrid-scale eddy viscosity which can lead to excessive damping of the turbulent fluctuation thereby

reducing the accuracy of the simulation. The eddy-viscosity is calculated similarly to the SL model, but the L_s is defined as shown below

$$L_s = \min(\kappa d, C_{ds}\Delta) \quad (2.29)$$

Wall-Adapting Local Eddy-Viscosity (WALE)

WALE SGS is used to overcome the limitations of the SL SGS model; for example, for complex geometries, the wall behaviour is not captured accurately, and because of a single constant, it is incapable of representing various turbulent flows (Lee and Cant, 2017). The formulation of the eddy viscosity in the WALE SGS model is based on the operator $S_{ij}^d S_{ij}^d$ (ref Equ 2.30). The v_{SGS} of WALE depend on the strain and rotation rate of the small, turbulent structures instead of the filter width. Thus, the WALE SGS model is well suited for LES in

$$v_{SGS(WALE)} = L_s^2 \frac{(S_{ij}^d S_{ij}^d)^{3/2}}{(\overline{S_{ij} S_{ij}})^{5/2} + (S_{ij}^d S_{ij}^d)^{5/4}} \quad (2.30)$$

complex geometries with structured or unstructured grids because no explicit filtering is needed, and only local information is required for eddy viscosity.

In the above equation, $\frac{(S_{ij}^d S_{ij}^d)^{3/2}}{(\overline{S_{ij} S_{ij}})^{5/2}}$ ensures the stability of the SGS near the wall, while adding $(S_{ij}^d S_{ij}^d)^{5/4}$ to the denominator ensures the numerical instability near the wall despite the type of grid used. Further, L_s in the WALE is defined as shown in Eq. 2.31, and the WALE constant C_w was equal to 0.325.

$$L_s = \min(\kappa d, C_w V^{1/3}) \quad (2.31)$$

To summarise, the choice of the SGS model for LES depends on the flow physics that is being investigated. Despite using different subgrid models as mentioned above for LES, the grid generated has to account for the filter width and the filter width still depends on the local cell size. Therefore, LES grid sizing significantly increases the overall cell count, substantially increasing computational resource requirements (Cheng et al., 2012; Keogh et al., 2016; Krajnović and Davidson, 2003; Krajnović and Davidson, 2002; Krajnović and Davidson, 2005a, 2005b; Serre et al., 2013; Tsubokura et al., 2009).

2.3.3. Hybrid RANS-LES approach

RANS-based methods have limited capability for resolving the sources owing to the averaging approach. LES can be computationally expensive for resolving near-wall turbulent structures, as the filter width depends on the local grid size. Hence, hybrid RANS-LES methods

are proposed to overcome the high computational effort required for LES, especially for complex geometries at high Reynolds numbers, and the limited capability of RANS in resolving large-scale unsteady structures of turbulent flow.

The mesh resolution for hybrid RANS-LES

The principal idea of hybrid models is to resolve most of the flow using LES while modelling the wall behaviour using RANS, thus reducing the requirement of finer meshes near the walls compared with the traditional LES approach. The different mesh resolutions required for full RANS, full LES, and hybrid RANS-LES based on a flat-plate boundary layer are illustrated in Fig. 2.2. The lowest mesh resolution near the solid walls is required for most RANS models where near-wall treatments are used, however for specific RANS models such as $k - \omega$ SST, the near wall mesh should be denser, whereas the highest mesh resolution is required for the LES. In addition, for full LES, the most preferred are cube-type meshes close to the wall to keep the grid aligned with the flow, especially for complex geometries, which demand the highest grid resolution in three dimensions, resulting in a significant increase in the number of grid cells required for full LES.

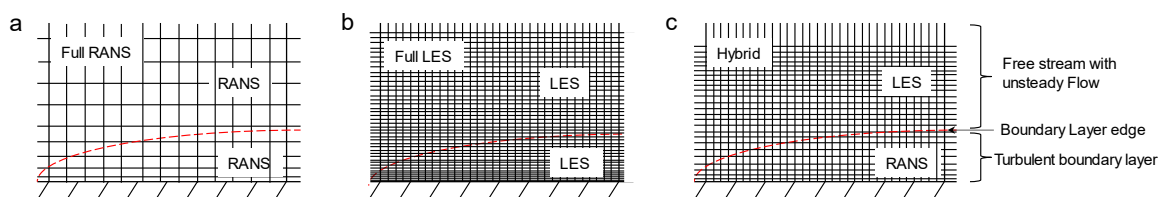


Fig. 2.2. Comparison of mesh resolution for a) full RANS, b) full LES, and c) Hybrid based on a flat plate boundary layer.

Spalart Allmaras (1992) first introduced the hybrid RANS-LES model by combining the one-equation RANS model with LES and termed the model Detached Eddy Simulation (DES). Many other formulations have been introduced to overcome the limitations of DES, and few formulations introduced a new definition for the spatial filter. Details of these models are presented in the following sections.

Detached Eddy Simulation (DES) and its variants:

The initial development of the DES was based on the Spalart-Allmaras (S-A) model, as the distance function present in the Spalart-Allmaras model is used to define the filter that indicates whether RANS or LES behaviour should be performed by comparing the length scale with the local grid size. The transition from RANS to LES in the near-wall flow region is obtained by replacing the near-wall distance (d) of the Spalart-Allmaras model with the expression shown below

$$\tilde{d} = \min (d, C_{DES}\Delta) \quad (2.32)$$

Where Δ represents the maximum edge length of the local computational cell, and C_{DES} represents a constant value of 0.65. The RANS model is employed where $d < C_{DES}\Delta$ in the proximity of the solid wall and $d > C_{DES}\Delta$; then, the model switches to LES. The switching process is illustrated in Fig 2.3.

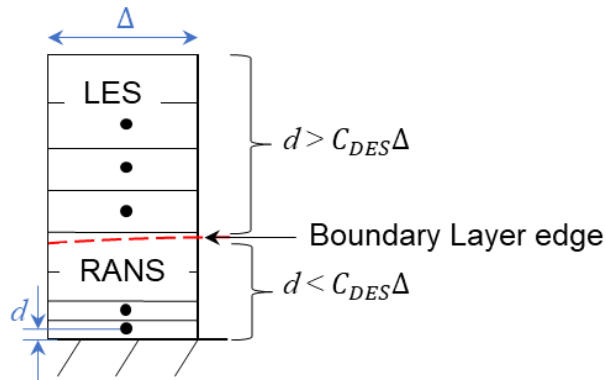


Fig. 2.3. Illustration of the switch between RANS and LES in the DES approach

Ideally, when using DES, RANS is performed within the boundary layer and LES in regions with flow separation is desired. However, if the grid resolution is sufficiently fine for switching but not sufficiently fine to resolve local turbulent structures, the eddy viscosity is reduced from RANS to LES. In such situations, the modelled Reynolds stress is reduced without any sizeable resolved stresses to restore balance, leading to Modelled Stress Depletion (MSD). Furthermore, excess MSD can cause non-physical (grid-induced) flow separation often referred to as GIS, significantly impacting flow development. Therefore, several suggestions have been made to solve both MSD and GIS problems.

Spalart et al. (2006) proposed a formulation called Delayed DES (DDES) with a generalised shielding function, f_d , which relies on both RANS and turbulent viscosity (see Eq. 2.33) to overcome both MSD and GIS. In the DDES formulation, the switching function was redefined to include the local grid size and eddy viscosity of the flow. Thus, shielding is introduced to regions where the boundary layer is attached, and the RANS behaviour is preserved. The shielding function is designed to reach zero inside the wall boundary layer where RANS is activated, and away from the wall, it reaches unity where the LES is activated.

$$l_{DDES} = l_{RANS} - \max(0, l_{RANS} - C_{DES}\Delta) \quad (2.33)$$

where f_d is empiric blending function and is defined as

$$f_d = 1 - \tanh[(C_{d1}r_d)^{C_{d2}}] \quad (2.34)$$

$$r_d = \frac{v_t + \nu}{\kappa^2 d_w^2 \sqrt{0.5 \cdot (S^2 + \Omega^2)}} \quad (2.35)$$

However, in some instances, such as flow past a vehicle body, at the boundary layer edge, the shielding function fails to provide perfect shielding because the ratio between the maximum edge length of the local computational cell (Δ_{max}) and the boundary layer thickness (δ) should be between 0.2 – 0.3. This ratio is often reached in the case of vehicle aerodynamic studies and causes grid-induced separation owing to less control over the grid spacing at sudden changes in vehicle surfaces, such as the curved edges windshield and bonnet. In addition, DES and DDES fall short in the quick transition from RANS mode to LES in separated shear layers (SSL) and provide no clear distinction between the RANS and LES regions. To overcome the limitations of the standard DES and DDES methods, SDES and SBES were introduced. The details of SDES and SBES are presented in the sections below

Shielded Detached Eddy Simulation (SDES)

In the SDES, the shielding function of the DDES is reformulated to achieve more reliable shielding such that the RANS information is preserved even after severe mesh refinements in the attached boundary layers. This strong shielding is achieved by replacing the DDES shielding in the sink term as follows

$$\varepsilon_{SDES} = -\beta^* \rho k \omega F_{SDES} \quad (2.36)$$

where,

$$F_{SDES} = \left[\max \left(\frac{L_t}{C_{SDES} \Delta_{SDES}} (1 - f_s), 1 \right) - 1 \right] \quad (2.37)$$

$$\Delta_{SDES} = \max \left[\sqrt[3]{vol}, 0.2 \Delta_{max} \right] \quad (2.38)$$

The introduction of a new definition of the length scale in SDES (Δ_{SDES}) results in a faster transition from RANS to LES, as the first part of the definition resembles the conventional LES grid length definition, and the second part of the definition is the maximum edge length defined in the original DES formulation. The value of 0.2 ensures that the length scale accounts for highly stretched meshes. Therefore, the new length-scale definition is small by a factor of five for highly stretched meshes compared to the DES/DDES definition.

On the other hand, the switch from RANS to LES is activated when the eddy viscosity is reduced to a level comparable to that of the LES model. This reduction in eddy viscosity was achieved by equating the source and sink terms in k and ω in the RANS equations, which resulted in an eddy viscosity equivalent to Eq. 2.39, which resembles the eddy viscosity definition of the SGS model.

$$v_t = \left[\left(\frac{\beta}{\alpha} \right)^{3/4} C_{SDES} \Delta_{SDES} \right]^2 S \quad (2.39)$$

The constant of the SDES (C_{SDES}) was calibrated to the product of $(\beta/\alpha)^{3/4}$, and C_{SDES} become 0.11, which is equal to the Smagorinsky constant (C_s). The combination of $C_{SDES} \Delta_{SDES}$ enters the eddy viscosity formulation quadratically, resulting in a higher reduction in eddy viscosity levels than the previous versions of DES/DDES (Menter, 2015). Therefore, owing to the smaller grid length definition and lower eddy viscosity levels, the transition from RANS to LES in SDES is rapid compared to other DES variants and stabilises the model even under severe grid refinements. In addition, the SDES turbulence model can be used for aeroacoustics studies where grids are refined locally to ensure the accurate capture of frequencies desired by the user.

Stress-Blended Eddy Simulation (SBES)

SBES is an extension of the SDES formulation with the same shielding function but adds the ability to blend from RANS models directly to any sub-grid scale model of LES. The shielding function of the SDES framework blends the stress levels of the RANS and LES formulations. The modified turbulence stresses tensors, and the eddy viscosity of the RANS and LES with the blending function is presented in the equations below

$$\tau_{ij}^{SBES} = f_s \cdot \tau_{ij}^{RANS} + (1 - f_s) \tau_{ij}^{LES} \quad (2.40)$$

$$v_t^{SBES} = f_s \cdot v_t^{RANS} + (1 - f_s) \cdot v_t^{LES} \quad (2.41)$$

The exact formulation of the SBES/SDES shielding function is proprietary to ANSYS and is not available in the public domain.

Due to the blending function (Eq. 2.40 and 2.41) used in SBES, any RANS variants and LES with any SGS model can be smoothly blended without additional modification needed for either v_t and τ_{ij} of both RANS and LES in contrast with the DDES and DES formulations. In addition to the advantages of the SDES model, on coarser grids, the transition from RANS-LES can be achieved using the SBES model.

The advantages and challenges of the above-mentioned numerical strategies used for vehicle aerodynamic and aeroacoustics studies are presented in a tabular form below:

Table 2.1 Overview of turbulence modelling approaches for road vehicles

Turbulence Model	Ability	Challenges
Direct Numerical Simulation (DNS)	<ul style="list-style-type: none"> – DNS solves the conservation equation presented in subsection 2.1.1. – Resolve all length and time scales; no modelling techniques are required in DNS 	<ul style="list-style-type: none"> – The number of spatial nodes needed equals $Re^{9/4}$, and the number of time steps is estimated at $Re^{3/4}$ for homogenous turbulence (Pope, 2001). As a result, computational effort estimated at Re^3 and hardware to perform such numerical simulation is yet to be realised for shapes beyond simple bluff bodies (Yokokawa et al., 2002).
Large Eddy Simulation (LES)	<ul style="list-style-type: none"> – LES solves conservation equations (see subsection 2.1.1) by filtering the dissipative scales. – The smallest local grid size is utilised as a filter. – Filtered scales are modelled using subgrid-scale models. – LES is modelled to resolve 80% of the energy present in the turbulent flow (Pope, 2001). – The ability to resolve most of the eddies in the inertial subrange, as shown in Fig. 2.1, is preferred for vehicle aerodynamics and aeroacoustics studies, such as bi-stability and noise propagation into the cabin, despite its high computational requirements. 	<ul style="list-style-type: none"> – The spatial and temporal resolution may be small for high Reynolds number flows. – The smallest structures are located at the wall, and fine spatial resolution is needed near-wall. – Estimated spatial resolution near the wall, $\Delta x^+ = 15 - 100$, $\Delta z^+ = 10 - 20$ and $\Delta y^+ < 1$. (Pope, 2001)

Unsteady
Reynolds-averaged
Navier-stokes
equations
(URANS)

- Reynolds Decomposition is introduced into the conservation of mass and momentum equations (see Subsection 2.1.1).
 - Model all the scales in the energy spectrum.
 - The additional unclosed term must be modelled due to the nonlinearity of the NS equations.
 - Introducing the unsteady term into RANS will allow RANS models to capture large-scale turbulent structures in the transient flow field, such as vortex street behind a blunt body when sufficient unsteadiness is present.
 - Various closures are available within RANS.
 - Two equation models are widely popular for vehicle aerodynamic studies.
 - Transport equations, namely turbulent kinetic energy (k), specific dissipation rate (ω), or dissipation rate (ε), are modelled.
 - Less computational resources are needed compared to LES and DNS.
- Due to the modelling assumptions made, all RANS models have limited capability in resolving the flow.
 - The low wavenumber components in a turbulent flow can be resolved.
 - The accuracy is reduced when predicting massive flow separation and numerous unsteadiness in the wake, as RANS is mathematically designed to resolve the largest scales, while the smaller scales are all averaged.
 - RANS models are only useful when broadband noise is of interest due to their limited capability to resolve flow.
 - Specific RANS models use near-wall modelling. As a result, transitional flow studies with RANS are limited.
 -
-

Scale Adaptive Simulations (SAS)	<ul style="list-style-type: none"> – Von Karman length scale is introduced into the transport equation of the URANS. – Dynamically adjust to resolved structures in URANS, providing LES-like behaviour in the unsteady region (Egorov et al., 2010). – LES-like resolution can be obtained with less computational effort (Menter, 2014). 	<ul style="list-style-type: none"> – Strongly relies on the unsteadiness in the flow field (Wang et al., 2017). – The grid and time step has to be carefully chosen to avoid stress depletion (Egorov et al., 2010).
Partially Averaged Navier-Stokes (PANS)	<hr/> <ul style="list-style-type: none"> – PANS decomposition of the velocity field is based on kinetic energy content rather than cut-off wavenumber in LES (Girimaji and Abdol-Hamid, 2005). – PANS uses an implicit filter and two-equation sub-filter closure. – The implicit filter is independent of grid spacing and dependent only on the ratio of unresolved to total kinetic energy (f_k) and dissipation (f_ε) parameter. – The PANS method adapts to the spatial resolution of a given mesh to provide a solution between URANS and DNS (Girimaji and Suman, 2012). – f_ε and f_k Parameters can be constant throughout the computational domain or vary as a function of space and time. <hr/>	<ul style="list-style-type: none"> – Grid independency study is mandatory to ensure the parameters f_ε and f_k to find an optimal numerical grid.

Hybrid RANS-LES

- Hybrid RANS-LES was introduced to overcome LES disadvantages.
 - Decrease the demand for grid resolution at the wall regions by adopting the RANS at the wall region and LES away from the wall.
 - A spatial-based filter is used, similar to that of LES, for switching between RANS and LES modes.
 - They are widely used in aeroacoustics studies for ground vehicles due to their capability to resolve the flow to a level that is in reasonable agreement with experimental data and also adequate to predict noise generation and its mechanisms at much lower computational effort than LES as evidenced by the list is not restricted to Dawi Akkermans (2019, 2018), He et al., (2020), Wang et al. (2020).
 - Certain Hybrid RANS-LES models are sensitive to grid resolution near the walls as they lead to GIS, MSD and LLM, as discussed in the above sections.
-

It is worth mentioning that additional methods exist, as shown in Table 2.1, for resolving turbulence based on the URANS approach, such as SAS, which was proposed by (Menter et al., 2003) and PANS, proposed by Girimaji and Suman (2012). However, these models are not discussed in this work, and the reader is referred to the literature mentioned above. The usefulness of the hybrid RANS-LES models in vehicle aerodynamics and aeroacoustics studies is summarised in Table 2.8.

Hybrid RANS-LES models are widely used in automotive applications because of the lower computational costs involved in resolving the flow field (Ashton et al., 2016; Ashton and Revell, 2015; Chode et al., 2020; Guilmineau, 2008; Guilmineau et al., 2011) and acoustic fields around vehicles (Ask and Davidson, 2009; Chode et al., 2021; Dawi and Akkermans, 2019; Dechitre and Hartmann, 2009; He et al., 2020; He et al., 2021a; Islam et al., 2008a). However, the applicability of SBES and SDES for ground vehicle aeroacoustics applications is yet to be investigated, as they offer a quick transition from the RANS to LES mode, which can resolve the pressure fluctuations in the wake more accurately. Based on the clear distinction between the RANS and LES regions, mesh refinements near the body of interest can be adjusted to achieve better flow resolution. It should also be noted that hybrid RANS-LES models, such as IDDES, SBES, and SDES, use RANS modelling in the boundary layers to suppress the calculation of boundary-layer noise sources. For ground vehicle applications, sound waves are mainly generated by the interaction of turbulence with solid surfaces, such as side view mirrors for cars; in such cases, the boundary layer noise is negligible when compared to the noise generated by the interaction of turbulence with solid surfaces.

The different turbulence approaches used to describe the fluid flow dynamics around the vehicle are presented in the sections above. The acoustic field and the type of noise sources present around a vehicle are discussed in the following sections. A detailed description of different acoustic modelling present to describe the acoustic field is discussed.

2.4. Type of noise sources in ground vehicles

Aerodynamic noise is a significant contributor to the noise generated by a vehicle when travelling at speeds greater than 100 km/h. They are different mechanisms that can generate aerodynamic noise from vehicles owing to the complexity of the vehicle geometry. For instance, aerodynamic noise is generated by the flow separation, leading to a turbulent flow at exterior fixtures of the vehicle, such as windscreen wipers and roof-mounted racks, a-pillars, and side-view mirrors. The separated flow interacts with solid surfaces, such as side windows,

causing the side window to vibrate and radiate noise into the cabin and the free stream. Many potential noise sources are responsible for noise generation from a vehicle because of its complex features, such as the leakage noise that is created because of gaps between doors and b-pillars, which is also one of the dominant noises as a consequence of flow interacting with solid surfaces (Fig. 2.4), which are classified and summarised in Table 2.2.

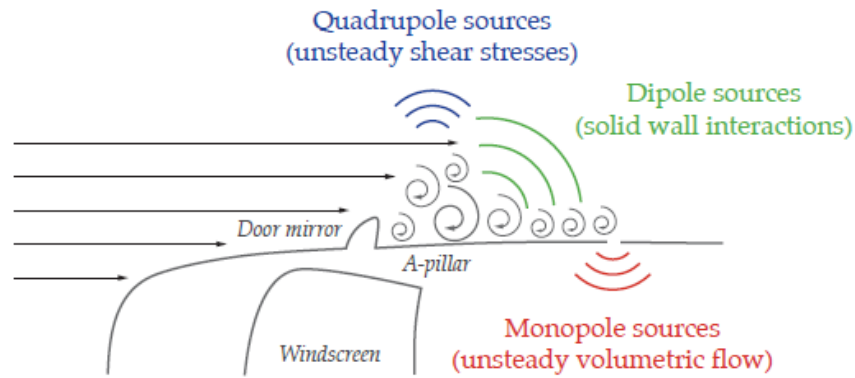


Fig. 2.4. Aeroacoustics sources in the side glass region (Oettle and Sims-Williams, 2017)^a

^a Reused with permission from Nicholas Oettle and David Sims-Williams , “Automotive Aeroacoustics: An Overview,” Proceedings of the Institution of Mechanical Engineers. Part D : Journal of automobile engineering., 231 (9). pp. 1177-1189. Copyright © 2017 SAGE Publications.

Table 2.2 Classification of noise sources and their generation mechanisms

Source Type	Description	Generation Mechanism
Monopole Source	<ul style="list-style-type: none"> – Small pulsating sphere, contracting and expanding with time. – The noise radiates equally in all directions. (Fig 2.5a) – The sound intensity of the monopole is proportional to the fourth power of fluctuating velocity. $I_{monopole} = \rho \frac{L^2 V^4}{r^2 c}$ <p>Here, L = area of noise, R = distance from Noise source, C = speed of sound, V = fluctuating velocity and ρ = air density</p>	<ul style="list-style-type: none"> – Movement of unstable volume airflow. – Leaks in the sealing of doors. (Helfer, 2005) – Vehicle exhaust pipe outlet (Watkins, 2010).
Dipole Source	<ul style="list-style-type: none"> – Two small adjacent spheres are pulsating precisely out of phase. (Fig 2.5b) – The sound intensity of the dipole source is proportional to the sixth power of fluctuating velocity. $I_{dipole} = \rho \frac{L^2 V^6}{r^2 c^3}$	<ul style="list-style-type: none"> – Time-varying momentum fluxes. – Unsteady pressures due to separated flows and vortex shedding are ideal dipole sources. (Ask and Davidson, 2010; Helfer, 2005; Watkins, 2010)
Quadrupole Source	<ul style="list-style-type: none"> – Quadrupole consists of pair of dipole sources with opposite phases. (Fig 2.5c) – The intensity of the sound source is proportional to the eight power of fluctuating velocity. $I_{quadrupole} = \rho \frac{L^2 V^8}{r^2 c^5}$	<ul style="list-style-type: none"> – Collisions of fluid elements generate unstable internal stress, forming the quadrupole sound source (Pang, 2018; Wolf et al., 2012). – Turbulent shear layers (Kumarasamy and Karbon, 1999).

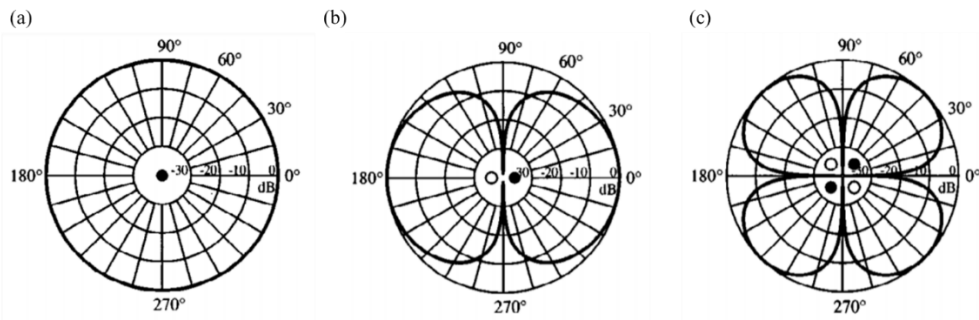


Fig. 2.5. Identification of type of noise source a) Monopole, b) Dipole, and c) Quadrupole (Russell et al., 1999)^b.

By comparing the intensities of the poles at low Mach number flows ($M < 0.3$), the monopole source is the most powerful, followed by the dipole source. The quadrupole source causes the lowest noise emission; thus, for vehicle aeroacoustics studies, quadrupole noise sources are neglected (Helfer, 2005; Pang, 2018; Watkins, 2010). Generic vehicle bodies used for numerical studies are leakproof, thus eliminating monopole sources; therefore, dipole sources dominate in numerical studies of generic vehicle bodies.

The dipole sources are generated due to the wall pressure fluctuations caused by the flow separation from side-view mirrors, a-pillar, and their interactions are evaluated using several Computational Aeroacoustics (CAA) methods coupled with turbulence modelling strategies. A review of CAA methods is presented in the following sections.

2.5. Computational Aeroacoustics (CAA) methods for road vehicles

Computational Aeroacoustics (CAA) are a powerful tool for investigating the noise generated by the vehicle. CAA approaches offer a deeper insight into the noise generation mechanism and enable a more detailed analysis of the results than experimental measurement due to the availability of information at every point in the domain and the ability to measure various flow quantities at places that are difficult to access in the experiment. CAA approaches are generally classified into two categories; Direct and Hybrid Methods, as illustrated in the flow chart below (Fig 2.6)

^b Reused with permission from Daniel A. Russell, Joseph P. Titlow, and Ya-Juan Bemmen, "Acoustic monopoles, dipoles, and quadrupoles: An experiment revisited," *American Journal of Physics* 67(8), pp. 660-664. Copyright © 1999 American Association of Physics Teachers.

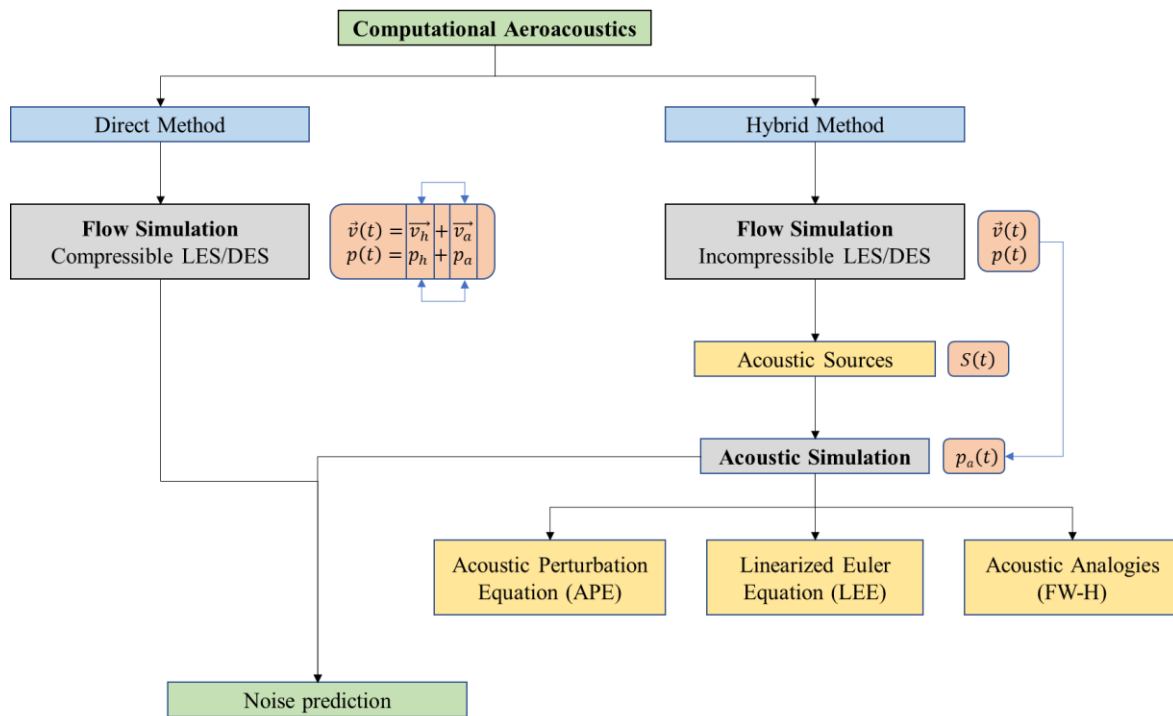


Fig. 2.6. Comparison of direct and hybrid methods used for evaluating aeroacoustics. Here $(\cdot)_h$ and $(\cdot)_a$ represents the hydrodynamic and acoustic components.

Table 2.3 Detail comparison between Direct and Hybrid methods

Computational Aeroacoustics Methods		
	Direct method	Hybrid method
Description	<ul style="list-style-type: none"> – The direct method (DM) computes the compressible Navier Stokes (NS) equation. – DM solves both hydrodynamic and acoustic pressure fluctuations simultaneously. – Captures the interaction between the flow field and acoustic waves propagation. 	<ul style="list-style-type: none"> – The hybrid method (HM) computes the incompressible Navier Stokes (NS) equation. – HM solves hydrodynamic pressure fluctuations separately as a first step, followed by acoustic pressure fluctuations as a second step. – Inability to capture the interaction between the flow field and acoustic waves propagation.
Grid Requirements	<ul style="list-style-type: none"> – Stringent grid requirements as the method should resolve the length scales associated with both flow and acoustic fields (Herpe et al., 2012). – No sudden changes in the grid imply a smooth transition between two different grid sizes. These sudden changes can lead to spurious noise generation (Dawi and Akkermans, 2019) 	<ul style="list-style-type: none"> – The grid-generation strategy used for aerodynamic studies can be extended to aeroacoustics as the grid requirements are less stringent. – Sudden changes in the mesh away from the body of interest is permissible.
Discretisation Schemes	<ul style="list-style-type: none"> – The strict requirement of using low dissipation and dispersion schemes (Dawi and Akkermans, 2018) 	<ul style="list-style-type: none"> – The discretisation schemes depend on the flow solver setup.
Reflections	<ul style="list-style-type: none"> – Damping functions and non-reflective boundary conditions are essential. 	<ul style="list-style-type: none"> – No reflections are considered in hybrid methods if acoustic analogies are used.

		<ul style="list-style-type: none"> – The damping and source masking is defined if the Acoustic perturbation wave equation (APE) is used (He et al., 2021c).
Time step and computational resources	<ul style="list-style-type: none"> – Smaller time steps are needed to ensure the pressure perturbations are captured, and this is done by replacing the fluid velocity with the sound propagation velocity in CFL (Wagner et al., 2007). – Higher computational costs as the flow and noise is computed simultaneously. 	<ul style="list-style-type: none"> – Time steps can be determined based on the number of time steps required per oscillation (Rung et al., 2002). – The lower computational cost for acoustic calculations as the flow and noise computed separately. Integral methods such as FWH can be employed which reduces the computational cost by orders of magnitude compared to Direct methods (Frank, 2017).
Limitations	<ul style="list-style-type: none"> – Measuring sound radiated from the body will be challenging due to the stringent grid requirements for example the effect of landing gear noise to an observer on the ground. 	<ul style="list-style-type: none"> – Additional equations are used to compute acoustic wave propagation (Ewert and Schröder, 2003; Nusser, 2019).

2.5.1. Hybrid methods

Hybrid methods consist of two steps: the solution of the incompressible NS equation as a first step and the calculation of the acoustic solution using an acoustic solver as a second step. Acoustic analogies such as APE and FW-H are derived from the limitations of Lighthill's analogy. The APE overcomes the main drawback of Lighthill's analogy, that is, the separation of acoustic and hydrodynamic pressure fluctuations in the source region. FW-H extends Lighthill's analogy by introducing a function that separates the fluid from the solid region. FW-H is valid for both the outside and inside solid boundaries. A review of these methods is described below

Lighthill's analogy

Lighthill analogy is an inhomogeneous wave equation for the fluid density proposed by Lighthill (1954, 1952). The equation was formulated by rearranging both mass and momentum conservation equations resulting in an equation containing a wave operator on the left-hand side and the sum of all non-linear and vicious terms on the right-hand side, which is given as follows:

$$\frac{\partial^2 \rho'}{\partial t^2} - c^2 \frac{\partial^2 \rho'}{\partial x_i^2} = \frac{\partial^2 T_{ij}}{\partial x_i \partial x_j} \quad (2.42)$$

Here, ρ' corresponds to the density fluctuations and T_{ij} to the Lighthill stress tensor

$$T_{ij} = \rho U_i U_j - \tau_{ij} + \delta_{ij}(p' - c^2 p') \quad (2.43)$$

Eq. (2.39) does not include any approximation or linearisation, and its analytical solution can be written as

$$\rho' = \frac{1}{4\pi c^2} \frac{\partial^2}{\partial x_i \partial x_j} \int_{-\infty}^{\infty} \frac{T_{ij}(y, t - \frac{r}{c})}{r} d^3 y \quad (2.44)$$

Here, y corresponds to the position of the noise source, r to the distance between the source, and x is the observer. The relation between these distances is defined as

$$r = |x - y(\tau)| \quad (2.45)$$

$y(\tau)$ represents the source position at the time τ , which corresponds to the retarded time. The difference between the retarded time and observation time t corresponds to the time needed for a sound signal to travel between the source and the observer. The following relation applies:

$$t = \tau + \frac{r}{c} \quad (2.46)$$

The solution obtained using Lighthill's equation is shown in Eq. 2.44 is valid for unbounded domains and is invalid in the presence of solid bodies inside the domain. Hence, the direct application of Lighthill's analogy is restricted to the noise generated due to turbulence alone, such as jet noise. Also, Lighthill's analogy is based on a compressible conservation equation, and the noise generated contains non-acoustic components such as vorticity in the source region, which do not propagate into the acoustic field but influences the solution in the flow field. Other perturbation equations, such as Acoustic Perturbation Wave Equations (APE), are needed to evaluate the acoustic flow field in the source region.

Acoustic Perturbation wave Equation (APE)

Ewert and Schröder (2003) formulated acoustic perturbed wave equations to overcome the main drawback of Lighthill's analogy which lies in the missing separating of acoustic and hydrodynamic pressure fluctuations in the source region. According to the flow, quantities can be divided into a mean and a fluctuating part, which further can be decomposed into acoustic and non-acoustic components, as shown in Eq. 2.47.

$$\begin{aligned} p &= \bar{p} + p' = \bar{p} + p^h + p^a \\ u_i &= \bar{u}_i + u_i' = \bar{u}_i + u_i^h + u_i^a \end{aligned} \tag{2.47}$$

The above decomposition of both pressure and velocity, when substituted in both the continuity equation and momentum equation and neglecting non-linear terms in both the equations and introducing an acoustic scalar potential φ , results in Eq. 2.48.

$$\frac{\partial^2 \varphi}{\partial t^2} - c^2 \nabla^2 \varphi = \frac{1}{\rho} \frac{\partial}{\partial t} p_{flow} \tag{2.48}$$

Here, $\varphi = \rho \frac{\partial \varphi}{\partial t}$ and p_{flow} represents the local instant value hydrodynamic pressure or static pressure of the flow obtained from resolving flow quantities using flow equations. c and ρ represent the speed of sound and density of the fluid, respectively.

The above method is used to determine the noise sources from the flow field obtained using turbulence models. However, the intensity of the noise radiated into the free stream is determined at a point, generally referred to as a probe, using surface integral methods described in the following sections.

Kirchhoff Integral

Kirchhoff integral is an inhomogeneous wave equation with source terms distributed on a surface which encloses the sound source. Application of the Kirchhoff integral requires the pressure perturbation (p') on and outside the surface to satisfy ($\nabla^2 p' = 0$) and must satisfy the homogenous wave equation. For detail derivation of Kirchhoff integral, the readers are directed to (Prieur and Rahier, 2001). The formulation of the Kirchhoff integral is shown in Eq. 2.49

$$p'_r(t) = \frac{1}{4\pi} \oint \left[\left(\frac{1}{cr} \frac{\partial p'_s(t)}{\partial t} + \frac{p'_s(t)}{r^2} \right) \frac{\partial r}{\partial n} - \frac{1}{r} \frac{\partial p'_s(t)}{\partial n} \right]_{t_{ret}} ds \quad (2.49)$$

Here, p'_r is the acoustic pressure evaluated at the non-moving receiver, which is located at a distance of r from the selected sound source surface (s). n denotes the vector normal to the surface, and t_{ret} represents the retarded time which is given as $t_{ret} = t - c/r$. The sound source in the present study is the mirror surface, and the normal pressure gradient on the mirror surface is equal to zero. Thus Eq. 2.50 can be reduced to

$$p'_r(t) = \frac{1}{4\pi} \oint \left[\left(\frac{1}{cr} \frac{\partial p'_s(t)}{\partial t} + \frac{p'_s(t)}{r^2} \right) \frac{\partial r}{\partial n} \right] ds \quad (2.50)$$

Ffocws William Hawking (FW-H)

FW-H analogy adopts the most general form of Lighthill's acoustic analogy and can predict sound generated by acoustic sources such as monopoles, dipoles and quadrupoles (Ffowcs Williams and Hawkings, 1969). FW-H formulation is an inhomogeneous wave equation that can be derived using continuity and NS equation and is defined as

$$\frac{1}{a_0^2} \frac{\partial^2 p'}{\partial t^2} - \nabla^2 p' = \left(\begin{array}{c} \frac{\partial^2}{\partial x_i \partial x_j} \{T_{ij} H(f)\} \\ - \frac{\partial}{\partial x_i} \{ [P_{ij} n_j + \rho u_i (u_n - v_n)] \delta(f) \} \\ + \frac{\partial}{\partial t} \{ [\rho_0 v_n + \rho (u_n - v_n)] \delta(f) \} \end{array} \right) \quad (2.51)$$

Where p' is the pressure perturbations, T_{ij} is the Lighthill stress tensor, $H(f)$ is the Heaviside function, P_{ij} is the compressive stress tensor, n_j the unit normal vector pointing into the fluid, u_n is the velocity of the fluid normal to the surface, v_n the velocity of the surface in the direction normal to the surface, $\delta(f)$ is the Dirac Delta function, and ρ_0 the density of the fluid. The function $f(\vec{x}, t)$ describes the moving integration surface.

T_{ij} Lighthill stress tensor is defined as in Eq. 2.52

$$T_{ij} = \rho u_i u_j + P_{ij} - a_0^2 (\rho - \rho_0) \delta_{ij} \quad (2.52)$$

Where P_{ij} is the compressive stress tensor.

The solution obtained for FW-H formulation using the Green's function contains surface integrals and volume integrals. The surface integrals represent the contributions from monopoles and dipole acoustic sources, whereas the volume integrals generally represent the contributions from quadrupole sources in the region outside the source surface. However, the contributions of volume sources become negligible as the cases investigated in this thesis are $M < 0.3$, and therefore, volume integrals are neglected. The obtained solution can be rewritten in terms of pressure perturbations as

$$p'(\vec{x}, t) = p'_T(\vec{x}, t) + p'_L(\vec{x}, t) \quad (2.53)$$

Where,

$$4\pi p'_T(\vec{x}, t) = \int_{f=0} \left[\frac{\rho_0 (\dot{U}_n + U_{\dot{n}})}{r(1 - M_r)^2} \right] dS + \int_{f=0} \left[\frac{\rho_0 U_n \{r\dot{M}_r + a_0(M_r - M^2)\}}{r^2(1 - M_r)^3} \right] dS \quad (2.54)$$

$$4\pi p'_L(\vec{x}, t) = \frac{1}{a_0} \int_{f=0} \left[\frac{\dot{L}_r}{r(1 - M_r)^2} \right] dS + \int_{f=0} \left[\frac{L_r - L_M}{r(1 - M_r)^2} \right] dS + \frac{1}{a_0} \int_{f=0} \left[\frac{L_r \{r\dot{M}_r + a_0(M_r - M^2)\}}{r^2(1 - M_r)^3} \right] dS \quad (2.55)$$

Generally, in a physical sense $p'_T(\vec{x}, t)$ and $p'_L(\vec{x}, t)$ are referred to as thickness and loading terms, respectively.

Hybrid methods offer two surface integral methods to evaluate externally generated noise: FW-H and Kirchoff Integral (KI). Both approaches have similar formulations if the contributions from quadrupole sources are neglected as assumed for vehicle aeroacoustics studies.

2.6. Mesh for the aerodynamic and aeroacoustics studies

The turbulence models are used to describe the flow field, while CAA is used to describe the acoustic field in the domain of interest. The numerical models discussed above are implemented on a domain containing the body of interest. The domain is discretised into small known mesh topologies such as hexahedral, tetrahedral, or polyhedral elements. In the following sections, the choice of mesh used for both aerodynamic and aeroacoustics studies is presented in detail.

For an external flow study such as the flow over a vehicle, the flow experiences laminar to turbulent transition, separation and reattachment at several locations due to its complex shape. The mesh resolution at the wall and the free stream must be estimated to ensure they capture such complex physics around the vehicle. An estimate for the mesh sizes near the walls and in the free stream can be obtained based on characteristic length scales as discussed in **section 2.1** (Fares, 2006; Guilmineau et al., 2018; Howard and Pourquie, 2002) and the wall-normalised units (Fröhlich and von Terzi, 2008; Piomelli and Chasnov, 1996; Pope, 2001; Shur et al., 2008). For aerodynamic studies, the mesh is locally refined in regions with strong gradients, while for acoustics studies, the mesh needs a uniform mesh size to preserve the acoustic wave propagation in the whole domain. Therefore, the mesh generated should satisfy these two criteria for an aeroacoustics study.

The mesh generation can be broadly classified into two categories, structured and unstructured, based on the element topology used to discretise the domain. Structured meshes are hexahedral elements with reasonably good node-node connectivity in the mesh through the domain (Thompson, 1987). Generally, generating a structured mesh (see Fig. 2.7a) for complicated geometries, such as vehicle geometry, is challenging and time-consuming due to the possible need to break the domain into several blocks depending on the shape of the geometry. However, the quality of the mesh using a structured approach is very high compared to any other mesh.

An unstructured mesh (see Fig. 2.7 b,c) can be defined as a set of elements, such as tetrahedrons or polyhedrons, with connectivity defined explicitly between the nodes in the mesh (Marcum and Weatherill, 1995). The unstructured mesh generation involves two basic steps: node creation and definition of the connectivity between these nodes. As a result, the unstructured mesh offers a high degree of flexibility when meshing complex geometries and the process of mesh generation can be automated. However, the solution accuracy may be

affected if the highly skewed meshes are present in sensitive areas such as boundary layers. The effect of the generation of poor-quality mesh on the solution accuracy is detailed in **Chapter 3**.

Hybrid meshes extension of unstructured meshes where the mesh combines the advantages of both structured and unstructured meshes (see Fig. 2.7d). In hybrid meshes, the near-wall are filled with prismatic elements, while the rest of the domain is either filled with polyhedrons, tetrahedrons, or hexahedrons elements . Also, hybrid mesh generates fewer cells in the viscous region than unstructured mesh with a similar resolution (Noack and Steinbrenner, 1995). Further, the concept of meshing with different elements is extended to form a generalised mesh (see Fig. 2.7e), where the mesh has no restrictions on the number of edges or faces in a cell (Koomullil and Soni, 1999).

Generalised meshes are referred to as mesh with hanging nodes (Finite Element Method -based meshing technique), generated using a mesh generation algorithm such as Cut-Cell (Ito, 2013). The merits and demerits of different meshes are presented in the table below:

Table 2.4 Merits and demerits of various meshes used in CFD

	Structured	Unstructured/Hybrid	Generalised
Geometry Flexibility	Low to Medium	High	High
Mesh Adaption	Low to Medium	High	High
Mesh Quality	High	Medium	Medium to low
High-order Schemes such as ENO and WENO, DG schemes	Yes	Yes	Yes
Numerical Dissipation and Dispersion	Low	Medium to High	Medium to High
Wall representation / Viscous sub-layer resolution	High	Medium	Medium
Local refinements	No	Yes	Yes
Computational efficiency	Excellent	Good	Excellent
Mesh interfaces (Transition zone between grid sizes)	No	Yes	Yes
CPU and memory requirements	Low to Medium	High	Low to Medium

Despite the advantages of unstructured and hybrid meshes, the quality of the mesh has to be ensured by performing additional checks for skewness, orthogonality, and aspect ratios.

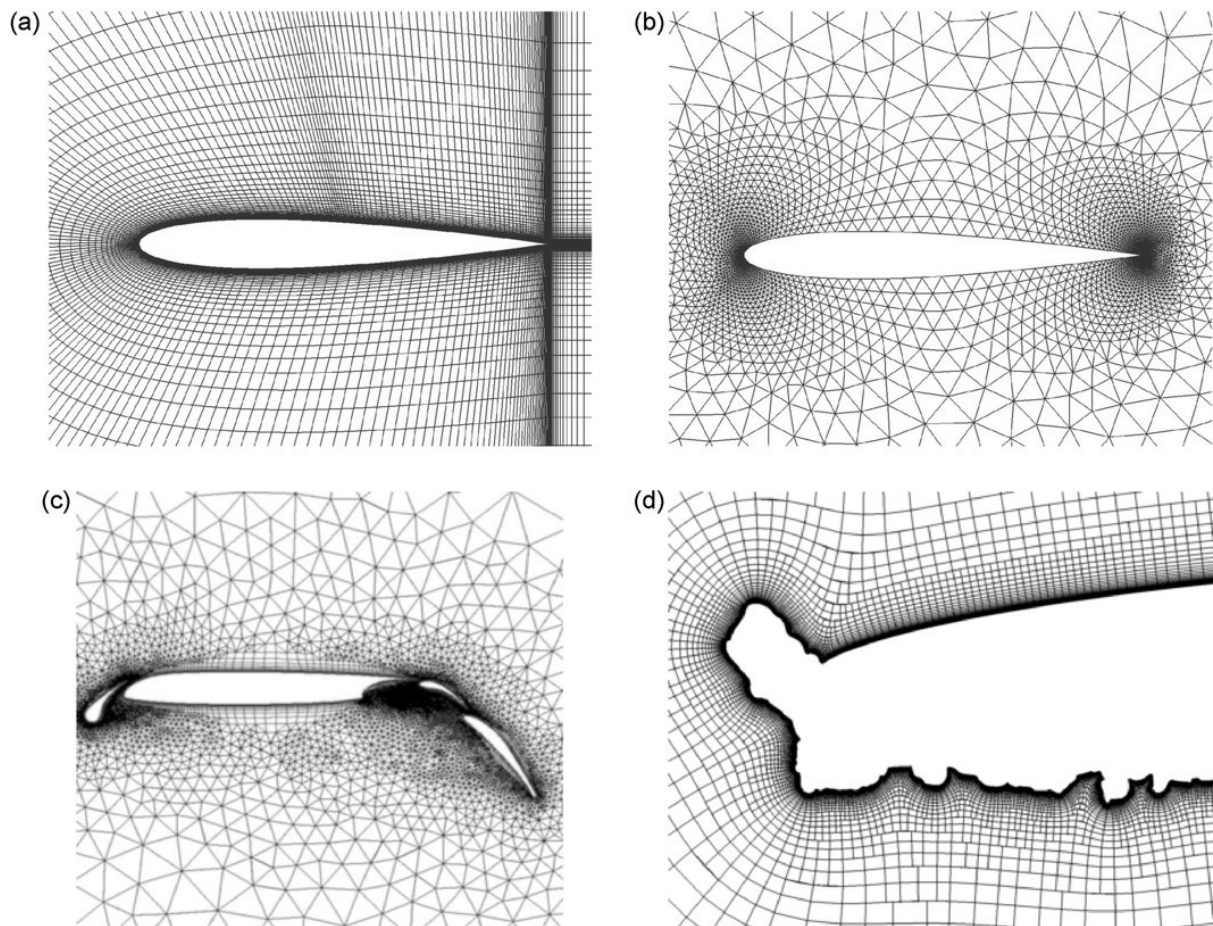


Fig. 2.7. Type of meshes: **a)** Structured Mesh, **b)** Unstructured mesh, **c)** Hybrid Mesh, and **d)** Generalised Mesh (Koomullil et al., 2008)[©].

Hybrid mesh such as hexcore and poly-hexcore meshes (See Fig. 2.8) with different topologies is proposed to reduce the overall cell count and adapt to the complex geometries while generating meshes. In both polyhedral - hex dominant core, and hex dominant core, the hexahedral elements are generated in the hex dominant core because of their accuracy and efficiency. Unstructured Polyhedral-dominant hex core mesh combines hexahedral, isotropic polyhedral cells as prism cells and polyhedral elements, as shown in Fig. 2.9. Poly-hex core grid uses polyhedron cells to capture complex geometrical surfaces accurately, and the volume region is filled with octree hexahedron elements. A smooth transition from surface mesh to free stream is obtained using layers containing regular polyhedral cells to adjust for the cell size difference, generally referred to as transition layer (Zore et al., 2019).

However, using unstructured and hybrid meshes for aeroacoustics studies is challenging due to the formation of mesh interfaces between different cell sizes and this

[©] Reused with permission from Koomullil, R., Soni, B. and Singh, R., 2008. A comprehensive generalized mesh system for CFD applications. *Mathematics and Computers in Simulation*, 78(5-6), pp.605-617.. Copyright © 2008 IMACS. Published by Elsevier B.V. All rights reserved.

interfaces can generate spurious noise which can be minimised by adopting low expansion ratios (Dawi and Akkermans, 2018). Further, Dawi and Akkerman (2018, 2019) have used KI and FW-H methods to evaluate the noise generated from the realistic mirror and generic vehicle bodies. They emphasised that the FW-H solution was not affected by spurious noise from mesh interfaces. Therefore, unstructured and hybrid meshes can be used to evaluate aerodynamics and aeroacoustics as long as the mesh interfaces smooth transitions are maintained between different meshes types and sizes used.

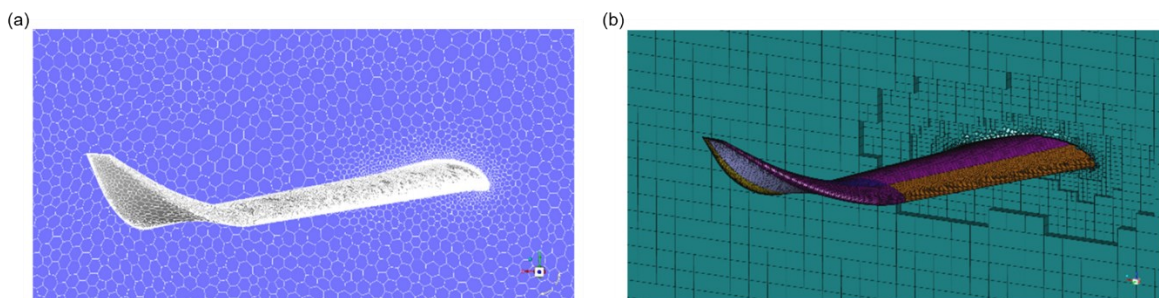


Fig. 2.8. Cut sections of a) hexcore and b) poly-hexcore generated for an aircraft wing with flaps (Karkoulias et al., 2022)^d.

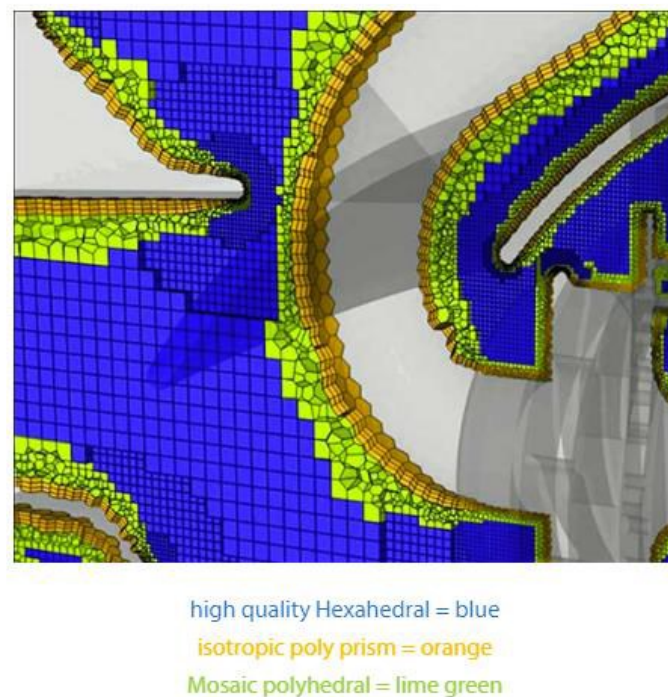


Fig. 2.9. Overview of transition layer generated in unstructured polyhedral-dominant hex mesh (Zore et al., 2019)^e.

^d Reused with permission from Karkoulias DG, Tzoganis ED, Panagiotopoulos AG, Acheimastos S-GD, Margaris DP. “Computational Fluid Dynamics Study of Wing in Air Flow and Air-Solid Flow Using Three Different Meshing Techniques and Comparison with Experimental Results in Wind Tunnel”. *Computation* 10(3):34. Copyright © 2022, licensed under Creative Commons 4.0.

^e Reused with permission from Zore, K., Azab, M., Sasanapuri, B., Shoaib, S., Stokes, J., 2019. ANSYS scale resolving simulations of launch-vehicle. 21st AeSi Annu. CFD Symp. 8–9. Copyright © 2019 authors. Permission obtained from Krishna Zore (Author).

2.7. Numerical Methods

The accuracy of the modelling approaches presented in **Sections 2.2 and 2.4** depends not only on the mesh types presented in **Section 2.5** but also on numerical schemes such as discretisation schemes, gradient approximation schemes and p-v coupling schemes. Each of the numerical schemes ensures the accuracy of the solution obtained. The solution is obtained by calculating the discrete distribution of variables as the finite volume method approach is used. The first step is to obtain gradients of flow variables obtained for each cell using gradient approximation schemes, then using discretisation schemes in space and time, the value of the flow variables (ϕ) is obtained at the cell centres (ϕ_c) and the cell face (ϕ_f). These obtained variables feed into the modelling equations presented in **Chapter 2**, thus obtaining a solution in space and time for the whole domain.

Table 2.5 Summary of the numerical schemes

Scheme			Description
Spatial Discretisation	First Order (FOU)	Upwind	<ul style="list-style-type: none"> • Simplest discretisation where the flow variable value ϕ evaluated at face is equal to cell, $\phi_f = \phi_c$ • Highly diffusive scheme and the grid has to be aligned with the flow to avoid numerical errors.
	Second Order (SOU)	Upwind	<ul style="list-style-type: none"> • Most widely used spatial discretisation for both Steady and Unsteady simulations. • The flow variable at the cell face using $\phi_f = \phi_c + \nabla\phi \cdot \vec{r}$. Where a gradient operator is used to ensure the scheme is stable for mesh with a high aspect ratio ($> O(1000)$) and skewness (> 0.98).
	Central Scheme (CDS)	Differencing	<ul style="list-style-type: none"> • Similar to SOU, the flow variable is evaluated as the average the value of ϕ with the neighbouring cell sharing faces. $\phi_f = \frac{1}{2}(\phi_0 + \phi_1) + \frac{1}{2}(\nabla\phi_0 \cdot \vec{r}_0 + \nabla\phi_1 \cdot \vec{r}_1)$
	Bounded Differencing (BCD)	Central	<ul style="list-style-type: none"> • Central differencing is unbounded and non-physical oscillations are introduced for high Re flows. • A hybrid scheme consists of the central difference, second order and first order, switching between them. The convection boundedness Criterion (CBC) defines the switch. The constant/parameter controlling the switch varies from 0 to 1. When the CBC value is 0 the BCD acts as the first order while closer to 1 it switches to central difference. • The switching constant needs tuning based on the complexity flow involved. In general, for complex flows, the switching constant is set at 0.75.
	MUSCL		<ul style="list-style-type: none"> • A hybrid scheme consists of the central difference and 2nd order. Its averages between 2nd order and Central difference at the cell centres. • $\phi_f = \theta\phi_{f,CD} + (1 - \theta)\phi_{f,SOU}$ • The blend factor in the MUSCL scheme is set at $\theta = 1/3$. • Lower levels of diffusion when compared to second order for unstructured meshes with higher aspect ratios.

	QUICK	<ul style="list-style-type: none"> • A hybrid scheme consists of the central difference and 2nd order. • Its averages between 2nd order and Central difference at the cell node. • Accuracy tends to be lower for non-conformal meshes such as unstructured compared to structured meshes. • The accuracy of the QUICK scheme can be sensitive to the aspect ratio (i.e. the ratio of the length to the width) of the cells in the grid.
Temporal Discretisation	Bounded Second Order Implicit	<ul style="list-style-type: none"> • The scheme ensures the time is 2nd order accurate throughout the domain using the boundedness of bounded variables. • The formulation is present in the appendix. • It can accommodate unstructured meshes where maintaining $CFL < 1$ is challenging.
Gradient Approximation	Least Squares Cell-based (LSC)	<ul style="list-style-type: none"> • The gradients are obtained using distance vectors between the neighboring cell centroids. • LSC is considerably more stable for unstructured grids with high aspect ratios and skewness.
P-V Coupling	SIMPLE SIMPLE C	<ul style="list-style-type: none"> • Both SIMPLE and SIMPLE-C obtain a relationship between velocity and pressure corrections by enforcing the mass conservation at each cell in the grid. • The process of obtaining corrected variables is presented in the flow chart in the appendix. • Additional skewness correction is offered in SIMPLE-C. SIMPLE-C adds another step in SIMPLE after obtaining the initial solution for pressure correction to account for skewness.

2.7.1. Numerical Errors

Round-off errors

Round-off errors are also referred to as machine accuracy. These error are simplest and are the result of representation of real numbers by means of a finite number of significant digits. With advanced computer resources, numbers are typically stored with 16, 32, or 64 bits. If round off errors become significant, then higher precision is used to run the code. However, large precision also means higher data storage requirements. For example in Fluent, the default precision is a single precision which stores values with 32-bits which can be changed to double precision where it uses 64-bits. In this study, all the simulations are run using double precision.

Iterative convergence errors

In CFD, the flow is resolved using an iterative process. Ideally, the solution obtained should exactly satisfy the discretised flow equation in the interior of the domain and the specified boundary conditions but while performing an iterative process, the obtained solution will be close to the final solution, the difference is considered as the iterative convergence error. For example, consider a flow variable ϕ at local cell i can be written as follows:

$$(a_p \phi_p)_i = \left(\sum_{nb} a_{nb} \phi_{nb} \right)_i + b_i \quad (2.56)$$

Here a_p is the center coefficient, a_{nb} are the coefficients of the neighbouring cells, b is the constant part of the source term and of the boundary conditions and i subscript indicates the control volume.

After, n th iterations the difference between the left and right hand side of Eq. 2.56 is called the local residual R_i^ϕ . While in most cases, the scaled residuals are used to monitor for various flow variables which is obtained by taking the average of all local residuals in the entire domain.

Discretisation Errors

Spatial discretisation of the domain should be properly built to accurately predict the physics of flow motion and avoid excessive numerical dissipation and dispersion. When evaluating the nonlinear terms on a discrete mesh, certain numerical errors occur, particularly for convection terms. As the flow over ground vehicles is high Reynolds number flows and generally preserves the geometrical features, unstructured grids are preferred; thus, discretisation of convection terms plays a significant role and ensures numerical stability.

Second-order central differencing (CD) creates an unstable solution in unstructured grids. To achieve a stable solution, first-order accurate differencing schemes such as the Lax-Wendroff schemes are used by combining spatial and temporal discretisation, leading to two-step and implicit schemes. However, such schemes were inaccurate in the steady state, and several second-order schemes were proposed which were independent of time integration which caused nonphysical oscillations in the solution, severely reducing the quality. Consequently, the obtained solution is outside the physical bounds of the problem. Therefore, bounded numerical solutions must be used when solving the transport equations with bounded properties. Initially, an Upwind Differencing (UD) scheme was proposed which guaranteed boundedness which ensured that all the coefficients in the system of algebraic equations were positive even in the absence of physical diffusion which was achieved by introducing an excessive amount of numerical diffusion. In highly skewed grids, the accuracy of UD schemes is unacceptable. To overcome this concept of flux limiting, schemes which lead to the formulation of total variation diminishing (TVD) schemes such as MUSCL.

In TVD schemes, the blending of higher-order unbounded and first-order bounded differencing schemes depends on the local solution shape. TVD schemes were accurate for smooth profiles; however, to capture sharp profiles and smooth profiles, a new condition which requires local boundedness on a cell-by-cell basis must be introduced which is achieved by Normalised Variable Diagram (NVD) schemes. The most widely used NVD-based scheme is Bounded Central Differencing (BCD), in which the NVD scheme is used along with the convective boundedness criterion (CBC). However, both the TVD and NVD schemes are computationally expensive, and implementing them will increase the run times. However, by carefully selecting complementary numerical schemes and grid sizes, discretisation errors can be minimised.

2.8. Standard Geometries

Several standard geometries are proposed for researching the fundamentals of flow and acoustics. The following sections introduce and review the most commonly used standard geometries. The section is divided into parts *i*) simplified vehicle geometries, where salient flow features, aerodynamic and aeroacoustics characteristics are reviewed for the most commonly used vehicle geometries, and *ii*) standard Mirror geometry, which is commonly used to understand the noise generation mechanisms are presented.

2.8.1. Simplified Vehicle Geometries

Simplified vehicle geometries are widely used in the study of vehicle aerodynamics. These models have been used mainly to validate turbulence models and comprehend the fundamental aspects of flow behaviour around ground vehicles. The models typically are classified as a fastback, square-back (or Estate) and notchback, as shown in Fig 2.10, similar to the classification made in production vehicles. Also, the models in Fig 2.10 are semi-realistic representations of production vehicles. Standard vehicle geometries such as the Ahmed body, Windsor body, SAE reference body, MIRA reference body, Davis model and ASMO model are more simplified than the models presented in Fig 2.10 but still have wake topologies representing realistic vehicles, as shown in Fig. 2.11.

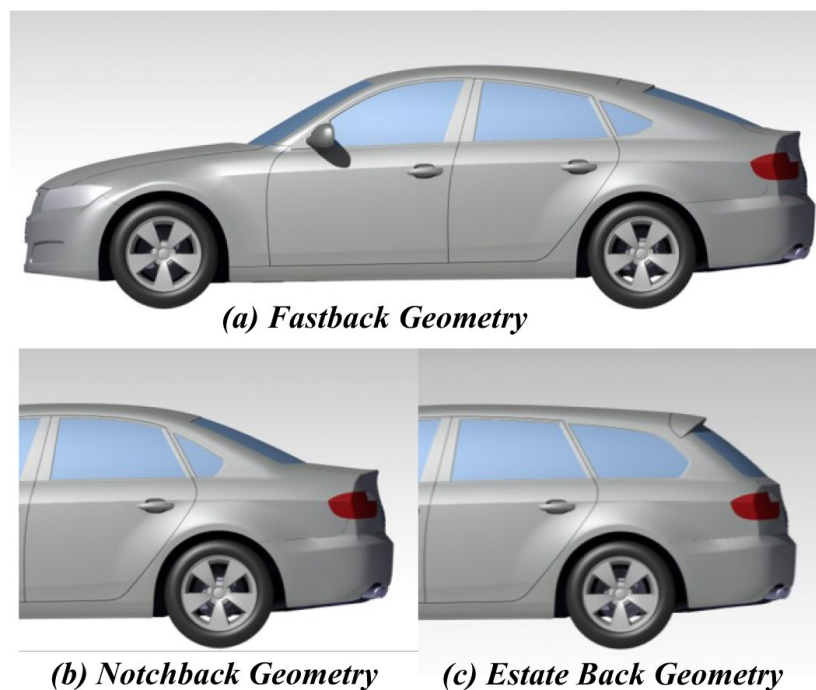


Fig. 2.10. Schematic representation of the DrivAer model in three configurations (Heft et al., 2012)^f.

^f Reused with permission from Heft et al., “Introduction of a New Realistic Generic Car Model for Aerodynamic Investigations”. SAE Technical Paper (No. 2012-01-0168). Copyright © 2012 SAE International.

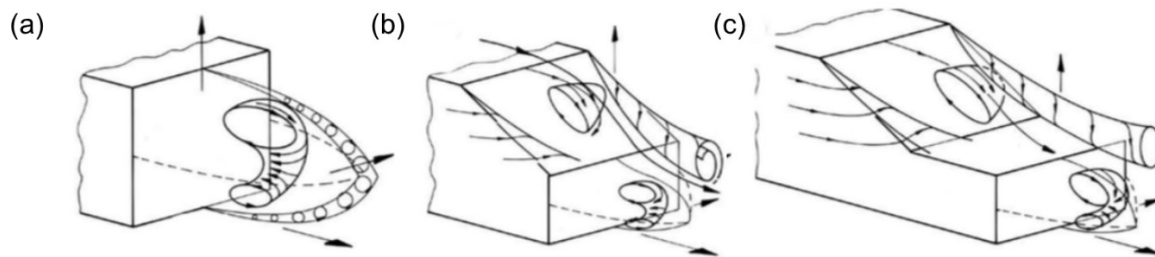


Fig. 2.11. Schematic representation of the wake topology behind (a) square-back, (b) fastback and (c) notchback geometries (Pavia, 2019)^g.

Fastback geometry

The fastback geometry represents realistic passenger cars such as hatchbacks where the rear end has a slant surface. The length and backlight angle (α) vary over a wide range; as a result, both the flow features and the vehicle's drag change. In the case of Ahmed Body, the time-averaged flow features indicate that for $0^\circ < \alpha < 12.5^\circ$, the flow remains attached to the rear slant and separates at the rear edge of the body. While for $12.5^\circ < \alpha < 30^\circ$, the flow separates at the leading of the slant and reattaches quickly, forming a recirculation bubble. The size of the recirculation increases with an increase in α until $\alpha = 30^\circ$. A pair of a counter-rotating longitudinal vortices are generated from lateral edges of the slanted surface, and their strength increases with an increase in α from 12.5° (Ahmed et al., 1984; Ashton and Revell, 2015; Guilmineau, 2008; Guilmineau et al., 2018). Similar flow features are observed for another simplified fastback geometry called the Davis model.

The pair of the counter-rotating longitudinal vortex also dominates the wake of the Davis model, as seen in Ahmed's fastback models. However, when the edges of the Davis model are rounded, a weaker pair of trailing vortices are seen, which significantly alters overall flow structures at the rear. Fuller and Passmore (2014) concluded that the near wake flow structures depend on the curvature of the edges of the vehicles. MIRA fastback model is an improvement over the Ahmed and Davis model, as it replicates a more representative-like fastback vehicle with a bonnet and A-pillar (Hoffman et al., 2001). Specific features such as pair of trailing vortices and vortex generated from the side represent flow similar to Ahmed or Davis models, but additional vortices are generated due to introducing A-pillar and Diffuser. While on the rear slant, the flow is attached and separates only at the trailing edge of the body, similar to the Ahmed body with rear slant angles $\alpha < 12.5^\circ$. A similar flow pattern is observed

^g Reused with permission from Pavia, Giancarlo. 2019. "Characterisation of the Unsteady Wake of a Square-back Road Vehicle," PhD thesis, Loughborough University. Copyright 2019 © Giancarlo Pavia, license under Creative Commons 4.0.

for the DrivAer fastback, which resembles an actual production vehicle, as shown in 2.10(a) (Heft et al., 2012). The effect of change in the rear slant angles on the aerodynamic characteristics is quantified in the table below. Despite several exciting flow features and potential noise generators, a detailed study of acoustics on fastback is not conducted to date; one possible explanation is that the focus of noise studies is on the noise transmitted inside the cabin through the side window due to the complex interaction of side-view mirror and A-pillar.

Table 2.6 Aerodynamic characteristics of the standard fastback geometries

Fastback Vehicle Geometries	Rear slant Angle (α)	Coefficient of drag (C_D)	Coefficient of lift (C_L)
Ahmed Body (Ahmed et al., 1984)	5°	0.231	-
	12.5°	0.230	-
	20°	0.252	-
	25°	0.286	-
	30° (High)	0.378	-
	30° (Low)	0.260	-
Davis Model (Fuller and Passmore, 2014)	20°	0.282	0.427
MIRA fastback (Personal communication, 19, December, 2022)	23.6°	0.227	0.021
DrivAer fastback (Wieser et al., 2014)	-	0.258	-0.107

Notchback Geometry

Notchback Geometry of simplified vehicles represents realistic vehicles classified as sedans; see Fig 2.10 b. Notchbacks have specific flow topologies similar to fastbacks, such as the trailing counter-rotating vortex and are similarly sensitive to the rear slant angles, as shown in Fig 2.11 c. However, the behaviour becomes complex with introducing the boot deck to the geometry. The flow over the roof separates at the trailing edge of the roof and forms a hairpin vortex over the rear slant; the counter-rotating longitudinal vortices influence the strength of the hairpin vortex and the structure. Many experimental studies on notchback geometries, such as the SAE Reference model (Wood et al., 2014), the DrivAer model (Wieser et al., 2014), the Windsor notchback model (Gaylard et al., 2007), the MIRA notchback model (Gaylard et al., 2007) and the Ford reference model (Gilhome et al., 2001), identified an asymmetrical hairpin vortex over the rear slant. The asymmetry on the rear tends to increase with an increase in the rear slant angle.

Further, the reattachment point for the separated flow on the boot deck tends to move towards the lateral edge of the boot deck when the rear slant angle is increased, which increases

the drag coefficient. The aerodynamic characteristics of the notchback models are presented below in Table 2.7. Also, a comparison of flow topologies on the rear slant of the notchback configuration is shown in Fig 2.12.

Table 2.7 Aerodynamic characteristics of the standard notchback geometries

Notchback Geometries	Vehicle	Rear slant Angle (α)	Coefficient of drag (C_D)	Coefficient of lift (C_L)
SAE Reference Model (Wood, 2015)		20°	0.207	0.054
		25°	0.229	0.055
		30°	0.260	0.066
		35°	0.275	0.105
		40°	0.284	0.088
DrivAer notchback Model (Wieser et al., 2014)		-	0.254	-0.095
MIRA notchback Model (Gaylard et al., 2007)		45°	0.263	-0.062

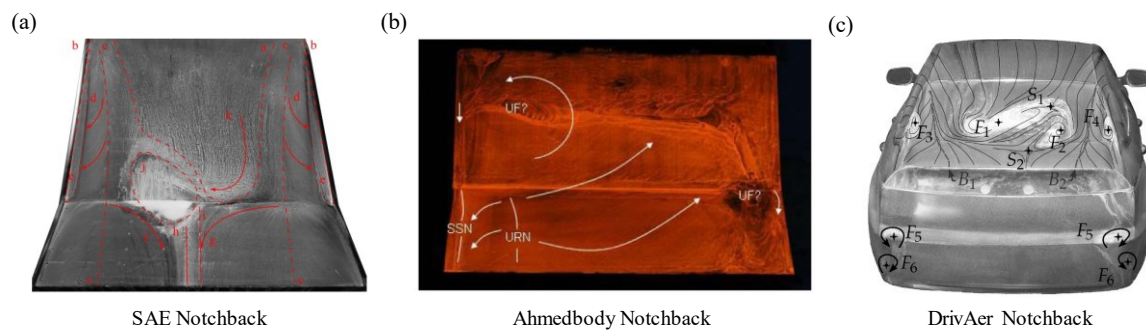


Fig 2.12. (a) SAE notchback model (Wood, 2015)^h, (b) Ahmedbody Notchback Model (Sims-Williams et al., 2011)ⁱ, and (c) DrivAer Notchback Model (Wieser et al., 2020)^j.

Square-back Geometry

Square-back geometry is a simplified estate-like vehicle with no to little tapering at the rear edges, forming a sizeable low-pressure region in the wake, increasing the vehicle’s drag. The time-averaged flow topology of the wake for a square-back is commonly described as a ring vortex, as shown in Fig. 2.10 (a) and 2.12(a). The ring vortex is sensitive to the tapered edges, ground effect, and wheels. Due to the sizeable low-pressure region in the wake, the drag reported for the square-back models is high among all the three-vehicle configurations and is

^h Reused with permission from Daniel Wood, “The Effect of Rear Geometry Changes on the Notchback Flow Field,” Loughborough University. Copyright © 2015 by Daniel Wood. Licensed under Creative Commons 4.0.

ⁱ Reused with permission from Sims-Williams et al. “Links between notchback geometry, aerodynamic drag, flow asymmetry and unsteady wake structure”. SAE International journal of passenger cars. Mechanical systems., 4(1), pp.156-165. Copyright © 2011 SAE International.

^j Reused with permission from Wieser et al., “Wake Structures and Surface Patterns of the DrivAer Notchback Car Model under Side Wind Conditions,” Energies 13(2):320. Copyright © 2020 by the authors. Licensed under Creative Commons 4.0 (CC BY).

widely used for researching various drag reduction techniques. The most commonly used to investigate drag reduction technique introduces tapered edges, cavities (no-blowing) and blown cavities at the base of the vehicle (Choi et al., 2014; Varney et al., 2017; Wassen et al., 2010).

Grandemange et al. (2012) have reported the existence of bi-stability for low Reynolds numbers. As the Reynolds number based on the height of the geometry is increased from $Re_H = 310$ to 410, the wake oscillated periodically, breaking reflection symmetry. Similar wake bi-stability is demonstrated even at a high Reynolds number of $O(10^7)$ (Grandemange et al., 2015), which led several researchers to comprehend the presence of bi-stability and factors influencing the bi-stability experimentally (Grandemange et al., 2015, 2013, 2012; Volpe et al., 2015) and numerically (Evstafyeva et al., 2017; Fan et al., 2020; Lucas et al., 2017; Rao et al., 2018) using a square-back Ahmed body (see Fig. 2.13b). Further, (Perry et al., 2016) reported similar bi-stability modes for the Windsor body, even though the Windsor body has a refined slanted front end (Pavia, 2019; Pavia et al., 2018). The effect of the W/H ratio of the square back, ground clearance, wheels, and taper rear edges on bi-stability is presented in detail by Pavia (2019) for the Windsor body. Despite the interesting flow topologies, to investigate the presence of bi-stability numerically, the overall run times are higher and extending the effect of bi-stability on noise radiated from the vehicle will be challenging due to the computational expense. For instance, to comprehend bi-stability behaviour, around ~ 6 s of simulated time must be predicted.

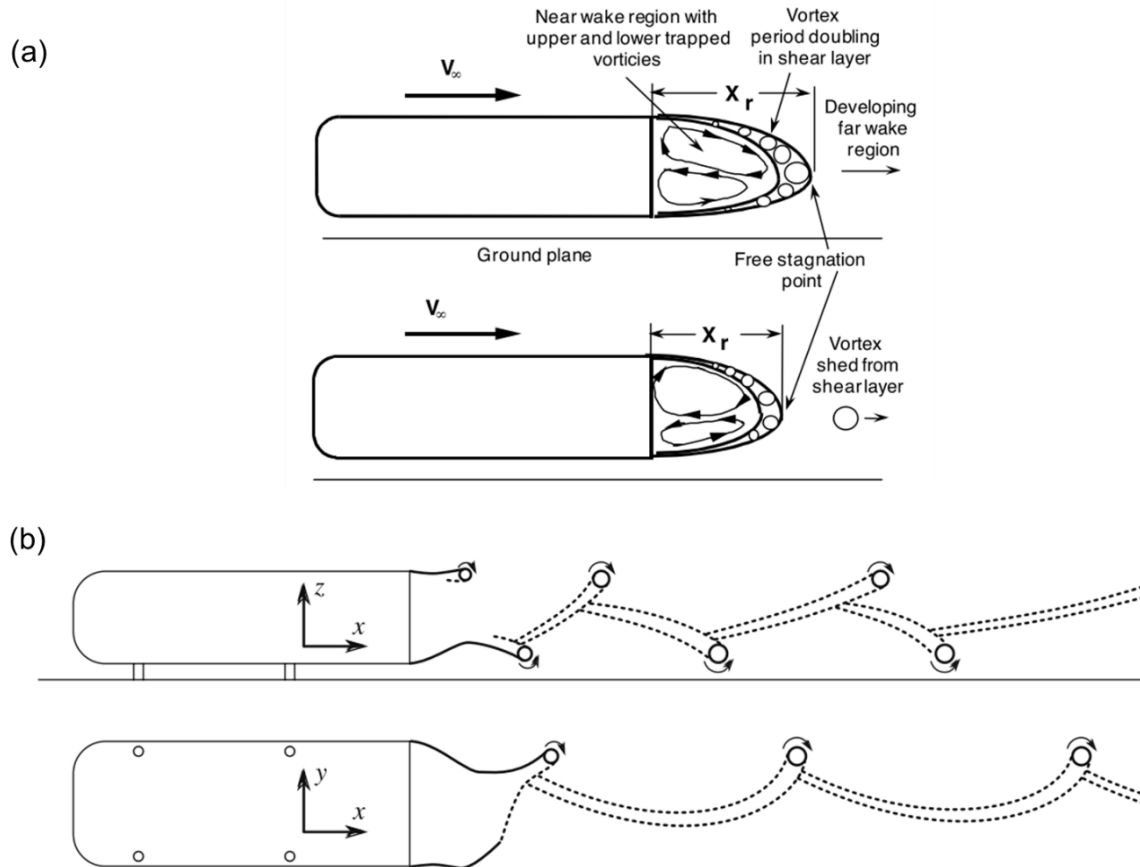


Fig. 2.13. a) Schematic representation of the wake topology behind a square-back geometry (Duell and George, 1999)^k and b) schematic representation of the short time scale modes for the wake behind a square-back Ahmed body (Grandemange et al., 2013)^l.

The square-back geometries such as SAE reference body are recently used to investigate the noise radiated inside the cabin due to the presence of the side-view mirror (Dawi and Akkermans, 2019; Hartmann et al., 2012; Islam et al., 2008a; Müller et al., 2013; Nusser and Becker, 2021). The vortex generated from the A-pillar tends to shift upwards in the presence of the side-view mirror, changing the pressure distribution on the side window (Dawi and Akkermans, 2019; Yuan et al., 2017). However, the correlation between the noise radiation and the vortex structures is not yet investigated.

2.8.2. Summary of numerical simulations performed using standard vehicle geometries.

In the section, a summary of numerical studies conducted by several researchers using a) square-back, b) fastback, and c) notchback configurations of simplified vehicle geometries are presented.

^k Reused with permission from Duell, E.G. and George, A.R., 1999. Experimental study of a ground vehicle body unsteady near wake. SAE transactions, pp.1589-1602. Copyright © 1999 Society of Automotive Engineers.

^l Reused with permission from Grandemange, M., Gohlke, M., & Cadot, O. Turbulent wake past a three-dimensional blunt body. Part 1. Global modes and bi-stability. Journal of Fluid Mechanics, 722, 51-84. Copyright ©2013 Cambridge University Press.

Table 2.8 List of previous studies conducted using simplified geometries.

Aerodynamics studies					
Case Study	Flow condition	Re	Geometry	Cfg.	Numerical models
Krajnović and Davidson (2005a, 2005b)	Incompressible	$Re_H = 2 \times 10^5$	Ahmed body	b)	LES
Fares (2006)	Incompressible	$Re_H = 7.6 \times 10^5$	Ahmed body	b)	VLES
Guilmineau (2008)	Incompressible	$Re_L = 2.78 \times 10^6$	Ahmed body	b)	RANS
	Incompressible	$Re_L = 2.78 \times 10^6$	Ahmed body	b)	EARSMD DES
Serre et al. (2013)	Incompressible	$Re_H = 7.6 \times 10^5$	Ahmed body	b)	DES LES
Aljure et al. (2014)	Incompressible	-	Ahmed body ASMO	b) -	LES
Ashton and Revell (2015)	Incompressible	$Re_H = 7.6 \times 10^5$	Ahmed body	b)	DDES
Ashton et al. (2016)	Incompressible	$Re_H = 7.6 \times 10^5$	Ahmed body	b)	RANS
		$Re_H = 1.48 \times 10^6$	DrivAer	a) b)	DDES
Islam and Thornber (2017)	Compressible	$Re_L = 2 \times 10^5$	SAE	c)	Implicit LES
Collin et al. (2016)	Incompressible	$Re_L = 5.2 \times 10^6$	DrivAer	a)	DDES
				b)	
				c)	
Guilmineau et al., (2018)	Incompressible	$Re_H = 7.6 \times 10^5$	Ahmed body	b)	RANS EARSMD DES and IDDES
Viswanathan (2021)	Incompressible	$Re_L = 2.7 \times 10^6$	Ahmed body	b)	RANS
Minguez et al. (2008)	Incompressible	$Re_H = 7.6 \times 10^5$	Ahmed body	b)	LES
Corallo et al. (2015)	Incompressible	-	Ahmed body	b)	RANS
Evstafyeva et al. (2017)	Incompressible	$Re_H = 310 - 435$	Ahmed body	a)	LES
Lucas et al. (2017)	Incompressible	$Re_H = 3.9 \times 10^5$	Ahmed body	a)	LBM
Rao et al. (2018)	Incompressible	$Re_L = 2 \times 10^6$	Ahmed body	b)	PANS
Ekman et al. (2020)	Incompressible	$Re_H =$	DrivAer	b)	SBES
				c)	
Chode et al. (2020)	Incompressible	$Re_H =$	SAE	c)	SBES
Aeroacoustics studies					
Islam et al. (2008)	Compressible	-	SAE	a)	LES
Hartmann et al. (2012)	Incompressible	-	SAE	a)	DES
	Compressible				LBM
Murad et al. (2013)	Incompressible	$Re_L = 2.169 \times 10^6$	SE Model ^a	a)	RANS
		$Re_L = 3.165 \times 10^6$			

$Re_L = 5.061 \times 10^6$					
Yang et al. (2014)	Compressible	-	Semi realistic Model ^b	- c)	SAS
Gu et al. (2015)	Compressible	-	Semi realistic Model ^b	- c)	LES
Becker et al. (2016)	Incompressible Compressible	$Re_H = 2.2 \times 10^5$ $Re_H = 1.47 \times 10^5$	SAE	a)	RANS LES DDES (compressible)
Dawi and Akkermans (2019)	Compressible	-	SAE	a)	IDDES
(He et al., 2020)	Compressible		DrivAer	c)	DES
He et al. (2021a)	Compressible		DrivAer	c)	DES

^a SE model – Small Ellipsoidal (SE) model represents a simplified square-back geometry as shown in figure 2.14 a, and ^b Semi-realistic model – represents a simplified realistic sedan as shown in figure 2.14 b.

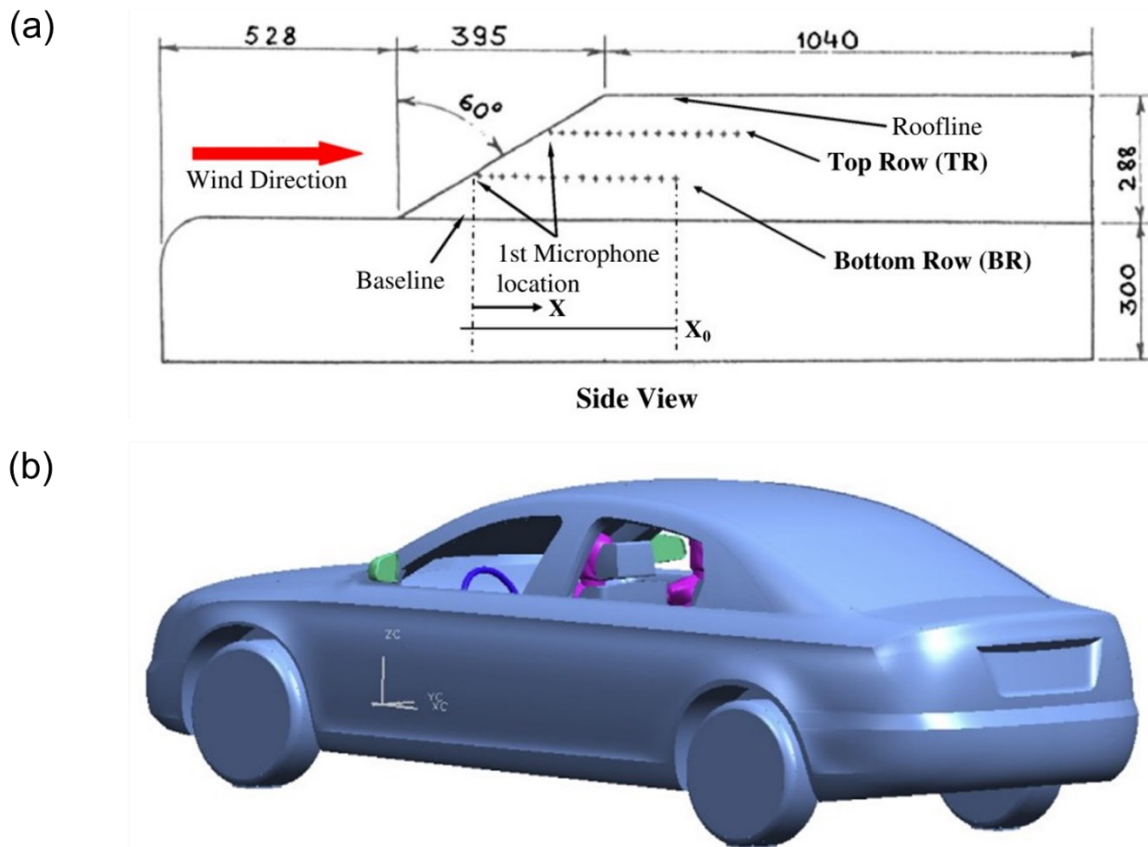


Fig 2.14. a) side view representation of the Semi-Ellipsoidal (SE) model (Murad et al., 2013)^m and b) semi-realistic simplified notchback geometry (Yang et al., 2014)ⁿ.

^m Reused with permission from Murad, N., Naser, J., Alam, F. and Watkins, S., 2013. Computational fluid dynamics study of vehicle A-pillar aero-acoustics. *Applied Acoustics*, 74(6), pp.882-896. Copyright © 2013 Elsevier Ltd.

ⁿ Reused with permission from Yang, Z., Gu, Z., Tu, J., Dong, G. and Wang, Y., 2014. Numerical analysis and passive control of a car side window buffeting noise based on scale-adaptive simulation. *Applied Acoustics*, 79, pp.23-34. Copyright © 2014 Elsevier Ltd.

Table 2.8 shows that the Ahmed body with fastback geometry is widely used for aerodynamics studies, while the SAE Square-back model is used to comprehend the noise generation mechanism. Notchback geometries are the least investigated for aerodynamic studies despite having complex flow topologies in the near-wake, which can assess the robustness of the proposed methodology. Further, notchback and fastback geometries are the least investigated for aeroacoustics; one possible reason could be the lack of experimental acoustic data for these geometries that are freely available for academic use. Also, there is a possibility that the flow separated over rear slant surfaces on both notchback and fastback can also be a potential sound source that could influence the noise levels closer to the driver's window.

The main focus of the aeroacoustics studies presented in Table 2.8 is the noise generated by the airflow around the A-pillar and the side-view mirror mounted on a generic square-back model and its transmission into the interior cabin. However, isolated acoustic studies are carried out initially to validate and verify the methodologies for predicting noise generation and comprehending the noise generation mechanism. The widely used geometries are the side-view mirror geometry mounted on a flat plate. Therefore, the following section reviews the standard side-view mirror geometry widely used to verify and validate the numerical methodologies.

2.8.3. Standard Mirror Geometry

The Half-Round Mirror (HRM) is a standard side-view mirror geometry developed by Höld et al. (1999) and Siegert et al. (1999) based on a half-cylinder model complemented by a quarter-sphere geometry at the top edge of the cylinder. The HRM is placed perpendicularly on a plate to represent an idealised assembly of the side view mirror and the side window on a vehicle, as shown in Fig. 2.15.

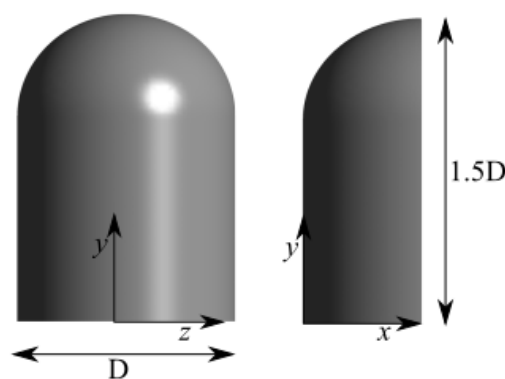


Fig 2.15. Schematic of a Half Round Mirror placed on a plate with normalised dimensions ($D = 200$ mm) shown in front and side view.

Preliminary experimental studies were conducted by Höld et al. (1999) and Siegert et al. (1999) to predict sound generated by HRM when subjected to a free stream velocity of 200 km/h corresponding to a Reynolds Number of $Re_D = 7.06 \times 10^5$ based on the diameter of the mirror. The experiment was performed to determine the plate's Hydrodynamic Pressure Fluctuations (HPF) and the sound radiated from the HRM. Rung et al. (2002) conducted a similar experimental study with a lower Reynolds Number (Re_D) of 5.2×10^5 , representing an average driving speed of ~ 140 km/h.

From a numerical perspective, Unsteady RANS with FW-H approach was used by Höld et al. (1999) and Siegert et al. (1999) to evaluate the noise radiated, and they indicated the limitation of the RANS models in resolving the intricate details of the flow to capture high-frequency modes however, the radiated noise predicted using FW-H underpredicted the noise by 2-4dB against experimental measurement which is achieved by refined grid. Ask and Davidson (2009, 2006, 2005) compared both Detached Eddy Simulation (DES) with Spalart-Allmaras (SA) and Large Eddy Simulation (LES) models with grid resolution following LES recommendations by Pope (2001) with specific modifications made to the grid on HRM to avoid Grid Induced Separation (GIS) which was one of the checks carried out in this thesis to ensure the grid sizes follow the condition. The prediction of the laminar separation point and the point of transition of the boundary layer from a laminar to turbulent by the LES models based on Smagorinsky-Lilly and Dynamic Smagorinsky Sub-grid Scale (SGS) models are in reasonable agreement with the experiment. By analysing the flow patterns using velocity contours around the HRM, Ask and Davidson (2009) demonstrated that the LES methods resolved the horseshoe vortex in front of the mirror accurately and thereby predicting the unsteady pressure fluctuations and wide range of turbulence scales which are in good agreement with experimental data for a wide range of frequencies (Höld et al., 1999; Siegert et al., 1999).

Chen and Li (2019) recently employed other hybrid formulations based on Shear Stress Transport (SST)-DES and SST-DDES to study the flow past HRM. Despite encouraging results on fundamental aerodynamic predictions such as the horseshoe vortex on the front of the mirror, wake profiles and the resulting drag, the wall pressure fluctuations were not compared with experimental and numerical data. In addition, both the SST-DES and SST-DDES models evaluated by Chen and Li (2019) appear to under-predict the pressure magnitude in the stagnation region and overestimate the wake compared to the LES results presented by Ask and Davidson (2009). Further, the separation point on the mirror is also under-predicted for the

DES and DDES cases owing to excessive production of turbulent viscosity, which is in line with the observations made by Ask and Davidson (2009, 2006) for their DES-SA.

The noise radiated from the HRM is computed by Lokhande et al. (2003) using the LES approach with the FW-H analogy and DNC method for evaluating acoustic and compared the numerical prediction against the experimental by Siegert et al. (1999). The prediction of noise radiated was in reasonable agreement with experiments at high frequencies against the experimental results of Siegert et al. (1999). A similar deviation in the predicted noise level by DES with the FW-H analogy is observed by Rung et al. (2002) in their work. The authors point out that the deviations in the studies mentioned above were attributed to the low resolution of the grid in the wake and the larger time steps used. Tosh et al. (2018) employed the SST-DES and APE to determine the noise radiated from the HRM and the pressure fluctuations exerted on the plate. The HPF predicted was in good agreement with the experimental results of Ask and Davidson (2009), up to frequencies of up to 1200 Hz.

From the reported case studies above, HRM is widely used to understand the noise generation mechanism and validate the methodologies proposed to evaluate aeroacoustics, which can be extended to full-scale vehicle studies.

2.9. Noise Mitigation

The literature in Section 2.3 shows that the noise generated from the walls is directly related to the surface excitation due to associated flow unsteadiness. The flow features responsible for inducing the surface excitation on the body were of significant interest in understanding the noise generation mechanism. Initial studies on a forward-facing step, backwards-facing step and humps indicate that the pressure fluctuations exerted are due to the large recirculation zones formed; the size of the recirculation zone depends on the *height* (H) of the step and hump. The strongest pressure fluctuation regions are typically found near the reattachment point of the recirculation zone (Devenport et al., 2018; KIM and SUNG, 2006). Further, Becker et al. (2008) conducted a similar study using a square cylinder with an aspect ratio (Ar) of 6 mounted on a flat plate; two distinctive flow features re identified that contribute to the wall pressure fluctuations from the cylinder. The horseshoe vortex formed due to the incoming flow separation due to adverse pressure gradient-inducing vortices that are stretched around the cylinder, and a spanwise vortex formed on the lateral side of the cylinder, forming two side recirculation zones in the wake. Also, flow on the lateral edges of the square cylinder produces negligible pressure fluctuations on the sides due to the sharp corner of the square

cylinder. Similar flow structures are reported for HRM when mounted on a flat plate by Yao and Davidson (2018). The flow also separates from HRM before reaching the trailing edge on all sides due to the curvature, which also induces pressure fluctuations on the surface of HRM (Ask and Davidson, 2009; Yao and Davidson, 2018).

Further, when the Ar of square cylinders is changed to less than unity, the separated flow from the leading edge reattaches to the square cylinder's lateral surfaces, reducing the noise radiated from the cube. While for larger Ar ($Ar > 1$), a secondary vortex is formed near the trailing edge while significantly increasing the noise generated, specifically the tonal peaks observed at Strouhal frequency (Wang, Thompson, et al., 2020). While rounding off the edges of the sharp corners of the cube with $Ar = 1$ reduce the flow separation. As a result, it reduces the noise radiated from the cube; however, if the radius is more than $1/3$ of the length of the cube, then the cube experiences large vortex shedding, increasing the radiated noise (Wang, Hu, et al., 2020). In addition, when additional bodies such as wedges and elliptical bodies are attached to the front face of the square cylinder this decreases the noise generated, while attaching the same bodies at the rear face indicates an increase in noise generated (Becker et al., 2008). These changes were attributed to the changes in the flow separation and reattachment zones. Therefore, such changes in geometrical features may be effective in mitigating noise.

From an automotive perspective, side-view mirrors are the major contributors to noise generation; therefore, several studies have been conducted to mitigate noise by introducing geometrical changes. A review of these studies is presented in Table 2.9. The noise reduction of less than $\sim 8 - 10$ dB with subtle modifications introduced to the geometry. However, care is needed in choosing the appropriate geometrical feature for mitigating noise. Also, the consequence of these geometrical changes on the overall aerodynamic characteristic of a vehicle has yet to be investigated. Also, the studies were conducted in isolation, where the influence of A-pillar flow on noise generation is not considered.

Table 2.9 A review of studies using geometrical features to mitigate noise

Case Study	Base Geometry	Geometrical Variation	Noise reduction	Numerical / Experimental
Grahs and Othmer (2006)	Standard Mirror	Foot Height Foot Width Diffuser Angle	1-3 dB 2-3 dB 4-8 dB	N
Hartmann et al. (2012)	Realistic Mirror	Enlarged Mirror	-3 dB	E
Kabat Vel Job et al. (2016)	Realistic Mirror	Post Change	5 – 8 dB	E/N
Chu et al. (2018)	Realistic Mirror	Outer duct Inner duct	-143 dB 1 dB	N
Wang et al. (2018)	Realistic Mirror	Enlarge Front Face Stretch Rear Edge Bar Pits Hemispherical Pits	1 – 2 dB 2 – 3 dB 2 – 3 dB 4 – 8 dB	N
Evans et al. (2019)	Realistic Mirror	Groove (Rain Gutter) Ridge and Groove		N
Ye et al. (2021)	Realistic Mirror	Bionic Shark Fin	7.3 dB	N
Chode et al. (2021)	Standard Mirror	Aspect Ratio ($Ar > 1$) Aspect Ratio ($Ar < 1$) Sweep Angle	-4 dB 5 dB 4 dB	N

Summary

The cruising speed for an automobile is around 100 km/h, and the aerodynamic noise emitted from the vehicle is dominant compared to rolling noise. The major contributors to the aerodynamic noise from cars are the A-pillar and the side view mirror. Especially the side view mirror, where the geometry is altered constantly to improve the aesthetics and include features such as rain gutters and turn indicators. As a result, affecting the noise levels heard inside the vehicle's cabin; thus, research on evaluating noise from side view mirrors is necessary to produce a quieter cabin car.

Both experimental and numerical approaches have been widely adopted to investigate the flow and noise generation from the vehicle. However, numerical techniques are preferred as they allow a better understanding of the noise generation mechanism. The combination of CFD and CAA methods is used due to the availability of computational resources. The selection of appropriate formulations depends on the resolution of the flow and the noise evaluation requirements. The numerical methodology initially shall be evaluated for flow resolution, followed by assessing the noise using surface integral acoustic methods; thus, a reliable numerical approach for estimating noise generated from a full-scale vehicle can be formulated. Also, evaluating flow behaviours around the standard bodies, extensively studied experimentally, will aid in assessing the numerical approaches and provide a deeper understanding of the flow feature and their relation to the noise generation mechanism.

Chapter 3

Computational Modelling Methodology

This chapter presents the numerical strategies for predicting the noise radiated from the turbulent flow field used in this thesis. The justification of the turbulence models and the acoustic analogies that are used in the study is presented. Along with models solving flow and acoustic fields, complementary numerical discretisation schemes for both space and time for different turbulence models are also presented to ensure the accuracy of the methodology employed. The numerical simulations are performed in two stages; aerodynamic calculation was performed using the turbulence model in the first step, followed by the prediction of noise radiated into the far field using an acoustic analogy. The simulations performed in the thesis are solved using ANSYS Fluent. More details of the methodologies used in the current work are introduced in the following section.

3.1. Turbulence Modelling

Several turbulence models available to resolve the flow field around a vehicle are presented in **Chapter 2** of this thesis. The flow around a vehicle experiences local separation and reattachment before separating at the trailing edges, and due to the vehicle's shape, a sizeable turbulent wake is generated. To accurately capture these flow features, the turbulence model employed should predict the flow separation, resolve the flow features at least up to the Taylor microscale, and resolve the energy content up to 80% of TKE (Pope, 2001). However, to capture these features, the grid is refined locally to capture the complex features in the geometry of a vehicle, which can potentially lead to MSD and GIS issues, as discussed in **Chapter 2**. Therefore, SBES and SDES models have been chosen to perform the simulations presented in this study, as the capabilities of both the SBES and SDES models, such as offering asymptotic shielding of the RANS layer and providing a rapid transition to LES mode, could be advantageous for vehicle aerodynamic studies.

The capabilities of SBES and SDES are achieved by introducing a new shielding function. The study conducted by Menter (2018) has evidenced that the shielding function used in both SBES and SDES is not affected by the grid refinement due to introducing a new length scale definition, as shown in Eq. 3.1.

$$F_{SDES} = \left[\max \left(\frac{L_t}{C_{SDES} \Delta_{SDES}} (1 - f_s), 1 \right) - 1 \right] \quad (3.1)$$

$$\Delta_{SDES} = \max[\sqrt[3]{\nu \omega l}, 0.2\Delta_{max}] \quad (3.2)$$

Here, the Δ_{max} represents the maximum grid length, L_t is the integral turbulent length scale while C_{SDES} represents model constant, the constant is equal to 0.4, calibrated for shear layers.

For SDES, Eq. 3.1 replaces the length scale in the DDES formulation, thus providing a more efficient RANS shielding region than the DDES model. Also, the introduction of $0.2\Delta_{max}$ ensures a viable limit for a grid with high aspect ratios and, together with C_{SDES} , results in much lower eddy viscosity levels, resulting in a much smoother and rapid transition from RANS to LES mode and faster generation of resolved turbulent structures, compared to DDES model.

For SBES, due to such a strong shielding function, a blend of RANS and LES models is achieved at stress levels. The blended stresses are presented in Eq. 2.36 and 2.37. The shielding function in SBES varies from 0 to 1, and the eddy viscosity (ν_t) and stress tensor (τ_{ij}) switch to LES mode when f_s is zero, and if f_s is equal to one, then stress tensor and eddy viscosity will be in RANS mode. As a result, a clear distinction between RANS and LES zones can be visualised within the flow regime. Further, the user can include a different SGS model in LES rather than the standard Smagorinsky-Lilly SGS model for LES as offered by both the SDES and DDES formulation because of the blending function used in the SBES formulation does not introduce any modification into Eq. 2.36 and 2.37.

SBES and SDES formulations are based on a two-equation RANS formulation, where the dissipation term is modified using the function shown in Eq. 2.32 for the transport equation of k . Therefore, the choice of choosing RANS model in the SBES and SDES formulation is limited to modified $k - \varepsilon$, $k - \omega$ models such as realisable $k - \varepsilon$, Baseline Line $k - \omega$ model, and $k - \omega$ Shear stress Transport (SST). For cases such as the aerodynamics of vehicles, investigating the flow behaviour near the wall are essential; therefore, $k - \omega$ models based models are preferred. SBES and SDES with the $k - \omega$ SST model are used in the study due to the stability that the $k - \omega$ SST model offers in predicting the flow separation under adverse pressure gradients, as no damping function at the wall is used which is inherent feature of $k - \omega$ and the capability of handling high aspect ratio meshes. For LES mode, the Smagorinsky-Lilly model is formulated into SDES, while for SBES, the choice of using different SGS models is offered; both Smagorinsky - Lilly and WALE models are used with SBES to explore the advantages of SBES and SDES in the context of vehicle aerodynamic studies. Also, a summary of the SBES turbulence model with WALE are used to predict various flow scenarios which

are presented in the Table 3.1. As seen in from the table below, flow characteristics such as separation and vortex structures are predicted in good agreement with the experimental data. However, limited studies were conducted using SDES.

Table 3.1 Review of case studies - accuracy of SBES predictions

Flow Characteristics	Case study	Author	Predicted results are compared against
Turbulent Energy Spectrum	Heliostat – Fluid-Structure interaction SAE T20	Wolmarans Craig (2019) Chode et al. (2020)	Experiment
Robust Shielding	DrivAer SAE T20	Ekman et al. (2020) Chode et al. (2020)	DDES/IDDES SDES
Flow separation	Back Step Half Round Mirror	Menter (2018) Chode et al. (2021)	DDES Experiment
Vortex Structures	Marine-propeller SAE T20	Cai et al. (2019) Chode et al. (2020)	DDES/LES/URANS SDES
Fluctuating quantities – Velocity and pressure	Hub less Propeller Heliostat – Fluid-Structure interaction	Witte et al. (2019) Wolmarans Craig (2019)	Experiments Experiments / RANS
	Crystalliser – Internal flow	Brown et al. (2020)	DDES/SAS/SDES/SBES
	Half Round Mirror	Chode et al. (2021)	Experiment/LES/DES/DDES

Therefore, in this thesis, both SBES and SDES with same SGS model are used to evaluate the flow field around for aerodynamic study, while for aeroacoustics study, SBES with the WALE SGS model is used for computing the flow while acoustic methods are used to obtain acoustic field.

3.2. Acoustic Methods

A hybrid CAA approach is used to obtain the noise radiating from the body of the interest. In the hybrid approach, the flow is solved by using the turbulence model, such as the SBES model, to identify the noise sources, and in the second step, the noise is computed from the noise sources using acoustic analogies. In other words, acoustic analogies isolate noise computation from flow computation. Lighthill (1952,1954) was the first to propose an acoustic analogy to predict the noise generated due to the flow in the free space through volume integration of Lighthill tensor T_{ij} (Ref: Appendix for formulation). The solution obtained from Lighthill's equation is only valid for unbounded domains and is invalid in the presence of solid bodies inside the domain. Hence, the direct application of Lighthill's analogy is restricted to the noise generated due to turbulence alone, such as jet noise. Curle (1955) has generalised Lighthill's equation to include the effect of the stationary wall within the flow. Ffocws Williams

and Hawkings (1969) have extended the Curles analogy to include moving walls. The contributions of the solid walls to noise generated are obtained using integrals over the wall in both Curle's and FW-H formulations. Specifically, in the FW-H formulation, the volume integral is eliminated by assuming the solid body surfaces as permeable.

Similarly, another analogy based on surface integral, the Kirchoff method, assumes that the integral surface should be located within the flow region where the wave propagation condition is fulfilled. However, in the Kirchoff method, the integral surface must enclose all non-linear sound sources, unlike the FW-H formulation, where the non-linear sound sources can be on and outside the integral surface. The mathematical form of both Kirchoff and the FW-H methods are presented in Eq. 2.46 and Eq. 2.49 respectively.

When a comparison is drawn between Eq. 2.46 and 2.49, the three additional non-linear source terms are considered in the permeable form of the FW-H formulation. However, if employed with a precondition such as a wall is stationary and neglecting the volume integral of T_{ij} due to the low Mach number flow, then the FW-H formulation is similar to that of the Kirchoff integral. Even though the formulations are similar under specific conditions, each method's definition of the integral surface is different. The integral surface in the Kirchoff method must satisfy the wave propagation and must be large enough to contain the non-linear quantities $\rho u_i u_j$ be weaker than the linear terms such as p' , dp/dn , and dp/dt . Therefore, defining such a large surface for complex geometries, such as a vehicle, be challenging, and thus, the application of the Kirchoff integral is limited to isolated body study in this thesis, where the Kirchoff method is used as a verification method.

Several aeroacoustics studies mentioned in **Chapter 2**, which have used hybrid CAA methods, used DES and its variants or LES in conjunction with either FW-H acoustic analogy, where the noise generated and radiated away from the body had a reasonable agreement with the experiments. Mainly the quantitative differences were attributed to the limitation of the turbulence models in the case of hybrid RANS-LES models or the resolution of the mesh for LES, even for simplified geometries such as HRM. Therefore, there is a requirement for an optimal methodology adaptable to both simplified and complex geometries and robust enough to handle high aspect ratio meshes for aeroacoustics studies. Also, this thesis aims to investigate the noise radiated and propagated from the isolated and full-scale vehicle bodies. As both KI and FW-H are capable of predicting the noise radiated, both of the methodologies are initially investigated to determine the challenges and limitations of the models in vehicle aeroacoustics.

Thus, the thesis uses a methodology based on the SBES/SDES turbulence model and acoustic analogies such as FW-H and KI with unstructured meshes to investigate the noise radiated from standardised geometries, as presented in **Section 2.5**.

3.3. Numerical schemes

The numerical schemes in this study were selected based on the quality of the generated grid. To obtain gradients, Least Squares Cell-based (LSC), as LSC computes gradients by minimising the sum of the squared residuals between the cell-centred values and their surrounding values, results in a gradient that is continuous and smooth, whereas cell- or node-based gradient schemes result in piecewise linear or bilinear functions which are prone to produce numerical errors at the interfaces. Because of the varying grid sizes used to construct the grid, the LSC was chosen.

To discretise the convective terms in the steady-state simulation, both second-order and MUSCL schemes for steady calculations depend on the meshing type and quality of the mesh used for the study. In contrast, for unsteady calculations, the BCD scheme is used as it is a second-order accurate scheme by introducing strong boundedness based on CBC criteria. This avoids overshooting or undershooting the solution and ensures a numerically stable solution. In BCD, the local value representing the CBC value is first computed to determine the monotonous region, and the transported scalar value is computed using second – order interpolation and central-differencing interpolation. If the region is non-monotonous, then switches to first-order upwind to ensure that the boundedness is preserved, ensuring that the solution is stable and less dissipative. In addition, the accuracy of BCD is enhanced by using CFL values less than, for which bounded second-order implicit time integration is used for time marching. Furthermore, the NS equations are solved in a segregated manner using either the SIMPLE-C or SIMPLE schemes to obtain pressure-velocity coupling with under-relaxation factors (URF) to improve the convergence rate. For the highly skewed grids presented in this thesis, the SIMPLE-C coupling scheme is used, whereas for less skewed grids, SIMPLE coupling is used. To ensure that there is no influence of errors on the solution obtained, the residuals should be monitored for all quantities with a convergence criterion of less than 1×10^{-5} .

The numerical schemes presented above improve the stability of the numerical simulations, as the scheme selected is based on the best practices used for hybrid RANS-LES

simulations (Ashton et al., 2016; Ask and Davidson, 2009; Dawi and Akkermans, 2019; Guilmineau et al., 2018; Nusser and Becker, 2021). In addition to the high-order schemes used, the accuracy is improved by deploying appropriate grid sizes, thereby reducing numerical dispersion. Grid size estimates are presented in the following sections.

3.4. Grid Size estimates

The grid sizes used in the thesis are estimated by using two different approaches *a)* normalised wall units and *b)* length scale estimates. The normalised wall units in three dimensions (Δx^+ , Δy^+ , and Δz^+ are normalised wall units in x , y and z directions, respectively) are defined as shown in Eq. 3.5.

$$\Delta x^+ = \frac{(u_t)_x \Delta x}{\nu}; \Delta y^+ = \frac{(u_t)_y \Delta y}{\nu}; \Delta z^+ = \frac{(u_t)_z \Delta z}{\nu} \quad (3.5)$$

Where (u_t) represents the friction velocity in all three directions, and ν represents the viscosity of the fluid.

The values of Δx^+ , Δy^+ and Δz^+ are defined to obtain surface sizes, while to obtain mesh sizes in the flow regime, length scale estimates are used. In this thesis, the length scales are obtained using height (H) and length (L) as the reference or characteristic length. The turbulent boundary layer thickness is estimated using $\delta/H \approx 0.37Re_H^{-0.2}$, and the viscous boundary sub-layer is estimated using $\eta_{nw}/L \approx 5.9Re_H^{-0.9}$. The largest energy-containing anisotropic structures (l_o) can be estimated by $l_o \approx \eta Re_H^{3/4}$, whereas the inertial subrange, l_{EI} and dissipative range, l_{DI} can be estimated by $l_{EI} = l_o / 6$ and $l_{DI} = 60\eta$. The Taylor microscale associated with the integral motion in the wake and Kolmogorov length scale associated with the smallest turbulent scale of the wake is estimated using $\lambda_t \approx 4.6Re_H^{-0.5}$ and $\eta \approx 0.998Re_H^{-0.75}$, respectively.

Further, to estimate the freestream size, where a suitable amount of eddy dissipation needs to be resolved, a ratio of the maximum length of the local cell (Δ) to the smallest length scale (η) is defined by the Kolmogorov length scale is obtained. For LES simulations, the recommendations were made by Pope (2001) based on the normalised wall units. Similarly, for DDES simulations, an estimate is obtained by Ashton et al. (2015); these values are represented in table below

Table 3.2 Mesh resolution recommendations for LES and DDES cases

Model	Δx^+	Δy^+	Δz^+	Δ/η
LES	50 – 150	< 2	15 – 40	< 12
DDES	10 – 150	0.1 – 0.5	5 – 70	40 – 110

3.5. Simulation methodology

The simulation methodology used for the aeroacoustics study in this thesis is presented below

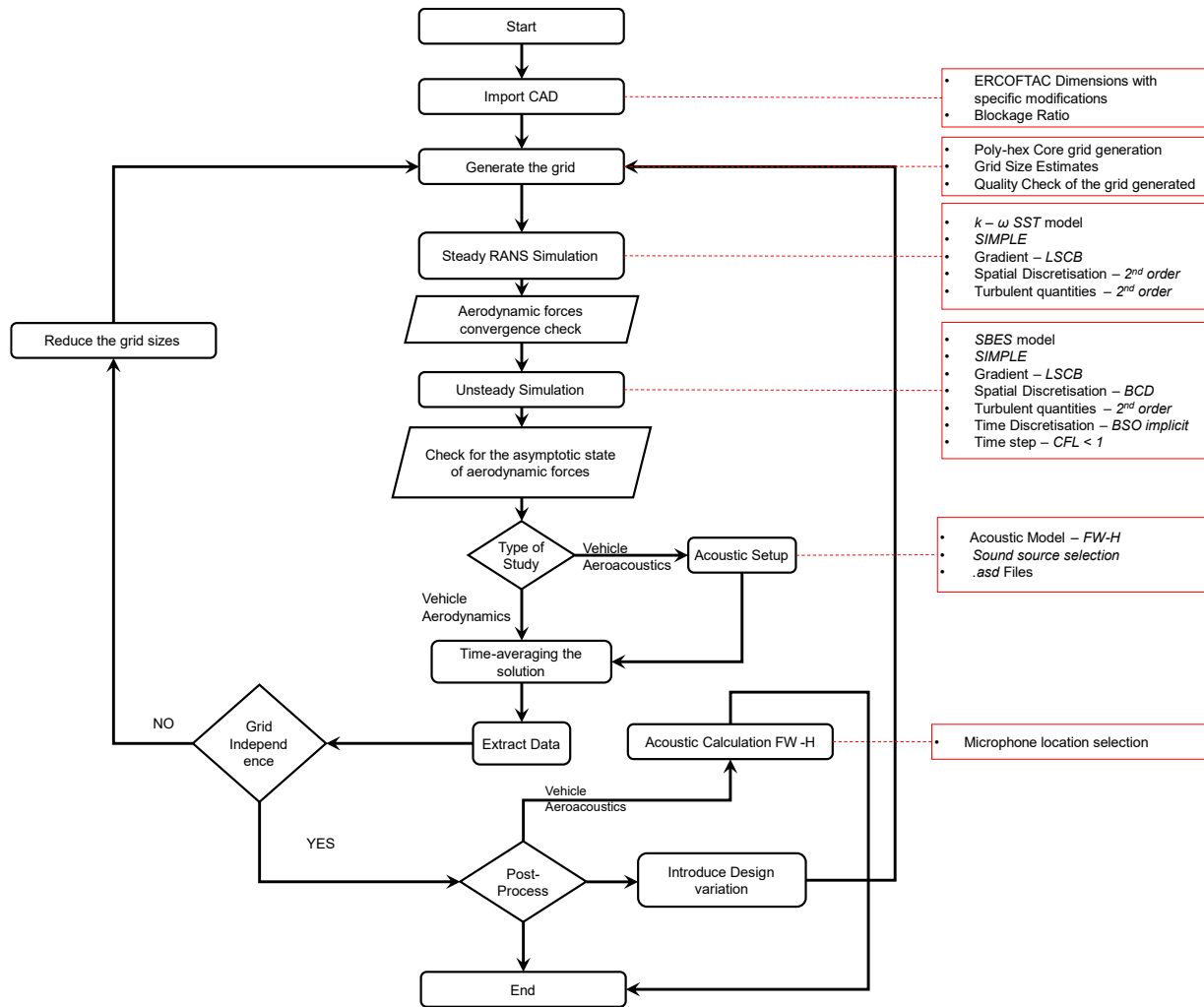


Fig. 3.1. Flow chart presenting the simulation procedure for performing an aeroacoustics study

For all the simulations performed in this study, the converged solution of steady-state is used for initialising the unsteady problem. The steady state is run to ensure the stability of the simulation. For the aeroacoustics study, additional data of the pressure fluctuations on the sources selected has to be recorded along with time averaging data. Then an additional step of solving FW-H is performed to generate noise at several microphone positions around the body of the interest. The acoustic calculation is performed as a *post-processing* step, and the

computation resources required for the acoustic calculation are negligible compared to solving the flow.

3.6. Methodology verification and validation

In this thesis, the experimental analysis is not carried out due to their complex setups, availability of test facilities and high operational costs. Therefore, to validate and verify the methodology used for both aerodynamic and aeroacoustics studies is verified against the published experimental data. Further, a comparison is drawn between the numerical methods used against the prediction made by other numerical methods presented in the published literature. In this thesis, at every stage verification and validation procedure is followed to ensure the accuracy and validity of the methods used. For example, the aerodynamic study presented in the thesis is validated using the experimental data presented by Wood (2015). Wood (2015) published the raw experimental data in a repository which was post-processed using in-house developed MATLAB codes to extract data such as velocity and pressure plots. The MATLAB codes used for post-processing are presented in the appendix for the reader's reference. While some data which are presented in the published papers are extracted using plot digitising techniques available on open source.

3.7. Computational resources

The simulations for aerodynamic and aeroacoustics studies have been performed using SHU HPC (High-Performance Computing) and MIRA HPC facilities. The solvers perform a parallel computation based on domain decomposition and the MPI (Message passing interface) communication protocol. The simulations were performed three variants of ANSYS, namely 19.1, 2020 R2 and 2021 R2. The HPC features are reported in the table below

Table 3.3 HPC specifications used for computing both aerodynamic and aeroacoustics simulations

HPC	Number of nodes	Total Number of cores	RAM per node (GB)	Time Taken to Run in Days		
				SAE T20	HRM	SAE T4
HPC – 1	8	224	6	-	12	40
HPC – 2	18	216	2	18	15	-
HPC – 3	-	220	-	12	8	-

Summary

This chapter outlines the choices made to formulate a methodology capable of predicting noise radiated from flow past a bluff body. The choices are justified based on each method's advantages in unstructured meshes with a high aspect ratio and skewness. The estimates of grid sizes are presented along with the simulation procedure followed throughout the thesis and the validation strategies. Data analysis techniques used are presented along with visualisation techniques to visualise turbulence. This chapter also presents the computational resources used in carrying out the research. In summary, using the methods presented in this chapter, the standard bodies presented in **Chapter 2** will be studied to comprehend the capabilities of the proposed methodology for aeroacoustics studies.

Chapter 4

Assessment of hybrid RANS - LES approaches using standard notchback configurations

The hybrid CAA approaches discussed in **Chapter 3** must be validated systematically to assess the usability, repeatability, and limitations for predicting the noise generated from the body of interest. A hybrid approach is a two-step approach where *i*) the flow past the body of interest is resolved using flow solvers in the first step and *ii*) obtaining the noise generated and radiated using acoustic methods in the second step. Therefore, the flow solver's capability must be assessed as the primary step.

In this thesis, the body of interest is ground vehicles; specifically, the standardised vehicle geometries, where the flow configuration falls in the high-Reynolds number and low-Mach number regime. Flow solvers based on a hybrid RANS - LES approach, such as SBES and SDES, have been deployed to resolve the turbulent flow past these bodies. Several benchmark cases with similar flow configurations can be used to validate the SBES and SDES, as discussed in **Chapter 2**. SAE reference notchback geometry is chosen to assess the SBES and SDES as the SAE geometry includes features similar to production-like vehicles, such as front slant and curved edges, but mainly due to the availability of detailed aerodynamic wind tunnel measurements.

A detailed study of SAE reference notchback geometry was presented by Wood (2015) using the Loughborough University model scale wind tunnel to study the influence of rear geometry changes on the notchback flow field. The experiments were carried out for different configurations of backlight angles ranging from 20° to 40° in increments of 5°.

This chapter aims to validate the SBES and SDES for vehicle aerodynamic computations and verify their predictions with widely used $k - \omega$ SST URANS predictions. A description of available experimental data and assumptions made for numerical setup is presented, followed by the grid size calculations and grid independency study. This chapter is presented in two sections: the first one involves notchback geometry with 20° as a validation case (See Fig. 4.1), and the second involves notchback geometry with different backlight angles without changing any numerical setup. All the results presented in this study are compared against the available experimental data.

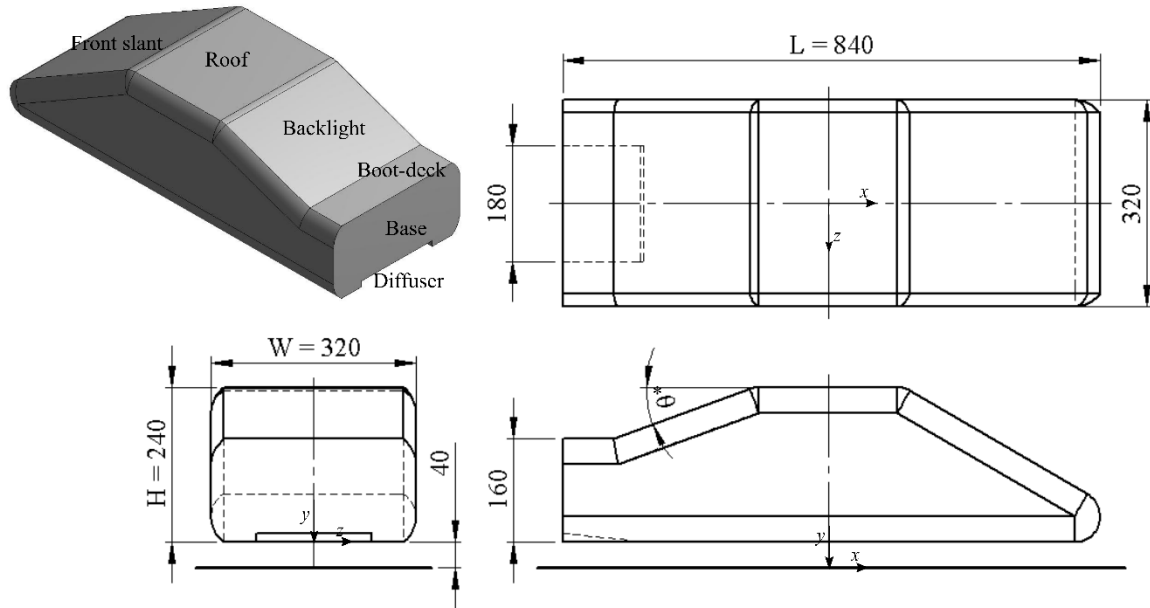


Fig. 4.1. The dimensions of the SAE notchback geometry are in mm, and the backlight angle θ^* in degrees ranges from 20° - 40° .

4.1. Experimental data

The experimental data used to validate the numerical prediction conducted by Wood(2015) at Loughborough University and the data is shared openly through the Loughborough University repository under Creative Commons (CC) License 4.0. The available experimental data was obtained using an open-circuit, closed-working-section wind tunnel with constant ground. The notchback geometry was mounted on a force balance using cylindrical struts at the height of 40mm above the ground. The closed-working section had a blockage ratio of $\sim 2.9\%$, and Mercker's blockage corrections were used to correct the force measurements. The data contains pressure measurements taken at the central plan of the notchback geometry, the base of the vehicle, the front slant, the backlight and the boot deck for all the backlight configurations. The force measurements, such as drag and lift, are obtained using force balance. The velocity measurements were obtained using Particle Image Velocimetry (PIV) on the rear end, and front end of the notchback at several locations, and the data available was in the RAW data. The PIV raw data was processed into user-readable contours using MATLAB, and the code is presented in the Appendix for the readers' reference.

4.2. Numerical Setup

In this section, the numerical setup for the SAE notchback is presented. The computational domain used for validation is kept constant while the backlight of the notchback is changed.

The assumptions, boundary conditions, and numerical methods used remain constant when the backlight angle is changed and are presented in the below sections.

4.2.1. Model and computational domain description

The geometry analysed in the present study is a 1:5 scale SAE reference body with 20°, 30°, and 40° backlight angles (θ^*) representing a notchback configuration that was experimentally investigated by Wood (2015) is shown in Fig. 4.1. The geometry is placed above the ground at the height of $y/H = -0.166$ where $H = 240\text{mm}$. In this chapter, the SAE reference body with a 20° backlight angle is referred to as SAE T20, while the SAE reference body with a 30° and 40° backlight angle is referred to as SAE T30 and SAE T40, respectively.

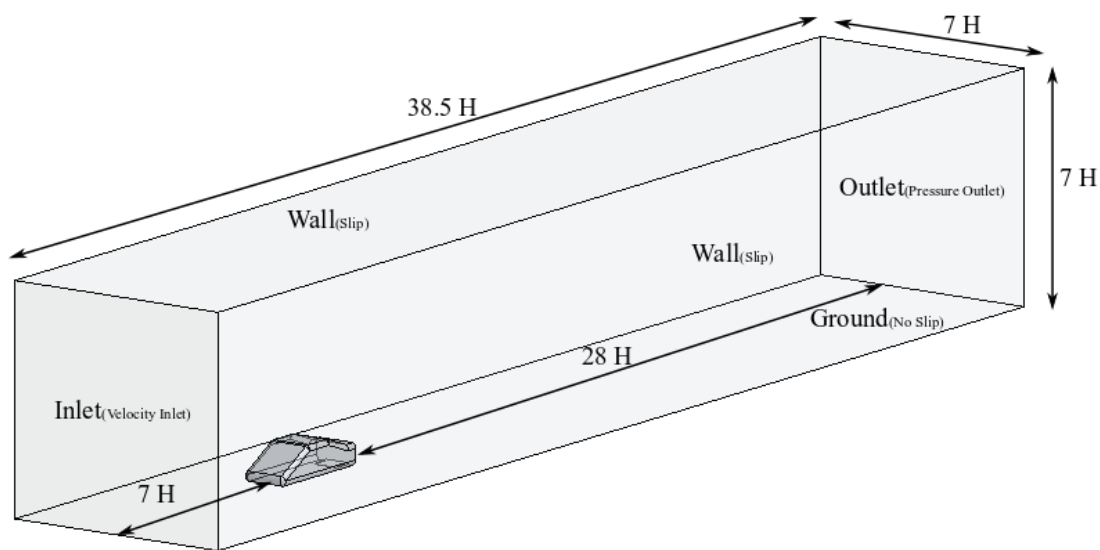


Fig. 4.2. Layout of the computational domain with normalised dimensions and the specified boundary conditions

The computational domain $\Omega = 38.5H \times 7H \times 7H$, shown in Fig. 4.2. is defined based on the ERCOFTAC guidelines adopted by several established research groups (Aljure et al., 2018, 2014; Ashton et al., 2016; Ashton and Revell, 2015; Evstafyeva et al., 2017; Guilmineau et al., 2018). The blockage ratio with the domain cross-section is 2.7%, whereas the reported experimental blockage ratio is 2.9%. Both the solid blockage and wake blockage corrections as per Mercker's Blockage Correction (Carr and Stapleford, 1986; Mercker, 1986) are applied for aerodynamic coefficients reported in the present computational effort for the sake of consistency with the experimentally reported values by Wood (2015) and Wood et al. (2014).

Assumptions made:

In the experimental study of Wood (2015), the reference bodies were mounted on four cylindrical struts at the height of $y/H = -0.166$ above the ground, which contributes to 15.38%

of the projected frontal area of the geometry shown in Fig. 4.1. The struts were neglected in the present study to avoid additional grid complexity and are assumed to be negligible in their contribution.

4.2.2. Length scale estimations and grid generation

For the SAE T20 configuration, the length scale estimates are calculated based on the estimates presented in **Chapter 3**. The grid sizes are estimated based on the normalised units using Eq. 3.5 presented in **Chapter 3**. A grid independence study is carried out by employing five grids with grid size reducing by a factor of 2 to obtain the least sensitive solution to grid size changes. The length scale estimates and grid sizes used for SAE T20 are summarised in Tables 4.1 and 4.2, respectively.

Table 4.1 Characteristic length scales of SAE T20

SAE T20	η	λ_t	l_0	l_{EI}	l_{DI}	η_{nw}
in mm	0.012	1.6282	266	48	0.776	0.0093

For Grid 4, the flow domain is divided into four sub-domains from the centre of the model, as illustrated in Fig. 4.3. The height of the Focus Region (FR) is determined by analysing the wall shear effects, and the length of FR to capture the near wake effects behind the vehicle adequately. A refinement box called a Taylor Box (TB) is added around the backlight angle of the body, in which the cell sizes are equal to the Taylor microscale (λ_t). Further, refinement boxes called Domain Refinement (DR) are added to ensure a smooth transition. According to Fröhlich et al. (2005), a Δ/η value for Wall Resolved LES (WRLES) simulation should be < 12 in the freestream to ensure that a suitable amount of eddy dissipation is resolved. The Δ/η reported is as high as 240 near the backlight on the midplane at point ($x = 140$ mm, $y = -208$ mm) and $\Delta/\eta = 320$ at ($x = 580$ mm, $y = -190$ mm) behind the model on the midplane for Grid 1. While for Grid 4 and Grid 5, at the same location, the values of Δ/η are 58 and 48 near the backlight and 120 for both behind the model respectively. The estimated grid sizes for grid 4 align with the values reported for hybrid RANS-LES methods, as discussed in **Chapter 2**.

Table 4.2 Comparison of grids generated for obtained SAE T20 with WRLES recommendations

	Δx^+	Δy^+	Δz^+	Δ/η	Cell Count
WRLES Recommendation (Fröhlich et al., 2005; Piomelli and Chasnov, 1996)	50 – 150	< 2	15 – 40	<12	–
Grid 1	200 – 380	0.9	200 – 380	240 – 650	2.91×10^6
Grid 2	100 – 250	0.9	100 – 250	80 – 320	8.57×10^6
Grid 3 (on the backlight) (includes TB on the backlight)	100 – 250 100 – 150	0.9	100 – 250 100 – 150	64 – 320	14.55×10^6
Grid 4 (on the backlight) (includes TB on the backlight and DRs in the wake)	100 – 250 100 – 150	0.9	100 – 250 100 – 150	58 – 280	18.56×10^6
Grid 5	100 – 150	0.9	100 – 150	48 – 120	33.18×10^6

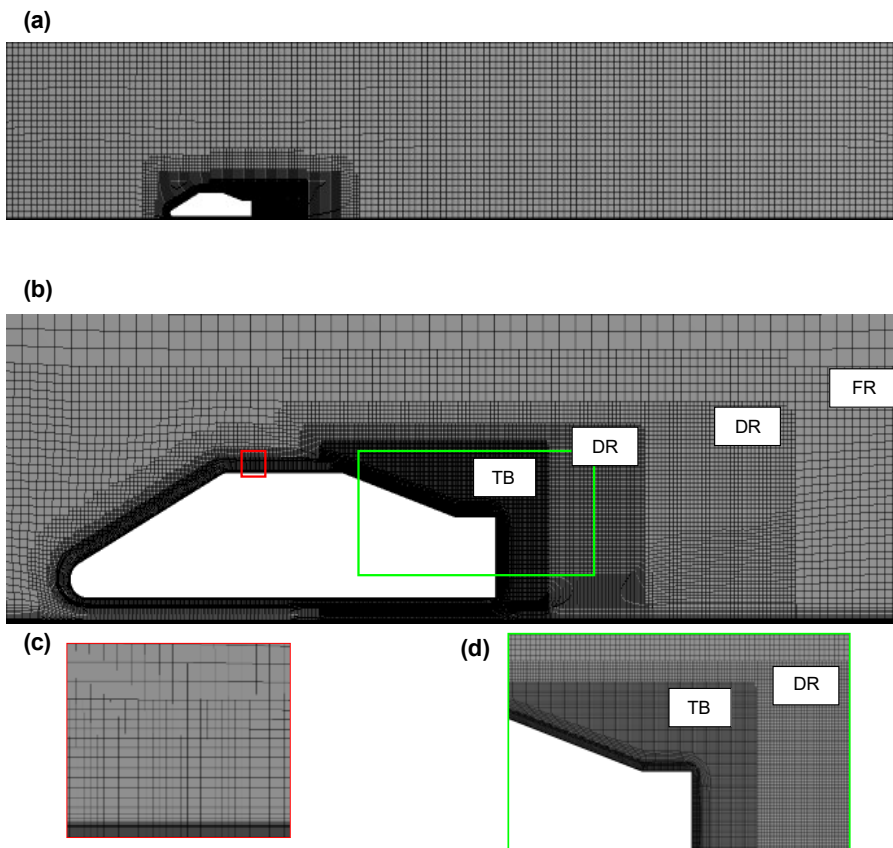


Fig. 4.3. Grid used in assessing turbulence models **a)** Cut in the xz plane showing the grid distribution around the body. **b)** Detailed view of the mesh with highlighted zones TB – Taylor Box, DR 1,2 – Domain Refinement, and FR – Focus Region. **c)** a detailed view of the boundary layer, and **d)** a detailed view of refinements behind the model.

4.2.3. Boundary conditions and numerical setup

The flow is at a Reynolds number of $Re_H = 6.57 \times 10^5$ based on the height of the body H and the freestream velocity of $(U_\infty, 0, 0)$, where $U_\infty = 40 \text{ ms}^{-1}$. The turbulence intensity in the wind tunnel experiment reported by Wood et al. (2014) and Wood (2015) is approximately 0.2% which is specified at the inlet boundary. The flow was ensured to be fully developed with the boundary layer thickness of 60 mm before reaching the body as the inlet is placed $x = 7H$ upstream of the vehicle. A zero-static pressure condition was applied to the outlet boundary located at $x = 28H$ downstream of the vehicle. A no-slip wall condition is imposed on the ground floor and body, whereas a slip condition is imposed on the remaining walls of the domain. The numerical schemes used in this chapter, with all the turbulence models used, are summarised in Table 4.3.

Table 4.3 Numerical methods used for SAE notchback

	Scheme used
Pressure-Velocity Coupling	SIMPLEC
Gradient	Least Square Cell Method
Pressure	Second Order
Momentum	Bounded Central Differencing
Turbulent Kinetic Energy	Third-Order MUSCL
Specific Dissipation Rate	Third-Order MUSCL
Transient Formulation	Bounded Second order Implicit

The flow field was initialised with the solution obtained through a steady-state RANS simulation based on the $k - \omega$ SST model. For SBES and SDES cases, the time step size of 2×10^{-5} s ensures that the CFL number is < 1 in most regions. However, for the URANS case, a time step size of 2×10^{-4} s was used. The simulations were performed for over 30 convective cycles ($30 \times L/U_\infty$) for all the cases, and the unsteady statistics were obtained by averaging the flow for over the last 20 convective flow units after it is first checked to have reached an asymptotic state.

4.3. Grid evaluation study

The grid evaluation study was conducted using the SBES turbulence model. The aerodynamic force coefficients for all the grids are measured and are summarised in Table 4.4. The values of the aerodynamic force coefficients indicate a convergence at grid 4. At the same time, the time-averaged streamwise velocity plots presented in Fig. 4.4 indicate a negligible difference between the velocity profiles predicted by grids 3,4 and 5. Also, both grids 3, 4 and 5 indicate the presence of a shear layer from the backlight, which grows into the wake. It should be noted that difference between grid 4 and 5 is minimal in both velocity profiles and the fore coefficients. Therefore, the solution obtained is grid independent at grid 4 and any further refinements added to grid 5 may not result in a significant modification in the values. Therefore, grid 4 is appropriate for assessing the turbulence models.

Table 4.4 Aerodynamic force coefficients assessed using various grid sizes shown in Table 4.3.

Solver		Drag Coefficient (C_D)	Lift Coefficient (C_L)
SBES	Grid 1	0.1868	-0.1202
	Grid 2	0.1889	-0.1226
	Grid 3	0.1887	-0.1259
	Grid 4	0.1883	-0.1272
	Grid 5	0.1883	-0.1273

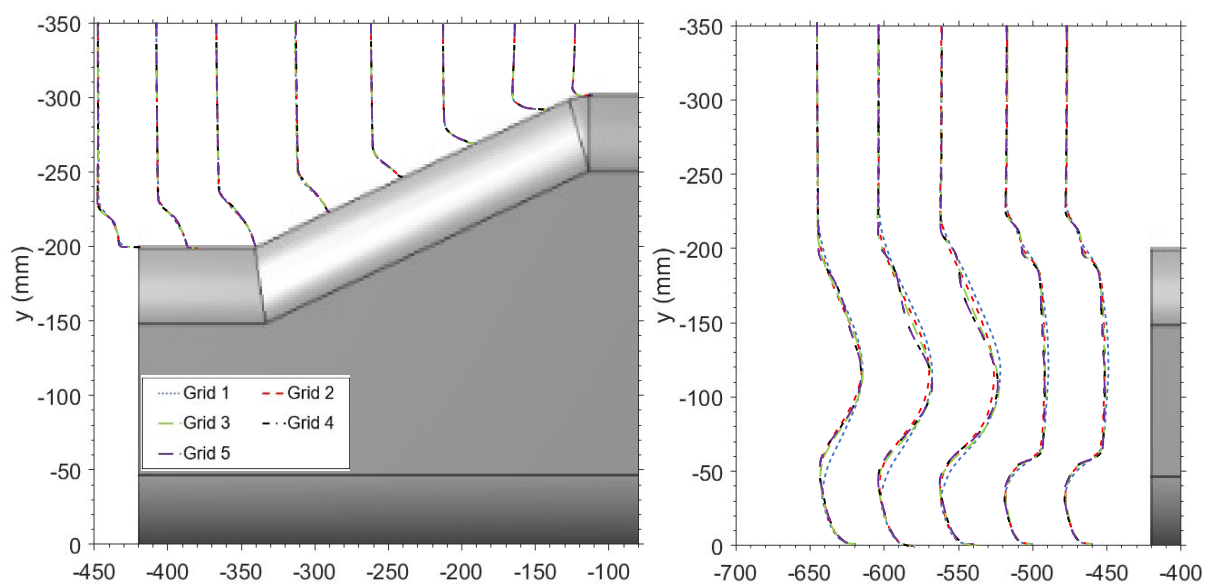


Fig. 4.4. Time-averaged Streamwise velocity profiles (right) over the backlight and in the wake (left) of SAE T20 body compared against the grids used in this study.

4.4. Verification and Validation of SAE T20

4.4.1. Aerodynamic force coefficients:

The overall drag coefficient is underpredicted by $k-\omega$ SST, SBES, and SDES by 9.14%, 9.46% and 10.3% respectively. When compared to other numerical results presented by Islam and Thronber (2017) for the SAE T20 indicate an overprediction of value by $\sim 20\%$, this difference is attributed to the more smoother curvatures used in their model compared to the experiment. Conversely, the overall lift coefficient predicted by all the turbulence models is less encouraging as the values predicted by the numerical simulation shows a negative lift, whereas the experiment values indicate the presence of a positive lift. The difference in lift coefficient is most likely due to the inaccuracies in the underbody flow prediction over the smooth surface of the model. Forbes et al. (2017) and Grandemange et al. (2015) have reported similar discrepancies in the lift coefficient owing to sensitivity issues. The overall difference in force coefficients reported is mainly due to ignoring the struts, and the reported percentage of error is in line with previously published results where struts have been neglected (Aljure et al., 2014; Ashton and Revell, 2015; Guilmineau, 2008).

Table 4.5 Time-averaged Aerodynamic Force Coefficients for SAE T20

	Experiment (Wood et al., 2014)	Numerical (Islam and Thronber, 2017)	$k-\omega$ SST	SBES	SDES
Drag Coefficient (C_D)	0.2070	0.237	0.1889	0.1883	0.1866
Lift Coefficient (C_L)	0.0056	0.062	-0.1251	-0.1276	-0.1275

The main contributor to the drag experienced by the vehicle is mostly due to the pressure drag. The contribution of drag from each body part, such as the front slant C_{Df} , backlight C_{Dr} and base C_{Db} of the SAE T20 to the total time-averaged pressure drag $C_{D,p}$ is summarised in Table 4.6. The component-wise investigation of pressure drag for each component predicted by the turbulence models underpredicts the base pressure drag a maximum difference of 7.07% by $k-\omega$ SST and SDES predicts a maximum difference of 18.51% in the rear slant pressure drag. However, a more significant difference is seen to be predicted in the front slant when compared to the experiment. However, the pressure coefficient predicted by turbulence models on the front slant midplane shows a good agreement with the experiment (Fig. 4.5). These differences seen may be attributed to the smaller sampling data points considered in the experiment to evaluate the pressure drag, which is apparent in the layout of pressure tapping, as illustrated by Wood (2015).

Table 4.6 Contribution of each body part to the total time-averaged pressure drag coefficient

Model	C_{Db}	$C_{Db}/C_{D,p}$ [%]	C_{Dr}	$C_{Dr}/C_{D,p}$ [%]	C_{Df}	$C_{Df}/C_{D,p}$ [%]
Experiment (Wood et al., 2014)	0.1053	57.4354	0.036	19.6349	0.042	22.929
$k-\omega$ SST	0.0981	72.7745	0.0306	22.7003	0.0061	4.5252
SBES	0.1005	72.0510	0.0300	21.4992	0.0090	6.4498
SDES	0.1005	72.0450	0.0299	21.4322	0.0091	6.5228

4.4.2. Pressure Coefficient (C_p) on midplane and base of the model

The time-averaged pressure coefficient (C_p) on the mid-plane of the body is illustrated in Fig. 4.5. The overall pressure profile predicted by numerical simulations is in good agreement with the experimental data. Numerical simulations predict two distinctive low-pressure peaks at the leading and trailing edges of the roof, which are under-represented in the experiment. The impingement on boot-deck predicted by $k-\omega$ SST is overestimated by 5.28%, whereas both SBES and SDES underpredict the impingement by 2.34% and 2.36%, respectively.

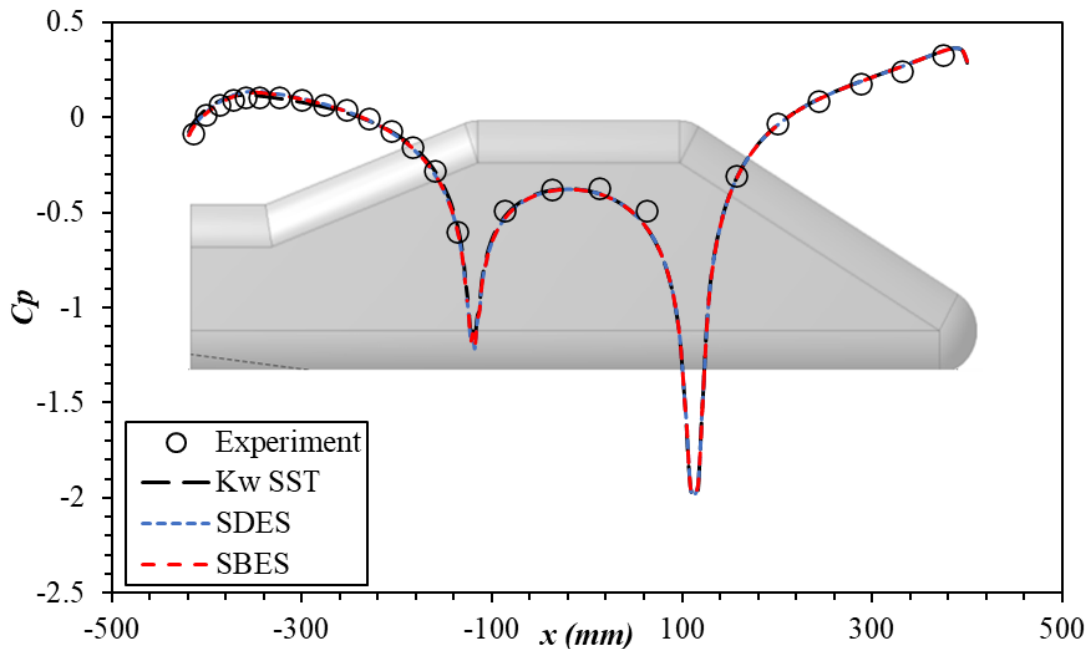
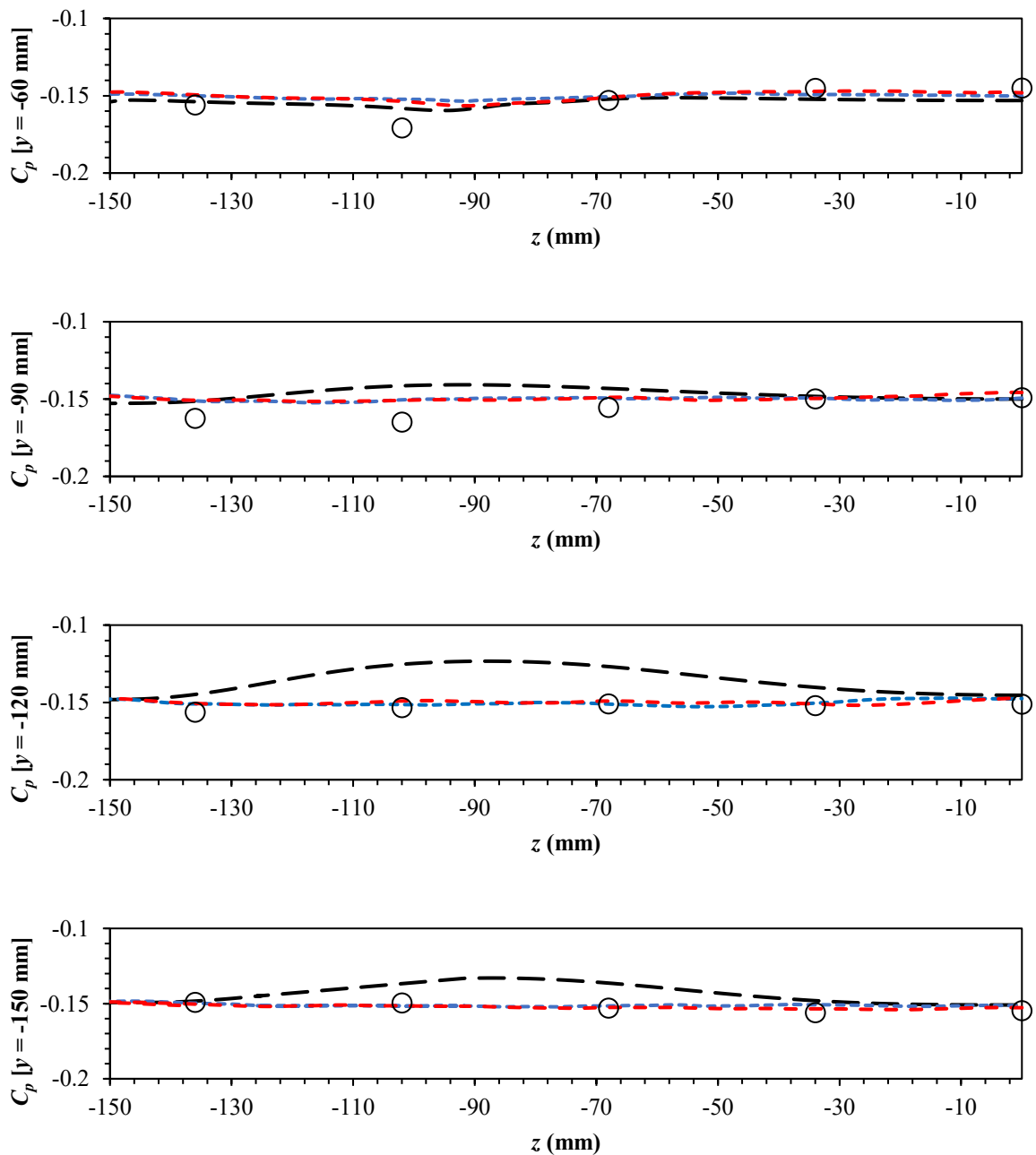


Fig. 4.5. Time-averaged pressure coefficient (C_p) obtained from turbulence model predictions on the midplane of the SAE T20 body compared against the experimental data (Wood et al., 2014).

The distribution of the pressure coefficient (C_p) at the base of the model is illustrated in Fig. 4.6. Both SBES and SDES predictions of overall C_p are in good agreement with the

experiment except at $y = -90$ mm, where the numerical simulation predicts a higher C_p value, indicating the flow is aligned to the surface in the experiment indicates the presence of flow separation. In $y = -60$ mm at $z = -99.2$ mm, a shift of 12.2% can be observed in the low-pressure peak between the experiment and the numerical data presented. The presence of a low-pressure region is expected as the flow accelerates over the diffuser tends to separate at the lateral edges of the diffuser, which is evidenced by the numerical simulation at $z = -89.6$ mm. A subsequent effect of this separation is seen in $y = 90$ mm plot, where the numerical simulations overpredict the C_p value by a maximum of 15.3%.



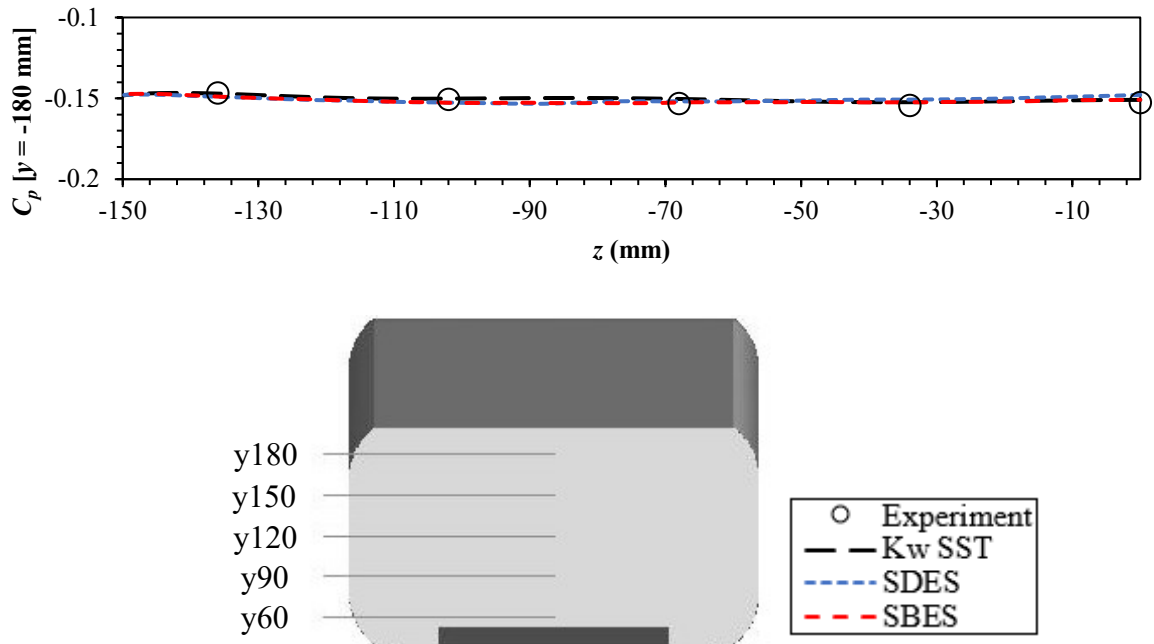


Fig. 4.6. Numerical predictions of the time-averaged pressure coefficients (C_p) obtained at the base of the SAE T20 compared against the experimental data (Wood et al., 2014).

4.4.3. Near wake structure

The near wake structures predicted by numerical simulation and experimental data detail the presence of two recirculation bubbles, as seen in Fig. 4.7. The upper recirculation bubble is formed due to the flow separation from the boot deck. In contrast, the lower recirculation bubble is formed due to the flow separation from the diffuser. The upper recirculation bubble is generally dominant over the lower one, which tends to reduce the thickness of the lower bubble, as evidenced in the experiment (Wood et al., 2014), as well as the SBES and SDES results. The centre of the upper recirculation bubble e'' is overpredicted by SBES and SDES by 1.33% and 1.9%, respectively, when compared to the experiment, whereas the $k - \omega$ SST underpredicts the results by 1.1%. The centre of the lower recirculation bubble, e' , is overpredicted by SBES and SDES by 3.0% and 4.3%, respectively, whereas the $k - \omega$ SST underpredicts the results by 0.5%. The overall length of the near wake predicted by $k - \omega$ SST, SBES, and SDES models is overpredicted by 4.01%, 3.2%, and 1.6%, respectively, when compared to the experiment, which agrees with the overall drag predicted by respective turbulence models.

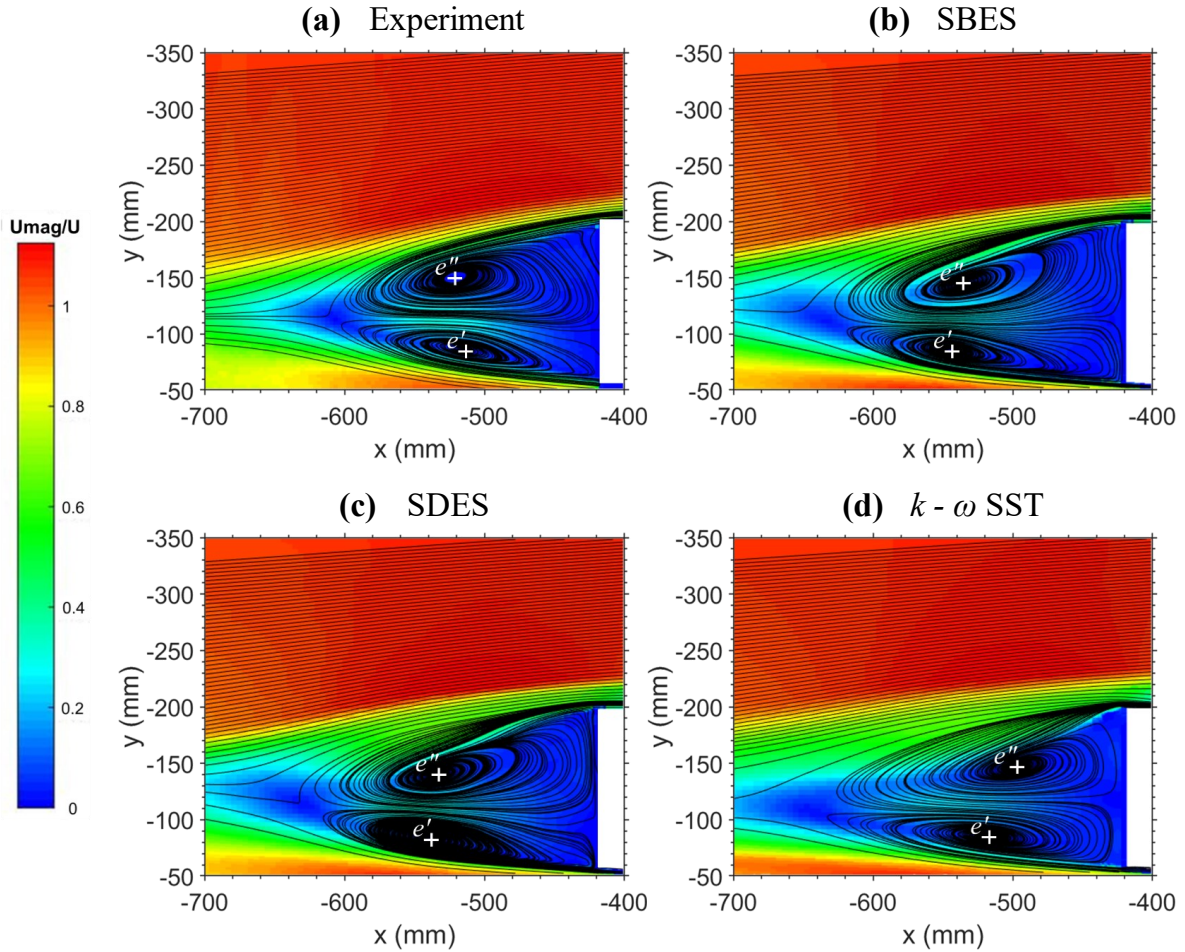


Fig. 4.7. Wake structure comparison of turbulence models used in the present study against experimental data (Wood et al., 2014). The centres of the upper and the lower recirculation bubbles are indicated by e'' and e' , respectively.

4.4.4. Streamwise velocity profiles

The experimental data presented in Fig 4.8 indicates the presence of strong separation on the backlight, which is evident from $x = -190$ mm; this grows downstream and impinges just after $x = -340$ mm. However, such strong separation is not predicted by any of the turbulence models used in the current study.

The velocity profiles in the wake of the body show that all the turbulence models predict a shear layer which starts at $x/L = -460$ mm and grows as it moves away from the body, which influences the lower recirculation bubble to be squeezed, as seen in the streamline plots in Fig. 4.7. The shear layer grows into the wake of the body at $x = -620$ mm the velocity profile predicted by all the turbulence models follow the trend observed in the experimental data. However, the streamwise velocity is overpredicted due to the absence of struts resulting in smooth underbody flow. As a result, the length of the lower recirculation bubble is overpredicted, as seen in Fig. 4.7.

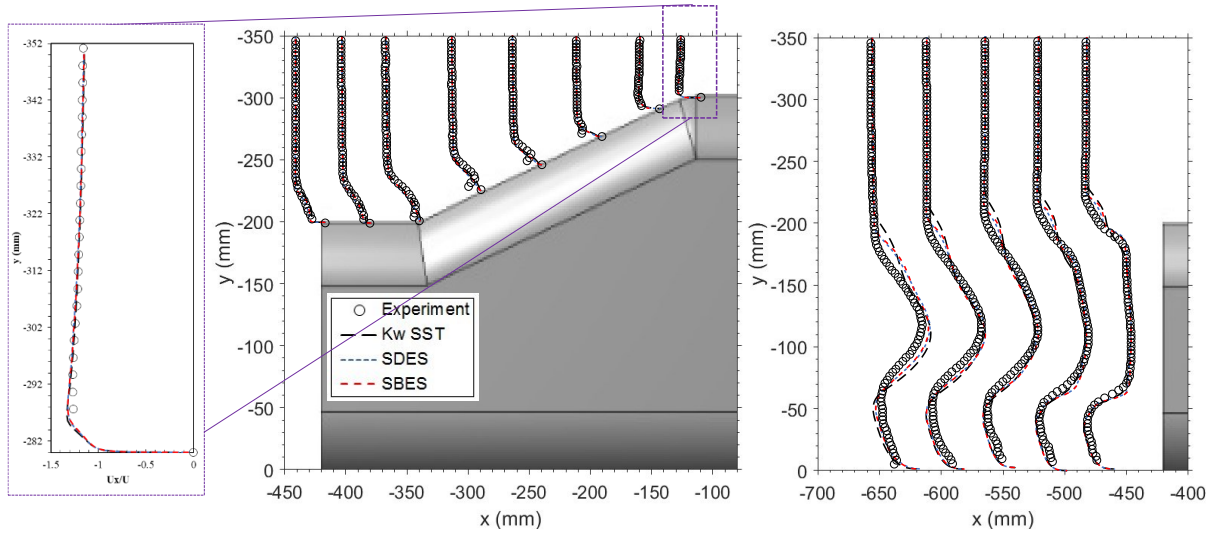


Fig. 4.8. Predictions of the normalised, time-averaged streamwise velocity profiles from different turbulence models at several locations compared against the experimental data (Wood et al., 2014). In the zoomed image indicate the axis for the velocity profiles presented.

4.4.5. Streamwise velocity contours

The time-averaged normalised velocity magnitude ($U_{mag} = U_{mean}/U_{\infty}$) behaviour on the spanwise velocity contours from $x = -190$ mm to -420 mm is illustrated in Fig. 4.9. the experimental data shows there is no flow separation at $x = -190$ mm. In contrast, SBES and SDES predict a slight flow separation, but $k - \omega$ SST predicts the flow separation distinctly, as seen in Fig. 4.9. Moving downstream to $x = -240$ mm, it is observed that all the turbulence models predicted flow separation with $k - \omega$ SST showing a stronger separation region in contrast to experimental data where there is no flow separation. At $x = -290$ mm, the experimental data reports a recirculation bubble which is in line with the velocity profile prediction in Fig. 4.8.

Interestingly, the experimental data reports a non-symmetric flow structure moving downstream, most visible at $x = -420$ mm. In Fig. 4.9, it is evident that the SBES and SDES models predict strong C-pillar vortex structures at $x = -290$ mm and -340 mm, which appear to be weaker in the experimental result. The velocity contours from the SBES and SDES show a negligible difference between them but differ from $k - \omega$ SST. In the case of $k - \omega$ SST, flow structures on the backlight and boot deck appear symmetrical.

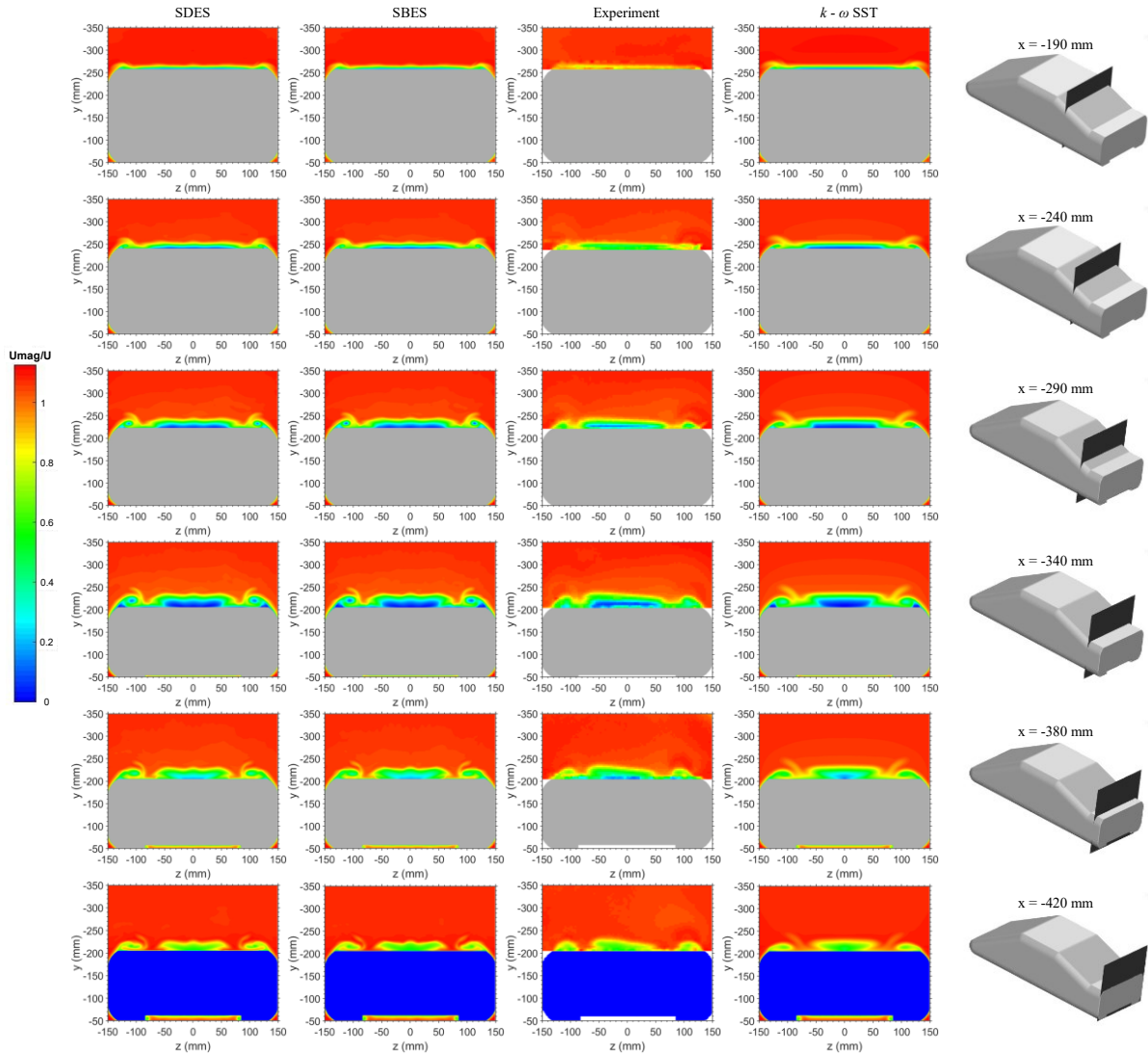


Fig. 4.9. Normalised time-averaged velocity magnitude contours compared with the experimental data (Wood et al., 2014). From top to bottom, each row corresponds to the locations $x = -190$ mm, -240 mm, -290 mm, -340 mm, -380 mm and -420 mm, respectively.

4.4.6. Assessment of flow resolution:

All the turbulence models predict the generic flow features of a typical notched-back configuration, such as A-pillar vortex (*a*), flow separation over the backlight (*b*), and C-pillar vortex (*c*), as seen in Fig. 4.10. Qualitatively, no appreciable difference between flow structures predicted by SBES and SDES is evident except for the prediction of A-pillar vortex. SBES and SDES predict the internal flow features of the flow separation on the backlight much better than the $k - \omega$ SST model. However, quantitatively the near wake resolution in SBES appears to be better than that predicted by SDES. At the location highlighted (*d*) in Fig. 4.10, the average TVR predicted by SBES and SDES is approximately 7 and 13, respectively, indicating that the resolution is better in SBES. This is further highlighted in the turbulence spectrum in the near wake shown in Fig. 4.11.

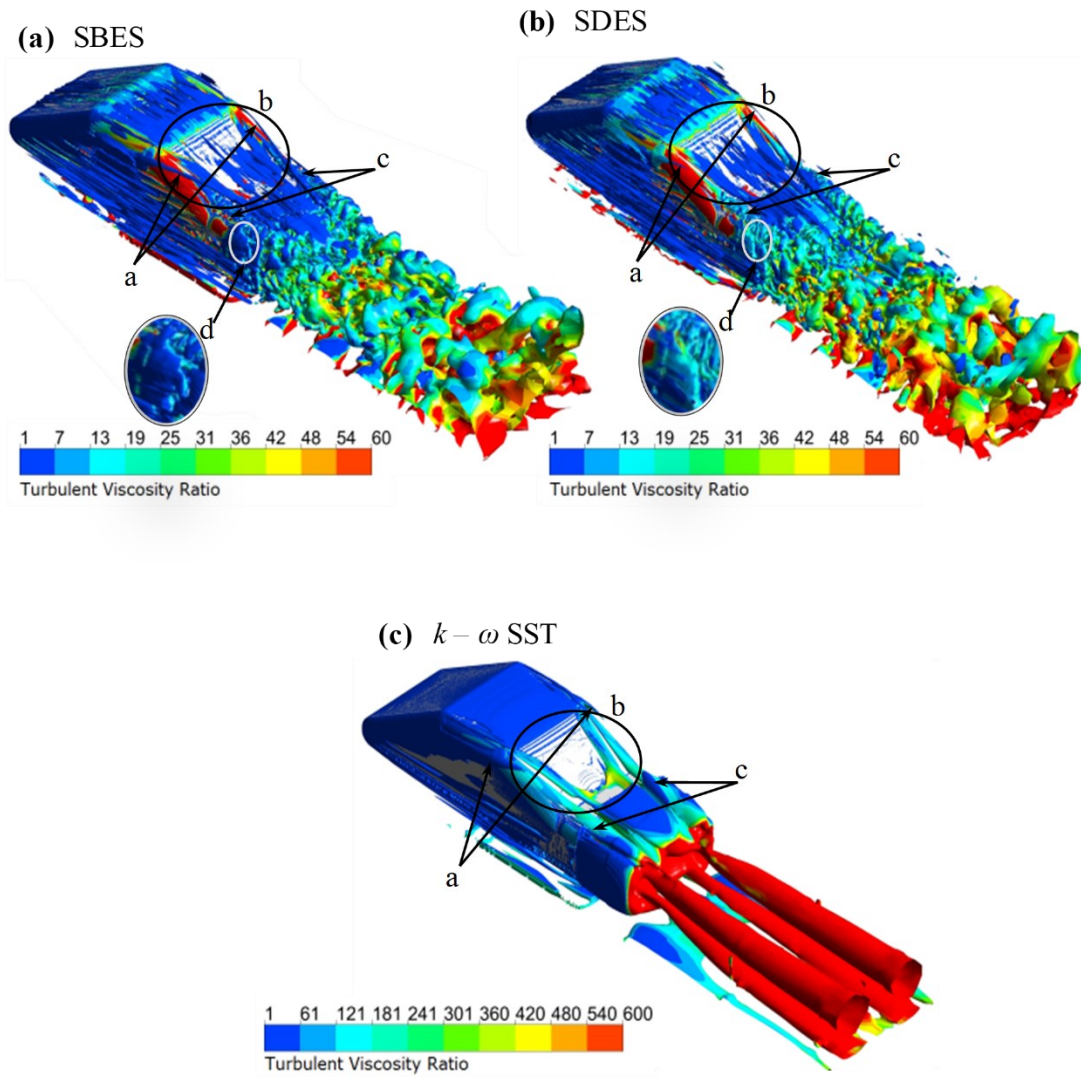


Fig. 4.10. Iso-surface of the instantaneous Q-criterion generated at 0.014 s^2 for all turbulence models and coloured by Turbulent Viscosity Ratio.

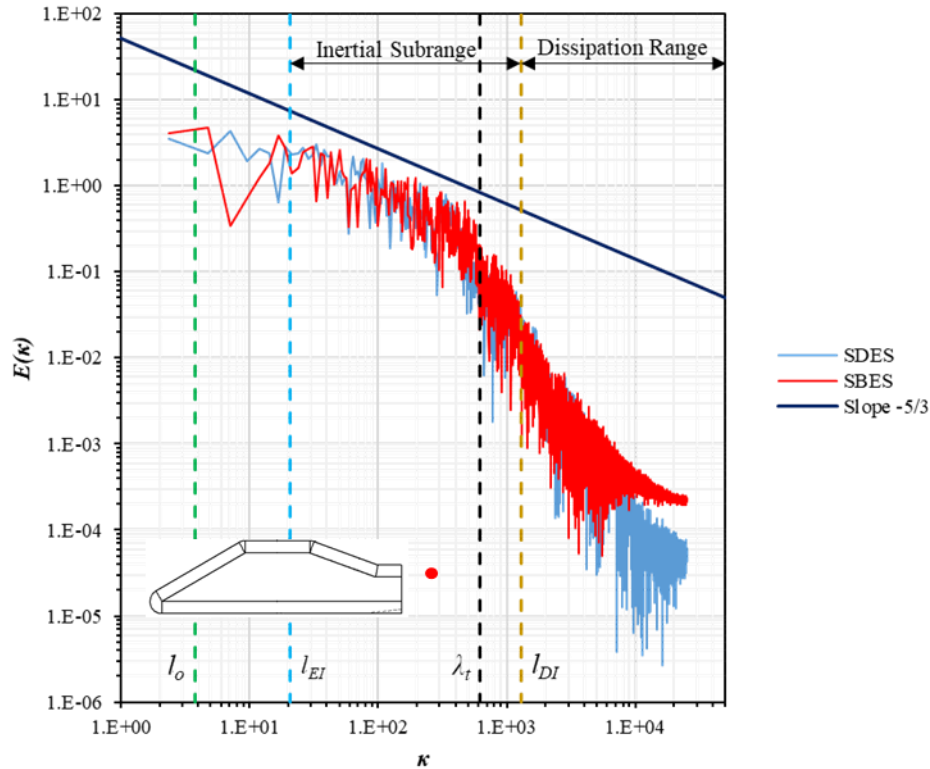


Fig. 4.11. The turbulence energy spectrum ($E(k)$) of SDES and SBES in the near wake of the model at point ($x = 440$ mm, $y = -180$ mm, $z = 0$).

Shielding function

A further assessment is carried out by examining the shielding of the RANS boundary layer and levels of TVRs. Figs. 4.12 (a) and (c) indicate the switch from RANS to LES for both SBES and SDES at the backlight and boot deck, respectively. Both SBES and SDES exhibit a well-preserved modelled RANS layer; however, the transition to LES in the SSL appears to be comparatively rapid and sharp with SBES, slightly improved compared to SDES. This sharp and rapid transition may be attributed to the improved asymptotic shielding formulation that blends the Reynolds Stresses between the RANS-LES regions discussed in **Chapter 2**. Figs. 4.12(b) and (d) show the corresponding eddy viscosity ratios indicating that the SBES produces a lower eddy viscosity level at the SSL than the SDES, and therefore, the shielding behaviour in SBES appears more refined to the flow topology. Considering that they are negligible differences between the SBES and SDES models, the results for the influence of backlight on the in-flow topology of the notchback are presented using the SBES turbulence model. A detailed assessment between SBES and SDES is presented by Chode et al. (2020).

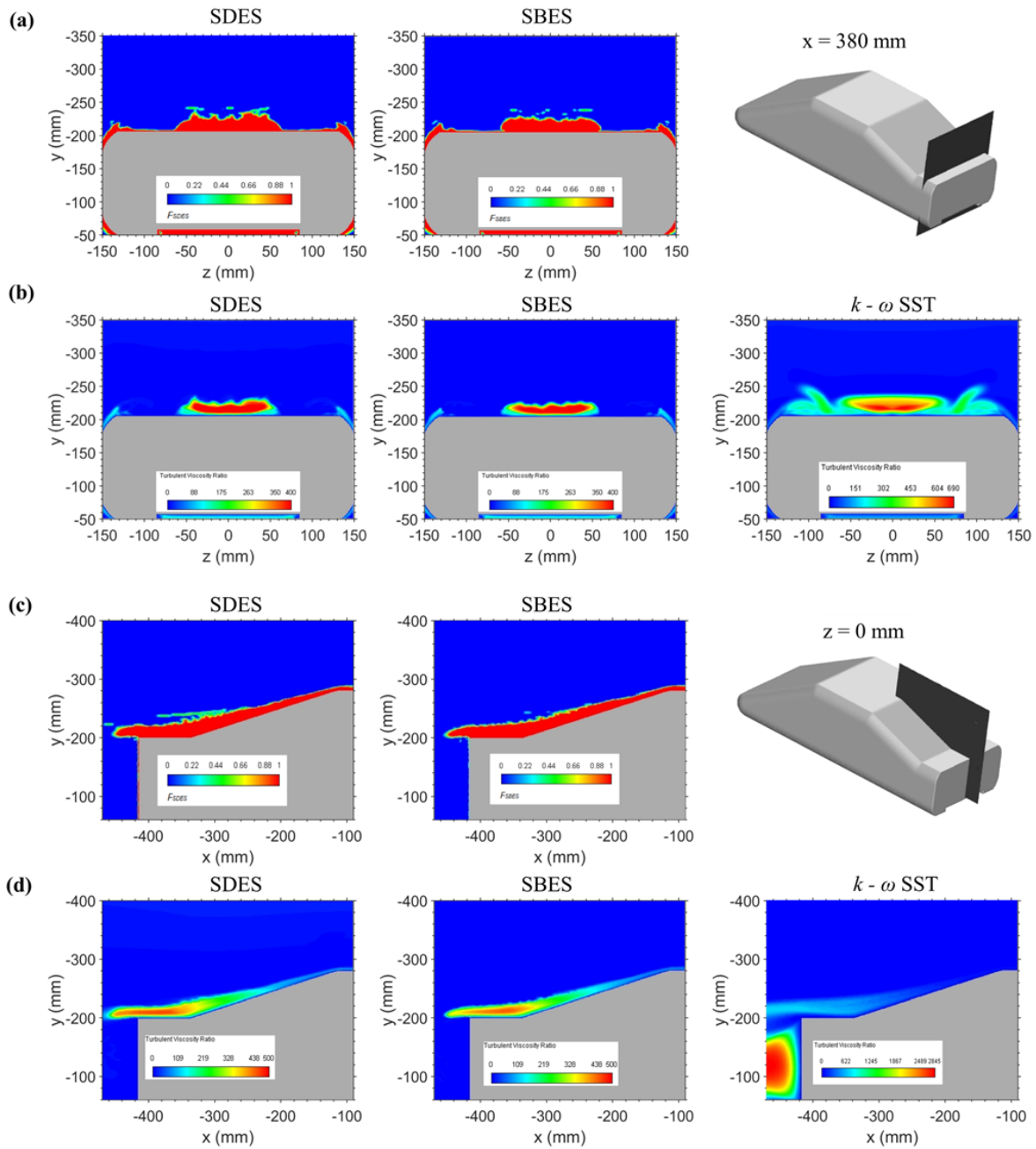


Fig. 4.12. Assessment of flow resolution **a), c)** Shielding function of SBES and SDES in streamwise and spanwise direction at $z = 0$ mm and $x = 380$ mm respectively, **b), d)** TVR of all the turbulence models in streamwise and spanwise direction at $z = 0$ mm and $x = 380$ mm respectively.

4.5. Influence of backlight angle on the flow

4.5.1. Flow behaviour on the surface of the backlight

Fig. 4.13 illustrates the flow behaviour on the surface of the vehicle using time-averaged wall shear stresses. In SAE T20, a pair of trailing vortices is seen to emerge from the leading lateral edges of the backlight at point *b*. These free shear layers traverse downstream along line *c* and impinge on the boot deck, which increases the pressure at the intersection of the backlight and boot deck, as seen in Fig. 4.14(a). The direction of rotation of these vortices is marked by

d. The flow separated from the backlight is seen to be squeezed towards the centreline of the model due to the presence of these vortex structures. The region of flow separated by backlight is marked by *a*, and the direction of the flow within this region is marked by *k* and *l*. The secondary flow structures marked by *e* are predicted on the lateral edges of the backlight, representing stagnation zones. The vortex structures impinge along *c* on the boot-deck flow towards the centreline (*i*) along the directions *f* and *g*, respectively, resulting in parting line *h*. The prediction of line *h* from numerical simulation lies close to the centreline. However, the experimental data (Fig. 4.13(b) – SAE T20) indicates that the parting line *h* is offset from the centreline due to the difference in the strength of the trailing vortices. This difference results in forming a small region of separated flow (*j*), which contributes to the non-symmetrical flow behaviour on the backlight. Such a feature is not predicted by numerical simulation.

As the backlight angle changes to 30°, the predicted flow pattern changes, giving a non-symmetrical flow behaviour on the backlight. The separated region has grown in size compared to SAE T20, and the negative pressure it induces across the backlight (Fig. 4.14(a)) contributes to an increase in overall drag, as seen in Table 4.7. The flow in this region rotates about points *b* and *c*. The stronger vortex *b* governs the flow direction (*j*) and moves the flow upwards, covering most of the backlight. Points *b* and *c*, being closer to the lateral edges of the backlight, influence the formation of vortex structures as the point being closer to the leading edge of the backlight draws the flow into *b* and, on the other side, into *c*. Usually, these vortices are expected to roll up to form a roughly symmetric trailing pair vortex, as seen in Fig. 4.13(a) – SAE T20. Interestingly, a reattachment line *d* is seen on the lower half of the backlight, indicating the presence of weak trailing vortex-like structures. However, on the other side, such vortex structures are absent.

Further, the flow direction (*k*) at *c* is in the opposite direction as predicted at *b*, forming a parting line *g*. On the boot deck, the direction of flow rotation in the region *a* is strong, which influences the flow on the boot deck to move up the backlight leading to the formation of another parting line, *n*. Further downstream, the flow tends towards the edge of the boot deck in directions *l* and *m*. However, for the SAE T30 configuration, the differences between the model results and experimental data are noticeable, especially with respect to the strength of the rotation of flow in the separated region *a*, formation of counter-rotating vortices, and the secondary flow structures shown in Fig. 4.13(b) – SAE T30. In the separated region *a*, the experiment recorded that the flow rotating around point *c* is stronger than the rotation of flow

at b , and the location of c is further away from the lateral edge of the backlight, which allowed the formation of a low strength trailing vortex on the right side of the model.

In SAE T40, it is evident that there is a dominating primary vortex emerging from the left side of the model, which grows towards the right side, covering most of the backlight, thus showing a strong non-symmetrical flow behaviour. The flow direction in the vortex marked by a indicates that the flow is being driven up the backlight, and because of its strength, there is a flow stagnation marked by region b . The presence of the vortex results in the pressure approaching a minimum on the edge of the backlight, as seen in Fig. 4.14(a), resulting in a higher drag coefficient (Table 4.7). The stagnated flow drains on the model's right side following c . The presence of a small secondary rotating structure, d , can be seen on the model's right side; however, the faint friction lines indicate that this structure is weak or unstable. On the model's left side, the flow tends to rotate around node e and attaches to the boot deck marked along with the line g . The reattachment of this rotating flow on the boot-deck results in a high-pressure zone on the boot deck, as seen in Fig. 4.14(a). The presence of another flow stagnation f can be seen as a result of the strong primary vortex a and secondary flow rotation at e . In the experimental data, the primary vortex tends to align with the centreline of the model as Fig. 4.13(b) – SAE T40 as it passes over the boot deck, whereas no such alignment is seen in the numerical prediction. As a result, the secondary vortices d and e predicted by the numerical result appear mitigated and smaller in size.

In summary, while there are apparent differences between the experimental oil flows and model predictions of time-averaged wall shear stresses, there are still many points of commonality that the model can predict, even if the separation lines and vortex cores are displaced in comparison with experiments.

Table 4.7 The time-averaged drag coefficient predicted by the numerical models for various backlight angles (θ) compared with experimental data (Wood, 2015).

Backlight Angle (θ)	Experiment (Wood, 2015)	SBES
20°	0.207	0.1883
30°	0.260	0.2646
40°	0.284	0.2883

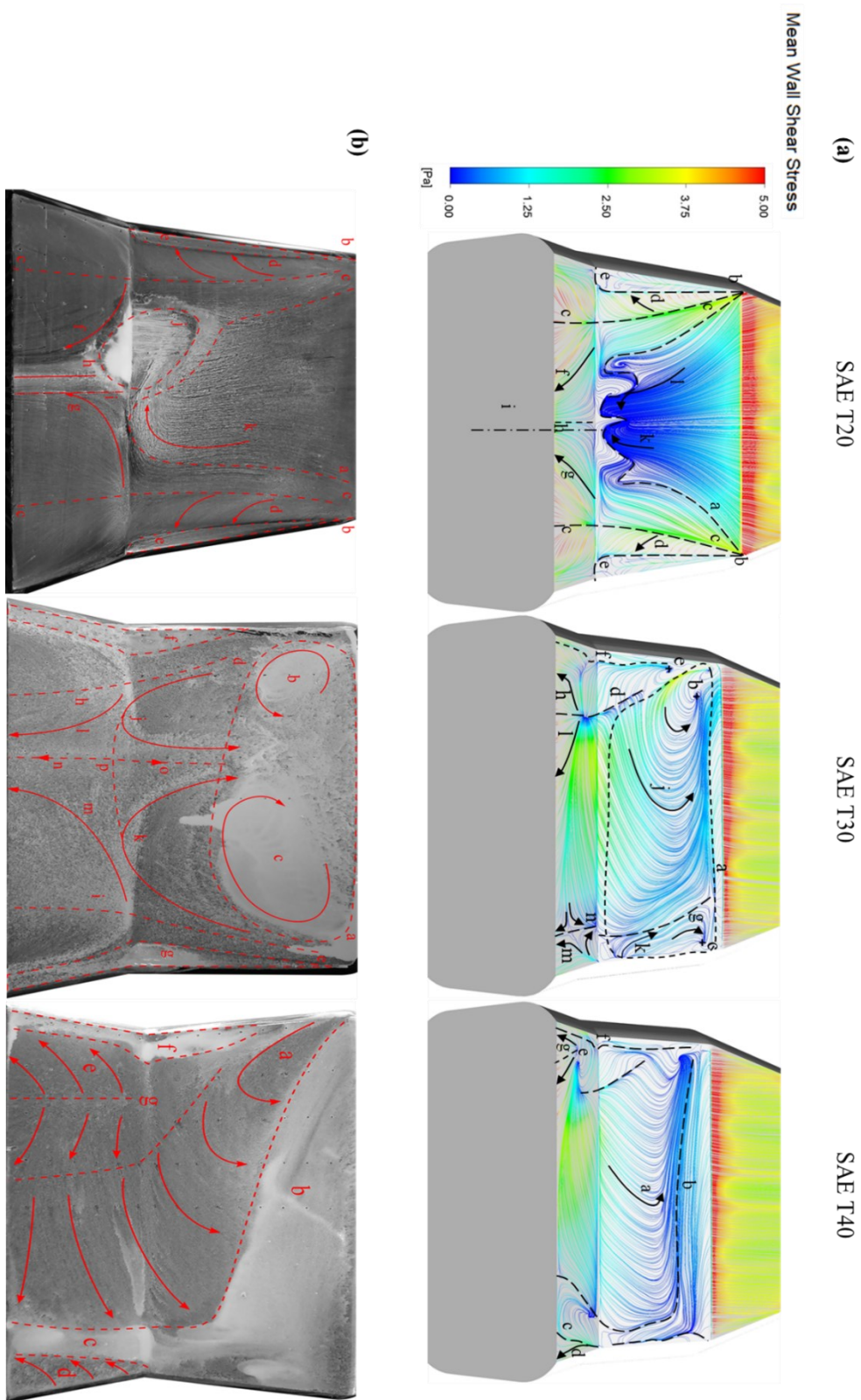


Fig. 4.13. Time-averaged values of **a)** Wall shear stresses (Friction lines) and **b)** Experimental results (Oil flow) presented by (Wood, 2015)^o plotted on the rear of the model for all the backlight angles used in this current study.

^o Reused with permission from Daniel Wood, "The Effect of Rear Geometry Changes on the Notchback Flow Field," Loughborough University. Copyright © 2015 by Daniel Wood. Licensed under Creative Commons 4.0.

4.5.2. Pressure footprint on the backlight

The impingement region predicted by numerical simulations agrees with the experiments for all the cases investigated, as seen in Fig. 4.14. Points *b* and *d* represent the impingement points in SAE T20 and SAE T30, whereas the impingement region is represented by *c* for SAE T40. The intensity of pressure predicted at the impingement region decreases with the increase in the backlight angle, and the location of the impingement point moves closer to the edge of the boot deck, as observed in experiments. In the case of SAE T30, the low-pressure region predicted for SAE T30 and T40 and the pressure predicted on the backlight for SAE T20 show a reasonable agreement with experiments. The predicted pressure at the backlight (Fig. 4.14b) for the SAE T20 and T30 bodies is higher than the measured values, although the predicted pressure gradient is reasonable. Conversely, predicting the actual separation points on each body correlates quite well with the experimental measurements.

The generation of the lateral vortex from the middle of the backlight represented by *b* and impingement of the vortex along line *e* is well predicted by numerical simulation for SAE T30, as seen in Fig. 4.14. However, the location of line *e* appears to be closer to the primary vortex, which contributes to the massive impingement zone on the boot deck. For the SAE T30, the low-pressure region (*a*) predicted by numerical simulation is lower in intensity than that observed in the experiments. The pressure at the impingement region at the boot deck is overpredicted by the model highlighting apparent quantitative differences with the experimental data. The differences in the pressure intensity can be attributed to the local flow behaviour on the curvature of the model and the lateral edge of the backlight, as shown in Fig. 4.13a. Although the overall agreement between the model and experiment appears to be reasonable for the case of SAE T40, the experimental results indicate the presence of a weak trailing vortex closer to the boot deck and backlight interaction which is less accurately predicted by the model as seen in Fig. 4.15c. The low-pressure region on the backlight of SAE T30 and T40 tends to recover across the mid-plane, evidenced in both numerical and experimental results, and this agreement appears reassuring.

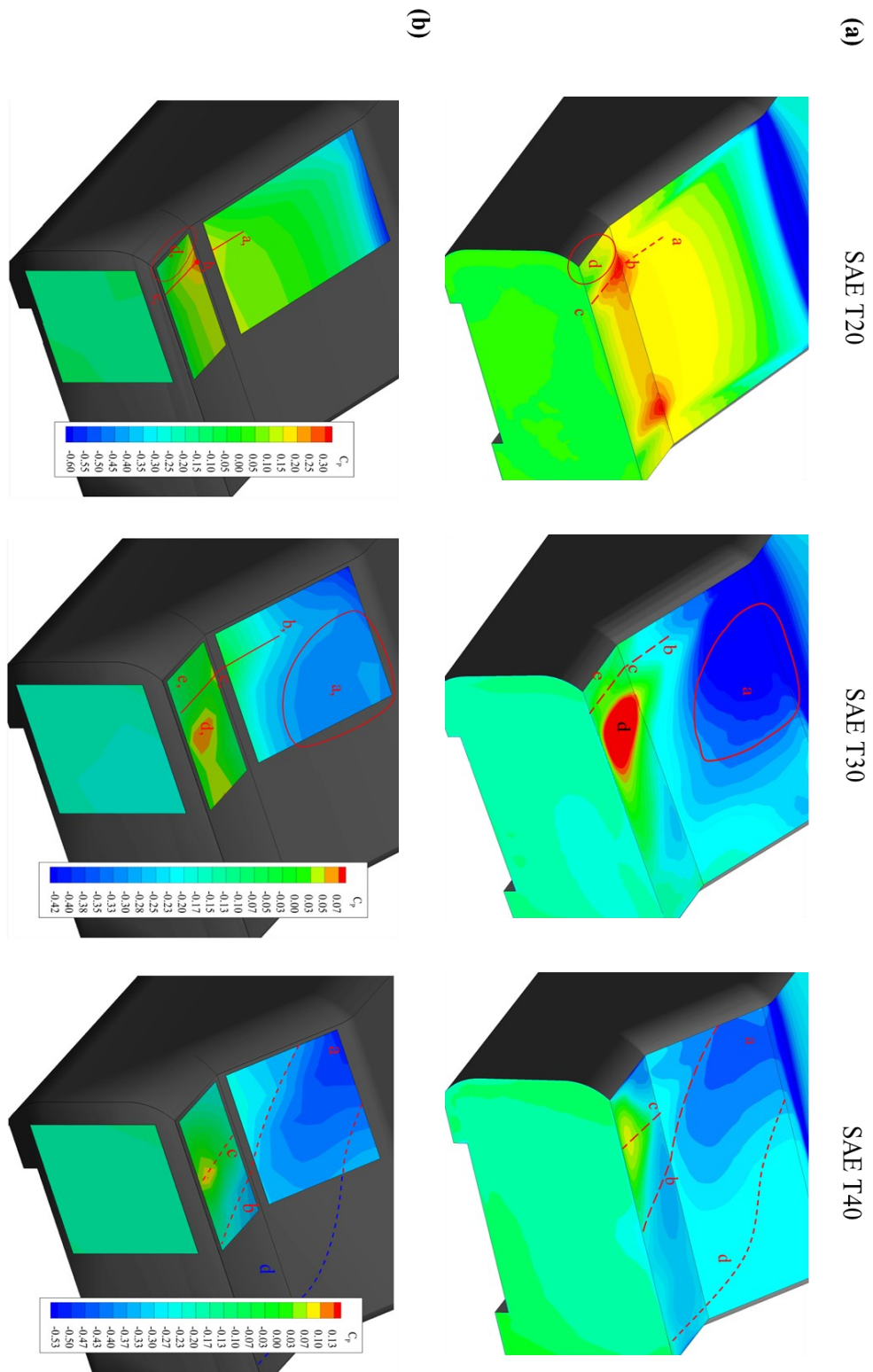


Fig. 4.14. Time-averaged values of a) pressure coefficient predicted by numerical simulation and b) Experimental pressure coefficient results presented by (Wood, 2015)^P, plotted on the rear of the model for all the backlight angles used in this current study.

^P Reused with permission from Daniel Wood, “The Effect of Rear Geometry Changes on the Notchback Flow Field,” Loughborough University. Copyright © 2015 by Daniel Wood. Licensed under Creative Commons 4.0.

4.5.3. Trailing vortex structures

In Fig. 4.15, a' and a'' show the trailing vortices generated from the leading edges of the backlight, whereas c' and c'' indicate the longitudinal vortex structures formed from the sides of the model. The size of these vortices increases when the trailing vortices merge downstream. A transverse vortex b' forms behind the backlight angle between the two trailing vortices on either side of the model. In SAE T20, this transverse vortex is seen to be squeezed between the two trailing vortices because the strength of these vortices is equal. With the increase in backlight angle to 30° , the trailing vortex a' tends to merge with transverse vortex b' because of the difference in the strength of the vortex, as seen in Fig. 4.15(b). On the other side, a'' is seen to emerge from the lower half of the backlight, which is due to the presence of the flow rotating around node b , as seen in Fig. 4.13. The transverse vortex downstream merges with c' and increases its length compared to c'' . A further increase in the backlight angle to 40° results in similar behaviour with an increase in the size of c' vortex is also seen in Fig. 4.15(c). Interestingly, it appears that there is no presence of the trailing vortices a'' and a' , emerging from C-pillars as they merge fully with the transverse vortex (b'), leading to a strong non-symmetrical flow behaviour.

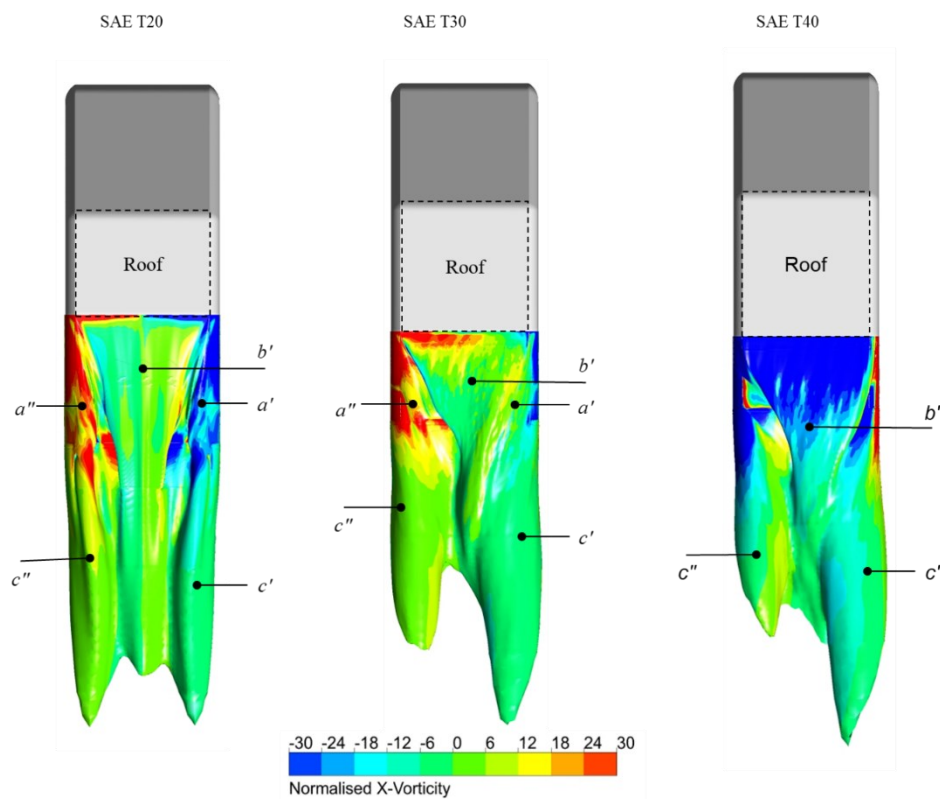


Fig. 4.15. Iso surface of time-averaged velocity magnitude (30 ms^{-1}) coloured with normalised time-averaged x vorticity for all the backlight angles investigated.

Summary

In this chapter, numerical simulations are presented for SAE T20 in uniform flow as a first step to investigate the most suitable grid resolution and to validate the feasibility of the adopted numerical methodology by comparing the results with experiments. Subsequently, the influence of the backlight on the flow at the rear of the notchback was examined in detail to achieve the first aim stated in **Chapter 1**. SBES and SDES prediction is compared to the experimental data and numerical predictions obtained from the $k - \omega$ SST model.

- SBES and SDES show capabilities in resolving the flow features compared to the $k - \omega$ SST model. However, qualitatively SBES appears to resolve the internal flow structures marginally better than SDES.
- The transition from RANS to LES was more rapid and definitive for SBES when compared to SDES, and the v_t/v ratio was the lowest for SBES, indicating a well-resolved turbulence flow field. Also, SBES provides more valuable turbulence information compared to URANS model in the study.
- The asymmetry flow observed over the backlight and boot deck region results from the difference in the flow separation over the lateral edges of the roof, and the results tend to show that the backlight angle tends to alter the strength of the C-pillar trailing vortex due to which the asymmetrical flow feature is seen. Similar observations were reported by Sims-Williams et al. (2011) and He et al. (2021). As the asymmetry increases in the region, the drag experienced by the body also increases until the flow is fully separated when the backlight angle reaches 90° (Sims-Williams et al., 2011). A similar observation can also be drawn from the investigation carried out in this chapter for SAE notchback configurations, where the drag reported for the 40° backlight angle was high among all the configurations investigated.
- Finally, SBES tends to resolve the flow features more accurately than the turbulence models presented, and the predictions of SBES are in reasonable agreement with the experiments. Thus, the SBES turbulence model can be used as a potential solver for resolving the flow field in the first step of the hybrid CAA approach.

Chapter 5

Investigation of Aspect Ratios and Inclinations of mirror on noise radiated

The assessment of the turbulence model presented in **Chapter 4** shows that the SBES turbulence model can resolve the turbulent flow beyond the Taylor scale in the energy spectrum, and the flow resolution obtained in the wake is sufficient to accurately predict the pressure behaviour on the backlight, boot deck and base of the notchback geometry. Also, the SBES shown to quickly transit from RANS to LES mode even when using unstructured grids. Therefore, SBES methodology, which is used in **Chapter 4**, is used in step 1 of the hybrid approach to obtain the flow field. Acoustic analogies such as KI and FW-H (presented in **Chapter 2**) are used in step 2 to conduct the acoustic computation.

The major contributor to the noise generated is the side-view mirror. The design of side-view mirrors tends to vary based on the aesthetics of the vehicle, while the changes made to the side-view mirrors for aesthetics can affect the noise generated. Therefore, understanding the physics of noise generated is essential to mitigate the noise. Most noise mitigation strategies are based on changing the mirror topology or location of the mounting the mirror or topology changes in conjunction with the A-pillar implemented. However, applying the similar geometrical changes to an idealised mirror geometry, the critical flow features that contribute to noise generation and the quality and structure of the radiated noise can be comprehend.

Thus chapter aims to investigate and assess the hybrid CAA approach based on SBES and FW-H for aeroacoustics studies using unstructured grids by validating and verifying the noise radiated from the standard half-round mirror (presented in **Chapter 2**), which has been extensively studied as a benchmark case for aeroacoustics, with two specific geometrical changes *i*) aspect ratio (AR) and *ii*) the inclination of angle w.r.t the mounting surface (θ). The change in the aspect ratio of bluff bodies, such as cylinders and cubes, affects the unsteady pressure footprint on the mounting surface away from the body resulting in a reduction in noise radiated up to 8-10dB (Dawi and Akkermans, 2019; Islam et al., 2008b; Ye et al., 2021; Yuan et al., 2020) while the inclinations angle selected represents the realistic side-view mirror inclinations which range from 8° to 32° .

5.1. Model and computational domain description:

The standard HRM with a diameter of D of 0.2 m is mounted perpendicularly on a flat plate of dimensions identical to studies conducted by Ask and Davidson (2009, 2006), representing a realistic vehicle side window, as shown in Fig.5.1(a). The aspect ratio ($AR = h/D$) of the HRM is 1.5, defined as the height of the HRM (h) in the crossflow direction along the y -axis over its diameter (D). For AR cases, the height (h) of the HRM is changed while the diameter (D) is kept constant, as shown in Fig. 5.1(b). Fig. 5.1(c) illustrates the sweep angle (θ) made by the back face of HRM with the plate in the streamwise direction.

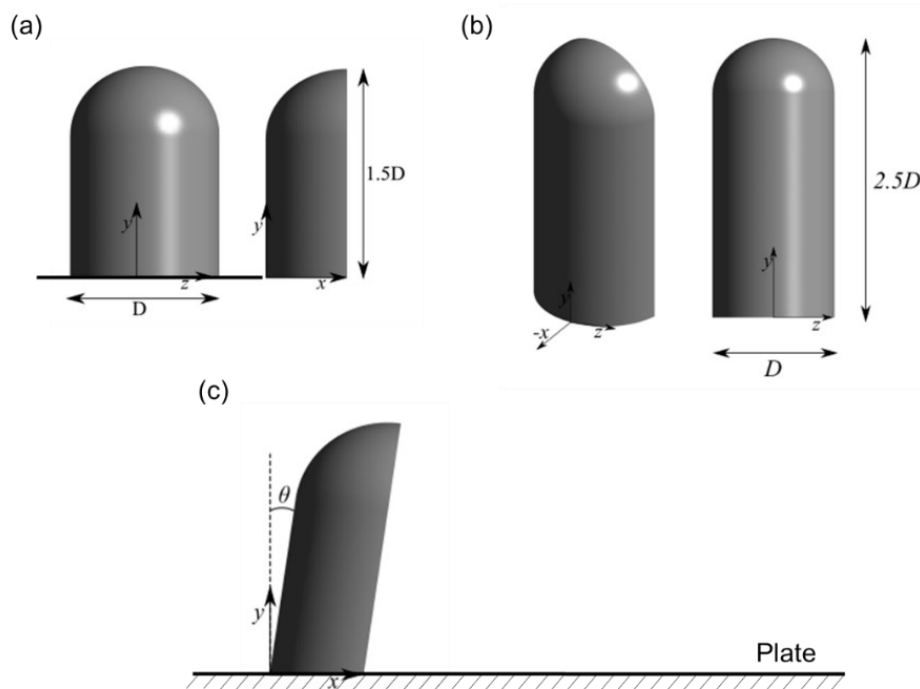


Fig. 5.1. Geometrical representation of **a)** Half-Round Mirror as proposed by Höld et al.(1999) and Siegert et al.(1999), **b)** Half-Round Mirror with an Aspect Ratio (AR) of $2.5D$ and **c)** Half-Round Mirror with sweep angle represented by θ .

The HRM mounted on the plate is enclosed in a computational domain of $12D \times 9D \times 10D$ (Fig. 5.2). The origin of the geometrical setup is located at the center of the front face of the mirror, as shown in Fig.5.1(a). The inlet is located at $4.5D$ from the origin, and a uniform velocity condition is imposed on the inlet with a turbulent intensity of 0.1%. A constant zero-pressure outlet is applied to the outlet located at $7.5D$. The walls surrounding the domain in spanwise, and normal direction are set as symmetry, and a no-slip boundary condition is applied to both the mirror and the plate, as shown in Fig. 5.2.

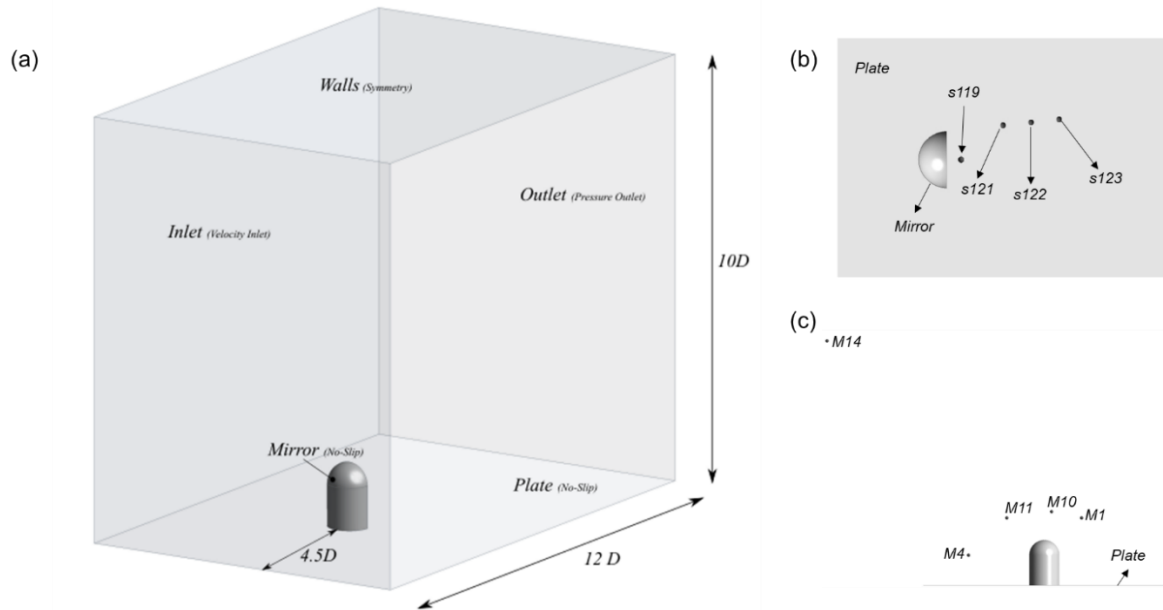


Fig. 5.2. a) Geometrical representation of the domain with normalised dimensions and boundary conditions used in the simulation, b) Layout of the sensor position in the wake of the mirror, and c) Layout of the microphones around the mirror.

5.2. Grid generation and solution setup

In this study, polyhedral – Hex dominant meshes are used; details of this grid are presented in **Chapter 2**. A grid evaluation study uses four grids: grid1, grid 2, grid 3 and grid 4. The surface sizes on the mirror are determined using normalised wall units presented in **Chapter 3**. While the free stream refinements were determined using Points Per Wave ($PPW = c/f_{max} \cdot \Delta x$), the maximum frequency for obtaining free stream grid sizes is 4 kHz based on the previously published HRM case studies. The values of the grid sizes used for all four grids are summarised in Table 5.1.

Table 5.1 Comparison of mesh resolution used in the current study.

Cases	Δx^+	Δy^+	Δz^+	PPW	Cell Count
Grid 1	360-680	< 1	360-680	7	0.85×10^6
Grid 2	120-520	< 1	120-520	10	3.42×10^6
Grid 3	120-320	< 1	120-320	22	6.86×10^6
Grid 4	120-210	< 1	120-210	28	12.28×10^6

The numerical schemes used are summarised in Table 5.2. The transient runs are initialised using a steady-state solution obtained from the $k - \omega$ SST model and solved for 0.5s, where the last 0.2s are considered for obtaining the time-averaged statistics. The time-step of 3×10^{-5} s is used for all the cases investigated, and at every time step, the pressure fluctuation on the mirror and the plate are recorded.

Table 5.2 Numerical methods used for HRM cases

	Scheme used
Pressure-Velocity Coupling	SIMPLE
Gradient	Least Square Cell Method
Pressure	Second Order
Momentum	Bounded Central Differencing
Turbulent Kinetic Energy	Second order
Specific Dissipation Rate	Second order
Transient Formulation	Bounded Second order Implicit

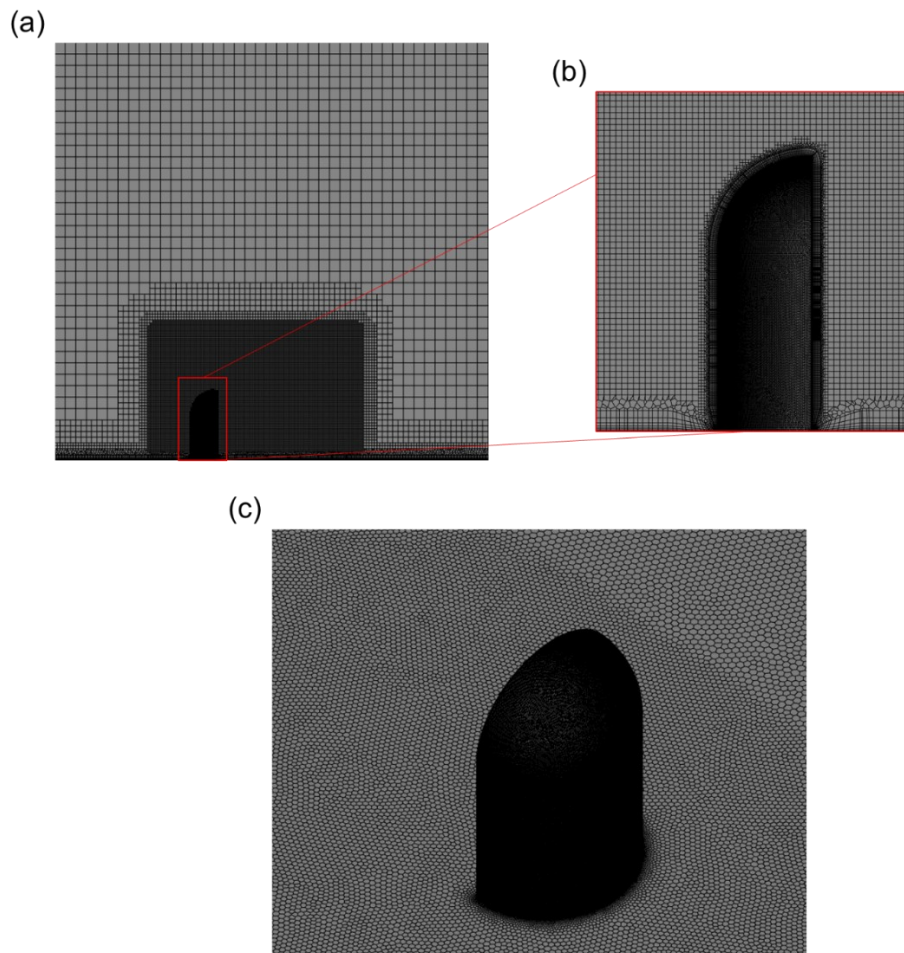


Fig. 5.3. Grid used for validation study a) Overview of the grid generated for the grid 3 with local refinement, b) Detailed view of the mesh on the mirror and its vicinity, and c) Isometric view of the cells on the surface of the mirror and the plate.

In addition to the poly-hex core grid, a structured grid with similar grid sizes was shared by ANSYS to verify the results predicted by the poly-hex core grid. For more details on the structured grid, readers are directed to Chode et al. (2021).

5.3. Grid Evaluation study

The drag coefficient predicted by the three grids lies well within the range of the drag values predicted by the other numerical studies. The difference in the predicted value of C_D is $< 1\%$ amongst the grids investigated (Ref: Table 5.3). A comparison is drawn between the predicted coefficient of pressure evaluated at several sensor locations on the mirror surface and the hydrodynamic pressure fluctuations (HPF) obtained from sensors on both the plate and the mirror (Ref: Appendix for coordinates of the sensor). The HPF spectra obtained from the sensors s112 and s120 indicate that the cut-off frequency, is higher for the grid 3 and grid 4 than the other two grids, as indicated by solid lines in Fig. 5.4(b). The difference in cut-off frequency between grid 3 and grid 4 is $< 3\%$ indicating that the grid is saturated at grid 3. The cut-off frequency is defined as

$$f_{mc} = \frac{\sqrt{\frac{2\langle k \rangle}{3}}}{2\Delta_c} \text{ Hz} \quad (5.1)$$

where $\langle k \rangle$ is the time-averaged turbulence kinetic energy, and Δ_c represents the length scale of the cell (Wagner et al., 2007).

At the centreline on the mirror, as shown in Fig. 5.4(a), the C_p predicted by the grid 1 at s16 is 9.14% lower than s20, whereas the grid 2 and grid 3 show a maximum difference of $< 3\%$ between C_p predicted at s16 and s20 and the difference between grid 3 and grid 4 is $< 2\%$. At sensor s32, the coarse grid predicts a lower C_p by 11% compared to all the other grids. Owing to several comparisons that appear more reasonable with the grid 3, grid 3 sizes were used for the rest of the HRM analysis.

Table 5.3 Comparison of Drag Coefficient against previously published numerical results

Published cases	C_D	Present Cases	C_D
Tosh et al.(2018)– DES	0.489	Grid 1	0.4741
Yu et al.(2020) – DDES	0.445	Grid 2	0.4690
Chen and Li(2019) – DDES	0.478	Grid 3	0.4721
Ask and Davidson(2009) – DES	0.425	Grid 4	0.4719
Chen and Li(2019) – DES	0.489		

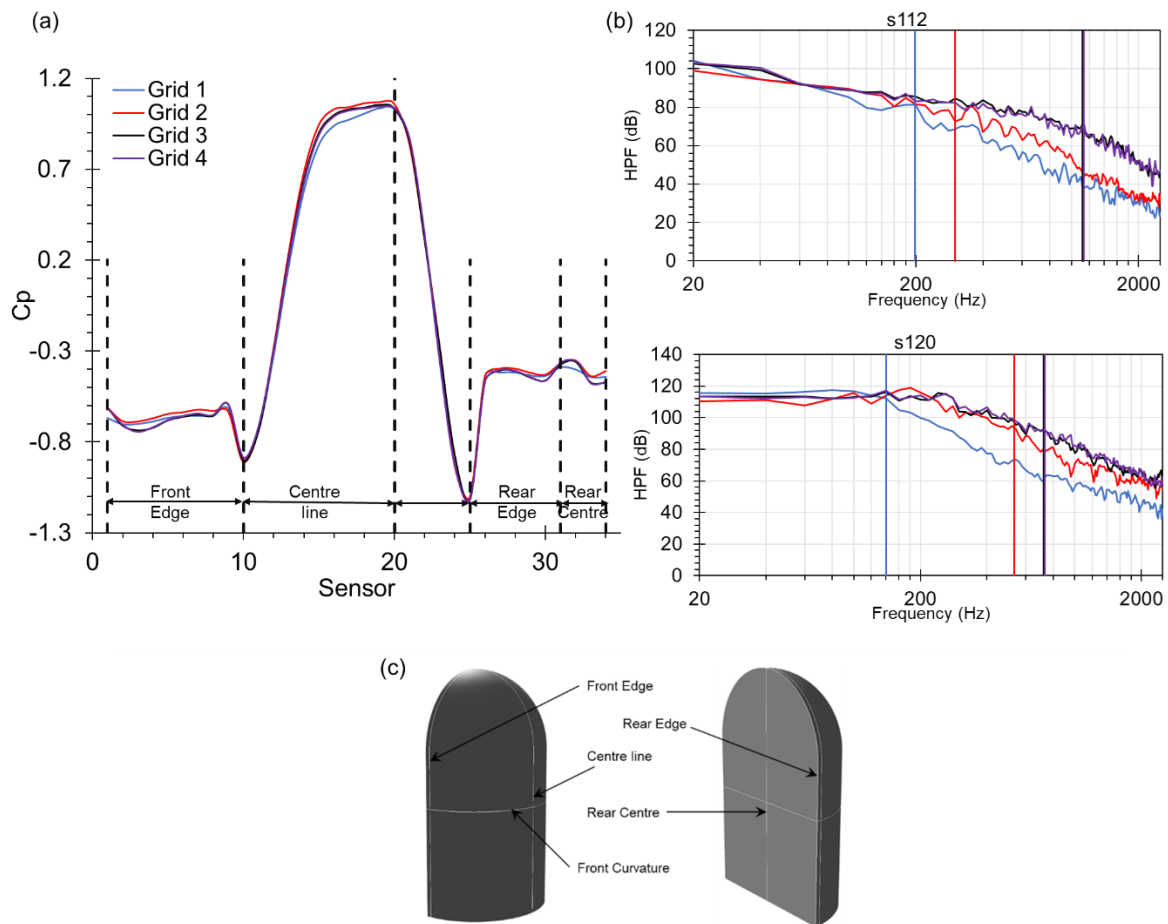


Fig. 5.4. **a)** time-averaged Pressure Coefficient (c_p) on the surface of the mirror, **b)** Hydrodynamic pressure fluctuations (HPF) extracted at two different sensor positions, s112 on the mirror and s120 on the plate. Solid vertical lines represent the mesh cut-off frequencies, and **c)** a schematic of the sensor placed for extracting pressure on the mirror.

5.4. Validation and Verification of standard HRM

The time-averaged pressure coefficient predicted by SBES with the poly-hex core grid at several locations on the mirror (See Fig. 5.5(b)) is in reasonable agreement with both experimental and numerical results, as seen in Fig. 5.5(a). The C_p predicted by the SBES with the poly-hex core grid on the front edge is lower than the measured C_p at the front edge, the C_p value predicted by sensor s3 being the lowest. The C_p predicted on the centreline of HRM is higher than the measured C_p by 2.8%, indicating the flow separation on the centreline is less well predicted by SBES. At the HRM's rear centre and rear edge, SBES prediction agrees closely with the experiment results and the published numerical results. The over-prediction of C_p on the front end and the centre line in Fig. 5.5(a) indicates a delayed flow separation which is in line with observations made by Ask and Davidson (2009, 2006), Capizzano et al.(2019), Rung et al.(2002), and Yu et al.(2020) for their numerical results.

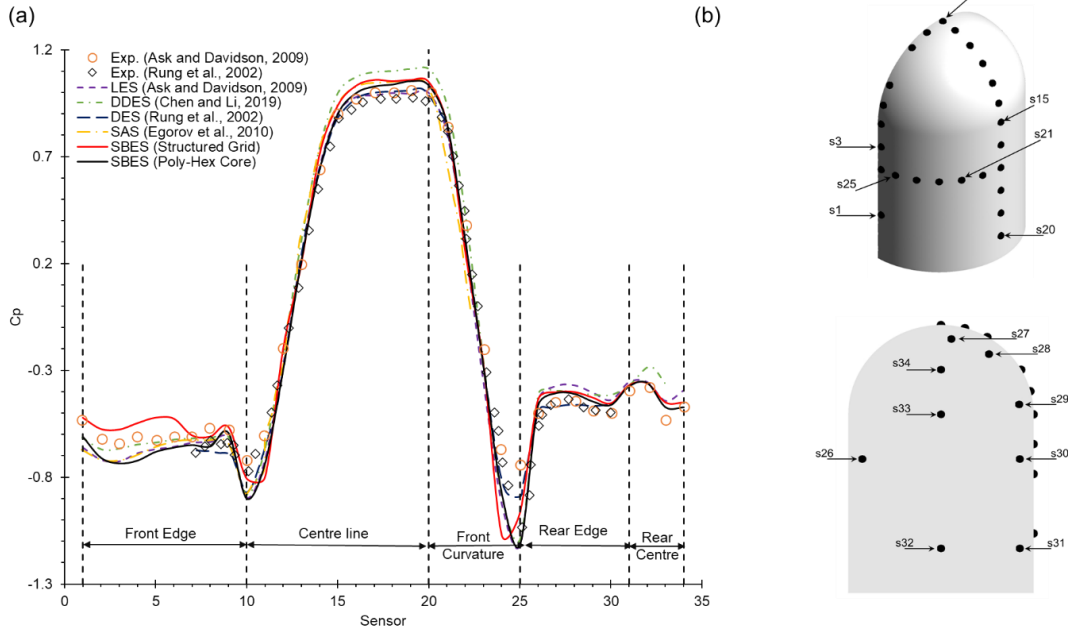


Fig. 5.5. **a)** Comparing the time-averaged Pressure Coefficient (c_p) on the mirror's surface generated at several sensors is compared against experimental data and published Numerical Results. **b)** schematic of the sensor layout on the mirror for measuring the pressure coefficients.

The formation of a horseshoe vortex upstream of the mirror results from flow stagnation at the front of the mirror. The size of the horseshoe vortex is defined as L_{hx} in streamwise, L_{hz} in the spanwise direction, respectively, in Fig. 5.6. The flow separated from the mirror results in the formation of a large recirculation bubble behind the mirror, which impinges on the plate at a distance of $2.59D$ from the mirrors trailing edge, as indicated by L_{ws} . These distances are measured on the surface generated at the height of $0.01D$ above the plate and compared against other published numerical results, as the experimental data is not available in Table 5.4. The horseshoe vortex predicted by the SBES is wider by 14% and 10% compared to the width predicted by LES presented by Ask and Davidson(2009) and DDES presented by Chen and Li(2019). The horseshoe vortex interacts with the vortex generated from the trailing edge of the mirror and exerts pressure fluctuations on the plate and the mirror.

Table 5.4 Normalised lengths of the time-averaged flow features compared against published numerical results.

Case	Solver	L_{hx}	L_{ws}	L_{hz}
Chen and Li(2019)	DES	$0.27D$	$3.25D$	$0.40D$
Chen and Li(2019)	DDES	$0.27D$	$2.66D$	$0.43D$
Present Study	SBES	$0.30D$	$2.59D$	$0.42D$

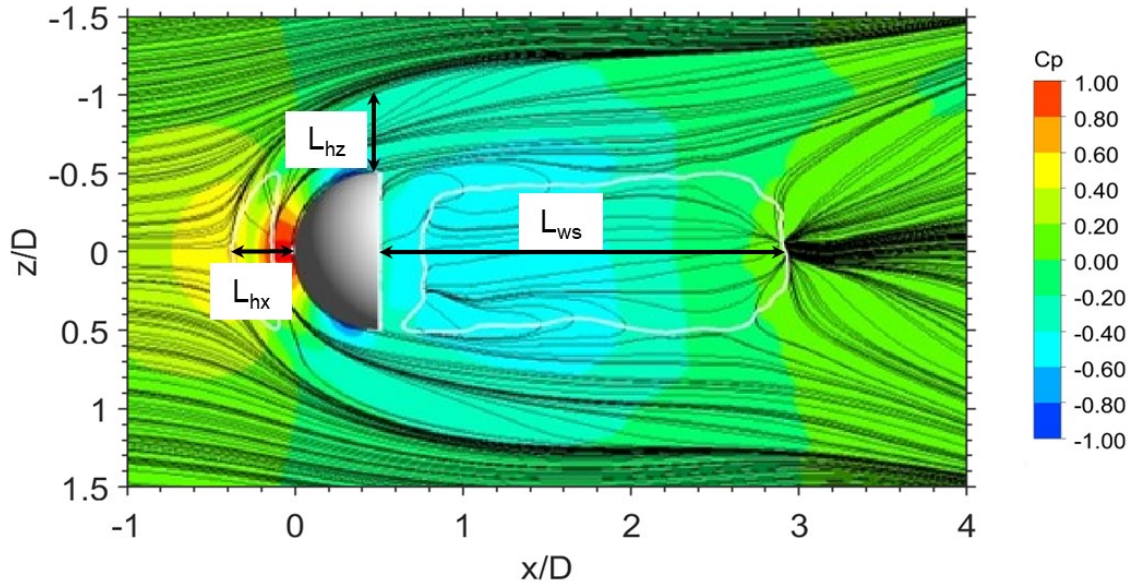


Fig. 5.6. Dominant Flow patterns around the HRM generated on the plane $y = 0.01D$ and coloured with Mean Pressure Coefficient. L_{hx} , L_{hz} and L_{ws} represent the normalised length of the horseshoe vortex from the mirror in the streamwise direction, the normalised height of the horseshoe vortex from the lateral edge of the mirror, and the normalised length of the wake structure measured from the rear face of the mirror, respectively.

The surface pressure spectra generated at s111 and s113 (Fig. 5.7) indicate lower dB levels by 9.7% and 9.3%, respectively, compared to experimental spectra in the low-frequency range ($f < 100$ Hz). At the mid frequencies range ($100 < f < 500$ Hz), the intensity levels were 4.5% and 5% lower for the two sensors, and a similar difference in the intensity levels can be found in the high-frequency range ($500 < f < 1000$ Hz). For frequencies ($f \geq 1000$ Hz), the predicted SBES spectra decay rapidly and deviate considerably from the experimental data, as seen in Fig. 5.7.

The HPF spectra obtained on the plate show a better agreement with experimental results throughout the spectra than the HPFs obtained on the mirror. The HPF spectra from experiments at sensors located on the plate predict a peak frequency at ~ 38 Hz, which corresponds to the Strouhal frequency of $St = 0.19$ ($St = fD/U$), the vortex shedding frequency for HRM (Ask and Davidson, 2009; Rung et al., 2002). This peak frequency is more evident in the sensors located downstream, such as s121 – s123 in the wake, as seen in Fig. 5.8. At s119, no distinct peak is observed at 40Hz in the experimental and predicted data. Whereas at s121 and s122, no distinct peak is seen in the predicted spectra by SBES. The SBES predicts a distinct peak with the structured grid at s123.

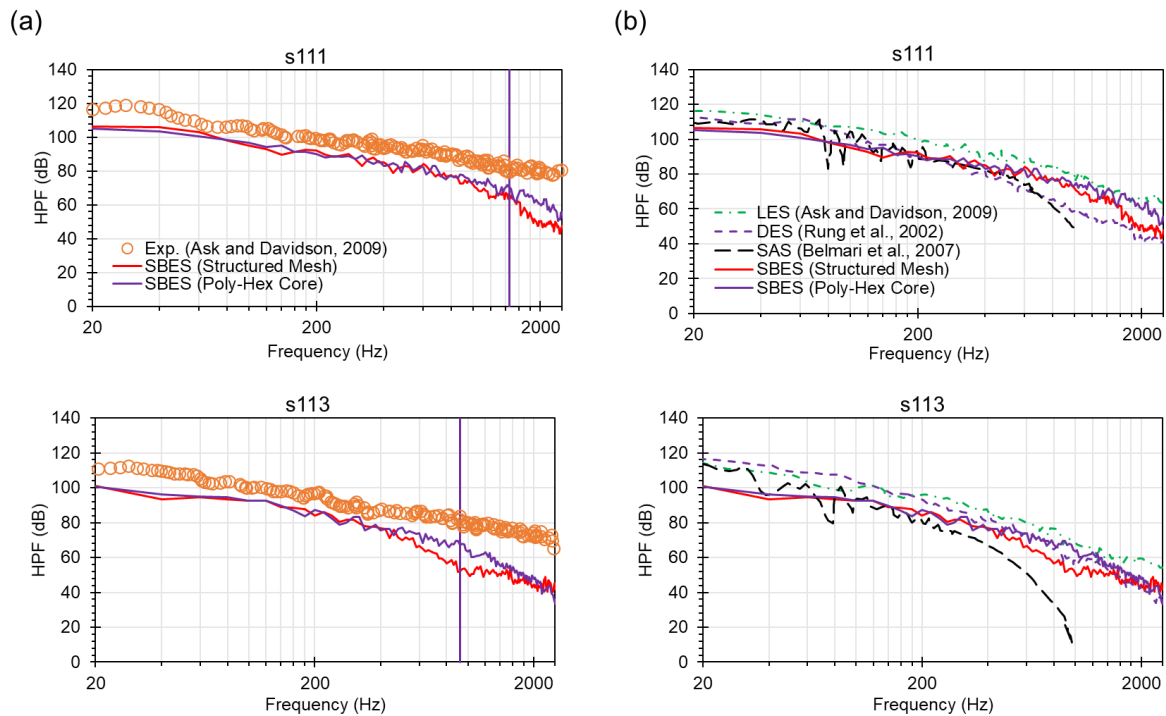


Fig. 5.7. HPF extracted at two locations on the mirror, s111 and s113, are compared between the grids used in the study against **a)** experimental data and **b)** numerical data. The legends in both s111 and s113 are same.

The pressure fluctuations on the plate and mirror are the source for producing noise, and this noise propagates within the domain. The propagated noise is evaluated at five different microphone locations using the FW-H acoustic analogy from the pressure fluctuations recorded at every frequency, and sound pressure level (SPL) computed at five microphone locations are shown in Fig. 5.9.

The SPL predicted by SBES with both poly-hex core and structured grid shows a good agreement in the trend compared with the measured data, as shown in Fig. 5.9. At M1 located in the mirror upstream, a maximum of 4 dB and 8 dB difference is observed at low-frequency for both the poly-hex core grid and the structured grid. A maximum difference of 1–2 dB is seen in the mid and high-frequency ranges between SPL spectra predicted by the structured and the poly-hex core grids. The SPL spectra predicted by the structured grid at M4 overpredict the SPL intensity compared to measured data, while the poly-hex core grid agrees well with the intensity in measured spectra (Ask and Davidson, 2005). At the high-frequency range, the prediction from both grids gives a maximum difference of 8–9 dB from experimental data, and this difference in the predicted spectra is consistent with the other numerical results published by Ask and Davidson(2006, 2005) and Caraeni et al.(2011). At M10 and M11, the predicted SPL is in good agreement with the measured data throughout the SPL spectra, as shown in Fig. 5.12.

At M14, as shown in Fig. 5.12, the pressure spectra predicted by the structured and poly-hex core grids indicate lower intensity levels than the measured spectra considering that the mesh is less refined in this region, and therefore the acoustic frequencies appear to be less resolved.

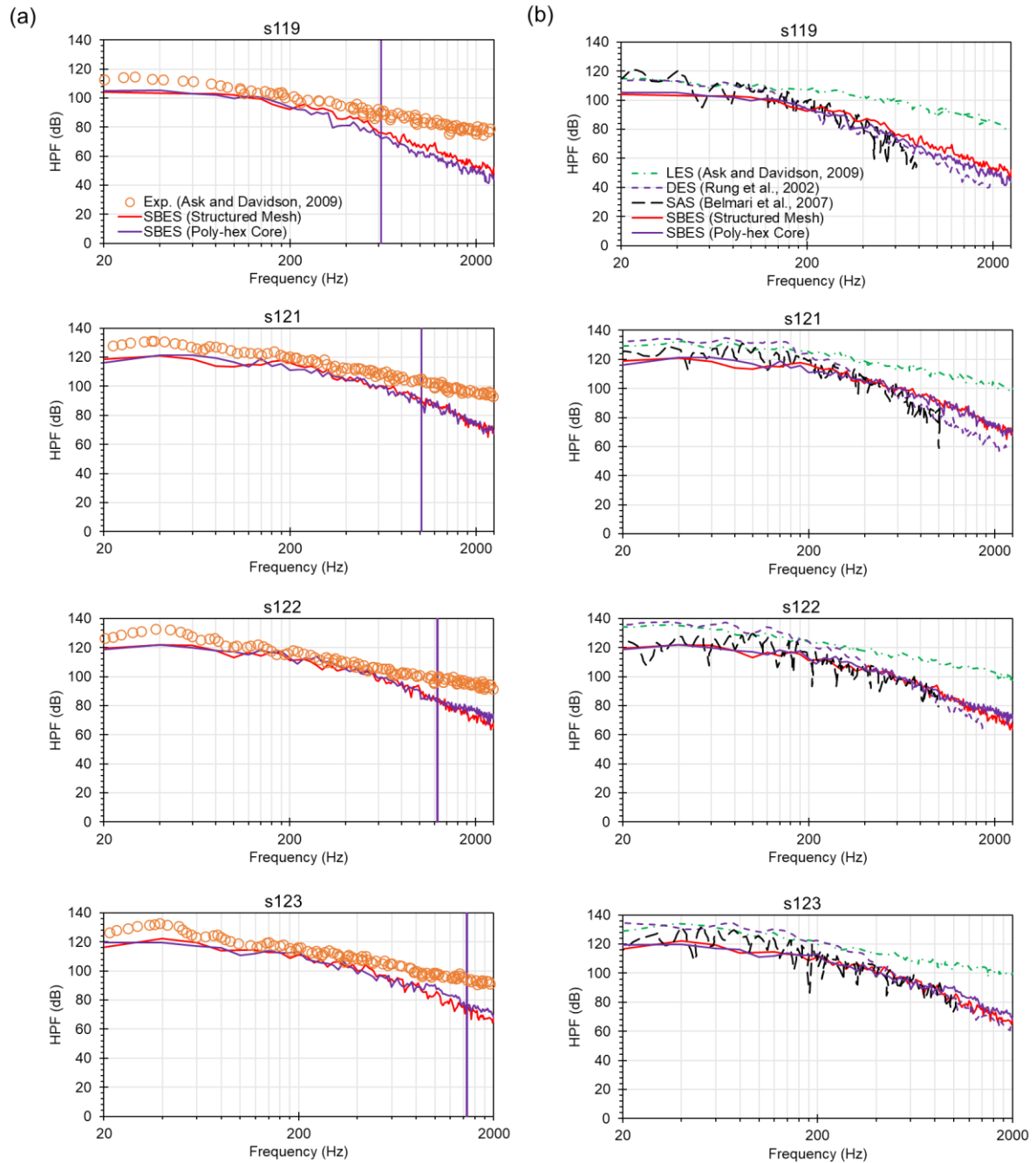


Fig. 5.8. HPF extracted at four locations on the plate, s119 and s121-s123, are compared between the grids used in the study against a) experimental data and b) numerical data. The legends are same for s119 and s121-s123.

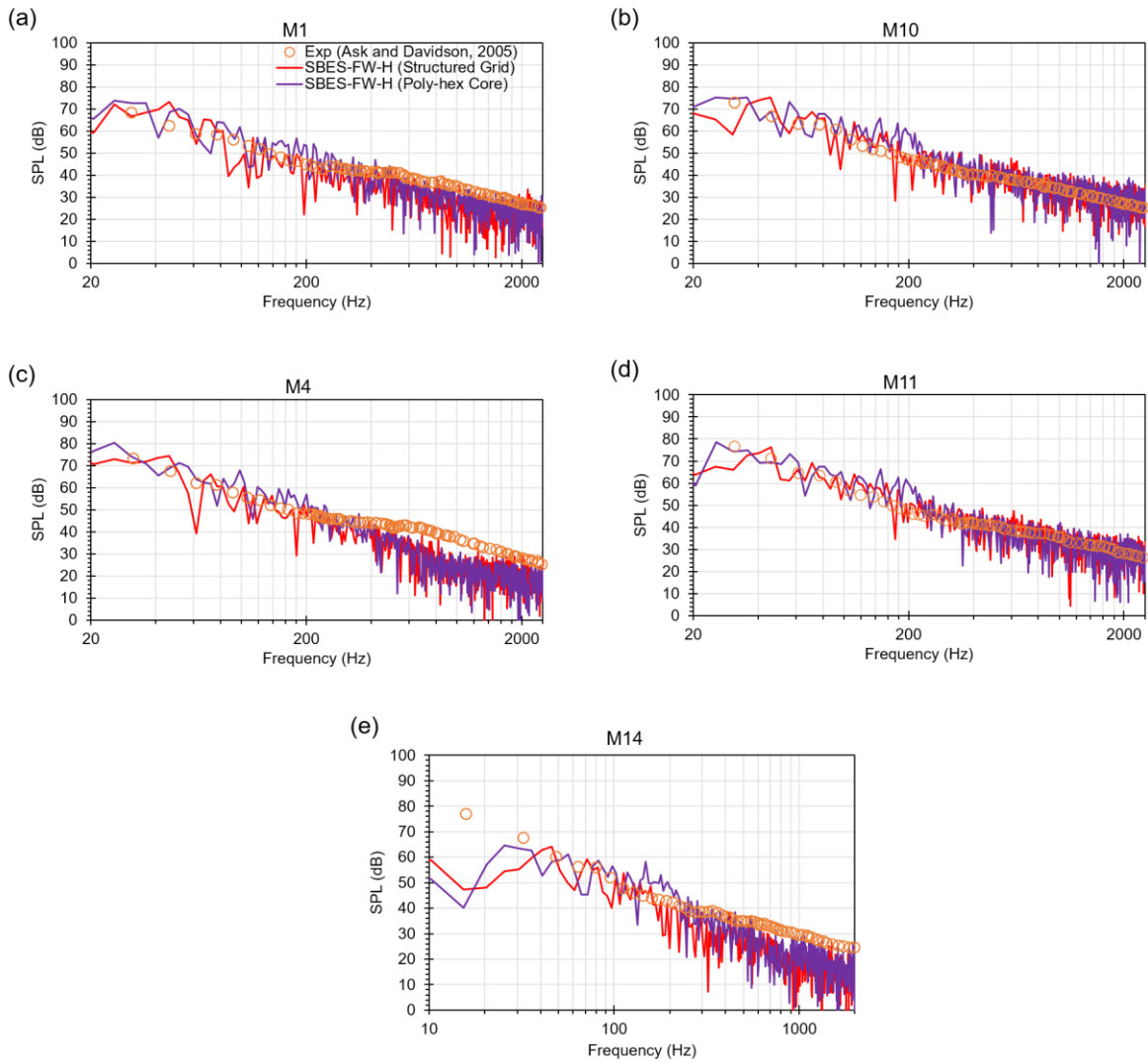


Fig. 5.9. SPL extracted at five locations around the mirror, M1, M4, M10, M11 and M14, are compared between the grids used in the study against a) experimental data and b) numerical data. The legends shown in M1 are same for all the plots.

5.5. Effect of Aspect Ratio on Flow and noise radiated by HRM

The size of the recirculation bubble formed behind the mirror increased in both streamwise and normal directions with an increase in AR , as seen in the streamline plots shown in Fig. 5.10. The smallest size of the recirculation bubble is seen for $AR = 1$, and the centre of the recirculation bubble (e) for $AR = 1$ is farthest in the streamwise direction while closest to the plate in the normal direction. The distance measured from the rear mirror surface to e reduced with increasing AR until $AR = 1.5$. A further increase in AR increases the distance measured from the rear mirror surface to e in the streamwise (x) direction. In the normal (y) direction, an increase in the AR increases the distance between the plate and e . The location of e in cartesian coordinates is tabulated in Table 5.5 for all the AR cases investigated.

Table 5.5 Comparison of the change in the centre of recirculation bubble (e) and normalised lengths of time-averaged flow features with change in AR

Coordinates	$AR = 1$	$AR = 1.25$	$AR = 1.5$	$AR = 2$	$AR = 2.5$
x/D	1.2	1.07	1.01	1.085	1.12
y/D	0.62	0.67	0.91	1.18	1.52
L_{ws}	$2.36D$	$2.40D$	$2.59D$	$2.97D$	$3.26D$
L_{hz}	$0.39D$	$0.41D$	$0.42D$	$0.43D$	$0.46D$
L_{hx}	$0.27D$	$0.29D$	$0.30D$	$0.26D$	$0.27D$

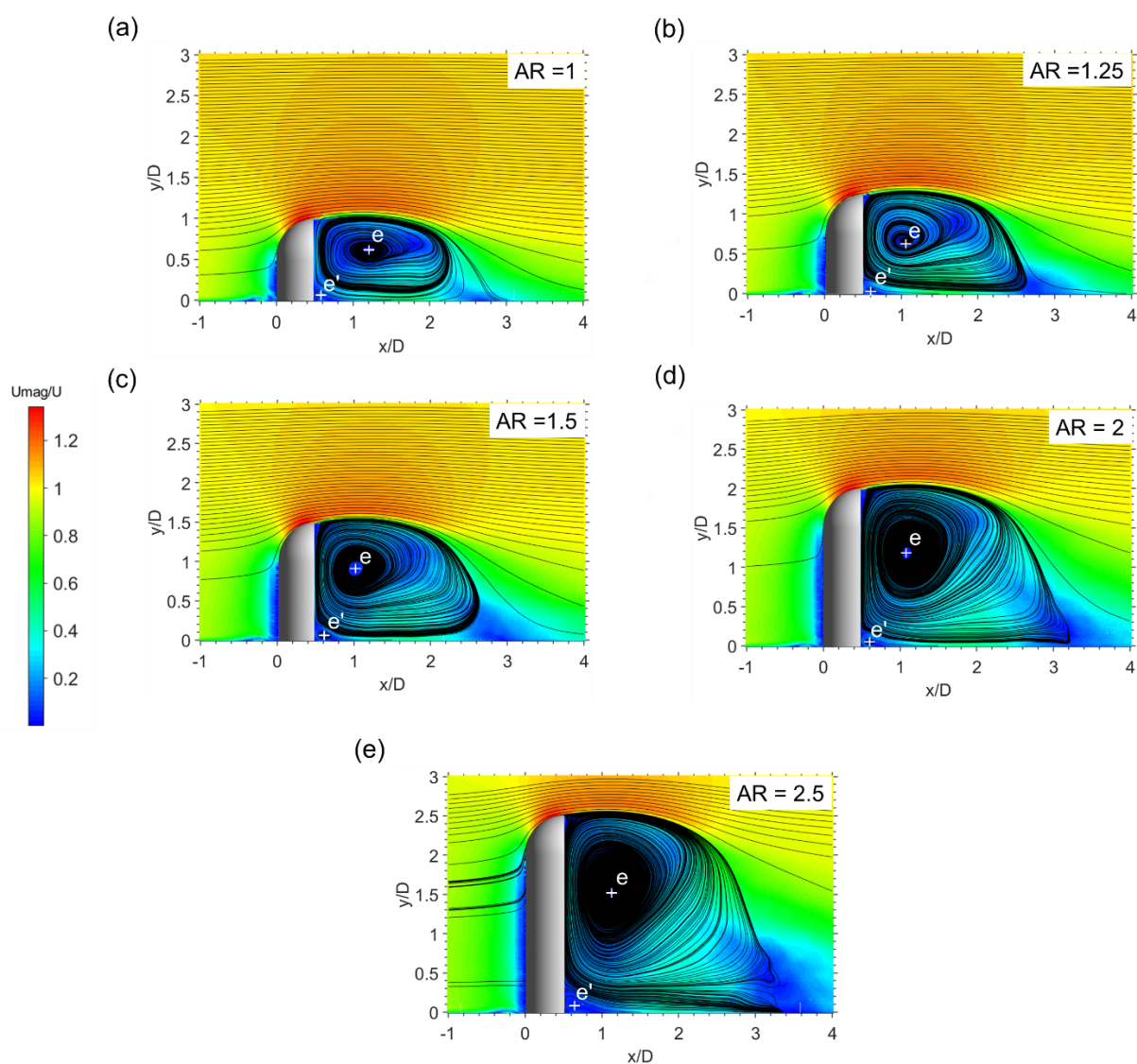


Fig. 5.10. Comparison of time-averaged velocity magnitude contour plots superimposed with velocity streamlines on midplane for a) $AR = 1$, b) $AR = 1.25$, c) $AR = 1.5$, d) $AR = 2$, and e) $AR = 2.5$. e and e' represent the centre of recirculation bubbles formed behind the mirror

The general flow features around the HRM for all the aspect ratios can be visualised using the Q criterion in Fig. 5.11. The Q Criterion is defined as $Q = 0.5(\Omega_{ij}\Omega_{ij} - S_{ij}S_{ij})$, where Ω_{ij} is the rotation and S_{ij} is the strain rate. The two distinct horseshoe vortices can be observed upstream of the mirror as indicated by h_a and h_b shown in Fig. 5.11.

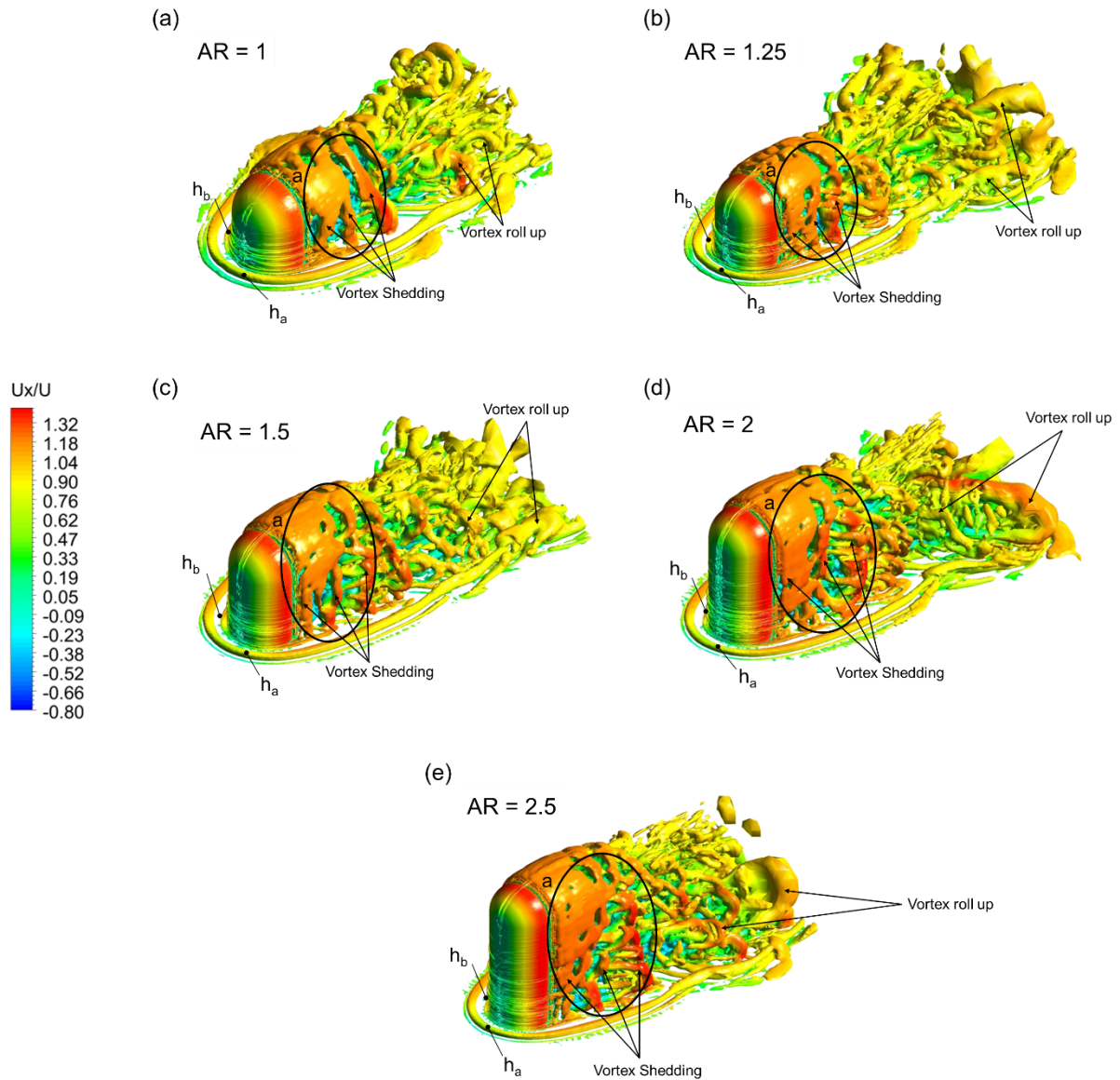


Fig. 5.11. Comparison of vortical structures of an instantaneous flow field visualised by iso-surfaces of $Q = Q = 10^3 \text{ s}^{-2}$ coloured with instantaneous x-velocity for all the investigated for a) $AR = 1$, b) $AR = 1.25$, c) $AR = 1.5$, d) $AR = 2$ and e) $AR = 2.5$.

The coherent structure of the instantaneous flow field shown in Fig. 5.11 suggests that the near-wake region represented by a , increase with an increase in AR . This finding is substantiated by Fig. 5.10, wherein the length of the separation bubble and the width of the horseshoe vortex (time-averaged) appears to increase with AR . Though the increase in near-wake region seems to be linear with increase in AR up to 2.5, however, further increase in the AR may increase the near-wake region similar to cube as evidenced by Wang et al. (2019). A

quantitative comparison of the normalised length (L_{ws}) and the width of the horseshoe vortex (L_{hz}) of the time-averaged wake for all values of AR are presented in Table 5.5. The horseshoe vortex traversing downstream interacts with the shed vortices that tend to roll up into the wake. The roll-up of the vortices shown in Fig. 5.12 increases with an increase in the AR . These flow features induce pressure fluctuations on the plate, which are visualised using normalised pressure fluctuations $NPrms = prms/(0.5\rho U_\infty^2)$ in Fig. 5.12. The $NPrms$ on the plate shown in Fig. 5.12 show two distinct pressure zones P_u and P_d formed due to the lateral vortices seen in region a from Fig. 5.11. The intensity levels at both pressure zones P_u and P_d increase with an increase in AR . The intensity levels predicted at P_u are $\sim 4\%$ higher than those reported at P_d for $AR = 1.5, 2$ and 2.5 , respectively. The size of the pressure zones also increases with an increase in the AR , as shown in Fig. 5.12.

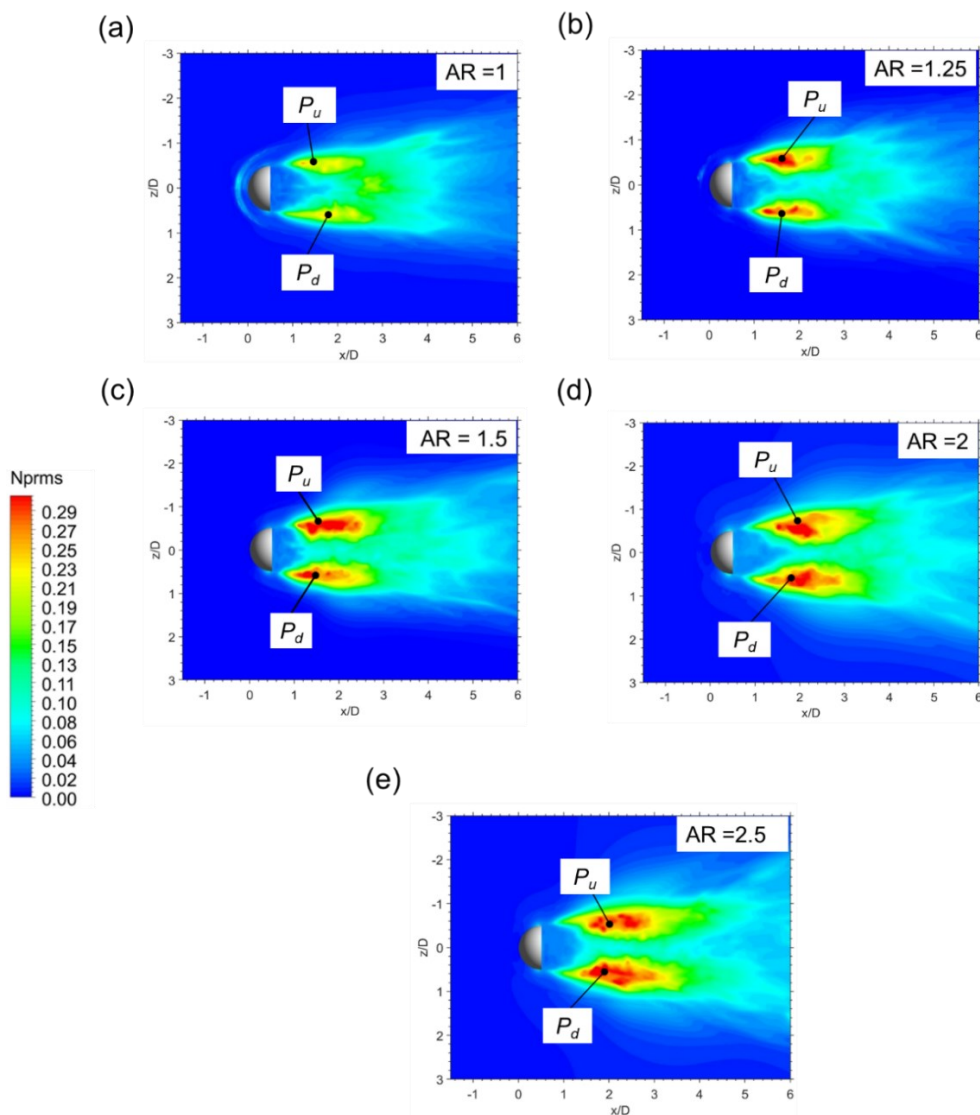


Fig. 5.12. Comparison of normalised pressure fluctuations on the plate between a) $AR = 1$, b) $AR = 1.25$, c) $AR = 1.5$, d) $AR = 2$, and e) $AR = 2.5$. Here P_u and P_d indicate the pressure zone formed due to the interaction of the lateral vortices with the plate.

The trend in pressure fluctuations generated on the mirror and closer to the plate at s111 and s113 indicates the intensity levels are lower for $AR = 2.5$, shown in Fig. 5.13. However, moving downstream, the intensity of the hydrodynamic pressure fluctuations increases for $AR = 2.5$, as shown in Fig. 5.14. This trend agrees well with the overall pressure distribution on the plate, as shown in Fig. 5.12. The microphone data shown in Fig. 5.15 for $AR = 2.5$ show a distinct peak at $\sim 36\text{Hz}$ in the frequency spectra plotted for all the microphone locations, while no such peaks are predicted in other AR cases.

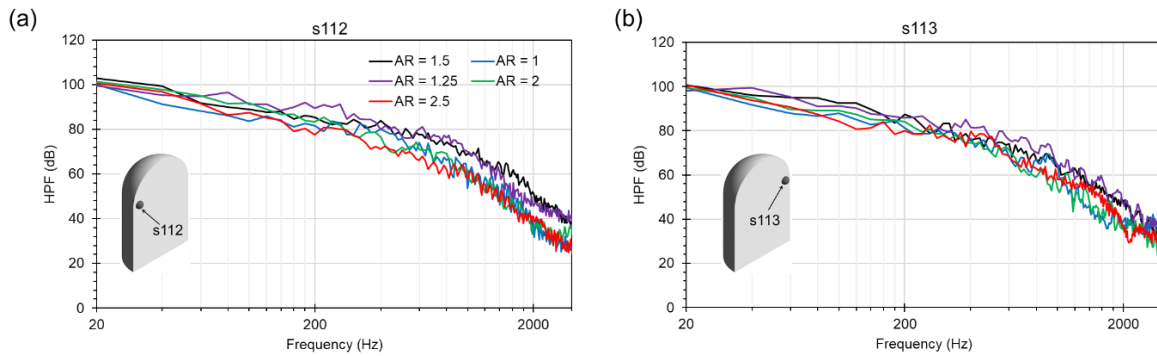


Fig. 5.13. Comparison of HPF extracted on the mirror at a) s112 and b) s113 between $AR = 1, 1.25, 1.5, 2$ and 2.5 . The sensor's location is represented by a black dot in the schematic shown in the plots.

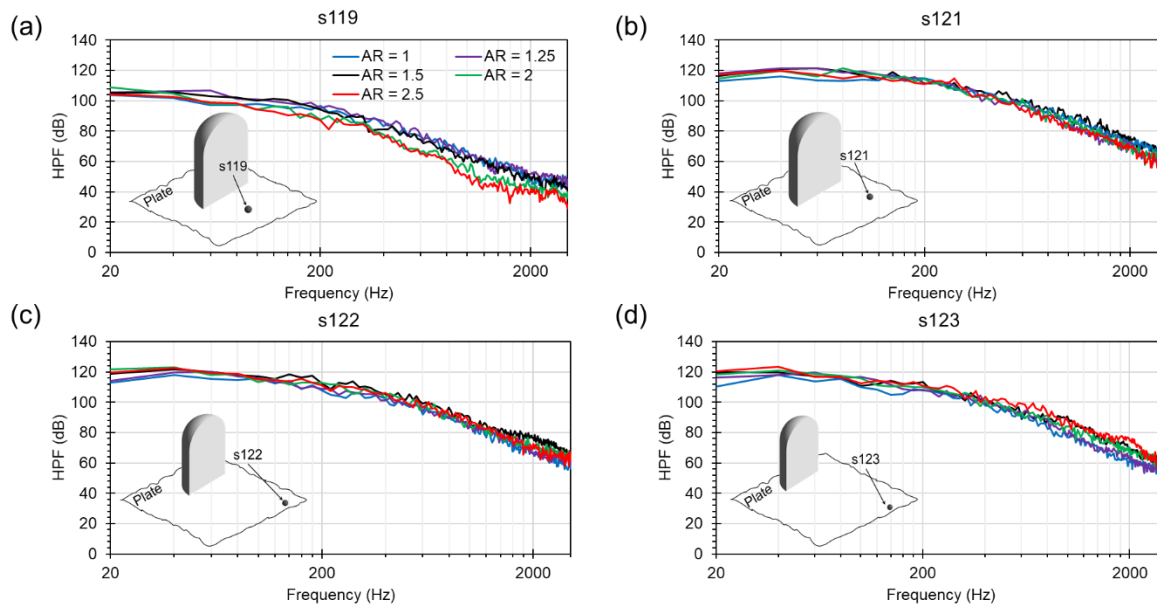


Fig. 5.14. Comparison of HPF extracted on the mirror at a) s119, b) s121, c) s122, and d) s123 between $AR = 1, 1.25, 1.5, 2$ and 2.5 . The sensor's location is represented by a black dot in the schematic shown in the plots.

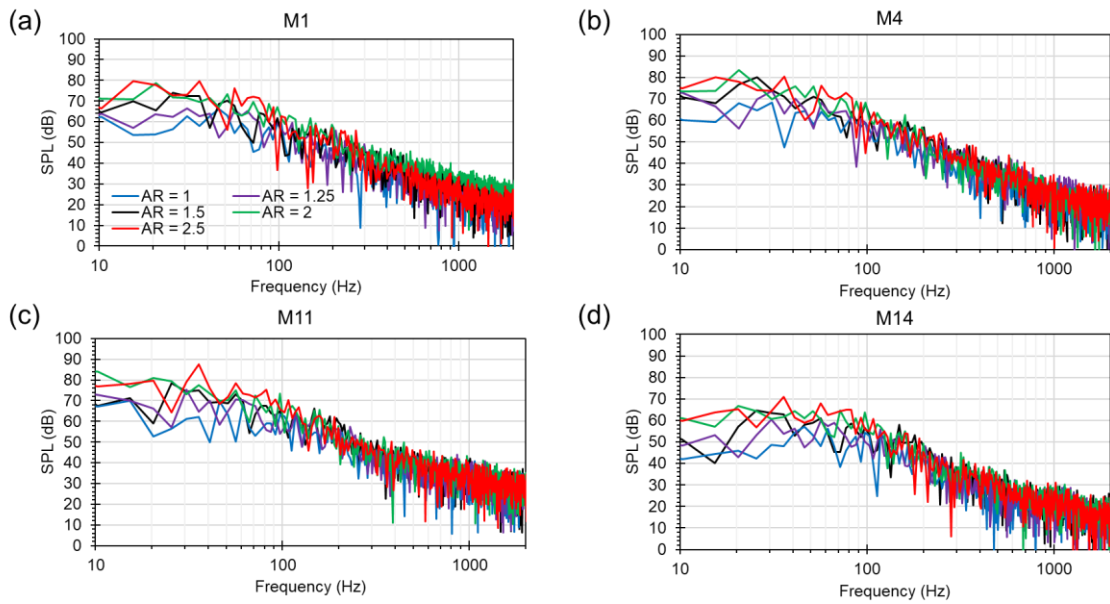


Fig. 5.15. Comparison of SPL extracted at four microphone positions: a) M1, b) M4, c) M10, and d) M14 between AR = 1, 1.25, 1.5, 2 and 2.5.

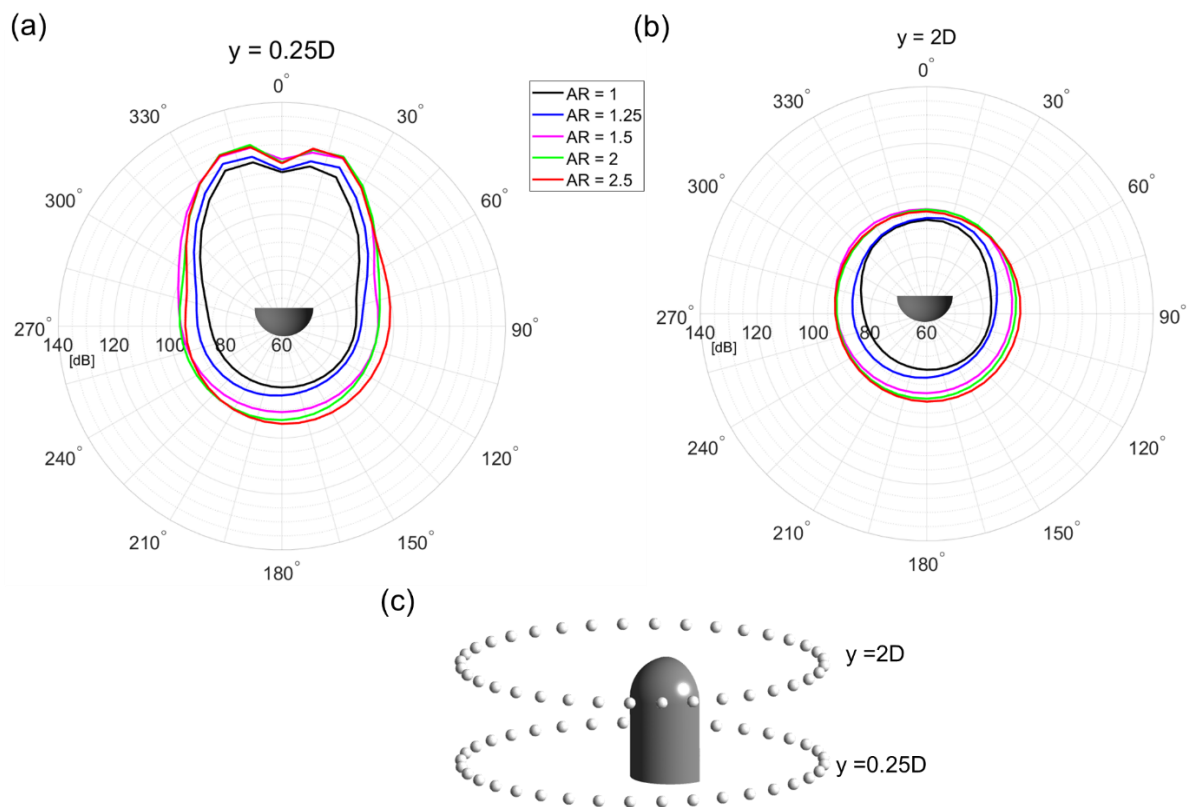


Fig. 5.16. The overall sound pressure level extracted at several microphones placed in a circular array at planes a) $y = 0.25D$ and b) $y = 2D$ plate are compared for AR = 1, 1.25, 1.5, 2 and 2.5 investigated, and c) illustrates the planes at which the directivity are plotted

The structure of the emitted noise is identified by plotting directivity using the Overall Sound Pressure Level (OASPL) at two planes, $y = 0.25D$ and $y = 2D$, as shown in Fig. 5.16. Each plane consists of 36 microphones placed in a circular array around the mirror with radius

of , as illustrated in Fig. 5.16(c). The structure of the emitted noise at $y = 0.25D$ is dipole-like, indicating that the induced noise has contributions from both the plate and the mirror. On the other hand, at $y = 2D$, the directivity plot shows a monopole-like structure. A decrease or increase in the AR indicates a negligible change in the overall structure of the emitted noise at both planes. From the perspective of a standard mirror with $AR = 1.5$, the numerical results predict that an increase in AR tends to increase the radiated noise, whereas a reduction in AR tends to reduce the same.

5.6. Effect of sweep angle (θ) on the flow and noise radiated by HRM

The HRM is swept towards the plate to make a series of swept cases with 8° increments. The maximum sweep angle (θ) used in this study is 32° . For $\theta = 0^\circ$ and 8° , the flow separates from the lateral edges of the HRM, as seen in Fig. 5.17 (a, b). At the same time, the flow separates from the top of the HRM for the $\theta = 16^\circ$, 24° and 32° cases as shown in Fig. 5.17(c,d). The streamwise length of the separated flow from the upper trailing edge of the HRM increases for 24° and 32° compared to $\theta = 16^\circ$. In Fig. 5.18, the centre of the recirculation bubble (e) tends to move downstream in a streamwise direction and decreases in the normal direction with an increase in θ . The location of the centre of the recirculation bubble for all θ is tabulated in Table 5.6. The length of the recirculation bubble formed behind the HRM reduces with the change in θ , and the width of the horseshoe vortex reduces with an increase in θ , as indicated by L_{ws} and L_{hx} , respectively shown in Table 5.6. As a result, a change in reattachment location can be observed with a change in θ , as shown in Fig. 5.18.

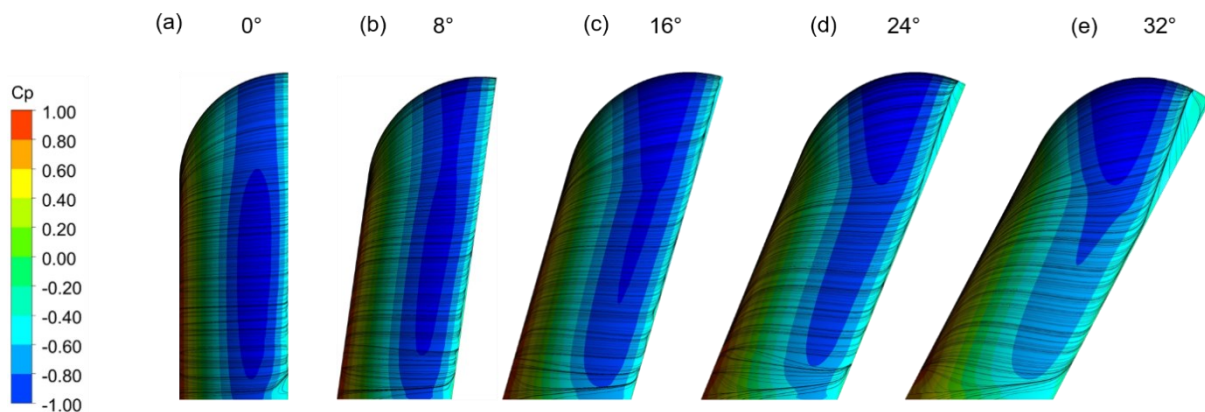


Fig. 5.17. Comparison of the flow separation between a) $\theta = 0^\circ$, b) $\theta = 8^\circ$, c) $\theta = 16^\circ$, d) $\theta = 24^\circ$, and $\theta = 32^\circ$ represented by friction lines superimposed on the contours of time-averaged pressure coefficient.

Table 5.6 Comparison of the change in the center of recirculation bubble (e) and normalised lengths of time-averaged flow features with change in θ

Coordinates	0°	8°	16°	24°	32°
x/D	1.01	1.105	1.23	1.305	1.455
y/D	0.91	0.78	0.72	0.65	0.55
L_{hx}	$0.30D$	$0.28D$	$0.21D$	$0.18D$	$0.13D$
L_{hz}	$0.42D$	$0.41D$	$0.40D$	$0.38D$	$0.34D$
L_{ws}	$2.59D$	$2.56D$	$2.39D$	$2.38D$	$2.36D$

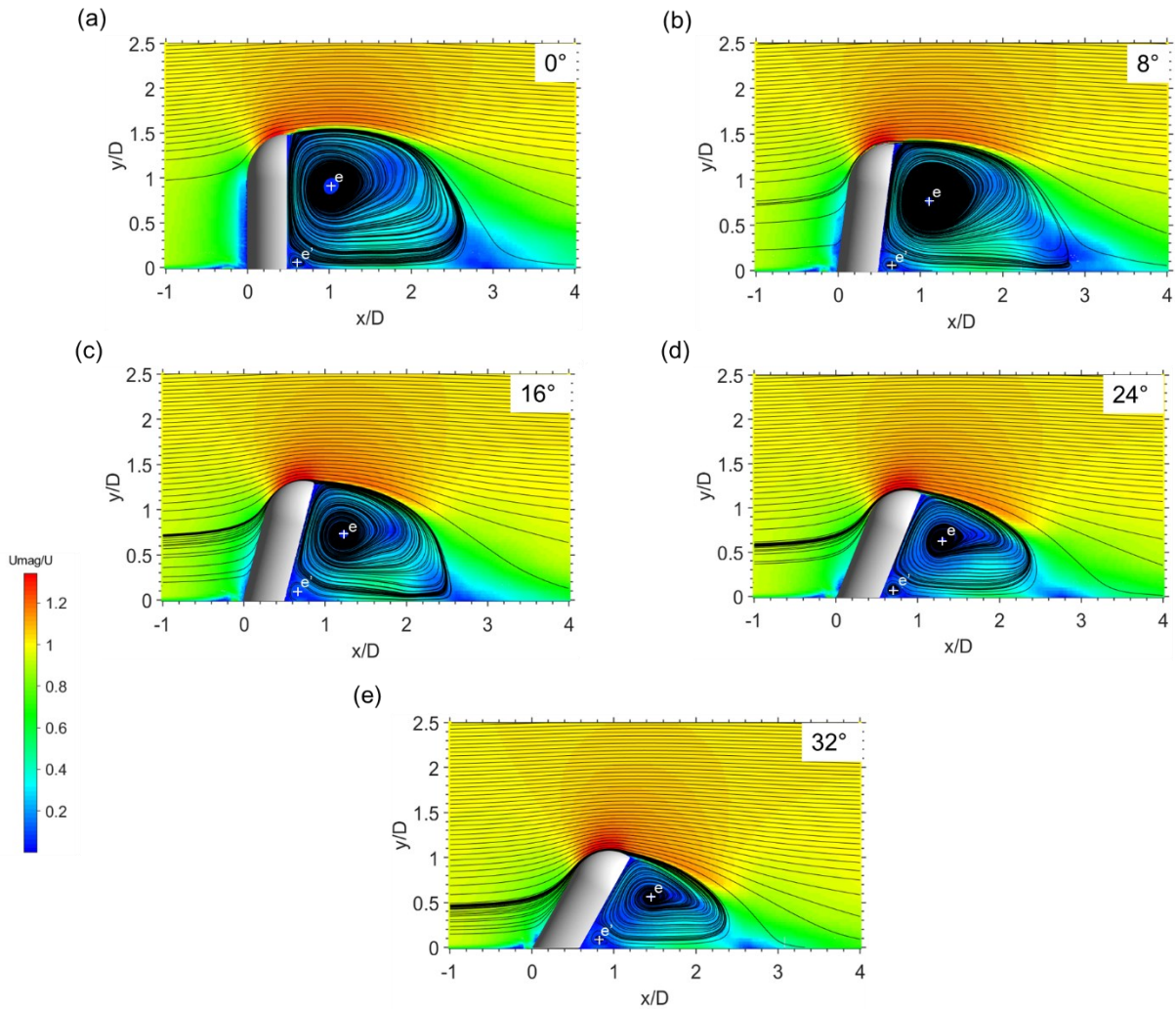


Fig. 5.18. Comparison of time-averaged velocity magnitude contour plots superimposed with velocity streamlines on midplane for a) $\theta = 0^\circ$, b) $\theta = 8^\circ$, c) $\theta = 16^\circ$, d) $\theta = 24^\circ$, and e) $\theta = 32^\circ$. e and e' represent the centre of recirculation bubbles formed behind the mirror.

Upstream of the mirror, the dominant flow feature is the formation of two distinct horseshoe vortices, h_a and h_b , for 0° and 8° , as seen in Fig. 5.19(a,b). The vortex h_b vanishes for larger

values in θ , and the formation of a secondary horseshoe vortex h'_a can be seen at 8° (Fig. 24b), which grows with higher values of θ . The presence of h'_a upstream of the HRM is visualised using the Q criterion, as shown in Fig. 5.20. These results predict that the horseshoe vortex originating from the upstream region to the side of the HRM moves closer to the mirror with the increase in θ as observed in Fig. 5.20. L_{hx} further substantiates the observation made in Table 5.6. The horseshoe vortices h_a and h'_a tend to roll up and merge into the wake as seen in $\theta = 8^\circ$ marked by region b , and with the increase θ , the roll-up of the vortex grows, resulting in the formation of two distinct vortex structures in the wake (w and w') as shown in Fig. 5.21. The near-wake region represented by a in Fig. 5.21 reduces in length with an increase in θ , the decrease in the near-wake region is due to a decrease in the length of the recirculation bubble as seen in Fig. 5.18.

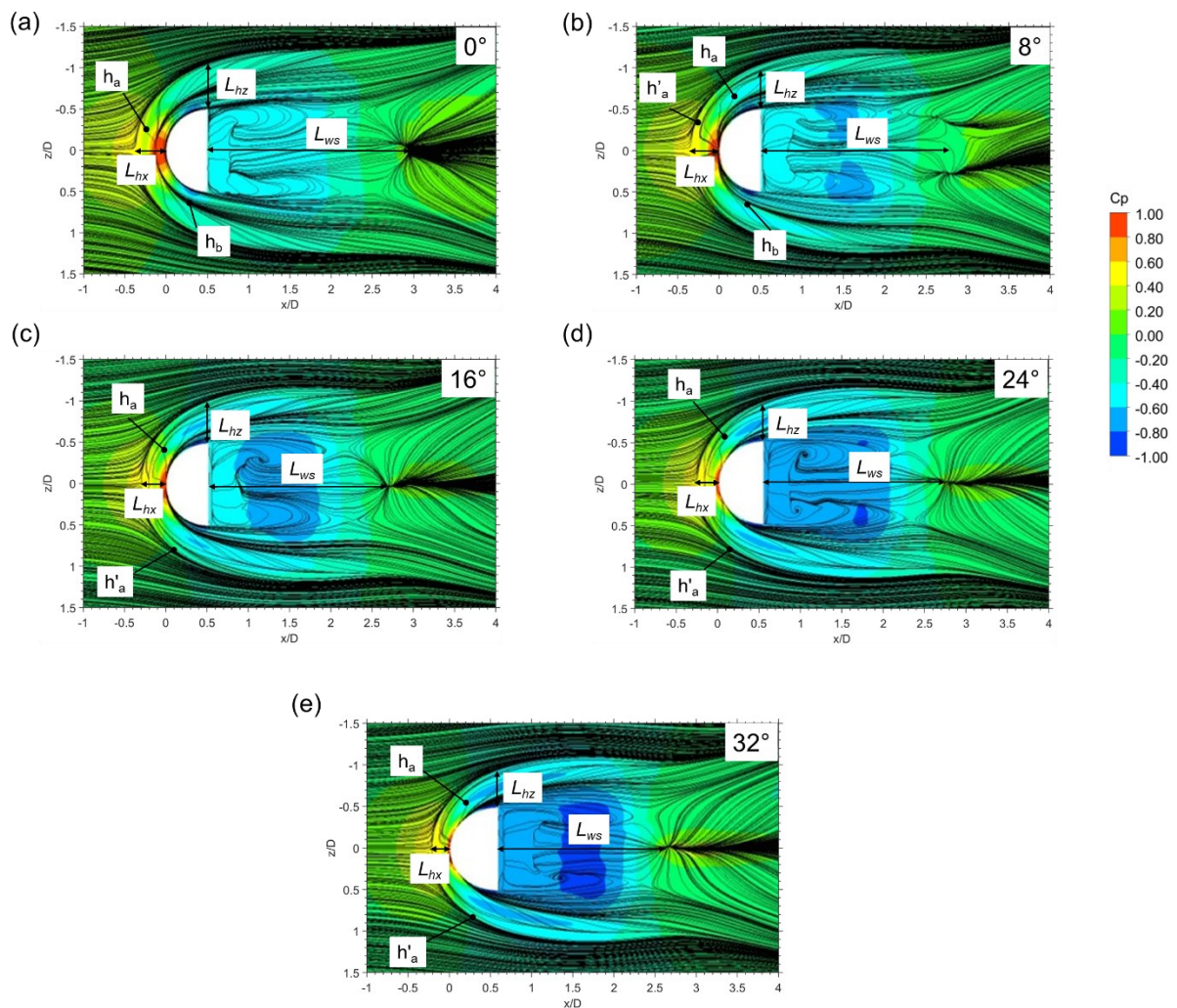


Fig. 5.19. Comparison of time-averaged velocity magnitude streamlines superimposed on pressure coefficient generated on a plane at $y = 0.01D$ between all the sweep angles investigated: a) $\theta = 0^\circ$, b) $\theta = 8^\circ$, c) $\theta = 16^\circ$, d) $\theta = 24^\circ$, and e) $\theta = 32^\circ$.

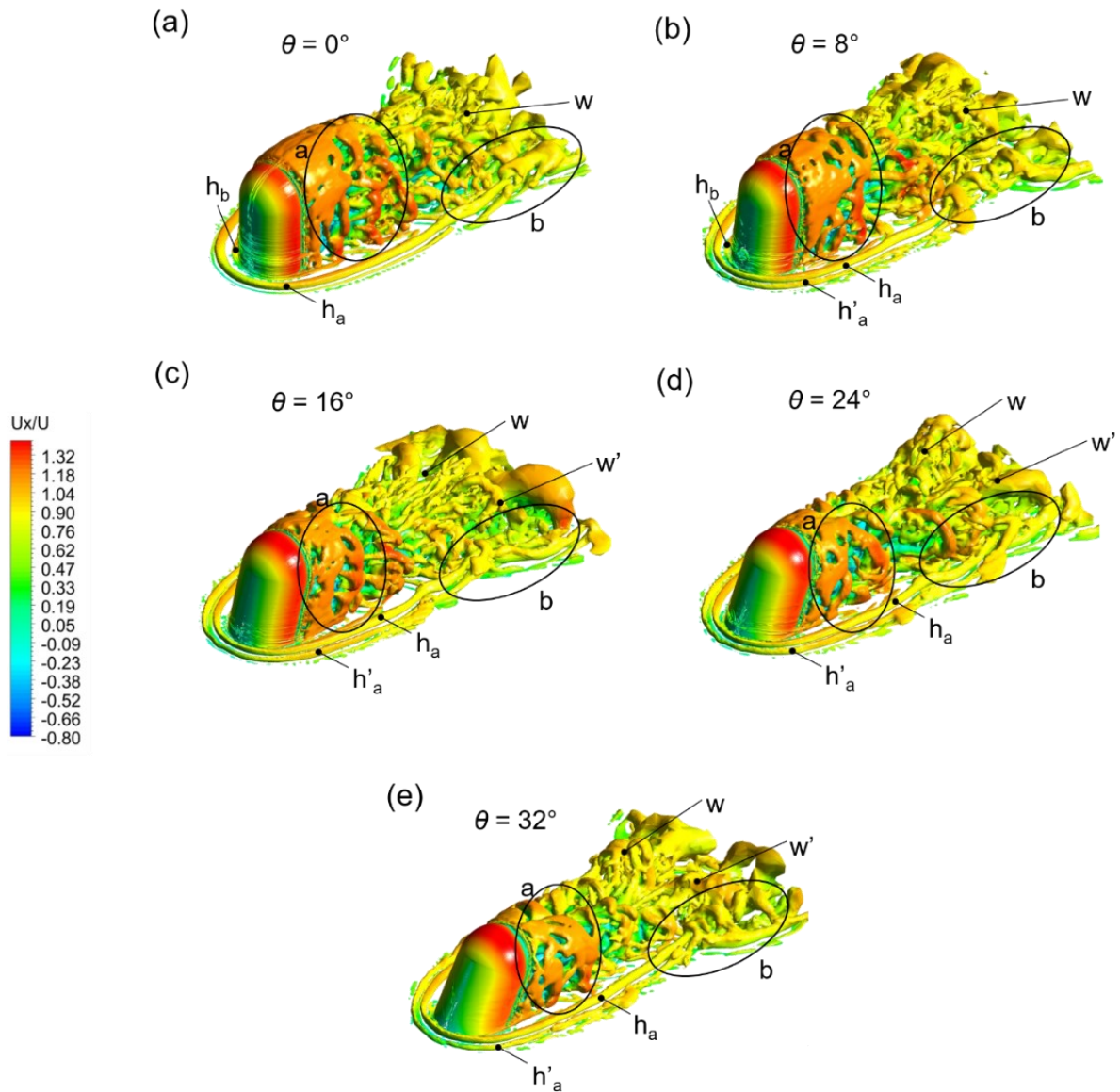


Fig. 5.20. Comparison of vortical structures of an instantaneous flow field visualised by iso-surfaces of $Q = 10^3 \text{ s}^{-2}$ coloured with instantaneous x-velocity between all the sweep angles investigated: a) $\theta = 0^\circ$, b) $\theta = 8^\circ$, c) $\theta = 16^\circ$, d) $\theta = 24^\circ$, and e) $\theta = 32^\circ$.

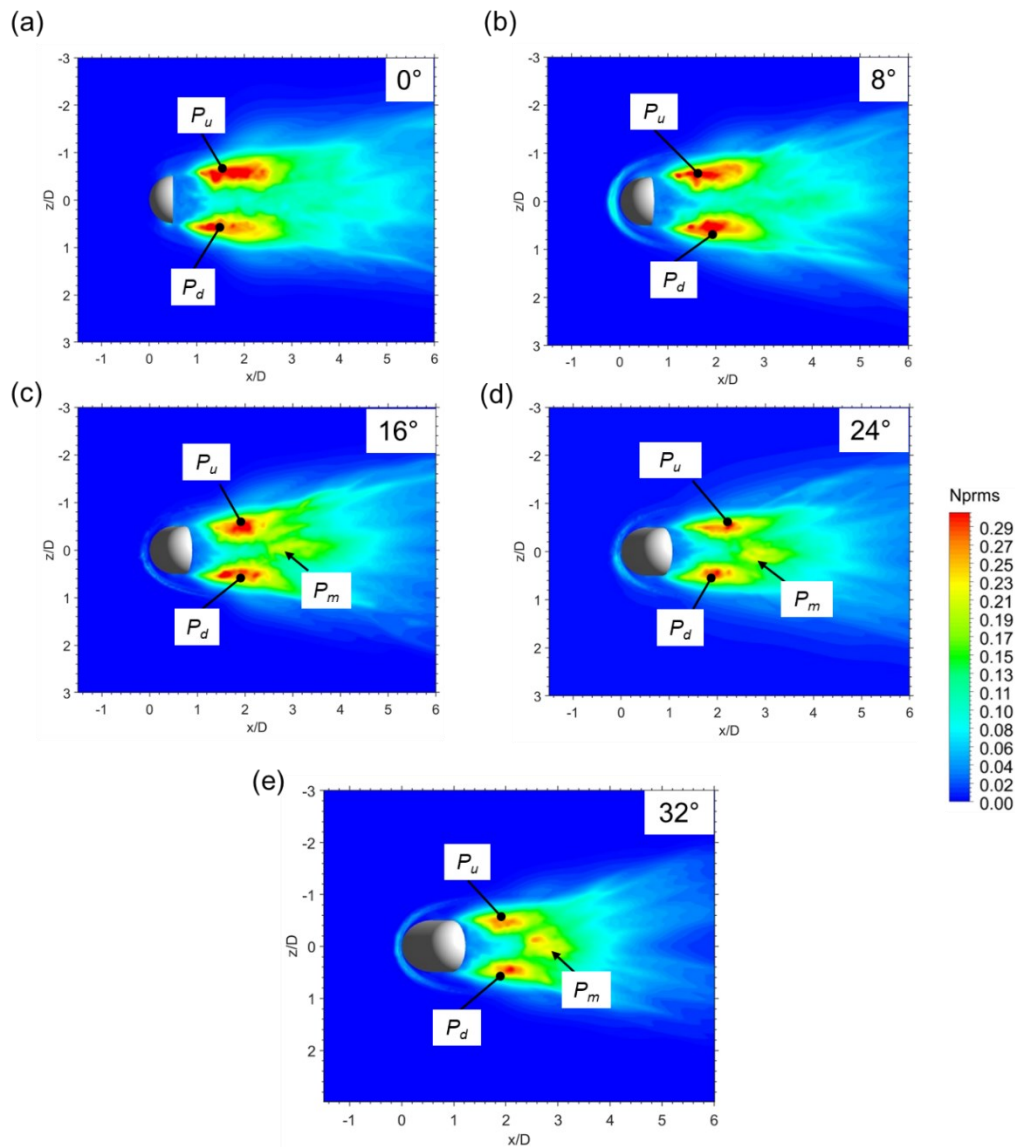


Fig. 5.21. Comparison of time-averaged normalised pressure fluctuations on the plate for all the sweep angles investigated: a) $\theta = 0^\circ$, b) $\theta = 8^\circ$, c) $\theta = 16^\circ$, d) $\theta = 24^\circ$, and e) $\theta = 32^\circ$. P_u and P_d represent the pressure regions formed due to the lateral vortex, and P_m represents the pressure region formed due to the impingement of the flow.

The sensors located on the mirror at s111 and s114 show a maximum reduction of ~ 5 dB at the vortex shedding frequency (~ 40 Hz) with the increase in θ from the standard HRM configuration (0°) as shown in Fig. 5.22, with $\theta = 24^\circ$ reporting the lowest intensity levels in both low and mid-frequency ranges. A similar trend is observed at s119 located on the plate, but moving downstream to sensors s120, s122, and s123 (Fig. 5.23), the intensity levels are lowest for the $\theta = 32^\circ$. The radiated noise measured at all four different microphone locations indicates a decrease in the SPL for $\theta = 32^\circ$, as seen in Fig. 5.24.

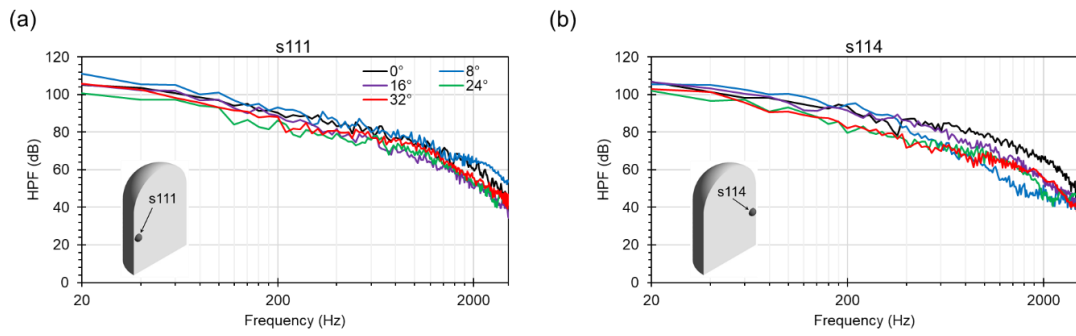


Fig. 5.22. Comparison of HPF extracted on the mirror at a) s111 and b) s114 for all the sweep angles investigated: 0°, 8°, 16°, 24° and 32°.

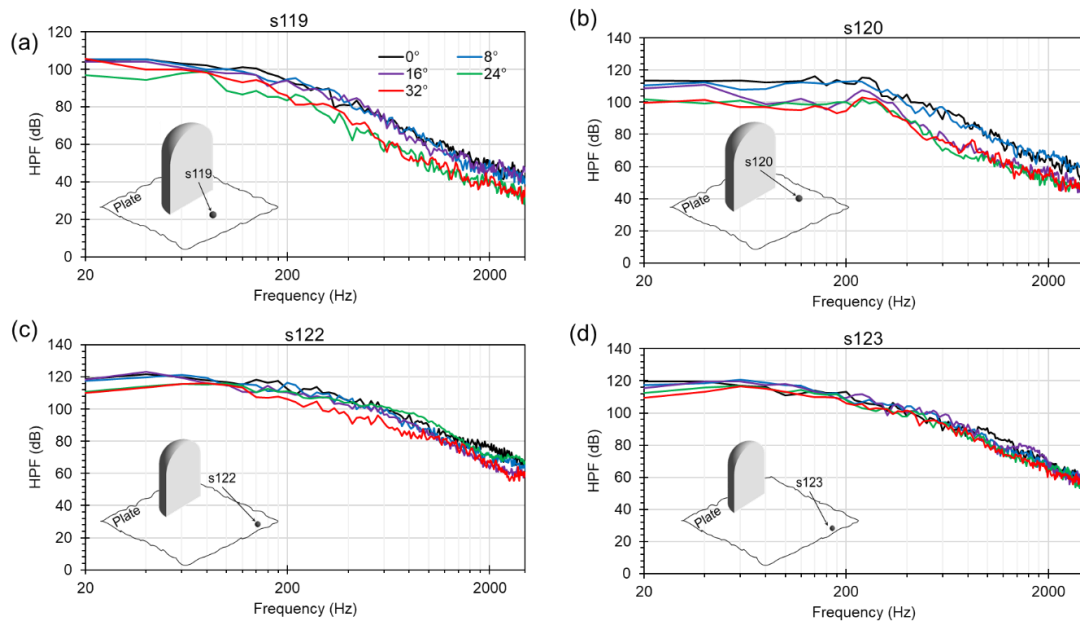


Fig. 5.23. Comparison of HPF extracted on the plate at a) s119, b) s120, c) s122 and d) s123 for all the sweep angles investigated: 0°, 8°, 16°, 24° and 32°.

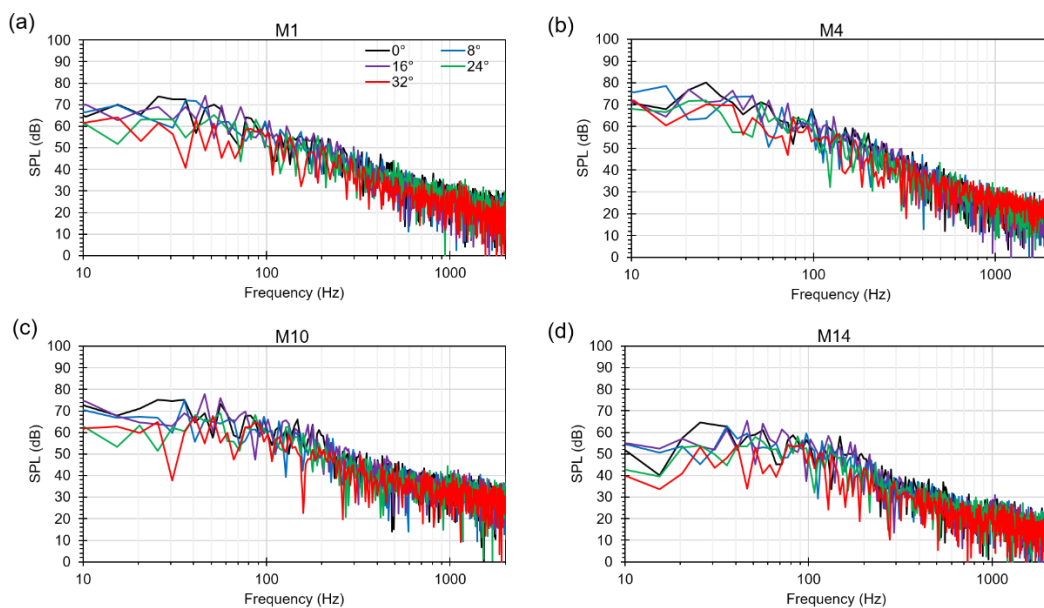


Fig. 5.24. Comparison of SPL at four microphone positions a) M1, b) M4, c) M10, and d) M14 for all the sweep angles investigated: 0°, 8°, 16°, 24° and 32°.

The radiated noise closest to the plate shown at $y = 0.25D$ in Fig. 5.31 resembles a dipole-like structure for all the angles investigated in this study. However, away from the plate, at $y = 2D$, the noise radiated resembles a monopole-like structure. This suggests a dipole-to-monopole transition in the structure of the induced noise that takes place closest to the plate and regions further away from the plate for all the cases investigated in the study. Also, the intensity levels of the induced noise decrease with an increase in θ .

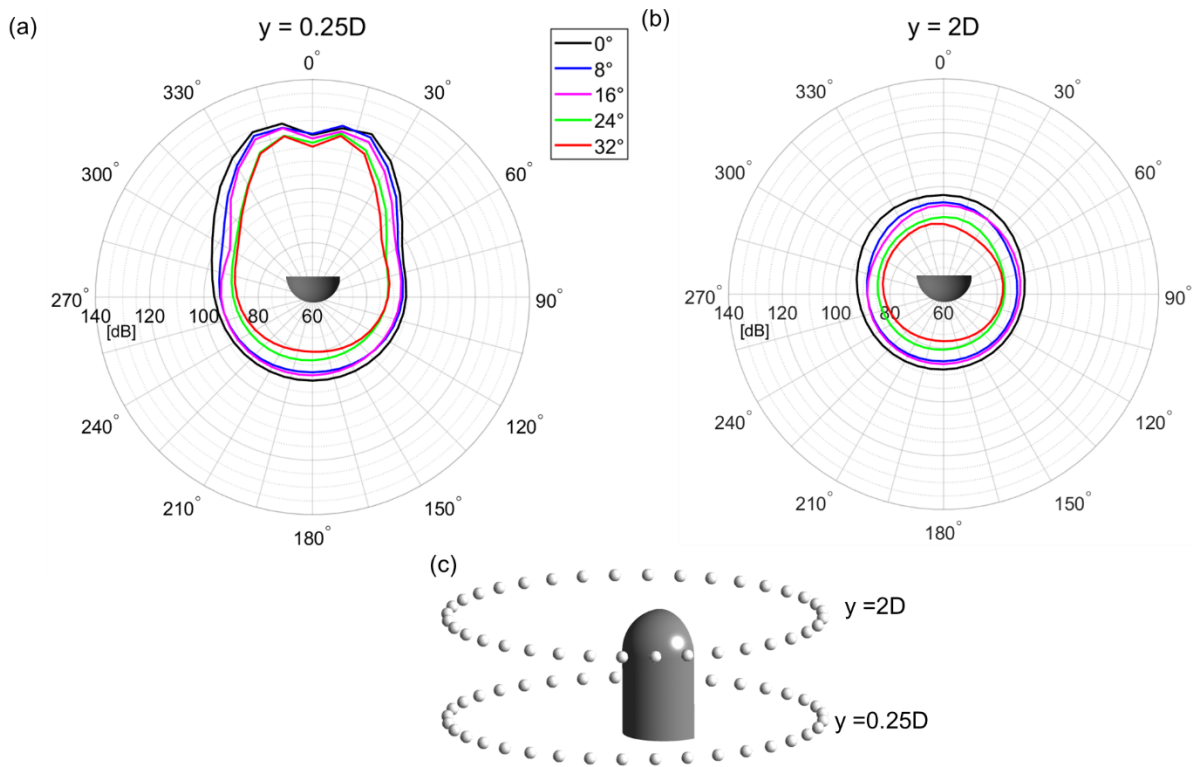


Fig. 5.25. Comparison of overall sound pressure level extracted at 36 microphones placed in a circular array at planes a) $y = 0.25D$ and b) $y = 2D$ for all the sweep angles investigated: 0° , 8° , 16° , 24° and 32° , and c) illustrates the layout of the sensors located.

Summary

In this chapter, the effect of the aspect ratio and sweep angle on the flow past a standard HRM and the noise radiated is investigated numerically using a hybrid CAA approach. The detailed flow features, fluctuating pressure distributions on the plate and mirror, and noise radiated in the vicinity were obtained and compared against both experimental and numerical data obtained from the literature presented in **Chapter 2**, thereby achieving the second aim presented in **Chapter 1**.

- The hybrid CAA method based on SBES and FW-H provided a reasonable agreement with experiment and numerical data. Extending the same methodology for structured grids where the predictions between structured and unstructured grids are found to be

negligible. Therefore, SBES and FW-H can potentially be used for aeroacoustics of full vehicle cases.

- For the AR cases, the overall noise radiated increases with an increase in AR from the standard configuration.
- For Sweep cases, the overall noise radiated decreases with an increase in sweep angle as the flow appears to separate more from the mirror as the sweep angle increases.
- Change in AR and sweep angles (θ) may not necessarily affect the overall structure of the induced noise. However, the overall SPL levels of the induced noise can vary depending on the configuration of the HRM.
- The radiated noise primarily depends on the pressure footprint on the mirror and the mounting surface.

Based on the methodology proposed in **Chapter 5**, the noise radiated from a full-scale simplified vehicle is carried out in **Chapter 6**, and the noise mitigation strategies are assessed for a full-scale vehicle body.

Chapter 6

Noise radiation from a standard vehicle and its mitigation

In **Chapter 5**, the hybrid CAA methodology based on the SBES and FW-H has shown to accurately predict both flow characteristics and radiated noise. The isolated case study of a standardised side-view mirror mounted on the plate showed that the radiated noise is influenced by both aspect ratio and inclination angle of the mirror. The maximum reduction in noise radiated is shown to be achieved by inclining the mirror. However, the evaluation of employing such noise mitigation techniques to side-mirror requires the simulation of the complete vehicle model to account for the changes in the upstream flow due to additional geometrical features present on a full vehicle model. Consequently, the complexity of the geometry increases rapidly, and the methodology used in both **Chapter 4** and **5** for generating the grid has to be modified to account for the complexity of the geometry. Therefore, a grid independent study and a validation study must be conducted for a vehicle model that represents features of an idealized production car.

In this chapter, the aforementioned CAA-methods are validated based on the flow past a full-scale standardized vehicle model. This model is a variant of the SAE reference model that is used in **Chapter 4**. The model in this chapter, is a full-scale SAE reference square-back body (SAE T4) with a standardised mirror geometry representing a square cylinder with a characteristic length ($l_c = 0.08$ m) mounted on one side of the body perpendicular to the surface, as shown in Fig. 6.1(a).

6.1. Geometry description and computational domain

The SAE squareback body was mounted on four struts with a height of $y/H = 0.14$. A freestream velocity $U_\infty = 27.78$ m/s, which corresponds to a Reynolds number $Re_L = 7 \times 10^6$ based on the length (L) of the SAE reference body which is identical to the experimental setup used by Nusser (2019) and Müller et al. (2013). Also, the pressure sensor probed on the side window shown in Fig.1(c) is identical to the experimental study. The computational domain is $12 L \times 3.6 L \times 3.6 L$, where L represents the length of the vehicle ($L = 3.76$ m) shown in Fig. 6.2 and the computational domain is defined based on ERCOFTAC guidelines adapted from the previous studies conducted (Islam et al., 2008a). The blockage ratio with the domain cross-section was $\sim 1.5\%$. The inlet was located at a distance of $3 L$ from the origin located at the centre of the nose end of SAE T4, and a uniform velocity condition was imposed on the inlet with a turbulent intensity of 0.1% . A constant zero-pressure outlet located at $12 L$ was applied

to the outlet. The walls surrounding the domain in the spanwise and normal directions were set as symmetrical, and a no-slip boundary condition was applied to both SAE T4 and the ground. The walls surrounding the domain in the spanwise and normal directions were set as symmetrical, and a no-slip boundary condition was applied to both the SAE squareback and the ground.

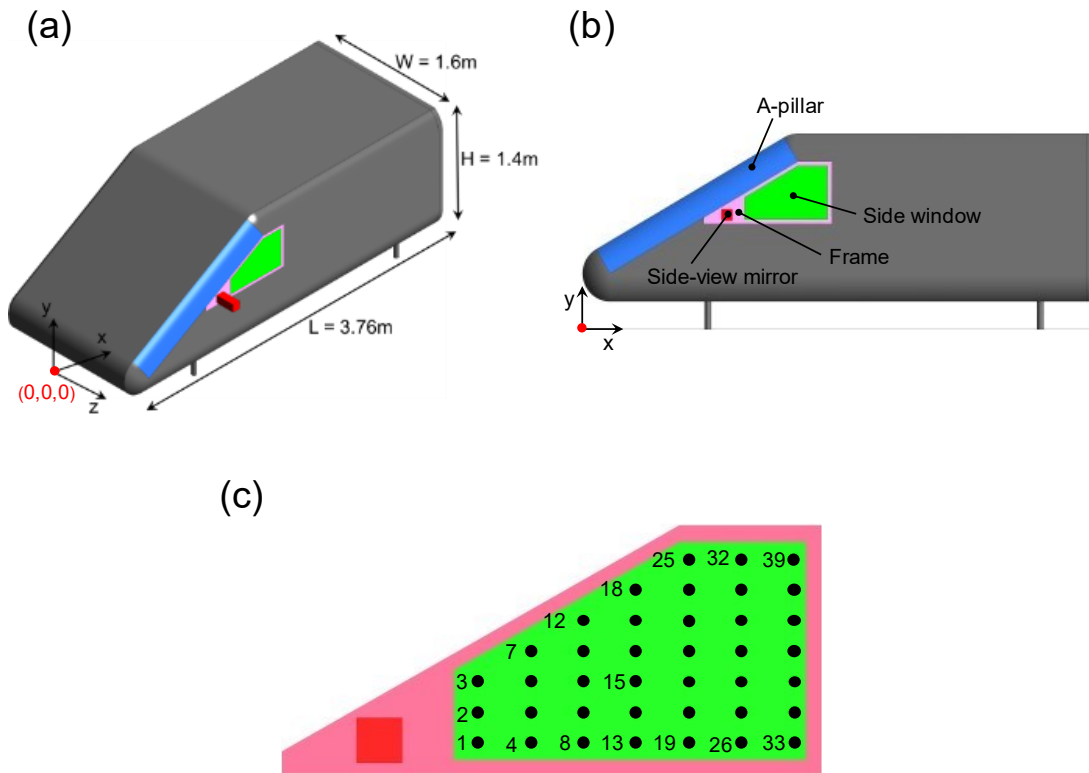


Fig. 6.1. a) SAE Reference squareback (SAET4) model with a bluff mirror mounted in the positive spanwise direction; b) naming conventions used for SAE T4 design features; c) schematic representation of surface pressure probe locations on the side window.

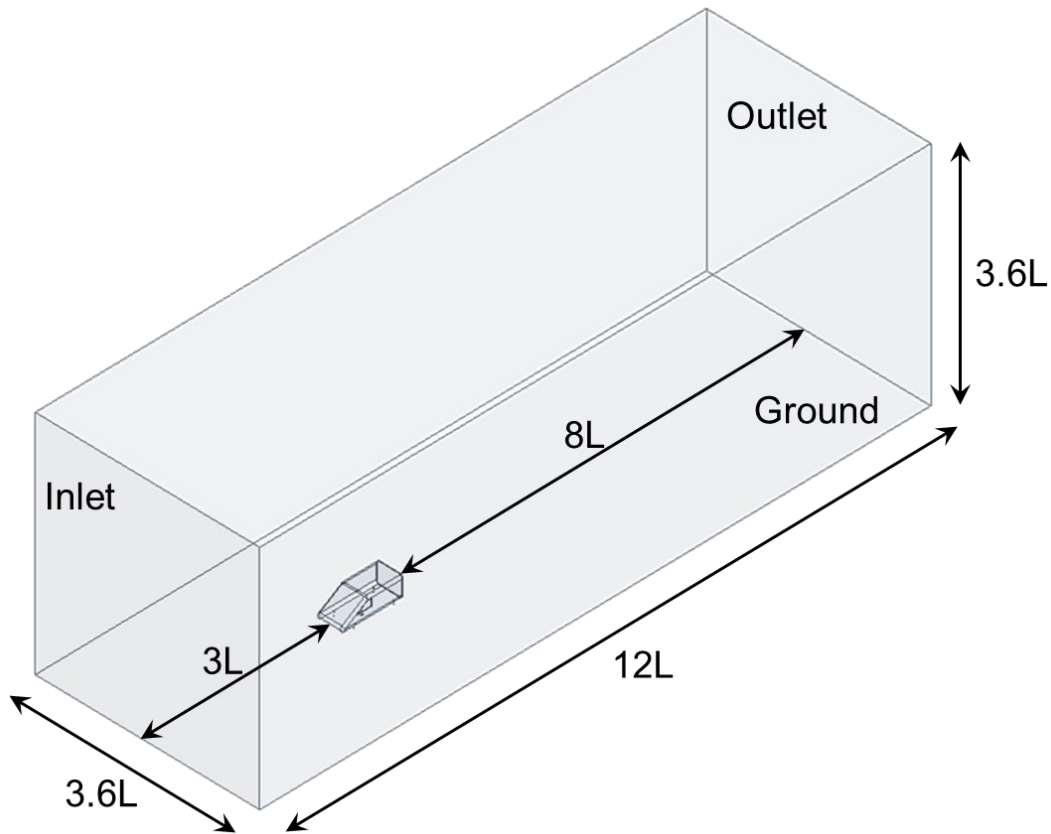


Fig. 6.2. Overview of computational domain with boundary conditions used in this study.

6.2. Grid generation and Numerical Setup

In this study, a poly hex core unstructured grid was used and generated using the ANSYS Mosaic meshing methodology similar to the grid used in **Chapter 5**. The grid sizes are calculated using the same strategy as shown in **Chapter 4**. The numerical schemes used in this chapter is derived from **Chapter 5** expect for the time step used. For this simulation, the total runtime was 0.65s. The unsteady simulation was run in three phases: in the first phase, a time step of 1×10^{-4} s was used for the first 0.3s after which the time step was changed to 2.5×10^{-5} s for the next 0.05s to flush out any instability induced by the change in the time step and to ensure that the residual error for the momentum and turbulent equations reached below 1×10^{-6} . The use of two different time steps reduces the computational expense; however, the residual drop is ensured to be less than 1×10^{-6} for all quantities. In the final phase, the time-step was changed to 2.3×10^{-5} s for the next 0.3s to collect time-averaged data. Along with the time-averaged flow data, the pressure fluctuations on the side-view mirror, A-pillar, Frame, and side window were recorded at every time step for the last 0.3s which is later used as an input for the FW-H acoustic analogy.

A grid independency study is conducted using three grids to find an optimal mesh that can be used to validate and verify the results presented in this chapter. For further details of the grid independence study the readers are referred to published work of Chode et al. (2023).

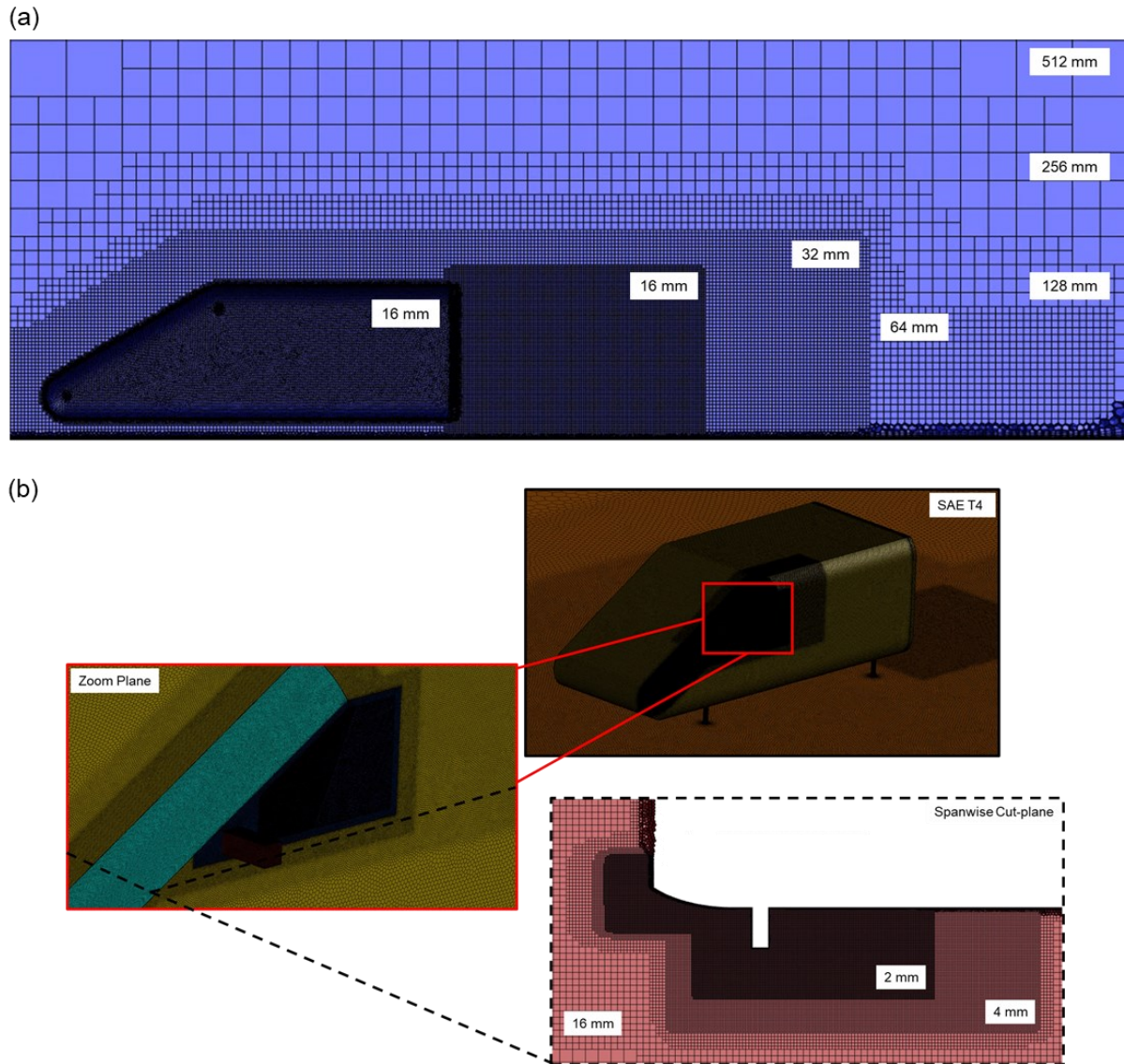


Fig. 6.3. a) Overview of a medium grid with local refinement zones used for validation study, b) grid generated closer to forebody, side window (zoom plane), and spanwise cut plane.

6.3. Comparison of current results against previously published results

The flow visualisation obtained from the SBES prediction is compared with the experimental data presented by (Müller et al., 2014) using the wall shear stress distribution on the surface of the SAE T4, as shown in Fig. 6.4. The SBES predicts the horseshoe vortex formed in front of the side-view mirror and the interaction between the flow past the A-pillar and horseshoe vortex. The location and dimensions of the flow interaction and horseshoe vortex are observed to be in good agreement with the experimental data.

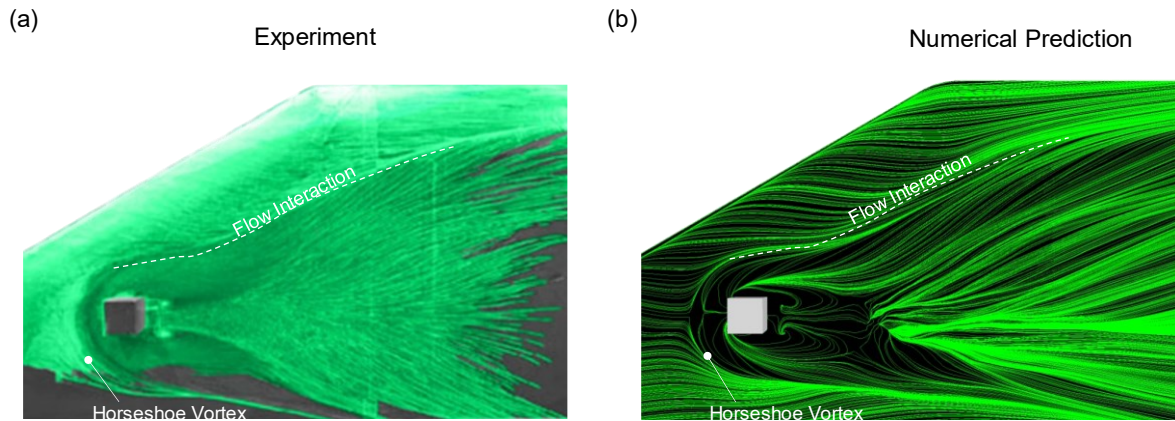


Fig. 6.4. Comparison of flow patterns on the side of SAET4 a) experimental data (Müller et al., 2014)⁹ and b) numerical prediction obtained from the SBES.

As the flow patterns are in good agreement, a comparison is made between the hydrodynamic pressure fluctuations exerted on the side window using the RMS of the surface pressure fluctuations p' . The predicted overall RMS agrees well with the experimental results. At 150 Hz and 500 Hz, the amplitudes of the pressure fluctuations are qualitatively in reasonable agreement with the experiment in reasonable agreement, but the amplitude levels and locations are different in the highlighted regions in Fig. 6.5(b) and (c). As the frequency increases the pressure fluctuations exerted by the A-pillar flow are dampened (see highlighted region *a* in Fig 6.5(b) and(c)). Therefore, the influence of A-pillar pressure fluctuations on the side window is limited to low-frequency ranges, and a similar observation is made by Nusser (2019) when comparing the numerical results with experiments.

A quantitative comparison is made between the predicted and measured hydrodynamic pressure fluctuations (HPF) as the flow patterns around the side window are in good agreement with the experimental results (See Fig. 6.6). The HPF was measured at two probe positions where the experiments indicated the presence of aeolian tones at 40 Hz and 80 Hz in Pos1, while in Pos15, the tonal peak was located at 40 Hz and no peak was evident at 80 Hz. The peaks in the experiments correspond to a Strouhal frequency of 40 Hz for the side-view mirror ($St \approx 0.116$), and the Strouhal frequency is obtained from Eq. 6.1, which corresponds to St of a square cylinder. The numerical results also indicated tonal peaks at the same frequency, as shown in Fig. 6.6. However, the intensity of the HPF predicted for the tonal peaks shows a difference of a maximum of 3-5 dB.

⁹ Adapted and reused with permission from Müller, S., Becker, S., Gabriel, C., Lerch, R. and Ullrich, F., 2014. Flow-Induced Airborne and Structure-Borne Noise at a Simplified Car Model. In *New Results in Numerical and Experimental Fluid Mechanics IX: Contributions to the 18th STAB/DGLR Symposium*, Stuttgart, Germany, (pp. 353-361). Copyright 2012 © Springer International Publishing.

$$St = \frac{f \cdot l_c}{U_\infty} \quad (6.1)$$

Here, f is defined as the frequency of vortex shedding and l_c is the characteristic length (side of the square) of the square cylinder.

Furthermore, a comparison is drawn to verify the predictions made by SBES with the LES predictions presented by Nusser (2019), indicating that the SBES predictions are under-predicted for all sensor locations, as shown in Fig. 6.7. For sensors located on the side window at Pos1 and Pos2 (See Fig.6.1 (c) for the number associated with the sensor), which are located in the wake of the side-view mirror, there is reasonable agreement between SBES and LES compared to positions Pos20 and 32, as shown in Fig. 6.7. A difference of ~5-10 dB is seen at low ($f < 100$ Hz) and medium ($100 \text{ Hz} < f < 500$ Hz) frequencies between the SBES and LES results for all sensor locations. This difference can be attributed to the denser grids used for the side window in LES compared with the grid used for SBES.

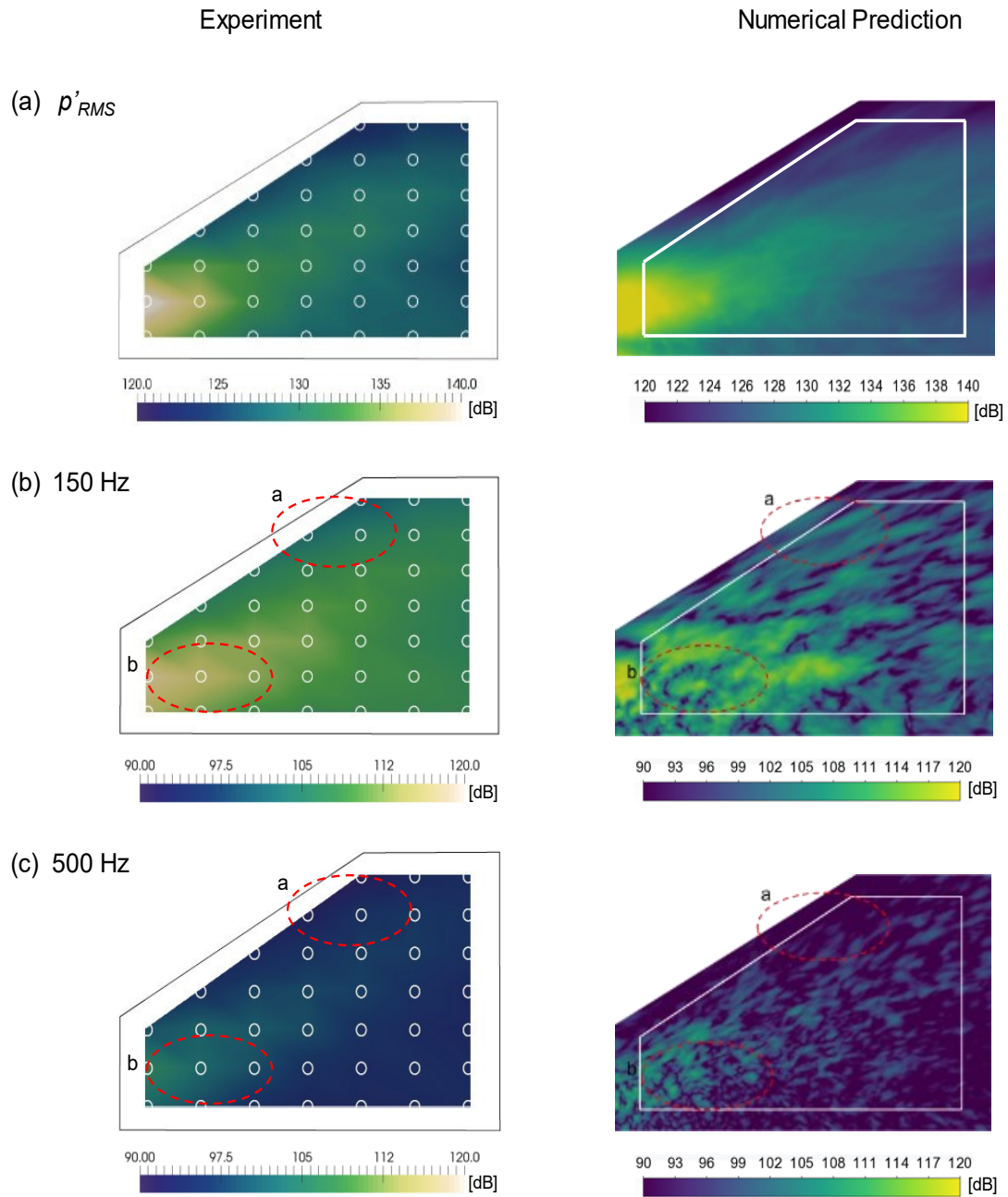


Fig. 6.5. Comparison of amplitude of pressure fluctuations in dB on the side window between experiment (Nusser, 2019)^r and numerical results for a) p'_{RMS} , b) 150 Hz, and c) 500 Hz. A reference pressure of 2×10^{-5} pa.

^r Reused with permission from Dr Katrin Nusser, “Investigation of the Fluid-Structure-Acoustics Interaction on a Simplified Car Model”, PhD thesis, Friedrich-Alexander-Universität Erlangen-Nürnberg. Copyright © 2019 by Dr. Nusser .

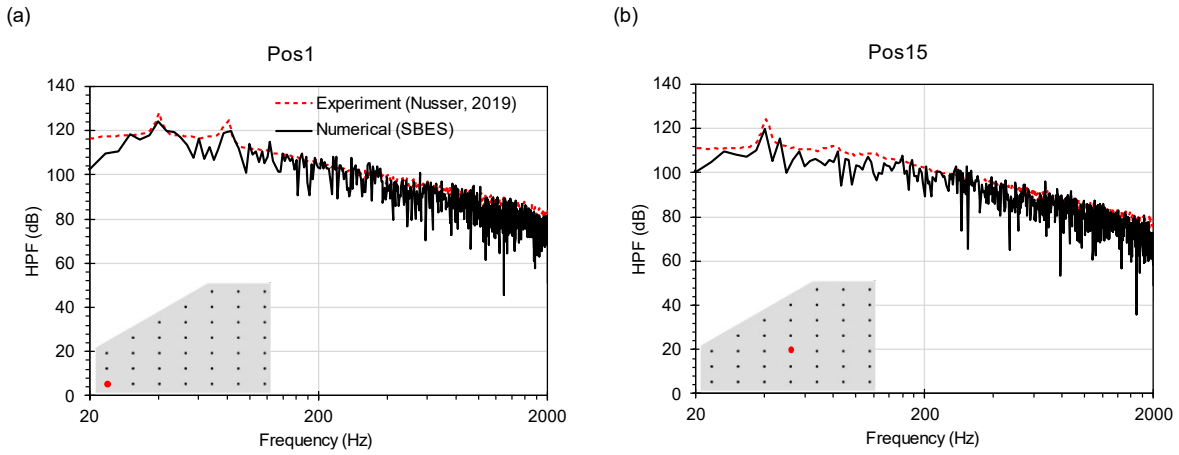


Fig. 6.6. Comparison of HPF between experiment (Nusser, 2019) and numerical (SBES) prediction for sensors a) pos1 and b) pos15. The locations of the sensors are marked with red dots in the schematic of the graph. Refer to Fig. 6.1(c) shows the number labelling of the sensors on the side window.

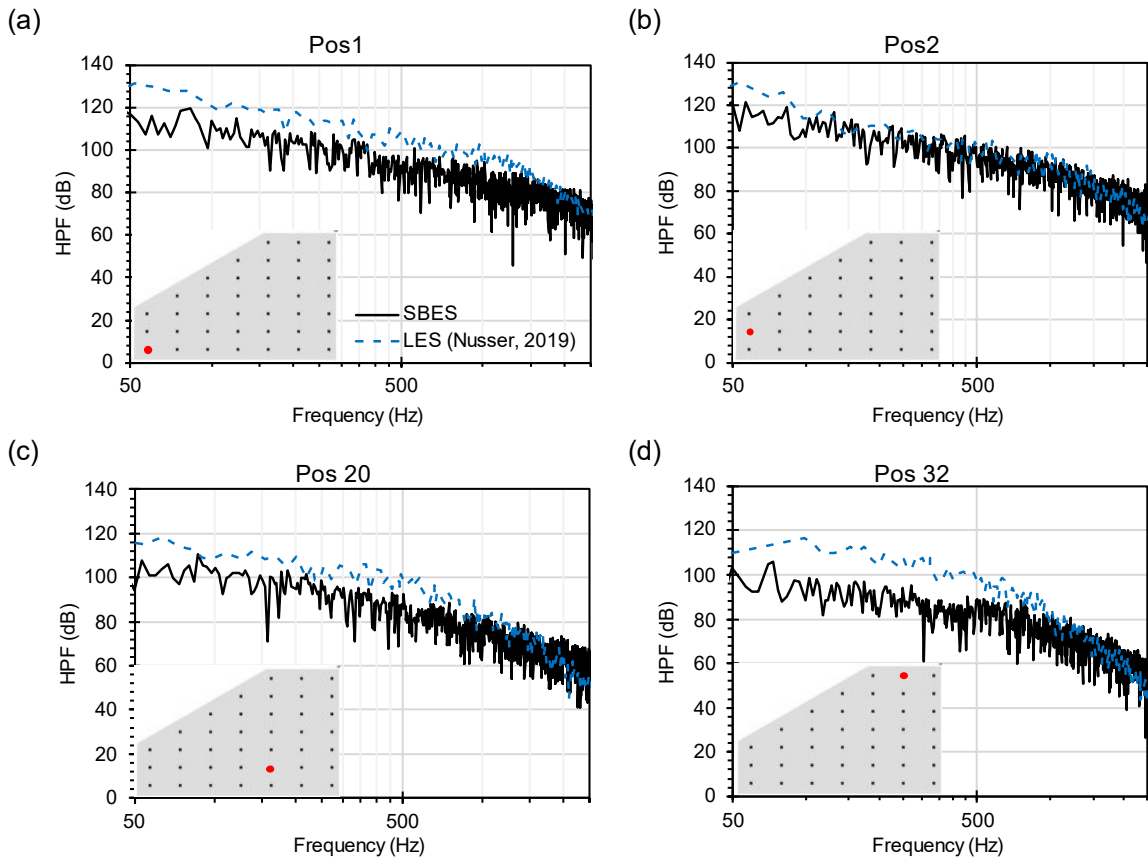


Fig. 6.7. Comparison between the predictions made by SBES and LES (Nusser, 2019) at four different positions in the side view, as illustrated by the red dots in the schematic: a) pos1, b) pos2, c) pos20, and d) pos32. Refer to Fig. 6.1(c) shows the number labelling of the sensors on the side window.

6.4. Side-view mirror and its influence on Drag Coefficient and Hydrodynamic pressure fluctuations

The side-view mirror is the major source of noise generation in vehicles; therefore, in this study, simulations were carried out without the mirror (no mirror) to investigate its effects.

The drag of the vehicle $Cd_{vehicle}$ is reduced by $\sim 13.13\%$ compared to SAE T4 with a mirror (See Fig. 6.1(a)), despite the change in the frontal area (F_A) of 0.82% between SAE T4 with and without the mirror (See Table 6.1). From a quantitative comparison of the flow features around SAE T4 with and without a mirror, which is visualised using the instantaneous Q criterion defined in Eq. 6.2.

$$Q = 0.5 * (\Omega_{ij}\Omega_{ij} - S_{ij}S_{ij}) \quad (6.2)$$

where Ω_{ij} is the rotation, and S_{ij} is the strain rate.

Based on the observations from Fig. 6.8 (a-b), there is a negligible difference in the length of the vehicle wake predicted in both scenarios. When the side-view mirror is present, the a high concentration of turbulent structures caused by horseshoe vortex in the upstream and the vortex shedding in the wake of the side view mirror are seen closer to the side window and these structures impact the flow originating from the A-pillar. While, in the absence of the side -view mirror, the flow around the A-pillar appears to be smooth without any significant detachment or reattachment, as illustrated in Fig. 6.8(c-d).

The pressure fluctuations experienced on the side window in the no-mirror case are potentially caused by the highly turbulent flow past the A-pillar, as shown in Fig. 6.8(d). However, in the mirror case, the pressure fluctuations experienced by the side window is primarily due to vortex shedding in the wake of the mirror, as shown in Fig. 6.8(c). The normalised pressure fluctuations, Np'_{rms} , shown in Fig. 6.9, indicate that the side window in the mirror cases experienced pressure fluctuations twice as high as those in the no-mirror case. A similar observation can also be made in the case of the A-pillar, as shown in the highlighted by dotted oval region in Fig. 6.9.

Table 6.1 Comparison of frontal area (F_A) and drag coefficient ($Cd_{vehicle}$) between SAET4 with and without mirror

Case	Frontal Area (F_A) m ²	% Change in F_A w.r.t mirror case	$Cd_{vehicle}$	% Cd_A w.r.t mirror case
With Mirror	1.9319	-	0.2604	-
Without Mirror	1.9160	0.82	0.2304	13.13

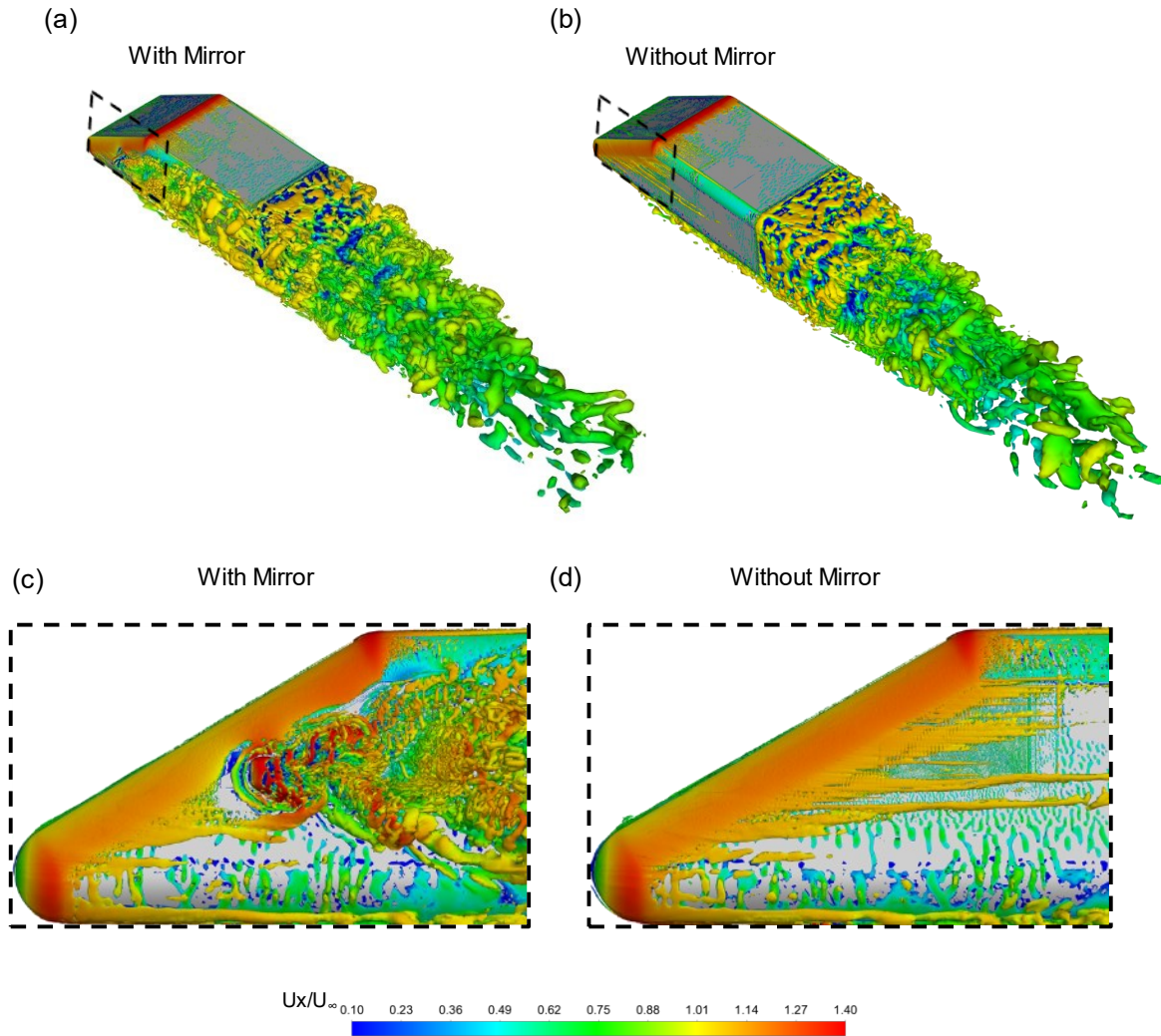


Fig. 6.8. Comparison of vortical structures of an instantaneous flow field visualised by iso-surfaces of $Q = 1100 \text{ s}^{-2}$ coloured with instantaneous x-velocity for SAE T4 a) with mirror and b) without mirror, while c) and d) represent the zoomed image of the flow structures around the A-pillar and side window.

Furthermore, the hydrodynamic pressure fluctuations exerted on the side window are reduced by 35 – 65 dB compared to SAE T4 with the mirror case, as illustrated in Fig. 6.10. The difference predicted in the amplitude at low frequencies is consistent with the results of previous studies (Dawi and Akkermans, 2019; Hartmann et al., 2012). The pressure fluctuations exerted on the side window in the no-mirror case are dominant at low frequencies up to 100 Hz, with the peak amplitude predicted at 40 Hz, similar to the mirror case, as shown in Fig. 6.10.

The Overall Sound Pressure Level (OASPL) is obtained using Eq. 6.3. The OASPL is measured at two probe positions; probe 1 (1.6m, 0.92m, 1.8m) and probe 2 (2.5m, 0.75m, 4m) from the origin of the vehicle body (See Fig. 1) suggests that the radiated noise decreases from 76.18 dB to 47.95 dB and from 61.63 dB to 31.65 dB, respectively, in the absence of the side-view mirror (See Table 6.2), and the A-pillar is the highest contributor to the overall noise radiated for both probe positions. Therefore, in the absence of a side-view mirror, the A-pillar is a potential noise source, which is consistent with the findings of Hartmann et al. (2012), Dawi and Akkermans(2019) and Lai et al.(2023)

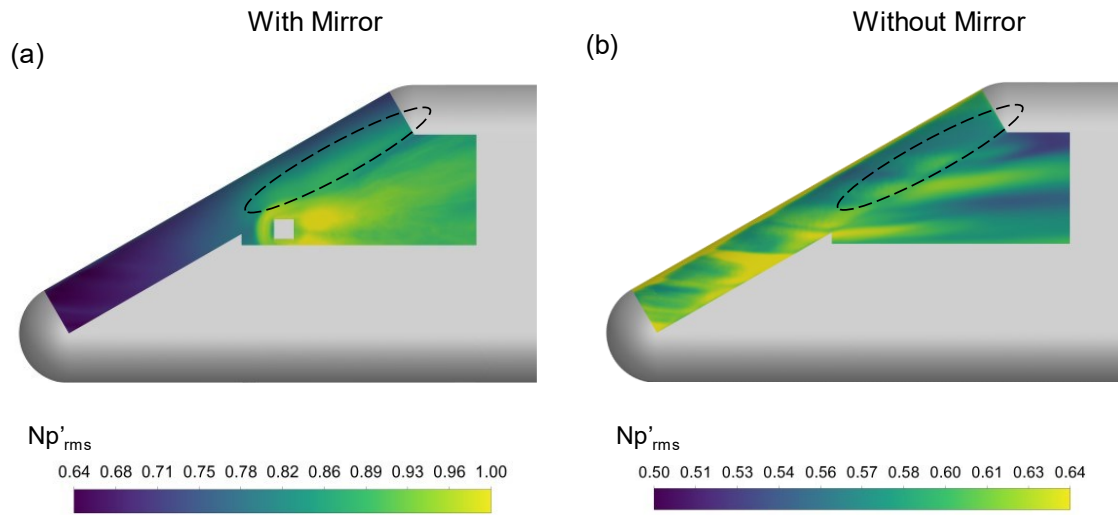


Fig. 6.9. Comparison of normalised p'_{rms} (Np'_{rms}) (defined as $Np'_{rms} = p'_{rms}/max.p'_{rms}$) where $max.p'_{rms} = 142.73$ dB (predicted from the case with mirror) between a) with mirror and b) without mirror cases. The scales presented are intentionally different due to the level of intensity predicted in both cases. The changes in the pressure fluctuations are highlighted using a dotted oval shape.

$$p'_{nrms} = \sqrt{\frac{1}{N} \sum_{n=1}^N (p'_n)^2} \quad (6.3)$$

$$OASPL = 10 \log_{10} \left(\frac{p'^2_{nrms}}{p_{ref}^2} \right)$$

Where, p'_n is the sound pressure obtained at the probe position and N is the number of samples.

Table 6.2 Comparison of noise radiated from SAE T4 with mirror and without mirror. The units for the values presented are in dB

	A-Pillar		Side window		Frame		OASPL	
	Probe 1	Probe 2	Probe 1	Probe 2	Probe 1	Probe 2	Probe 1	Probe 2
No Mirror	41.65	25.52	39.60	23.41	33.34	17.55	47.95	31.65
With Mirror	68.35	54.32	74.33	61.23	73.61	61.03	76.18	61.63

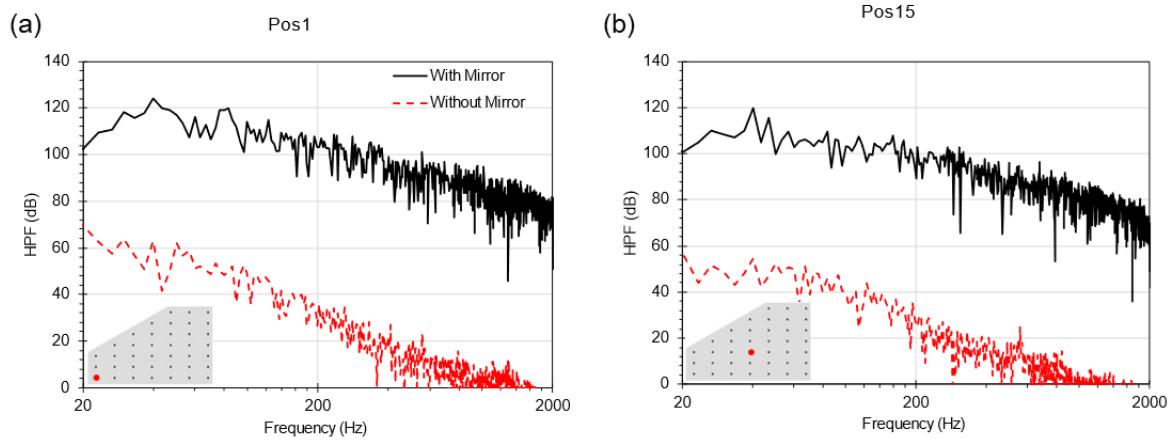


Fig. 6.10. Comparison of HPF between experiment SAET4 with and without a mirror at sensors a) pos1 and b) pos15. The locations of the sensors are marked with red dots in the schematic of the graph (see Fig.1(c) for the number labelling of the sensors on the side window).

6.5. Effects of Inclining the Mirror on the aerodynamic characteristics of SAE T4

In this study, the inclination of the mirror (θ) is defined as shown in Fig. 6.11. Hereafter, the mirror side is represented as w_m , whereas the side without a mirror is referred to as w'_m , as shown in Fig. 6.11. The $Cd_{vehicle}$ for various angles shows a constant decrease in the overall drag of SAE T4, except at 24° , where the $Cd_{vehicle}$ increased by $\sim 2.8\%$ compared to 16° . Also, SAE T4 with mirror mounted at 16° reports the lowest drag configuration. A similar trend is observed in CdA evaluated at the base of the vehicle. CdA was evaluated as shown in Eq. 6.4, which is also referred to as ‘micro drag’ by Cho et al. (2017) and Hucho (1998). In Eq. 6.4 the first term corresponds to the total pressure loss, the second term corresponds to the momentum deficit, and the last term represents the swirl drag, respectively. The overall lift coefficient tends to decrease up to 16° , after which SAE T4 experiences less downforce, with $Cl_{vehicle}$ being the lowest at 32° .

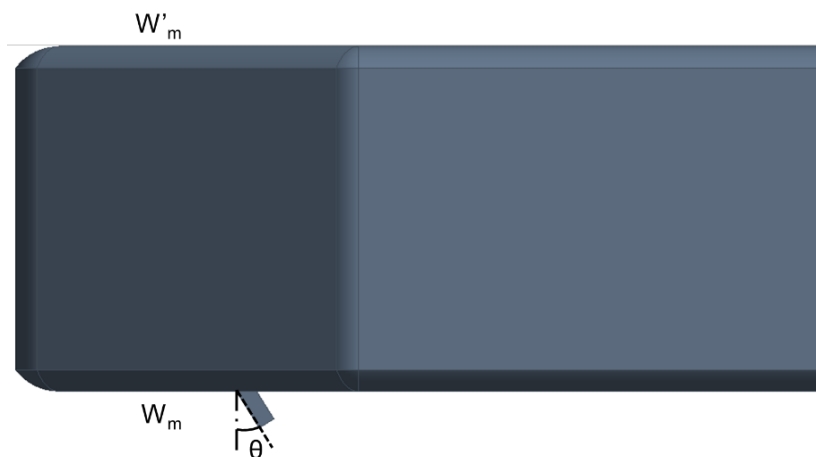


Fig. 6.11. Schematic of inclination of the mirror. Here, θ was varied from 0° to 32° in intervals of 8° . w_m and w'_m represent the sides with and without a mirror, respectively.

$$Cd_A = \int_s (1 - C_{p,tot}) dS - \int_s \left(1 - \frac{u}{U}\right)^2 dS + \int_s \left[\left(\frac{v}{U}\right)^2 + \left(\frac{w}{U}\right)^2\right] dS \quad (6.4)$$

Table 6.3 Comparison of force coefficients and pressure coefficients on the base between all the inclination angles (θ) investigated in this study.

Inclination Angle (θ)	$Cd_{vehicle}$	$Cl_{vehicle}$	$Cd_{A@base}$
0°	0.2604	-0.1187	0.2041
8°	0.2554	-0.1191	0.2037
16°	0.2489	-0.1197	0.2001
24°	0.2562	-0.1180	0.2082
32°	0.2493	-0.1074	0.2026

To further investigate the behaviour of drag, Cp on the base of SAE T4 for all θ is analysed along with the structure of the wake obtained using the iso-surface of the time-averaged mean total pressure, $Cp_{,tot} = -0.2$, as shown in Fig. 6.12. $Cp_{,tot}$ is obtained using Eq. 6.5.

$$Cp_{,tot} = \frac{p_{tot} - p_{ref}}{\frac{1}{2} \rho U_{\infty}^2} \quad (6.5)$$

where p_{tot} is the total pressure, and p_{ref} is the reference pressure considered as 1atm.

$$F_s = \oint p \, dA \quad (6.6)$$

$$C_s A = \frac{2 * F_s}{\rho * U_{\infty}^2}$$

Generic flow structures behind the squareback form a circular vortex ring as evidenced by Rouméas et al.(2009), Pavia(2019), and Bonnavion et al.(2019), a similar structure is predicted for all inclination angles. The vortex ring is a combination of the flow emanating from the roof, underbody, and sidewalls of the body which separate from the rear edges of the base of the square and together form a circular vortex ring. However, the circular vortex ring shape is affected when θ varies. For $\theta = 0^\circ$ to 16° , the flow emanating from the w_m side is dominant, as indicated in Fig. 6.12 (a) – (c), whereas the flow from the w'_m side tends to be less separated at the left edge of the base of the vehicle, which increases with an increase in θ from 0° to 16° . From the iso surface plots of the mean $Cp_{,tot}$, it is evident that the flow from w_m

deflects the wake towards the w'_m side. With an increase in θ , the movement of the wake towards the w'_m side decreased until $\theta = 16^\circ$. In addition, the low-pressure footprint seen on the base is dominant on the w_m side and roof of SAE T4. With an increase in the inclination angle from 0° to 16° , the low-pressure footprint tends to become smaller and concentrated closer to the w_m side of the body.

At 24° , the circular vortex ring formed indicates more flow emanating from the roof compared to $\theta = 0^\circ$ – 16° which is also indicated by the low-pressure footprint tending to decrease in magnitude and size compared with other angles from 0° to 16° , as shown in Fig. 6.12(d). The negative pressure region from closer to the roof of SAE T4, while the low-pressure footprint on the w_m side decreased in both size and magnitude. A similar observation can be made for the 32° case (see Fig. 6.12(e)), where a low-pressure footprint is formed closer to the roof but spreads between the lateral edges of SAE T4. This can be attributed to the decrease in the effect of mirror-induced vortices on the wake of the vehicle.

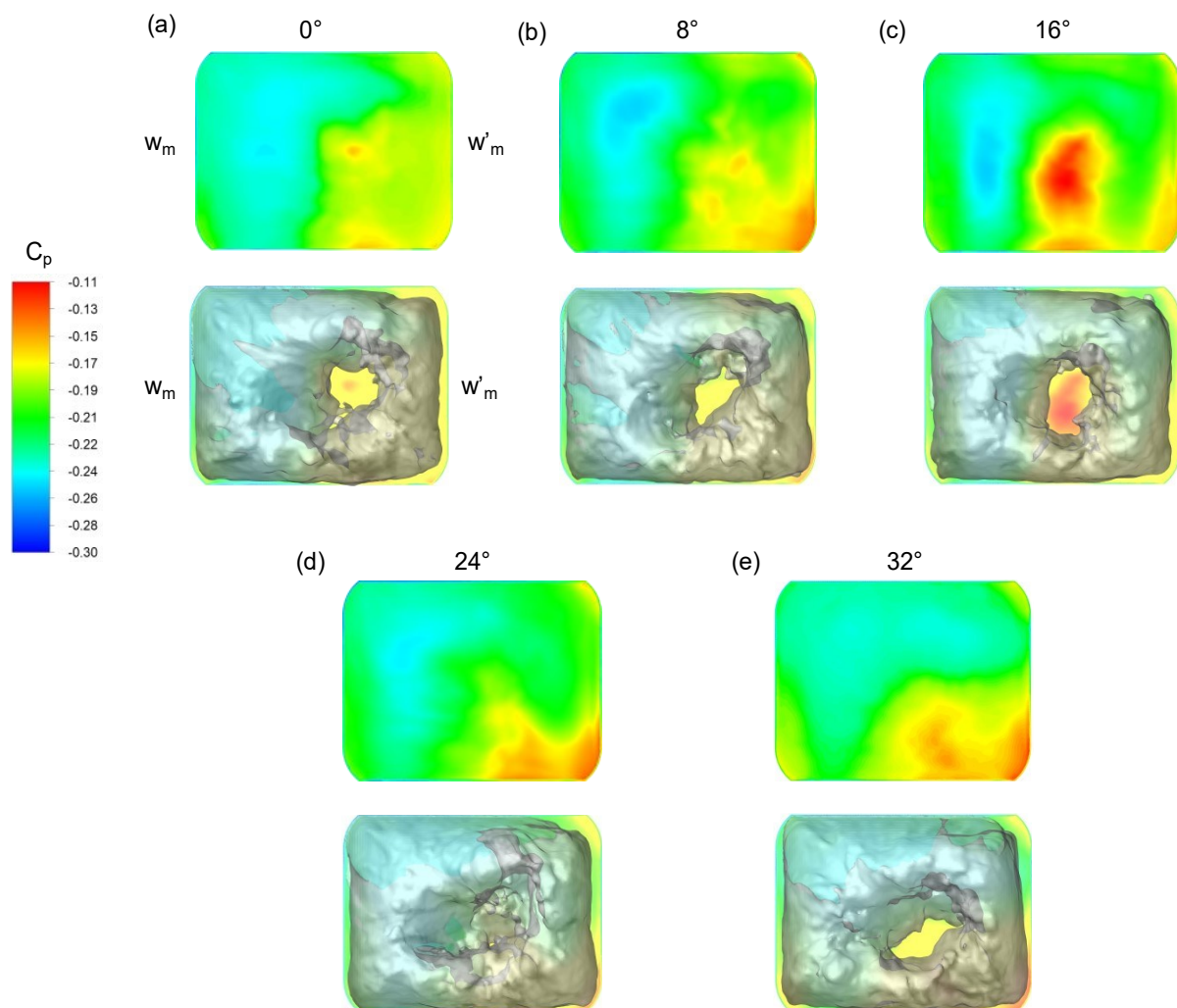


Fig. 6.12. Comparison of the coefficient of pressure at the base of SAE T4 (top) and the wake structure near the base visualised by the generated isosurface of the mean total pressure $C_{p,tot} = -0.2$ (bottom) between all the cases investigated.

From Fig. 6.12, it can be observed that the flow behaviour on the side governs the behaviour of the low-pressure region on the base. The forces exerted on the sides of SAE T4 were calculated using Eq. 6.6, adjusting for direction, and are summarised in Table 6.3 to identify the consequence of inclining the mirror on the force coefficients of SAE T4. The w_m side experiences a higher side force than the w'_m side for all the cases investigated in this study. The increase on the w_m side is attributed to the reattachment of the flow separated from the mirror on the w_m side of SAE T4. In addition, a constant decrease in the side force of the w_m side implies that with a change in θ , the reattachment of the flow on the side of SAE T4 is reduced which is visualised using the direction of the shear layer using streamlines and vorticity plots. Fig. 6.14 indicates that after $\theta = 16^\circ$, the shear layer from the lateral edge of the mirror becomes parallel to the side of SAE T4, resulting in less side force on the w_m side (See Table 6.4).

Table 6.4 Comparison of difference obtained for the CsA evaluated at the mirror side (w_m) and no mirror side (w'_m) between all the angles investigated.

Inclination Angle (θ)	w_m	w'_m	Difference in %
0°	0.1883	0.1711	9.58
8°	0.1875	0.1715	8.86
16°	0.1858	0.1729	7.19
24°	0.1854	0.1723	7.31
32°	0.1818	0.1716	5.40

The difference in side force causes an imbalance which results in the formation wake which is dominant towards the left side of the vehicle, as indicated by the circular vortex ring in Fig. 6.12. The imbalance in the force reduces the overall drag experienced by the vehicle, as shown in Tables 6.3 and 6.4 for $\theta = 0^\circ$ to 16° . When the imbalance increases, the overall drag also increases, as observed in the predicted $Cd_{vehicle}$ for $\theta = 24^\circ$. For 32° , the imbalance again decreases and is also the lowest among all cases. Therefore, it appears that the imbalance in the side force is proportional to the overall drag of the vehicle, and the relationship tends to be linear, as shown in Fig. 6.13.

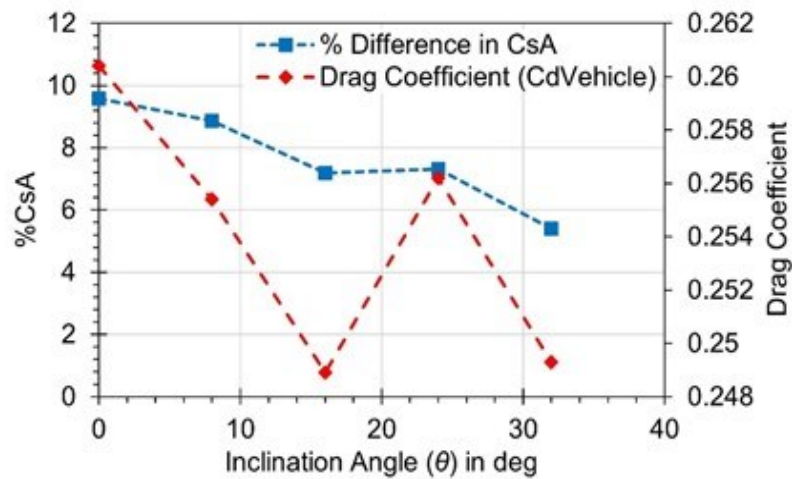


Fig. 6.13. Relationship between % difference in side forces and drag coefficient of vehicle ($C_{d_{vehicle}}$) with respect to inclination angle (θ).

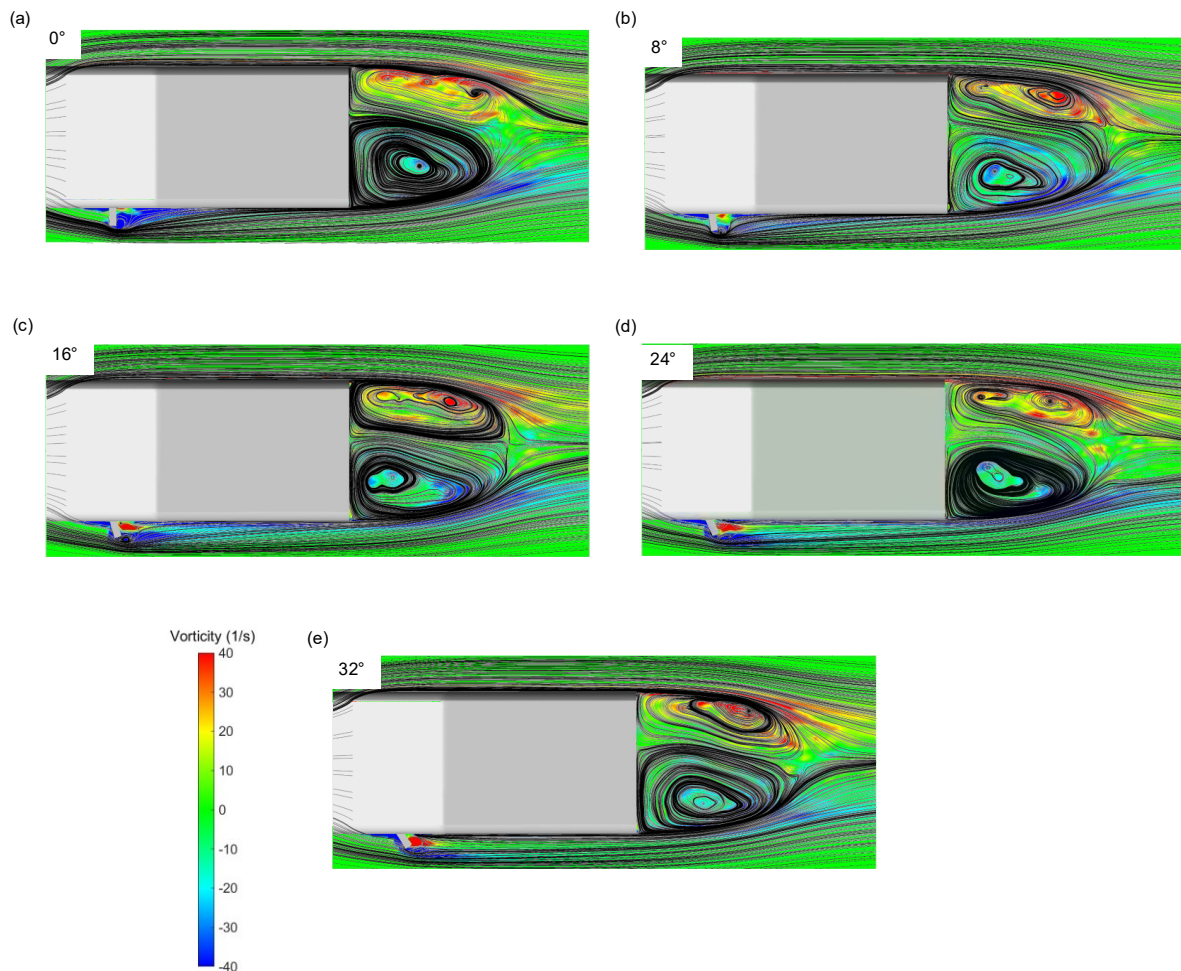


Fig. 6.14. Comparison of time-averaged vorticity contours superimposed with velocity streamlines on the midplane of the side-view mirror at $y/H = 0.68$ between a) 0°, b) 8°, c) 16°, d) 24°, and e) 32°.

For SAE T4 with a mirror mounted at $\theta = 0^\circ$, there are two vortices (V_1 and V_2), as shown in Fig. 6.15, which are formed as a result of flow separation from the top and bottom trailing edges of the side view mirror, which tend to diverge from each other as they traverse

towards the base of the body. Vortex V_1 tends to affect the flow not only from the side but also from the roof, as shown in Fig. 6.15(a), whereas V_2 tends to affect the underbody flow. This divergence of the vortex decreases with an increase in θ of the mirror up to 16° . A further increase in $\theta = 24^\circ$ results in the formation of a single vortex V_1 which is weaker than the other V_1 vortices, as shown in Table 6.5. However, for $\theta = 32^\circ$ even though a single vortex is formed the strength of the vortex is higher than that at 24° . This difference can be attributed to flow separation at the mirror. For $\theta = 0^\circ - 16^\circ$, the flow separated from the top and bottom faces of the mirror, while for the 24° and 32° , the flow separation is more pronounced from the lateral face of the mirror which is evident in the mean averaged vorticity plot presented in Fig. 6.14.

Table 6.5 Comparison of the vortex strength evaluated at streamwise planes between all the sweep angles investigated. All the values presented for vortex strength have units of ‘1/s’

θ	$x/L = 0.48$	Vortex definition	$x/L = 0.97$	$x/L = 1.05$	$x/L = 1.13$	$x/L = 1.21$
0°	3.1665	V_1	9.7561	28.9742	30.8604	23.8382
		V_2	-6.4112	-6.2319	-6.40352	-5.2130
8°	3.1172	V_1	9.7499	26.7323	28.7230	23.6986
		V_2	-6.5876	-5.1707	3.9549	3.499
16°	3.0781	V_1	8.0646	24.8017	23.8061	23.6664
		V_2	-0.1146	11.2560	17.6937	0.5103
24°	6.0164	V_1	2.1608	15.5168	16.7498	11.3650
		V_2	-	-	-	-
32°	5.4167	V_1	3.9709	16.7444	19.9076	9.2496
		V_2	-	-	-	-

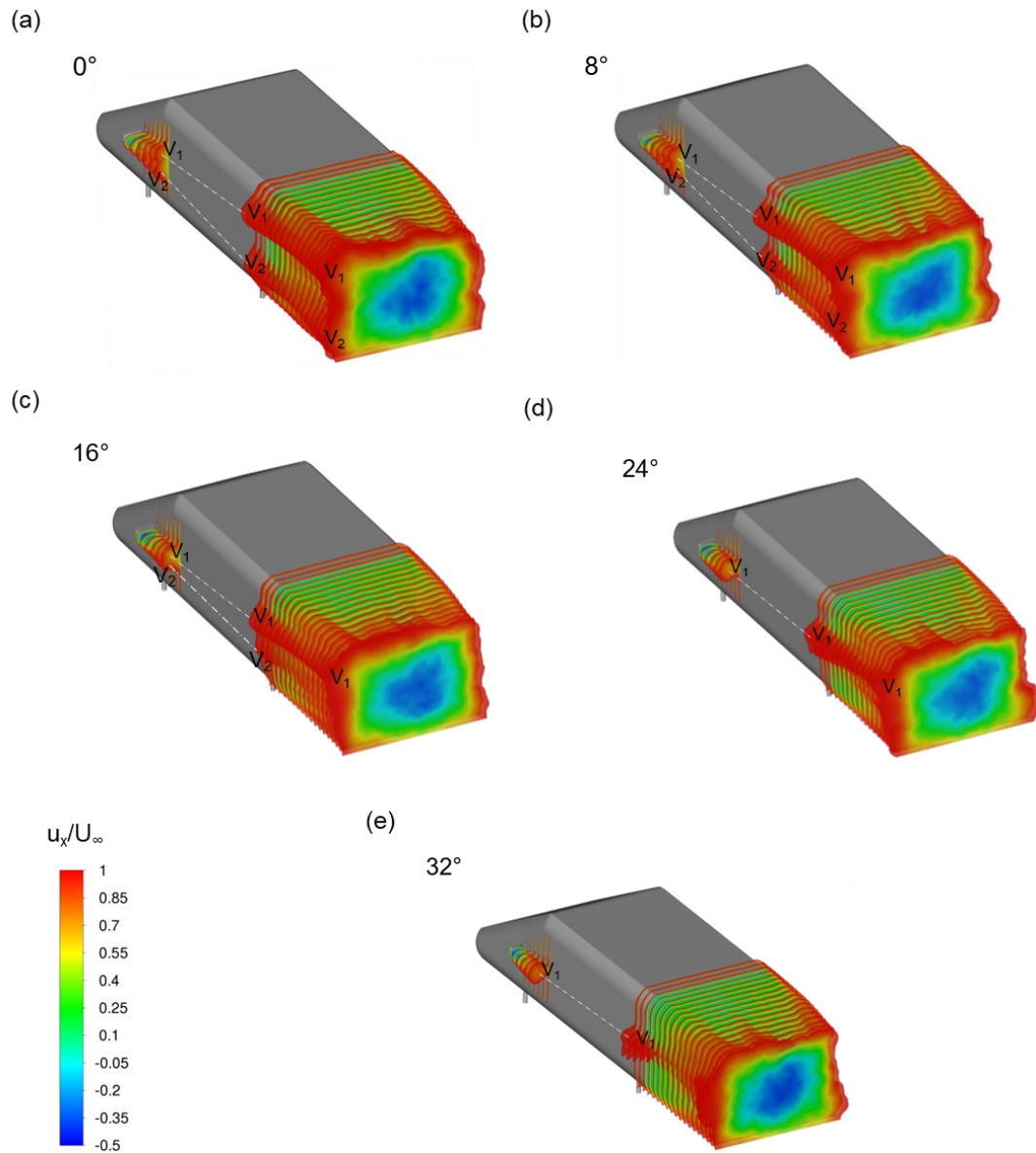


Fig. 6.15. Time-averaged velocity magnitude plotted in the wake of the mirror and SAE T4 for $\theta =$ a) 0° , b) 8° , c) 16° , d) 24° , and e) 32° . V_1 and V_2 represent mirror-induced vortices emerging from the top and bottom faces of the mirror, respectively.

6.6. Effects of inclining the mirror on the acoustic characteristics of SAE T4

The effect of inclining the mirror on the flow structures around the forebody is shown using the time-averaged wall shear stresses in Fig. 6.16. A horseshoe vortex is formed where the mirror is mounted on the side of SAE T4, similar to the half-round mirror mounted on a flat plate (Ask and Davidson, 2009; Chen and Li, 2019; Chode et al., 2021; Tosh et al., 2018; Yao and Davidson, 2018). However, the horseshoe vortex predicted for all inclination angles (θ) is asymmetric in the normal direction, in contrast to observations made in flat-plate cases (Chode et al., 2021). The horseshoe vortex dimensions tend to decrease with an increase in θ which is in line with the predictions made for isolated inclined mirror cases studied by Chode *et al.* (2021), Ask and Davidson (2009) and Yao *et al.* (2018), as summarised in Table 6.6. L_{hx} , L_{hy+} ,

L_{hy-} , and L_{ws} represent the normalised length of the horseshoe vortex from the mirror, the normalised height from the lateral edge of the mirror, the normalised height of the horseshoe vortex in the positive y -direction, the normalised height of the vortex in the negative y -direction, and length of the wake structure measured from the rear of the mirror, respectively. In addition, α represents the angle between the flow interaction line and A-pillar. A flow interaction line is defined where the flow from the A-pillar interacts with the side-view mirror horseshoe vortex (Fig. 6.4(b)).

Table 6.6 Comparison of the change in the angle made between A-pillar and streamline (α) and the normalised lengths of time-averaged flow feature with the change in θ

Sweep angle (θ)	L_{hx}	L_{hy+}	L_{hy-}	L_{ws}	Change in α w.r.t to 0°
0°	1.348D	1.117D	1.7175D	3.169D	-
8°	1.276D	1.221D	1.575D	3.185D	14.27%
16°	1.212D	1.237D	1.531D	3.067D	23.22%
24°	1.165D	1.088D	1.282D	3.023D	30.09%
32°	0.975D	0.924D	1.087D	2.315D	44.75%

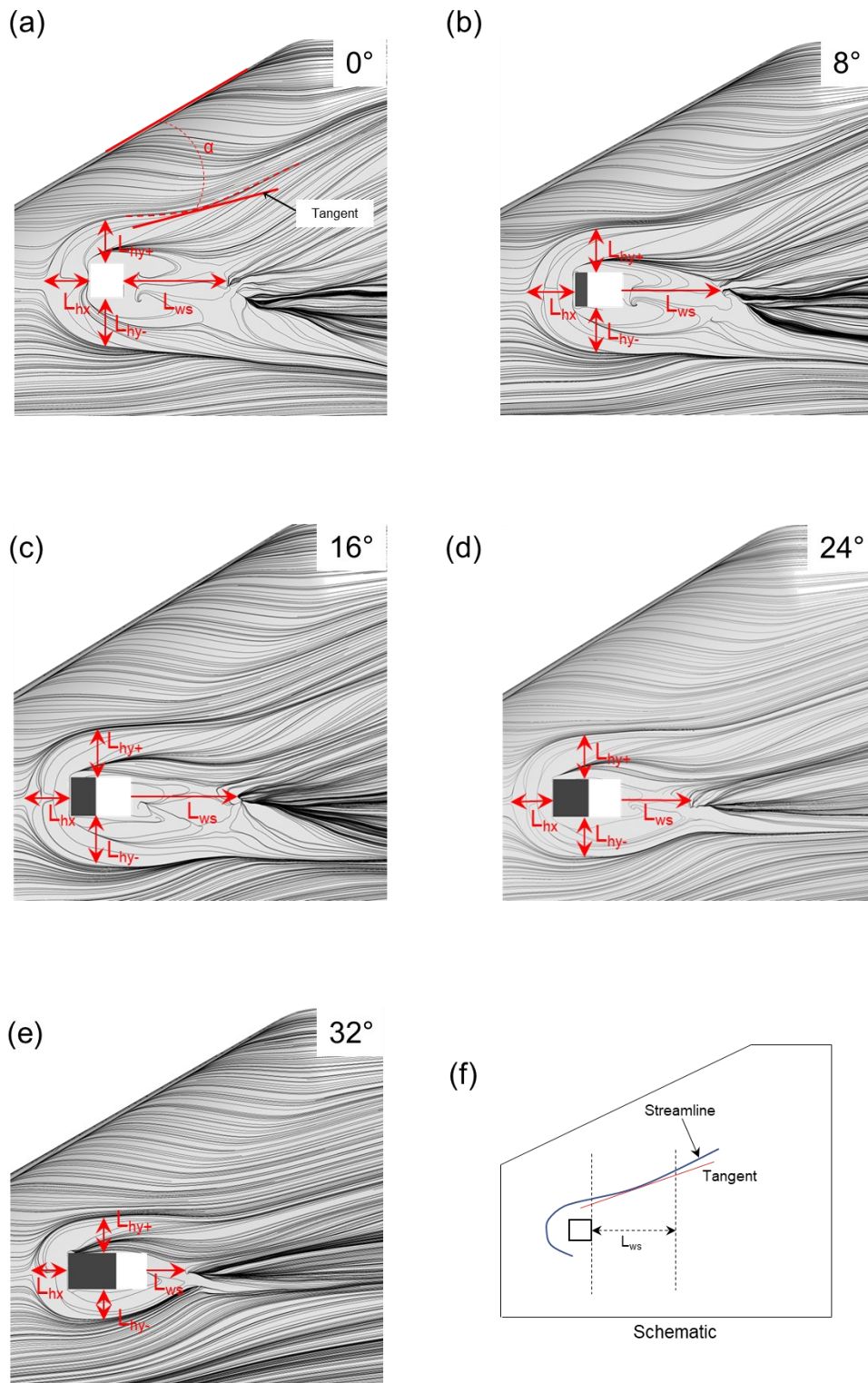


Fig. 6.16. Comparison of time-averaged wall shear stresses on the forebody of SAE T4 with varying sweep angles: a) 0°, b) 8°, c) 16°, d) 24°, and e) 32°. f) shows a schematic of obtaining a tangent for the streamline.

In addition, the wake formed behind the mirror decreased with an increase in θ , as indicated by L_{ws} in Table 6.6. The angle α between the flow interaction line (as defined in Fig. 6.4(b)) and the A-pillar increases with an increase in θ , indicating a decrease in the width of the horseshoe

vortex. Consequently, the pressure fluctuations exerted on the side window are concentrated closer to the mirror wake, as shown in Fig. 6.17.

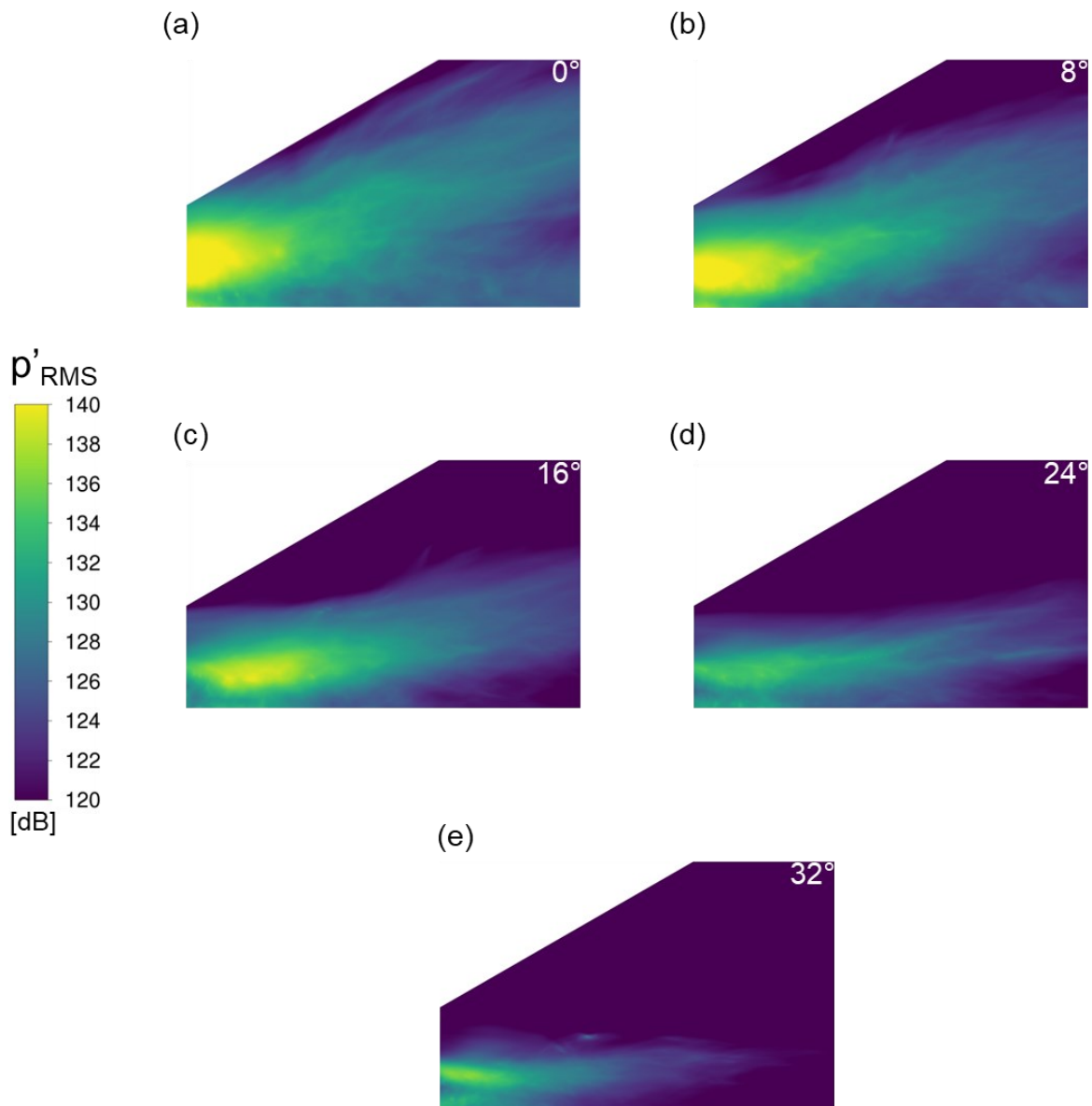


Fig. 6.17. Comparison of RMS of pressure fluctuations in dB on the side window for all sweep cases investigated for a) 0°, b) 8°, c) 16°, d) 24°, and e) 32°.

The pressure fluctuations on the side window are presented using the RMS of the pressure in Fig. 6.17, where the pressure fluctuations exerted on the side window are reduced when θ is increased which is in accordance with the observations made by Chode et al.(2021) for isolated inclined mirrors. To quantify this decrease, the HPF is obtained using two surface probes located on the side window (see Fig. 6.18), where aeolian tones were observed (ref: Fig. 6.6). The amplitudes of the aeolian tones at 40 Hz and 80 Hz decreased as the mirror inclination angle increased, which can be attributed to the amount of flow interacting with the surface of

the side window. As θ increased, the flow tends to separate more from the outboard faces of the mirror, which, if not reattached to the surface of the side window, leads to a decrease in the overall HPF, as evidenced by the decrease in the magnitude of the RMS of the pressure fluctuations presented in Fig. 6.18.

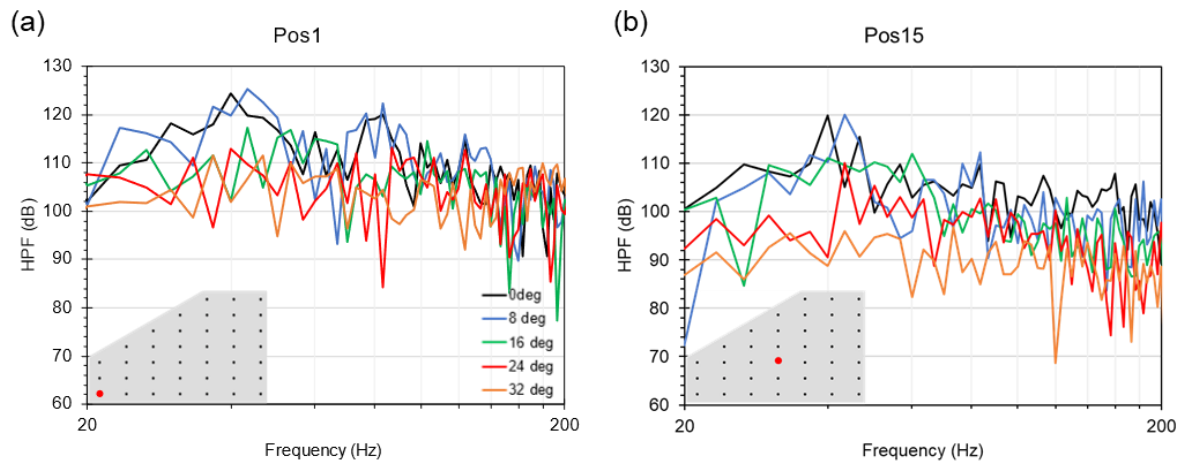


Fig. 6.18. Comparison of the HPF between all sweep angles investigated at specific sensor locations is illustrated by the red dot in the schematic for a) pos1 and b) pos15. Refer to Fig.6.1(c) shows the number labelling of the sensors on the side window.

As a result, the noise propagated from the vehicle when evaluated using FW-H at 1.8m and 4 m away from the vehicle, shows a consistent decrease in the Overall Sound Pressure Level (OASPL) when the inclination angle of the mirror is increased, as shown in Table 6.7. The contribution from each source, such as the side window, side-view mirror, A-pillar, and frame of SAE T4, is shown in Fig. 6.19. As shown in Fig. 6.19, the contribution from the surface pressure fluctuation exerted on the side window is the major contributor to the overall noise, whereas the side-view mirror contributes the least when measured at Probes 1 and 2. The contribution of the side-view mirror to the overall noise is reduced with an increase in the θ , and the lowest dB is reported for $\theta = 16^\circ$. In addition, directivity plots were plotted in the vicinity of the side-view mirror and away from the geometrical influence of the sources to evaluate the effect of θ on the structure of the radiated noise.

Table 6.7 Comparison of noise radiated OASPL (dB) in the vicinity of SAE T4 for all the sweep angles investigated.

Probe location	0°	8°	16°	24°	32°
Probe 1 (1.6m, 0.92m, 1.8m)	76.18 dB	73.48 dB	70.73 dB	69.20 dB	67.11 dB
Probe 2 (2.5m, 0.75m, 4m)	61.63 dB	59.80 dB	57.44 dB	55.83 dB	54.06 dB

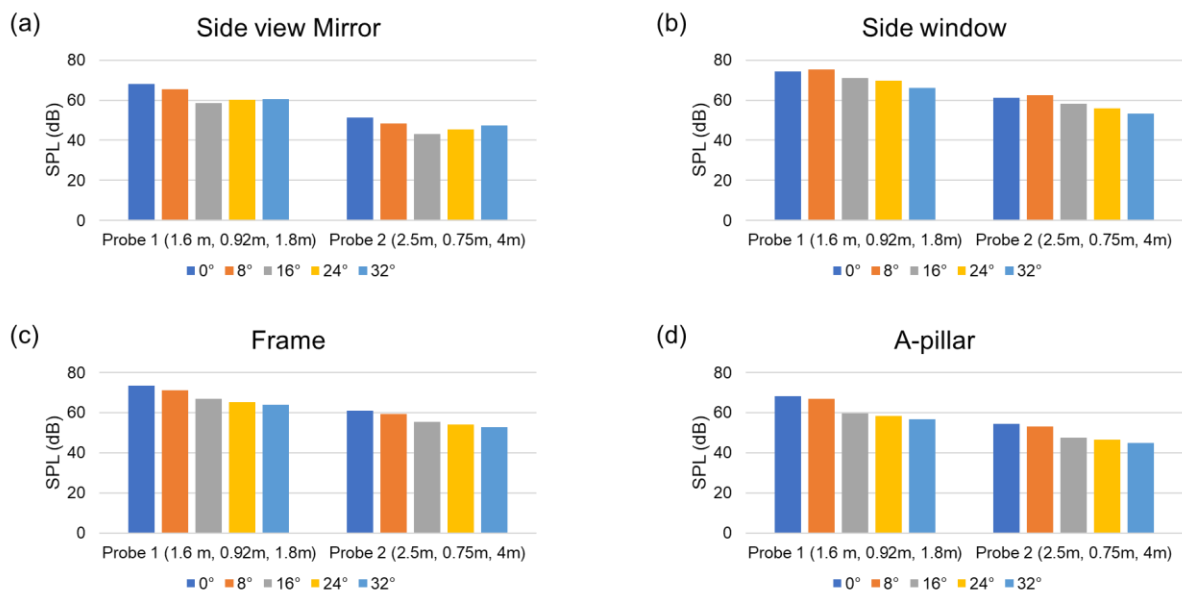


Fig. 6.19. Component-wise comparison of SPL evaluation at two probes positioned away from SAE T4. a) Side-view mirror, b) side window, c) frame and d) A-pillar.

Fig. 6.20 and 21 show the directivities of the noise radiating from the sources for the SAE T4 body with inclined mirrors. The OASPL was evaluated at four different planes located at $z = 0.56W$, $0.62W$, $1.13W$ and $2.5W$, and 36 probes were arranged to form a circle with the axis centre of the mirror as the centre of the circle. At each plane, the directivity is obtained using FW-H with a single source (side-view mirror) and all sources (side-view mirror, side-window, frame, and A-pillar). At $z = 2.5W$, located away from the vehicle in the free stream region, the noise radiated patterns resemble a monopole for all the angles investigated for all the sources with 32° predicting the lowest noise levels. For a single source, the radiated pattern is a monopole, but the intensity levels are lower than the dB levels predicted for all sources. The lowest noise radiated for a single source is 16° which is in agreement with the observations made in Fig. 6.19. As the measuring plane moves closer to the vehicle, at $z = 1.13W$, for a single source, 0° and 8° indicate a monopole-like pattern, whereas other angles preserve the monopole pattern which is in contrast to the observations made for all sources in the same plane, where the radiated pattern is monopole.

Probing closer to the vehicle, the radiated pattern changes from a monopole shape, typical of a single noise source, to a cardioid-like shape, indicative of multiple high-intensity noise sources, including the side window (as shown in Fig. 6.19(b)). The formation of a cardioid-like shape can be attributed to the combination of noise sources. Although the radiated pattern may resemble a dumbbell shape, which is commonly classified as a dipole, the shape predicted for 0° and 8° with a single source does not exhibit a strong representation of a

dumbbell-like shape. Previous studies conducted by Ask and Davidson (2010), Becker et al. (2016), Nusser et al. (2018), and Chode et al. (2021) classify the noise source closer to the side window as a dipole, and therefore, the pattern predicted for 0° and 8° can be assumed to have a dipole-like structure. From Fig. 6.20 and 21, it can be seen that the lowest radiated noise is recorded at 32° for all angles obtained using a single source and all sources, but the maximum reduction is observed for $\theta = 16^\circ$, which is in agreement with the observations made for OASPL in Table 6.7. Additionally, the directivity patterns suggest that the noise measured away from the vehicle sources can be considered monopole, which is useful for tests such as pass-by-noise-like scenarios, evaluating the risk for pedestrians from electric vehicles, and optimizing the placement of noise barriers for roads.

In conclusion, SAE T4 with 16° seems to have low drag and low noise configurations, as the reported drag for 16° is the lowest and the noise radiated is decreased by approximately 10 dB. This study also showed that there is no linear relationship between radiated noise and aerodynamic drag. This study found that the noise emitted is dependent on how the flow behaves closer to the mirror, whereas the consequence of the flow behaviour around the mirror and its interaction with the wake of the vehicle defines the drag.

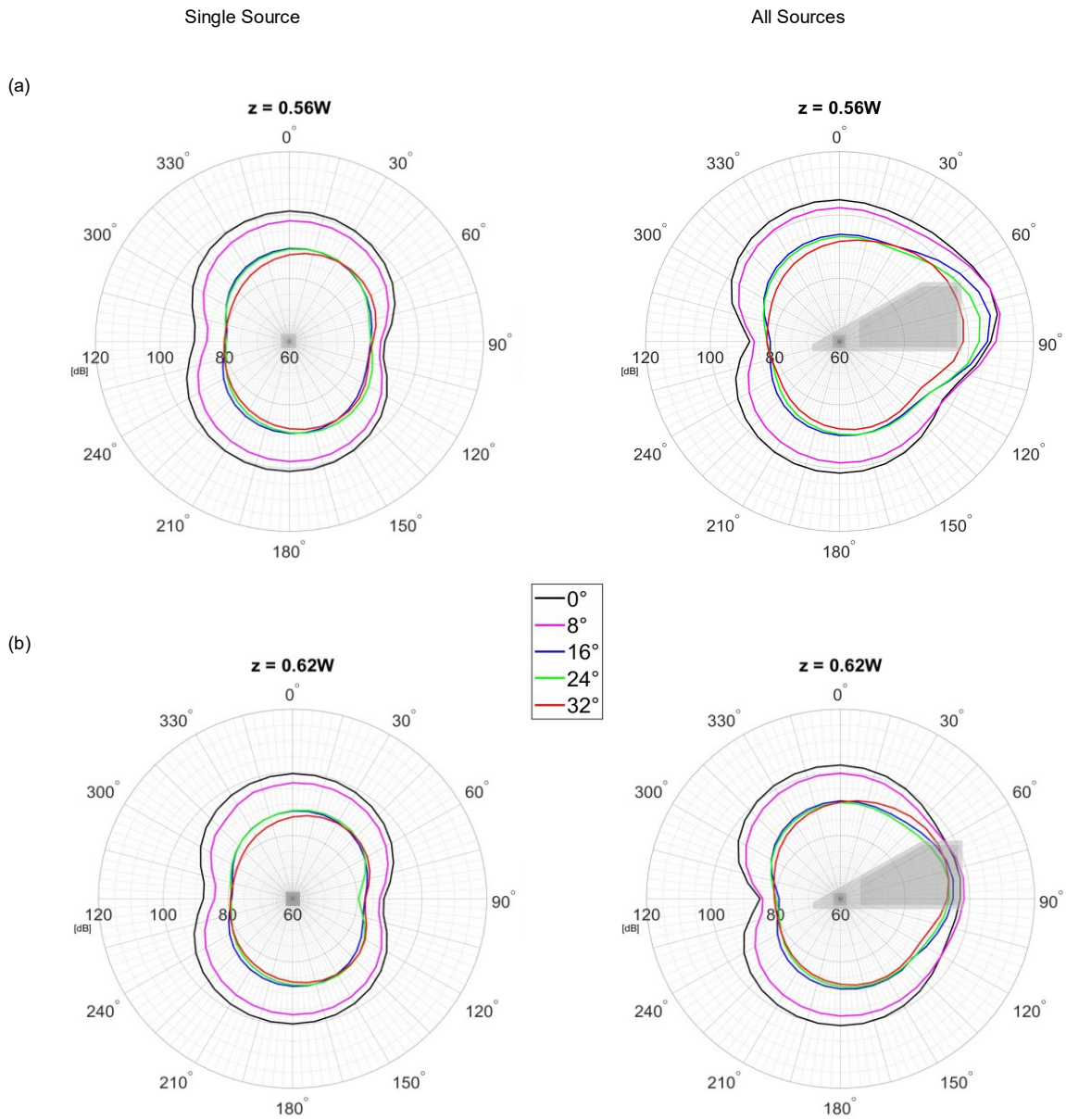


Fig. 6.20. Directivity plot comparison among all sweep angles investigated at a) $z = 0.56 W$ and $0.62 W$. On the left, a single source is used to evaluate directivity, while on the right, all the sources are selected.

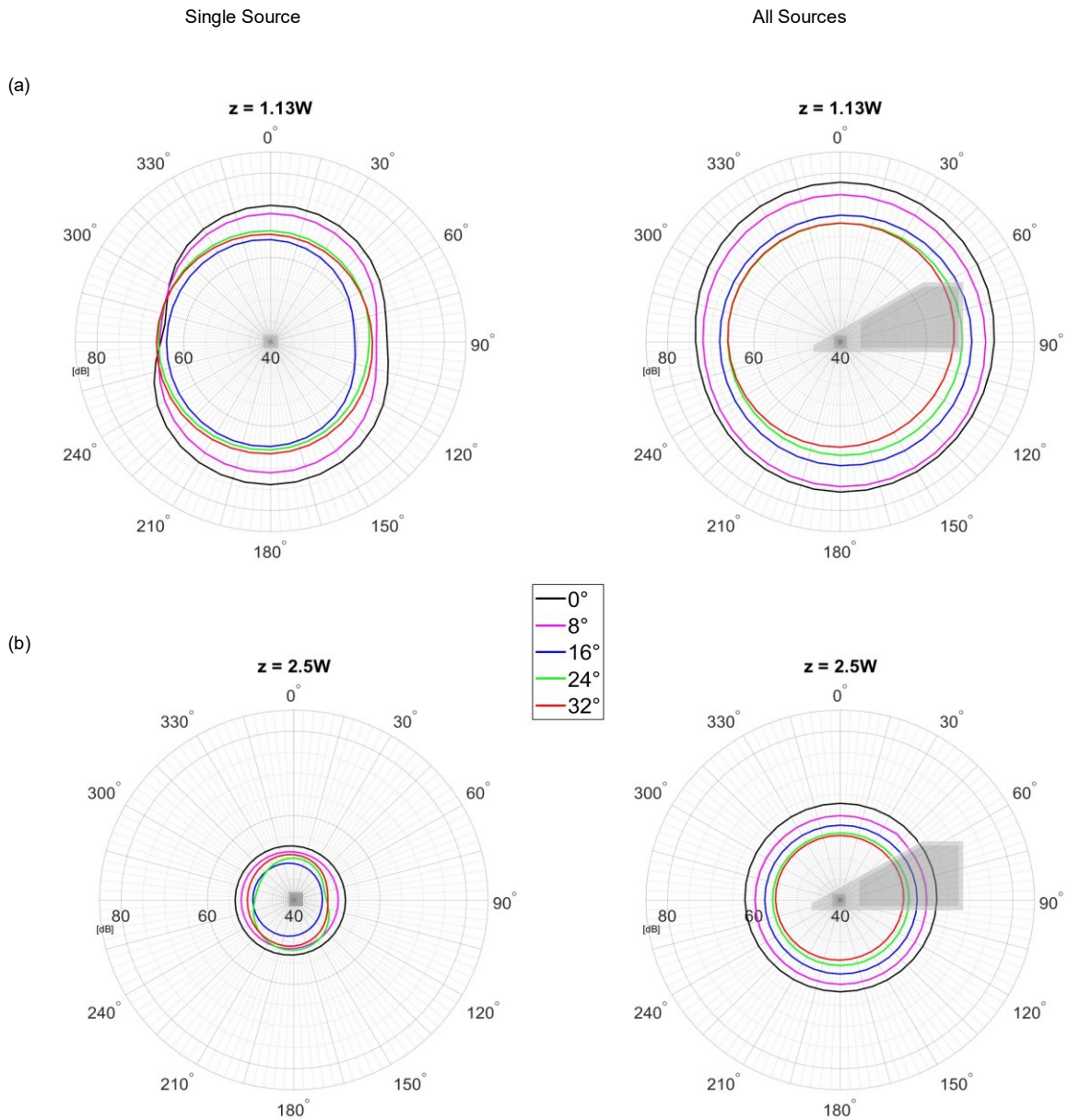


Fig. 6.21. Directivity plot comparison amongst all the sweep angles investigated at a) $z = 1.13 W$ and $2.5 W$. On the left, a single source is used to evaluate directivity, while on the right, all the sources are selected.

Summary

In this chapter, a numerical investigation was conducted to predict the noise generated and propagated from a standard squareback body with a bluff mirror mounted on one side of the body. A detailed study of the aerodynamic and acoustic characteristics of the SAE T4 body was conducted for various mirror inclination angles using a SBES coupled with the FW-H analogy to be achieve last the two aims set for this thesis. The summary of the results from this chapter is presented below:

- SBES-FW-H predicted results were in good agreement with both experimental and numerical data sets. Specifically on the hydrodynamic pressure fluctuations (HPF) spectra, where the aeolian tones are accurately captured at the frequencies observed in the measured spectra with amplitude being off by $\sim 3\text{-}5\text{dB}$ while when compared with LES data, a difference of $\sim 5\text{-}10\text{dB}$ was seen.
- In the absence of the mirror, the main source of hydrodynamic pressure fluctuations was the A-pillar and also the despite a small reduction in the projected frontal area the drag reduction was significant, as 13.3% reduction was observed.
- When inclinations are introduced, a nonlinear relation was found between the increase in inclination angle and the overall drag coefficient. This nonlinear behaviour of drag was attributed to the imbalance in side-force coefficients experienced by the vehicle. The imbalance in the side force was a result of the flow separated from the mirror reattaching to the side surface of the vehicle body and interaction of mirror included vortices with side surface.
- Finally, when mirror is inclined to 32° the noise radiated was the lowest. Also, the structure of the radiated noise when measured away from the vehicle at 1m and 4m was a monopole indicating that influence of sources on the radiated noise was minimal.

In the following chapters, discussion on the accuracy and applicability of the results are presented with concluding remarks for the thesis.

In this chapter, the critical outcomes of this thesis will be discussed based on a) numerical procedure and b) application. The limitations of the current work will be presented in this chapter along with the recommendations to further investigate and strategies that can be implemented to improve the outcomes of the simulations.

7.1. The relevance of SBES turbulence model for ground vehicle aerodynamics and aeroacoustics

In this thesis, SBES demonstrated reasonable agreement with the experimental data, offering valuable insights into flow characteristics. However, discrepancies were observed, particularly in predicting the flow behaviour closer to the wall, specifically in relation to the asymmetry of the rear slant of the notchback geometry and flow separation from the half-round mirror geometry.

The notchback geometries used in this thesis have effective backlight angles in the range of 15–24°, at which the flow at the backlight shows asymmetry, as observed experimentally (Gaylard et al., 2007; Lawson et al., 2007; Wieser et al., 2020). The cause of the asymmetry on the backlight is still an unanswered question. However, the underlying flow mechanism causing the asymmetry involves the interaction of the central vortex shed (hairpin vortex formation on the backlight) from the shear layer emanating from the leading edge of the backlight and the C-pillar vortices. SBES did not accurately capture the asymmetry or accurately predict it in some instances. The primary reason for This discrepancy can be attributed to the inaccuracies in resolving the shedding of the shear layer. For the SAE T20 case, the shear layer emerging from the leading edge of the backlight is covered by the RANS layer, and it is envisaged that the averaging process may lead to inaccuracies in predicting the velocity fluctuations in the shear layer, which are crucial for capturing the hairpin structure accurately. It is worth mentioning that attempts have been made by several researchers to predict the flow behaviour accurately on the backlight using hybrid RANS-LES methods, such as IDDES and DDES, with more refined grids; however, none of the models were able to predict this phenomenon (AUTO CFD, 2019). Therefore, simulating flow asymmetry appears to be an outstanding issue, and more rigorous research on numerical methods is still needed to gain a full understanding.

For the mirror geometry case, inaccuracies were found in the location of flow separation. It was observed that the turbulence viscosity ratio on the curvature of the mirror was higher near the reported flow-separation location in the experiment. These limitations observed in SBES align with those reported for other hybrid RANS-LES approaches in the literature (Islam et al., 2017; Ask and Davidson, 2006; Chen and Li, 2019).

It is worth mentioning that the flow resolution obtained using SBES was more accurate than that of other variants of DES, as previously reported (Chode et al., 2020; Ekman et al., 2020; Menter et al., 2021) in the separated regions. Consequently, SBES may provide a more reliable flow resolution, particularly for studies focusing on highly separated flows. Notably, the switching behaviour in SBES is rapid, and the blending of eddy viscosities enables SBES to promptly capture flow unsteadiness and effectively resolve small structures within the separated flow.

7.2. Accuracy of the adopted methodology

It is crucial to note that the observed inaccuracies in SBES predictions closer to wall can be a combination of several choices made while formulating the methodology. Some of the choices are discussed to check and improve the current methodology. The grid sizes could play critical role in improving accuracy of the results, throughout this thesis, the grid sizes are evaluated using wall-normalised units where the assumption of grid resolution in the stream and spanwise direction are identical and strictly the wall normal direction is resolved to ensure the viscous sublayer has at least 7 cells in normal direction. It is observed any further increase in the number of cells have no significant impact on the resolution of flow behaviour closer to the wall clearly indicated in grid evaluation studies conducted which have demonstrated that even the use of fine grids does not lead to any noticeable improvement in predicting velocity profiles or the C_p profile.

The discretization scheme employed in this thesis is the Bounded Central Difference (BCD) scheme, which combines first-order, second order, and central difference schemes. The BCD scheme incorporates the Normalized-variable Diagram (NVD) scheme, where the blending factor between central differencing and second-order upwind schemes is controlled within the range of 0 (Pure Central Differencing scheme) to 1 (Second-order Upwind). In this study, the blending parameter has been set to 0.75 to maintain a balance between stability and resolution quality. This choice has resulted in reasonably accurate predicted results, which are in good agreement with experimental data.

To further enhance the accuracy of the predictions, it is possible to assign a stronger weighting to the central difference scheme. However, this adjustment comes at the cost of relaxing the convective boundedness criterion, which can impact the stability of the solution (Jasak et al., 1999). Nonetheless, it is important to consider that modifying the blending parameter can also influence the transition from Reynolds-Averaged Navier-Stokes (RANS) to Large Eddy Simulation (LES). The RANS-LES transition depends not only on the grid sizes but also on the predicted stresses. With higher-order schemes such as pure central differencing scheme or discontinuous Galerkin methods, the transition can occur more rapidly as the velocity predictions obtained are more accurate with higher order schemes (Leonard, 1991).

In this thesis, the primary objective is to assess the methodology as it is formulated without introducing any modifiers such as changing the value of blending factor in BCD which suggests the combination of grid sizes, numerical schemes and turbulence models are reasonably acceptable considering that the predicted results have shown to agree well with the experimental data.

The attempt was also made in the thesis to obtain the grid recommendations which can be used for other hybrid RANS-LES methods such as DDES or IDDES where the grid obtained falls within the acceptable limits of cell counts. Though the attempt was based on the hexahedral grids but the recommendations made can be adapted to any type of grids. For the Poly-hex core grid used in the thesis, the grid sizes are obtained were consistent with the recommendations made for hexahedral grids.

7.3. Critical parameters affecting both drag and noise and their relationships

The side window of a vehicle is a significant source contributing to the overall noise radiated, mainly due to pressure fluctuations caused by the flow past the A-pillar and the shedding of vortices from the mirror. The analysis of the pressure fluctuations plot reveals that the areas with high intensity are predominantly located within the wake region behind the mirror. This finding remains consistent even in the case of a standalone mirror. The wake region can be characterised by a key parameter, the length of the wake (L_{ws}).

Additionally, the presence of a horseshoe vortex formed upstream of the mirror has a considerable impact on the flow past the A-pillar, resulting in the formation of a distinct flow interaction line. Both experimental and numerical results from SAE T4 report the presence of this flow interaction line. To quantify this flow interaction, the angle (α) between the A-pillar and the tangent drawn to the flow interaction line can be measured.

The introduction of mirror inclination (θ) demonstrates an interesting observation: both L_{ws} and α exhibits a linear variation. This linear variation is illustrated in the Fig. 7.1. The linear behaviour can be because of the linear reduction in the characteristic lengths associated with horseshoe vortex. The change in the mirror inclination led to less pressure stagnation on the front face of the mirror because of which the thickness of the horseshoe vortex formed upstream is reduce and the flow separation from the lateral edges tends to merge as a result the width of the horseshoe vortex decreases, leading to an increase in the angle between the A-pillar and the flow interaction line.

It is worth noting that the merging of vortex also influences the overall drag of the vehicle, the analysis of which is presented in the results of **Chapter 6**.

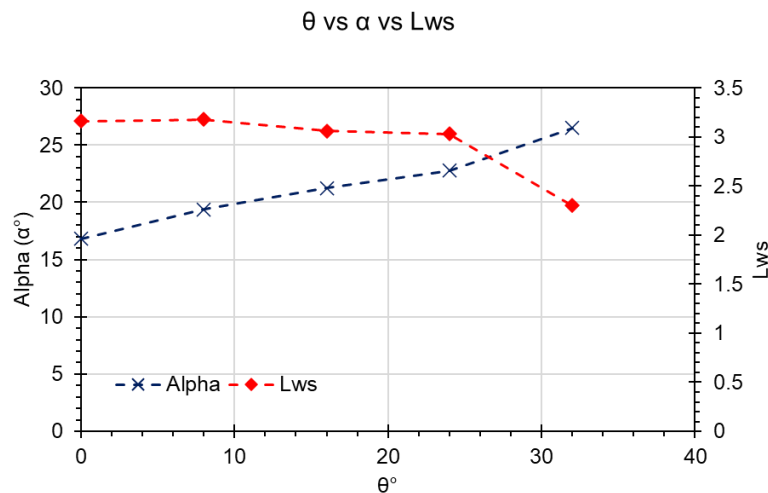


Fig. 7.1. Relationship between θ , α , and L_{ws} .

A similar observation at least can be drawn from point of view of horseshoe vortex if the changes in the Aspect Ratio (AR) of the mirror are changed. Larger the Aspect Ratio the L_{ws} tends to increase. However, as Aspect Ratio was not considered for vehicle noise studies, a similar behaviour can be expected, where the increase in the AR will result in decrease in the angle made between A-pillar and the flow interaction line.

It is worth mentioning that such relationships are a step towards understanding the critical flow features that contribute to the noise radiation. By performing more sensitive study such as varying the inflow velocities and changing the geometry can be realistic, it is possible to obtain a scaling equation between these parameters and noise radiated which will potentially help for optimisation the mirror geometries to reduce the overall noise radiation and drag experienced by the vehicle body.

7.4. Limitations of the work

A notable limitation of this study is the utilisation of simplified geometry, primarily relying on the standardised vehicle and mirror geometry, which may restrict the comprehensive assessment of the implemented methodology. Although the standardised vehicle model offers realistic features that enable the capture and analysis of essential data pertaining to flow properties, pressure distribution, noise generation, and acoustic characteristics, its simplicity compared to actual production-like vehicles such as DrivAer may introduce uncertainties when extrapolating the findings to real-world scenarios. The absence of more complex and representative geometries similar to production vehicles limits the ability to fully explore the robustness and generalisability of the proposed methodology. Future research should consider incorporating more intricate and production-based geometries such as DrivAer to enhance the reliability and applicability of the findings.

This PhD thesis focuses on studying the hydrodynamic pressure fluctuations and their contribution to the noise generated. However, it should be noted that the acoustic pressure fluctuations, which are also a source of noise, were not considered in this study. This limitation arises from the assumptions made in this research, particularly the assumption of incompressibility. Consequently, the effects of compressibility and rarefaction were neglected. Despite the incompressible assumption, the noise radiated obtained in the case of HRM is in good agreement with experimental results. While no such comparison was not made in the case of SAE T4 due to no availability of the microphone data.

The error estimates in the grid can be estimated using techniques such as Richardson extrapolation could have been used as addition check while performing grid independency study to understand the errors presents in the work more quantitatively. Furthermore, benchmark tests such as Taylor-Green Vortex or periodic hills test cases may further add confidence in the methodology and aide in tuning the numerical methods such as BCD schemes may be implemented to improve the accuracy and reduce the computational resource.

The overall runtime for all simulations can still be debated, in all the cases investigated convective cycles approach is used in accordance with best practices but a better runtime criterion based on doing time based independent study could further enhance the accuracy of the results predicted. Further, improvement may be achieved in the run time with $CFL > 1$; nevertheless, this needs more exploration of the adopted methodology.

7.5. Recommendations

To further expand the research presented in this thesis, the geometrical changes implemented here can be introduced to realistic mirrors, and mirrors mounted on realistic vehicles, such as DrivAer models, can further provide insights and additional flow parameters that govern the noise generation and overall drag. For example, A-pillar with rain gutter may result in strong flow separation near the A-pillar which alter not only the horseshoe vortex formation around the mirror but also the intensity of pressure fluctuations exerted on the side window. Similarly, geometrical features such as thickness of the foot and the height of the mirror foot may be critical parameters for noise generation.

In addition to the geometrical features, changing the assumption of flow from incompressible to compressible will allow the simulation to represent more realistic behaviour and the noise generated contain both hydrodynamic and acoustic components which by using techniques such as Wave Frequency Spectra (WFS), the hydrodynamic and acoustic pressure fluctuations exerted on the side window can be examined. And the analysis of which component is causing the mitigation of noise when geometrical changes are introduced will add more insights for optimising the mirrors. Furthermore, the noise transmitted inside the cabin can be determined given the meshing methodology used in this study is tailored such as adding an additional check to evaluate spurious noise generated at the interfaces and deploying acoustic damping mechanisms, the level of reduction in the noise transmitted inside the cabin can be obtained. Alternatively, this methodology may also be implemented with Acoustic perturbation wave equation and obtain the noise radiated inside at reasonable computational resource compared to compressible simulation. Subsequently, by including a vibroacoustic simulation that accounts for the interaction of vibration of the side window due to the pressure fluctuations exerted may be evaluated.

Lastly, the investigation into various models used to study the unique features of a notchback vehicle, the SAE T20, has shown a consistent inability to predict the observed asymmetry in experimental data. This asymmetry is primarily attributed to the shear separating layer on the vehicle's backlight. Given these findings, using hybrid RANS-LES methodologies to predict this subtle feature appears challenging due to their inherit modelling formulation closer to the wall. Instead, employing advanced wall-resolving formulations such as Large Eddy Simulation (LES) can potentially be a beneficial approach to better tackle the complexities associated with predicting asymmetry.

This study aimed to assess the feasibility of using a hybrid Computational Aeroacoustics (CAA) approach for evaluating the noise generated and radiated by the external flow past a vehicle, as well as identifying critical geometrical features that influence both drag and radiated noise. The findings can be summarised as follows:

1. The hybrid CAA method based on the Stress-Blended Eddy Simulation (SBES) and Ffowcs Williams-Hawkings (FW-H) analogy was found to be the most accurate approach for evaluating radiated noise. The obtained methodology was robust and accurate in predicting flow features and noise levels reasonable in good agreement with experimental data.
2. The SBES model showed enhanced capabilities in resolving flow features compared to the standard $k-\omega$ SST model. It also displayed better resolution of internal flow structures and a more rapid transition from Reynolds-Averaged Navier-Stokes (RANS) to Large Eddy Simulation (LES) than SDES.
3. Increasing the backlight angle of the vehicle led to an increase in drag force, as the location of flow impingement on the boot deck influenced the size of near-wake structures. The increase in backlight angle also caused the flow features on the rear slant to become more asymmetric.
4. Changing the aspect ratio (AR) of the half-round mirror (HRM) affected the recirculation bubble size, wake length, and pressure fluctuations, leading to increase in radiated noise with increase in AR.
5. While increasing the sweep angle (θ) of the HRM dampened radiated noise due to reduced pressure fluctuations exerted on the mounting surface. The changes made to the geometrical features of the mirror had no influence on the structure of the radiated noise.
6. The removal of side-view mirror from the vehicle showed that the A-pillar became a dominant noise source. Mirror inclinations had varying effects on aerodynamic drag, with an inclination of 16° resulting in minimal drag. The imbalance in the side force coefficient caused by mirror-induced vortices and separated flow reattachment on the side of the vehicle influenced the drag coefficient. While the radiated noise showed a

significant decrease with increase in the mirror inclination. The results also reveal that in presence of the mirror the dominant noise source was the side window.

Overall, the present work provides an assessment of hybrid RANS-LES methods and their limitations in detail by comparing the various numerical predictions against the experimental data. It was shown that SBES switches rapidly in Shear Separated Layers (SSL) giving distinct advantage over other Hybrid RANS-LES methods. Also, it was shown that asymmetry on the notchback increase because of depth of the rear slant and asymmetry seems to affect the component wise drag as the increase resulted in increase in the pressure drag experienced by the rear slant.

It is learned from the results that the mitigation of noise radiated from the vehicle may be achieved by the inclining the mirror such that the mirror is closer to the side window. However, such changes may have adverse effects on the drag therefore, such modifications should be carefully considered. Also, the structure of the radiated noise closer to the sources are highly influenced by the sources which results in dipole-like structures while moving away from the sources, the influence is reduced as a result the structure represents more like a monopole. This observation was consistent in both the aeroacoustics cases investigated.

The thesis has attempted to provide some insights into the influence of critical geometrical features on drag and radiated noise that can aid in the design and positioning of mirrors for improved aerodynamic performance and reduced noise levels. The findings and conclusions presented in this study can serve as a foundation for further research and development in the field of vehicle noise reduction and aerodynamic design.

Appendix – A

Location of Surface Probes and Microphones

Table A1

Cartesian coordinates of the sensors located on the standard HRM in m

Sensor	x	y	z	Sensor	x	y	z
s1	0.0936	0.0667	-0.0998	s18	0	0.1000	0
s2	0.0936	0.1333	-0.0998	s19	0	0.0667	0
s3	0.0936	0.1667	-0.0998	s20	0	0.0333	0
s4	0.0936	0.2000	-0.0998	s21	0.0034	0.1333	-0.0259
s5	0.0936	0.2258	-0.0964	s22	0.0134	0.1333	-0.0500
s6	0.0936	0.2499	-0.0864	s23	0.0293	0.1333	-0.0707
s7	0.0936	0.2864	-0.0499	s24	0.0500	0.1333	-0.0866
s8	0.0936	0.2964	-0.0258	s25	0.0741	0.1333	-0.0966
s9	0.0936	0.2998	0	s26	0.1000	0.1500	0.0850
s10	0.0741	0.2966	0	s27	0.1000	0.2850	-0.0111
s11	0.0500	0.2866	0	s28	0.1000	0.2674	-0.0517
s12	0.0293	0.2707	0	s29	0.1000	0.2111	-0.0843
s13	0.0134	0.2500	0	s30	0.1000	0.1500	-0.0850
s14	0.0034	0.2259	0	s31	0.1000	0.0500	-0.0850
s15	0	0.2000	0	s32	0.1000	0.0500	0
s16	0	0.1666	0	s33	0.1000	0.2000	0
s17	0	0.1333	0	s34	0.1000	0.2500	0

Table A2

Cartesian coordinates of the sensor location on the standard HRM and the plate in m

Sensor	x	y	z
s111	0.1	0.1167	0.085
s112	0.1	0.2517	0.0674
s113	0.1	0.2517	-0.0674
s114	0.1	0.1167	-0.085
s119	0.2	0	0

s120	0.1995	0	-0.1105
s121	0.2989	0	-0.1209
s122	0.3984	0	-0.1314
s123	0.4978	0	-0.1418

Table A3

Cartesian coordinates of the microphone locations in m

Microphone	x	y	z
M1	-0.248	0.446	0.2469
M4	0.1	0.2	-0.5
M10	0.453	0.5458	0
M11	0.453	0.446	-0.2469
M14	0.1	1.615	-1.4345

Table A4

Cartesian coordinates of the sensors located on the side window in m

Sensor	x	y	z	Sensor	x	y	z
s1	1.23221	0.81708	0.80001	s21	1.60021	0.92508	0.80001
s2	1.23221	0.87108	0.80001	s22	1.60021	0.97908	0.80001
s3	1.23221	0.92508	0.80001	s23	1.60021	1.03308	0.80001
s4	1.32421	0.81708	0.80001	s24	1.60021	1.08708	0.80001
s5	1.32421	0.87108	0.80001	s25	1.60021	1.14108	0.80001
s6	1.32421	0.92508	0.80001	s26	1.69221	0.81708	0.80001
s7	1.32421	0.97908	0.80001	s27	1.69221	0.87108	0.80001
s8	1.41621	0.81708	0.80001	s28	1.69221	0.92508	0.80001
s9	1.41621	0.87108	0.80001	s29	1.69221	0.97908	0.80001
s10	1.41621	0.92508	0.80001	s30	1.69221	1.03308	0.80001
s11	1.41621	0.97908	0.80001	s31	1.69221	1.08708	0.80001
s12	1.41621	1.03308	0.80001	s32	1.69221	1.14108	0.80001
s13	1.50821	0.81708	0.80001	s33	1.78421	0.81708	0.80001
s14	1.50821	0.87108	0.80001	s34	1.78421	0.87108	0.80001
s15	1.50821	0.92508	0.80001	s35	1.78421	0.92508	0.80001

s16	1.50821	0.97908	0.80001		s36	1.78421	0.97908	0.80001
s17	1.50821	1.03308	0.80001		s37	1.78421	1.03308	0.80001
s18	1.50821	1.08708	0.80001		s38	1.78421	1.08708	0.80001
s19	1.60021	0.81708	0.80001		s39	1.78421	1.14108	0.80001
s20	1.60021	0.87108	0.80001					

Table A5

Cartesian coordinates of the microphone locations in m

Microphone	x	y	z
Probe 1	1.26	0.82	0.9
Probe 2	1.06	1.06	0.9
Probe 3	1.06	0.82	1.2
Probe 4	1.4	0.95	1.15
Probe 5	2.3	1.1	1.3
Probe 6	1.6	0.92	1.8
Probe 7	2.5	0.75	4

In this section a detail list of procedures and scripts that are used to access the SHU-Cluster facility. For the benefit of the reader, several codes that are used throughout this work is detailed; such as User Defined Scalar functions (UDS), User Defined Functions (UDF) and Journal files.

B.1. Access to Cluster and File Management

SHU-cluster can be accessed using specific packages which have to be installed in the local PC through SHU-AppsAnywhere environment. Xming package has to be installed to access Fluent with Graphical User Interface (GUI). Xming package is installed using Multiple Windows Options to ensure robust control on the GUI.

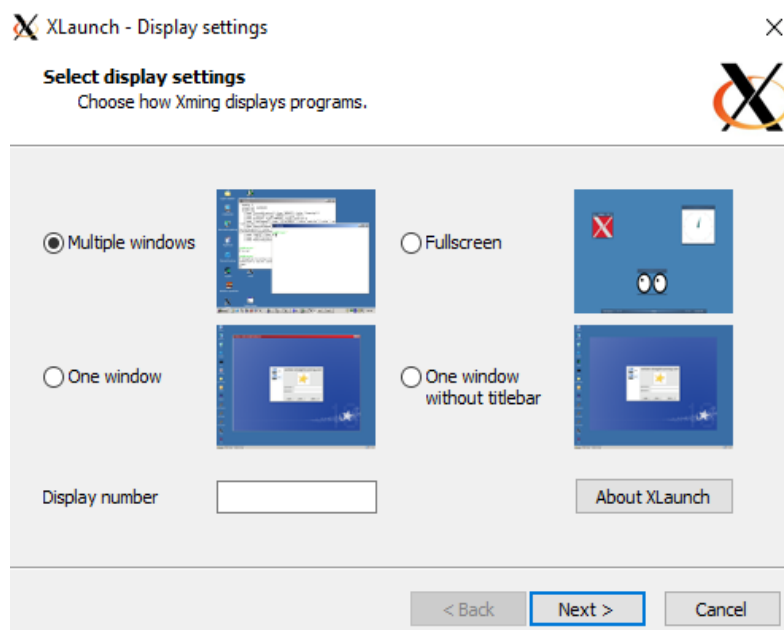


Fig.C1. Xming Installation window.

Open Putty using AppsAnywhere and run the application. To login into the SHU-Cluster, Putty is configured using Host Name: hpc.hallam.shu.ac.uk and port: 22 Fig.C2(a). Enable X11 forwarding with X display location as localhost: 0.0 to use Graphical User Interface (GUI) through Xming through SSH tunnelling as shown in Fig.C2(b). Login to the SHU-Cluster using login credentials.

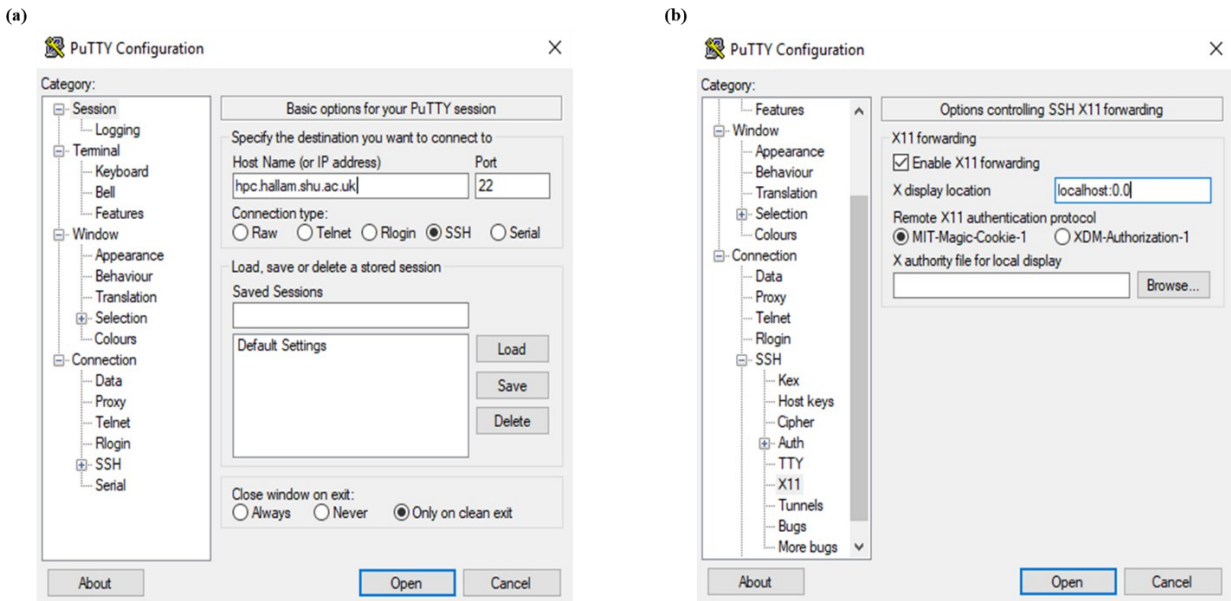


Fig.C2. Putty Configuration

FileZilla is used to manage file transfers from SHU-Cluster to local PC. FileZilla package is activated, and a connection is established with SHU-Cluster using the Host: sftp://hpc.hallam.shu.ac.uk with port:22 and user login credentials as seen in Fig.C3. The left side of the window in FileZilla indicates drives in local PC whereas on the right side they show the files in Cluster. Drag and drop operation is carried to transfer files from Cluster to local PC or vice-versa.

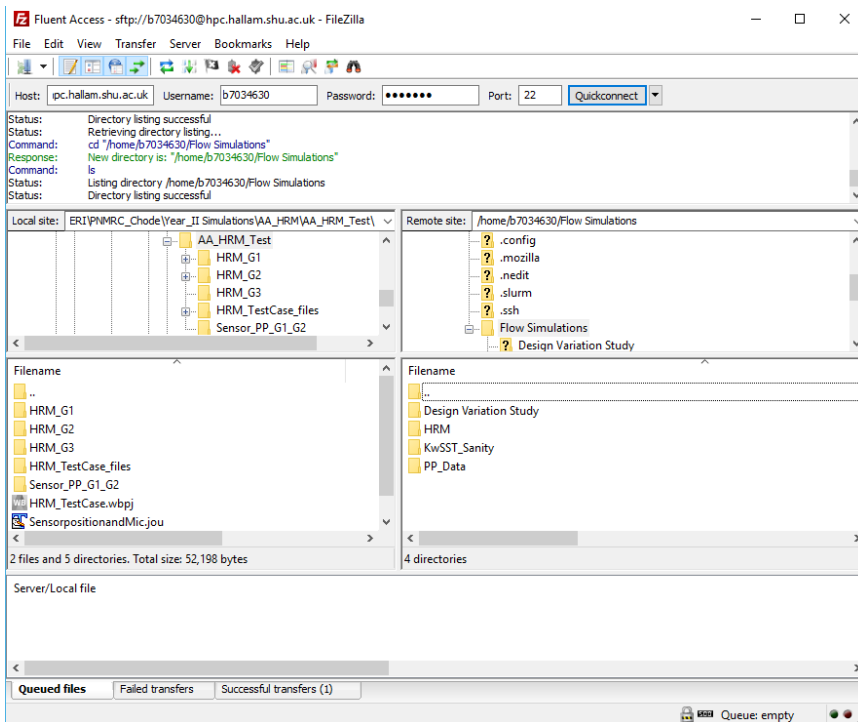


Fig.C. 3: FileZilla Window Outline

B.2. Fluent Activation files

B.2.1. Fluent in GUI mode

The script to activate Fluent module in Cluster using “**fluent-srun.sh**” script. Necessary changes can be made to the script to activate different versions of Fluent.

Script – 1: fluent-srun.sh

```
# Fluent Module Selection _ KKC_Original_17April2019

#!/usr/bin/env bash

module add ansys/ansys181research          #select the version of Fluent to
activate

HOSTSFILE=.hostlist-job$SLURM_JOB_ID

if [ "$SLURM_PROCID" == "0" ]; then

    srun hostname -f > $HOSTSFILE

    fluent 3ddp -t $SLURM_NTASKS -cnf=$HOSTSFILE -ssh -pinfiniband -
mpi=ibmmpi -driver x11                    #3d - Three Dimensions #dp -
Double Precision

    rm -f $HOSTSFILE

fi

exit 0
```

To run Fluent in GUI mode using Putty, the above script is called using the command “**sbatch -n 128 –nodelist=hp001,hp002,hp003,hp004,hp005 ./fluent-srun.sh**” where 128 specifies the number of CPU’s

B.2.2. Fluent in batch Mode

Script – 2. Unsteady_AA_HRM.jou

```
;;; Fluent- HRM - Aeroacoustic Setup
;;; V01 29Oct19 AA_KKC

(define CFILENAME "HRM_XXXX.cas.gz")
(define DFILENAME "HRM_XXXX.dat.gz")
(define AUTOSAVE_ROOT_NAME "HRM_XXXX")
(define NOTS "10000")
(define IITR "20")
(define TIMESTEP "3E-5")
```

```

(define AUTOSAVE_INTERVAL "854")
(define INTPHASE "HRM_xxxx_0.3")
(define FILE_OVERWRITE "yes")
(define FLOW_TIME "3")
;;;START TRANSCRIPT
(define command (format #f "/file/start-transcript ~a~a" AUTOSAVE_ROOT_NAME
"_transcript.txt"))
(ti-menu-load-string command)
;;; STEUP AUTOPARTITION - FORCE METIS
/parallel/partition/auto/use case-file partition method?
no
/parallel/partition/auto/method
metis
;;; Read case file
(define command (format #f "/file/read-case ~a" CFILENAME))
(ti-menu-load-string command)
;;; Read data file
(define command (format #f "/file/read-data ~a" DFILENAME))
(ti-menu-load-string command)
;;;Start parallel timer
/parallel/timer/reset
;;;Autosave Setup
(define command (format #f "/file/auto-save/root-name ~a~a~a"
AUTOSAVE_ROOT_NAME ".gz"))
(ti-menu-load-string command)
(define command (format #f "/file/auto-save/data-frequency ~a"
AUTOSAVE_INTERVAL))
(ti-menu-load-string command)
(define command (format #f "/file/auto-save/append-file-name-with/flow-time
~a" FLOW_TIME))
(ti-menu-load-string command)
;;; Solution Setup
(define command (format #f "/solve/set/time-step ~a" TIMESTEP))
(ti-menu-load-string command)
(define command (format #f "/solve/dual-time-iterate ~a~a" NOTS IITR))
(ti-menu-load-string command)
;;; Write Case and data files

```

```

(define command (format #f "/file/write-case ~a~a~a" "." INTPHASE
".cas.gz"))

(ti-menu-load-string command)

(define command (format #f "/file/write-data ~a~a~a" "." INTPHASE
".dat.gz"))

(ti-menu-load-string command)

;;;parallel timer end

/parallel/timer/usage

;-----Time Averaging Quantity runs-----

;;;parallel timer reset

/parallel/timer/reset

;;;Time averaging the quantities

(define YES "yes")

(define command (format #f "/solve/set/data-sampling ~a" YES 1 yes yes))

(ti-menu-load-string command)

;;;creating surface points for monitoring pressure fluctuations

;-----

(define sen_111 "S111")

(define command (format #f "/surface/point-array ~a ~d ~d ~d ~d ~d ~d ~d"
sen_111 1 0.100 0.11671 0.0850 0.100 0.11671 0.0850))

(ti-menu-load-string command)

(define sen_112 "S112")

(define command (format #f "/surface/point-array ~a ~d ~d ~d ~d ~d ~d ~d"
sen_112 1 0.10000000000000001 0.2517 0.0674 0.10000000000000001 0.2517
0.0674))

(ti-menu-load-string command)

(define sen_113 "S113")

(define command (format #f "/surface/point-array ~a ~d ~d ~d ~d ~d ~d ~d"
sen_113 1 0.10000000000000001 0.2517 -0.0674 0.10000000000000001 0.2517 -
0.0674))

(ti-menu-load-string command)

(define sen_114 "S114")

(define command (format #f "/surface/point-array ~a ~d ~d ~d ~d ~d ~d ~d"
sen_114 1 0.100 0.11671 -0.0850 0.100 0.11671 -0.0850))

(ti-menu-load-string command)

```

```

(define sen_116 "S116")
(define command (format #f "/surface/point-array ~a ~d ~d ~d ~d ~d ~d ~d"
sen_116 1 -0.040000000000000001 0.00 0.00 -0.040000000000000001 0.00 0.00))
(ti-menu-load-string command)

(define sen_117 "S117")
(define command (format #f "/surface/point-array ~a ~d ~d ~d ~d ~d ~d ~d"
sen_117 1 -0.080000000000000001 0.00 0.00 -0.080000000000000001 0.00 0.00))
(ti-menu-load-string command)

(define sen_118 "S118")
(define command (format #f "/surface/point-array ~a ~d ~d ~d ~d ~d ~d ~d"
sen_118 1 -0.120000000000000001 0.00 0.00 -0.120000000000000001 0.00 0.00))
(ti-menu-load-string command)

(define sen_119 "S119")
(define command (format #f "/surface/point-array ~a ~d ~d ~d ~d ~d ~d ~d"
sen_119 1 0.200000000000000001 0.00 0.00 0.200000000000000001 0.00 0.00))
(ti-menu-load-string command)

(define sen_120 "S120")
(define command (format #f "/surface/point-array ~a ~d ~d ~d ~d ~d ~d ~d"
sen_120 1 0.1995 0.00 -0.1105 0.1995 0.00 -0.1105))
(ti-menu-load-string command)

(define sen_121 "S121")
(define command (format #f "/surface/point-array ~a ~d ~d ~d ~d ~d ~d ~d"
sen_121 1 0.2989 0.00 -0.1209 0.2989 0.00 -0.1209))
(ti-menu-load-string command)

(define sen_122 "S122")
(define command (format #f "/surface/point-array ~a ~d ~d ~d ~d ~d ~d ~d"
sen_122 1 0.3984 0.00 -0.1314 0.3984 0.00 -0.1314))
(ti-menu-load-string command)

(define sen_123 "S123")
(define command (format #f "/surface/point-array ~a ~d ~d ~d ~d ~d ~d ~d"
sen_123 1 0.4978 0.00 -0.1418 0.4978 0.00 -0.1418))
(ti-menu-load-string command)

```

```

;-----
;;;Creating Sensor Reports Defintion
(define MP "Pressure_sensors")      ;;; Report name
(define RT "surface-areaavg")      ;;;Type of Report
(define FIELD "rmse-pressure")     ;;;Quantity to be monitored
(define YES "yes")

(define command (format #f "/solve/report-definitions/add ~a ~a \n surface-
names ~a \n field ~a \n per-surface? ~a"
MP RT sen_111 sen_112 sen_113 sen_114 sen_116 sen_117 sen_118 sen_119 sen_120
sen_121 sen_122 sen_123 () FIELD YES))

(ti-menu-load-string command)

;;;Creating Sensor Reporting Files for all the sensors
(define command (format #f "/solve/report-files/add ~a \n file-name ~a \n
report-defs ~a" MP MP MP))

(ti-menu-load-string command)

;;;Running the Simulation
(define NNOTS "6666")
(define NITR "15")
(define command (format #f "/solve/dual-time-iterate ~a~a" NNOTS NIITR))
(ti-menu-load-string command)

;;;Parallel Timer End
/parallel/timer/usage

;;;Saving final case and data file
(define FPHASE "HRM_0.5")
(define command (format #f "/file/write-case ~a~a~a" "." FPHASE ".cas.gz"))
(ti-menu-load-string command)
(define command (format #f "/file/write-data ~a~a~a" "." FPHASE ".dat.gz"))
(ti-menu-load-string command)

;;;STOP TRANSCRIPT
/file/stop-transcript
exit

```

B.3. User Defined Functions and Scalars

B.3.1. User-Defined Function

Defining the velocity profile at the inlet using a User Defined Function (UDF) and compiled using Fluent. The velocity inlet profile is based on 1/7th power-law, as observed in experiments conducted by Wood (2015).

Script – 3: InletVelocity.c

```
/**Velocity Inlet Profile_KKC_Original_12April2018**/  
#include "udf.h"  
#define Umax 39.6  
#define n 1./7.  
#define YMIN 0.0  
#define YMAX 0.06  
#define MaxVel 40.0  
DEFINE_PROFILE(Inlet_vel,t,i)  
{  
    real y,h,x[ND_ND],del;  
    face_t f;  
    begin_f_loop(f,t)  
    {  
        F_CENTROID(x,f,t);  
        y = x[1];  
        if (y<=YMAX)  
            F_PROFILE(f,t,i)=Umax*pow(y/YMAX,n);  
        else  
            F_PROFILE(f,t,i)= MaxVel;  
    }  
end_f_loop(f,t)  
}
```

To compile the above the script, under user-defined tab select functions command, a compiled UDFs window is seen as shown in Fig.C4. Load the script by adding the script under source files and then build the library.

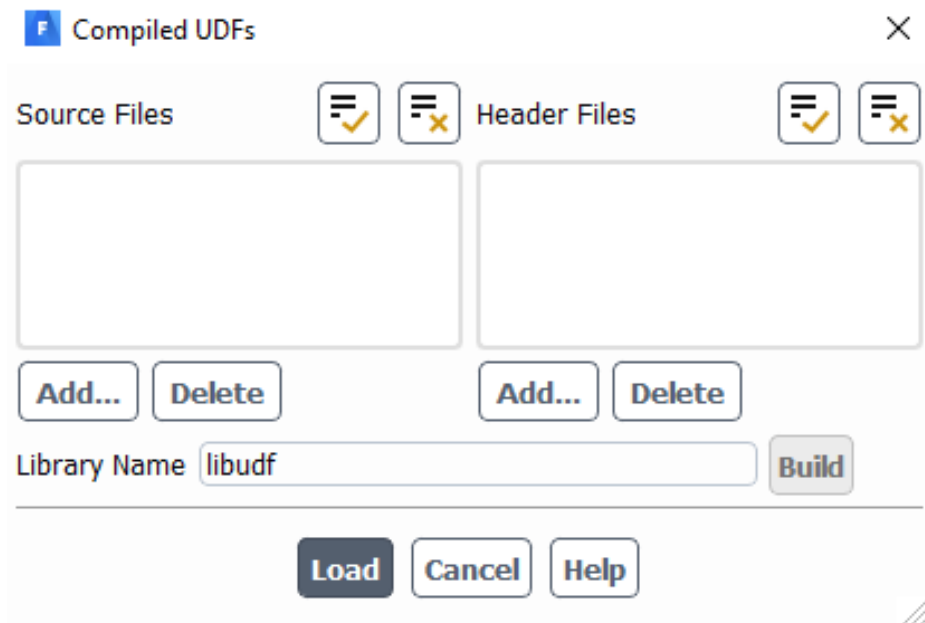


Fig.C4. Compiled UDF's window

B.3.2. User-Defined Scalar

Script – 4 represents the User Defined Scalar (UDS) code that is executed to calculate the average quantities on the vorticity.

Script – 4. Mean Xvorticity.c

```

/****Mean X Vorticity_UDS_KKC_Original_18Sept2019****/

#include "udf.h"
#include "sg.h"
#include "mem.h"

DEFINE_ON_DEMAND(Mean_Xvorticity)
{
    Domain *d = Get_Domain(1);
    Thread *t;
    cell_t c;
    real delta_time_sampled = RP_Get_Real("delta-time-sampled");
    thread_loop_c(t,d)
    {
        begin_c_loop(c,t)
        {
C_UDSI(c,t,0) = C_STORAGE_R(c,t, SV_U_MEAN)/delta_time_sampled;
C_UDSI(c,t,1) = C_STORAGE_R(c,t, SV_V_MEAN)/delta_time_sampled;
    C_UDSI(c,t,2) = C_STORAGE_R(c,t, SV_W_MEAN)/delta_time_sampled;
        }
    }
}

```

```

    }
    end_c_loop(c,t);
}
/*Taking Derivatives of dummy UDS values*/
Alloc_Storage_Vars(d,SV_UDSI_RG(0),SV_UDSI_G(0),SV_NULL);
Scalar_Reconstruction(d,SV_UDS_I(0),-1,SV_UDSI_RG(0),NULL);
Scalar_Derivatives(d,SV_UDS_I(0),-1,SV_UDSI_G(0),
SV_UDSI_RG(0),NULL);
Alloc_Storage_Vars(d,SV_UDSI_RG(1),SV_UDSI_G(1),SV_NULL);
Scalar_Reconstruction(d,SV_UDS_I(1),-1,SV_UDSI_RG(1),NULL);
Scalar_Derivatives(d,SV_UDS_I(1),-1,SV_UDSI_G(1),
SV_UDSI_RG(1),NULL);
Alloc_Storage_Vars(d,SV_UDSI_RG(2),SV_UDSI_G(2),SV_NULL);
Scalar_Reconstruction(d,SV_UDS_I(2),-1,SV_UDSI_RG(2),NULL);
Scalar_Derivatives(d,SV_UDS_I(2),-1,SV_UDSI_G(2),
SV_UDSI_RG(2),NULL);
thread_loop_c(t,d)
{
    begin_c_loop(c,t)
    {
        C_UDMI(c,t,0)=(C_UDSI_G(c,t,2)[1]-C_UDSI_G(c,t,1)[2]);
    }
    end_c_loop(c,t);
}
}

```

To compile the above script, a similar procedure has to be followed as shown above for script – 3. Once the script is loaded, under user-defined tool, set User Defined Scalars (UDS) as 1 and User Defined Memory (UDM) as 1 and then Executive on Demand.

B.4. Data Processing using MATLAB

B.4.1. Surface Plots from Experimental Data

The surface plots representing normalised velocity magnitude plots are generated from the experimental data available at Loughborough University Repository. The following MATLAB script is used to generate the plots.

Script – 5: 2D_Streamwise_VP_Exp_data.m

```
%Streamwise-velcoity-plot-Experiments_KKC_Original_07July2018%

clc;

%import file code

filename      = 'Red_Cam1_Y=-30mm_Average.dat';
delimiterIn   = ' ';
headerlinesIn = 6;

D = importdata(filename,delimiterIn,headerlinesIn);
Raw_Data = D.data;
x = D.data(:,1);
y = D.data(:,2);
z = D.data(:,3);
vx = D.data(:,4);
vy = D.data(:,5);
vz = D.data(:,6);

% Adding Velocity Contour
velocity = (sqrt(vx.^2 + vy.^2 + vz.^2)/40);
pointsize = 20;
scatter(x, z, pointsize,velocity, 'filled','s');
axis tight
set(gca,'Ydir','reverse')
set(gca,'TickDir','out')

%Adding colobar and axis labels
c = colorbar;
set(0,'DefaultFigureColormap',feval('jet'));
title(c,{'Umag'},'fontweight','normal','fontsize',12)
xlabel('x (mm)','fontweight','normal','fontsize',12)
ylabel('z (mm)','fontweight','normal','fontsize',12)
```

Further, the streamlines are generated from the same data which is superimposed on normalised velocity magnitude plot using Script – 6.

Script – 6. 2D_StreamlinePlot_Exp.m

```
%Streamlineplot-Experiments_KKC_Original_08July2019%
clc;
%import file code
filename      = 'Red_Cam1_Y=-30mm_Average.dat';
delimiterIn   = ' ';
headerlinesIn = 6;
D = importdata(filename,delimiterIn,headerlinesIn);
Raw_Data = D.data;
x = D.data(:,1);
y = D.data(:,2);
z = D.data(:,3);
vx = D.data(:,4);
vy = D.data(:,5);
vz = D.data(:,6);
% Adding Velocity Contour
velocity = (sqrt(vx.^2 + vy.^2 + vz.^2)/40);
pointsize = 20;
scatter(x, z, pointsize,velocity, 'filled','s');
axis tight
set(gca,'Ydir','reverse')
set(gca,'TickDir','out')
%Adding colobar and axis labels.
c = colorbar;
set(0,'DefaultFigureColormap',feval('jet'));
title(c,{'Umag'},'fontweight','normal','fontsize',12)
xlabel('x (mm)','fontweight','normal','fontsize',12)
ylabel('z (mm)','fontweight','normal','fontsize',12)
hold on
%Adding Streamline
Fvx = scatteredInterpolant(x,z,vx,'nearest','nearest');
Fvz = scatteredInterpolant(x,z,vz,'nearest','nearest');
[x1,z1] = meshgrid(linspace(min(x),max(x)),...
```

```

    linspace(min(z),max(z)));
Vx1 = Fvx(x1,z1);
Vz1 = Fvz(x1,z1);
[s_x,s_z] = meshgrid(linspace(-700,-420,8),linspace(-350,-50,100));
hlines = streamline(x1,z1,Vx1,Vz1,s_x(:,6),s_z(:,6));
hlines2 = streamline(x1,z1,-Vx1,-Vz1,s_x(:,6),s_z(:,6));
% colouring the streamlines
set(hlines,'LineWidth',0.5,'Color','k')
set(hlines2,'LineWidth',0.5,'Color','k')
axis tight
set(gca,'Ydir','reverse')
set(gca,'TickDir','out')
savefig('Streamline_Exp_y30')

```

Mean X vorticity is plotted for the same data using the Script – 7

Script – 7. Mean_Xvorticity_Exp.m

```

%Vorticityplot-Experiments_KKC_Original_30July2019%
clc;
%import file code
filename      = 'Exp_y_0_Avergae.dat';
delimiterIn   = ' ';
headerlinesIn = 6;
D = importdata(filename,delimiterIn,headerlinesIn);
Raw_Data = D.data;
x = D.data(:,1);
y = D.data(:,2);
z = D.data(:,3);
vx = D.data(:,4);
vy = D.data(:,5);
vz = D.data(:,6);
Fvx = scatteredInterpolant(x,z,vx,'nearest','nearest');
Fvz = scatteredInterpolant(x,z,vz,'nearest','nearest');
[x1,z1] = meshgrid(linspace(min(x),max(x)),...
    linspace(min(z),max(z)));
Vx1 = Fvx(x1,z1);
Vz1 = Fvz(x1,z1);

```

```

[s_x,s_z] = meshgrid(linspace(-750,-400,8),linspace(-350,-50,100));
vor = curl(x1,z1,Vx1,Vz1);
pcolor(x1,z1,vor);
shading interp;
axis tight;
set(gca,'Ydir','reverse')
set(gca,'TickDir','out')

```

Script – 8 is used to generate spanwise velocity magnitude plots for the experimental data

Script – 8. 2D_Spanwise_VP_Exp_data.m

```

%Streamwise-velcoity-plot-Experiments_KKC_Original_07July2018%
clc;
filename      = 'Green_X=-290mm.dat';
delimiterIn   = ' ';
headerlinesIn = 6;
D = importdata(filename,delimiterIn,headerlinesIn);
Raw_Data = D.data;
x = D.data(:,1);
y = D.data(:,2);
z = D.data(:,3);
vx = D.data(:,4);
vy = D.data(:,5);
vz = D.data(:,6);

% Adding Velocity Contour
velocity = (sqrt(vx.^2 + vy.^2 + vz.^2)/40);
pointsize = 20;
scatter(y, z, pointsize, velocity,'filled');
axis tight
set(gca,'Ydir','reverse')
set(gca,'TickDir','out');

%Adding colorbar and axis labels.
c = colorbar
set(0,'DefaultFigureColormap',feval('jet'));
title(c,{'Umag/U'},'fontweight','bold','fontsize',12)
xlabel('Z (mm)','fontweight','bold','fontsize',12)
ylabel('Y (mm)','fontweight','bold','fontsize',12)

```

B.4.2. Surface plots for CFD data

To maintain consistency with the experimental data plotting certain plots from CFD are plotted using MATLAB Codes.

Script – 9. 2D_CFD _StreamlinePlot.m

```
%Streamwise-velocity-plot-Experiments_KKC_Original_31July2018%
%Importing data using .dat file
filename = 'SDES.dat';
delimiterIn = '\t';
headerlinesIn = 1;
D = importdata(filename,delimiterIn,headerlinesIn);
Raw_data = D.data;
x = D.data(:,1);
y = D.data(:,2);
z = D.data(:,3);
Umag = D.data(:,4);
vx = D.data(:,5);
vy = D.data(:,6);
%Adding velocity contour
pointsize = 30;
scatter(x, y, pointsize,Umag, 'filled','s');
c = colorbar
%colormap(brg);
title(c,{'Umag'},'fontweight','normal','fontsize',12);
xlabel('x (mm)','fontweight','normal','fontsize',12);
ylabel('z (mm)','fontweight','normal','fontsize',12);
hold on
%Adding streamlines
[sx,sy] = meshgrid(linspace(-0.75,-0.4,10),...
linspace(0.05,0.35,100))
Fvx = scatteredInterpolant(x,y,vx,'linear');
Fvy = scatteredInterpolant(x,y,vy,'linear');
[x1,y1] = meshgrid(linspace(min(x),max(x)),...
linspace(min(y),max(y)));
Xv = Fvx(x1,y1);
Yv = Fvy(x1,y1);
```

```

hlines = streamline(x1,y1,Xv,Yv,sx(:,8),sy(:,8));
hlines2 = streamline(x1,y1,-Xv,-Yv,sx(:,8),sy(:,8));
set(hlines,'LineWidth',0.1,'Color','k');
set(hlines2,'LineWidth',0.1,'Color','k');
axis tight;
hold off
%savefig('SDES')

```

Script – 10 is used to generated surface plots of mean x vorticity component for CFD data

Script – 10. 2D_CFD_MeanXvorticity.m

```

%Streamwise-velcoity-plot-Experiments_KKC_Original_31July2018%
%Importing data using .dat file

clc;
filename = 'SAET40_SBES_Sym.dat';
delimiterIn = '\t';
headerlinesIn = 1;
D = importdata(filename,delimiterIn,headerlinesIn);
Raw_data = D.data;
x = D.data(:,1);
y = D.data(:,2);
z = D.data(:,3);
Umag = D.data(:,4);
vx = D.data(:,5);
vy = D.data(:,6);
[sx,sy] = meshgrid(linspace(-0.75,-0.4,10),...
linspace(0.05,0.35,100));
Fvx = scatteredInterpolant(x,y,vx,'linear');
Fvy = scatteredInterpolant(x,y,vy,'linear');
[x1,y1] = meshgrid(linspace(min(x),max(x)),...
linspace(min(y),max(y)));
Xv = Fvx(x1,y1);
Yv = Fvy(x1,y1);
vor = curl(x1,y1,Xv,Yv);
nomrVor = vor*(0.84/40);
pcolor(x1,y1,nomrVor);
shading interp;

```

```

c = colorbar;
set(0,'DefaultFigureColormap',feval('jet'));
title(c,{'Vorticity (1/s)'},'fontweight','normal','fontsize',12);
axis tight;
xlabel('x (mm)','fontweight','normal','fontsize',12);
ylabel('y (mm)','fontweight','normal','fontsize',12);
set(gca,'Ydir','reverse')
set(gca,'TickDir','out');
%savefig('SAET40_SBES_Sym')

```

B.4.3. Script for calculating pressure drag

Script -11: Pressure drag calculation

```

%Calculating Pressure drag for SAE T20

clc;
%%
%%Front Slant Pressure Drag
FD=readmatrix('SAET20_SBES_Front.txt');
Fdr=round(FD,4);
FD1u=unique(Fdr(:,1));
FD2u=unique(Fdr(:,2));
Fc1 =numel(FD1u)*numel(FD2u);
if (numel(FD(:,1))<Fc1)
    Na = [0 0 0];
    Far = (numel(FD1u)*numel(FD2u))-numel(FD(:,1));
    FDr=[Fdr;repmat(Na,Far,[])];
else
    FDr=Fdr;
end
Fy =repmat(FD1u.',numel(FD1u),1);
Fz =repmat(FD2u,1,numel(FD1u));
Fprs=reshape(FDr(:,3),numel(FD2u),[]);
intFpz=trapz(Fz(:,1),Fprs);
intF=abs(trapz(Fy(1,:),intFpz));
Fs=0.075848; %Frontalarea of front slant m2
Den = 1.225; %Density of the Fluid kg/m3
Vel = 40; %inflow velocity m/s

```

```

Cdf = (2*intF)/(Den*(Vel^2)*Fs)
%%
%%Rear Slant Pressure Drag%%
RD = readmatrix('SAET20_SBES_Rear.txt');
Rdr=round(RD,4);
RD1u=unique(Rdr(:,1));
RD2u=unique(Rdr(:,2));
Rc1 =numel(RD1u)*numel(RD2u);
if (numel(RD(:,1))<Rc1)
    Na = [0 0 0];
    Rar = (numel(RD1u)*numel(RD2u))-numel(RD(:,1));
    RDr=[Rdr;repmat(Na,Rar,[])];
else
    RDr=Rdr;
end
Ry =repmat(RD1u.',numel(RD1u),1);
Rz =repmat(RD2u,1,numel(RD1u));
Rprs=reshape(RDr(:,3),numel(RD2u),[]);
intRpz=trapz(Rz(:,1),Rprs);
intR=abs(trapz(Ry(1,:),intRpz));
%Fs=0.0217; %Frontalarea of Rear slant m2
Den = 1.225; %Density of the Fluid kg/m3
Vel = 40; %inflow velocity m/s
Cdr = (2*intR)/(Den*(Vel^2)*Fs)
%%
%%Base Pressure Drag%%
BD=readmatrix('SAET20_SBES_Base.txt');
Bdr=round(BD,3);
BD1u=unique(Bdr(:,1));
BD2u=unique(Bdr(:,2));
Bc1 =numel(BD1u)*numel(BD2u);
if (numel(BD(:,1))<Bc1)
    Na = [0 0 0];
    Bar = (numel(BD1u)*numel(BD2u))-numel(BD(:,1));
    BDr=[Bdr;repmat(Na,Bar,[])];
else

```

```

    BDr=Bdr;
end
By =repmat (BD1u.', numel (BD1u), 1);
Bz =repmat (BD2u, 1, numel (BD1u));
Bprs=reshape (BDr (:, 3), numel (BD2u), []);
intBpz=trapz (Bz (:, 1), Bprs);
intB=abs (trapz (By (1, :), intBpz));
%FAB=0.0479; %Frontalarea of front slant m2
Den = 1.225; %Density of the Fluid kg/m3
Vel = 40; %inflow velocity m/s
Cdb = (2*intB) / (Den* (Vel^2) *Fs)
%%
%%Total Pressure Drag
TPD = Cdf+Cdr+Cdb

```

References

- Ahmed, S.R., Ramm, G., Faltin, G., 1984. Some Salient Features Of The Time-Averaged Ground Vehicle Wake, in: SAE Technical Paper Series. <https://doi.org/10.4271/840300>
- Alam, M., Sandham, N.D., 2000. Direct numerical simulation of ‘short’ laminar separation bubbles with turbulent reattachment. *J. Fluid Mech.* 403, 223–250. <https://doi.org/10.1017/S0022112099007119>
- Aljure, D.E., Calafell, J., Baez, A., Oliva, A., 2018. Flow over a realistic car model: Wall modeled large eddy simulations assessment and unsteady effects. *J. Wind Eng. Ind. Aerodyn.* 174, 225–240. <https://doi.org/10.1016/j.jweia.2017.12.027>
- Aljure, D.E., Lehmkuhl, O., Rodríguez, I., Oliva, A., 2014. Flow and turbulent structures around simplified car models. *Comput. Fluids* 96, 122–135. <https://doi.org/10.1016/j.compfluid.2014.03.013>
- Ashton, N., Revell, A., 2015. Key factors in the use of DDES for the flow around a simplified car. *Int. J. Heat Fluid Flow* 54, 236–249. <https://doi.org/10.1016/j.ijheatfluidflow.2015.06.002>
- Ashton, N., Revell, A., 2014. Investigation into the predictive capability of advanced Reynolds-Averaged Navier-Stokes models for the DrivAer automotive model, in: *The International Vehicle Aerodynamics Conference*. Elsevier, pp. 125–137. <https://doi.org/10.1533/9780081002452.4.125>
- Ashton, N., West, A., Lardeau, S., Revell, A., 2016. Assessment of RANS and DES methods for realistic automotive models. *Comput. Fluids* 128, 1–15. <https://doi.org/10.1016/j.compfluid.2016.01.008>
- Ask, J., Davidson, L., 2010. Flow and Dipole Source Evaluation of a Generic SUV. *J. Fluids Eng.* 132, 0511111–0511112. <https://doi.org/10.1115/1.4001340>
- Ask, J., Davidson, L., 2009. A Numerical Investigation of the Flow Past a Generic Side Mirror and its Impact on Sound Generation. *J. Fluids Eng.* 131, 0621011–06110212. <https://doi.org/10.1115/1.3129122>
- Ask, J., Davidson, L., 2006. The Sub-Critical Flow Past a Generic Side Mirror and its Impact on Sound Generation and Propagation, in: *12th AIAA/CEAS Aeroacoustics Conference (27th AIAA Aeroacoustics Conference)*. American Institute of Aeronautics and Astronautics, Reston, Virginia, pp. 1925–1944. <https://doi.org/10.2514/6.2006-2558>
- Ask, J., Davidson, L., 2005. The near field acoustics of a generic side mirror based on an incompressible approach. *Div. Fluid Dyn. Dept. Appl. Mech.*
- AUTOCFD, 2019. Workshop 2019 [WWW Document]. URL <https://autocfd.eng.ox.ac.uk/#1st-workshop>
- Becker, S., Hahn, C., Kaltenbacher, M., Lerch, R., 2008. Flow-Induced Sound of Wall-Mounted Cylinders with Different Geometries. *AIAA J.* 46, 2265–2281. <https://doi.org/10.2514/1.34865>
- Becker, S., Nusser, K., Oswald, M., 2016. Aero-Vibro-Acoustic Wind Noise-Simulation Based on the Flow around a Car. *SAE Tech. Pap.* 2016-June. <https://doi.org/10.4271/2016-01-1804>

- Bonnaivon, G., Cadot, O., Herbert, V., Parpais, S., Vigneron, R., Détery, J., 2019. Asymmetry and global instability of real minivans' wake. *J. Wind Eng. Ind. Aerodyn.* 184, 77–89. <https://doi.org/10.1016/j.jweia.2018.11.006>
- Brown, G.J., Fletcher, D.F., Leggoe, J.W., Whyte, D.S., 2020. Application of hybrid RANS-LES models to the prediction of flow behaviour in an industrial crystalliser. *Appl. Math. Model.* 77, 1797–1819. <https://doi.org/10.1016/j.apm.2019.09.032>
- Cai, W., Li, Y., Liu, C., 2019. Comparative Study of Scale-resolving Simulations for Marine-Propeller Unsteady Flows. *Int. Commun. Heat Mass Transf.* 100, 1–11. <https://doi.org/10.1016/j.icheatmasstransfer.2018.10.009>
- Capizzano, F., Alterio, L., Russo, S., de Nicola, C., 2019. A hybrid RANS-LES Cartesian method based on a skew-symmetric convective operator. *J. Comput. Phys.* 390, 359–379. <https://doi.org/10.1016/j.jcp.2019.04.002>
- Caraeni, M., Aybay, O., Holst, S., 2011. Tandem Cylinder and Idealized Side Mirror Far-Field Noise Predictions Using DES and An Efficient Implementation of FW-H Equation, in: 17th AIAA/CEAS Aeroacoustics Conference (32nd AIAA Aeroacoustics Conference). American Institute of Aeronautics and Astronautics, Reston, Virginia, pp. 5–8. <https://doi.org/10.2514/6.2011-2843>
- Carr, G.W., Stapleford, W.R., 1986. Blockage Effects in Automotive Wind-Tunnel Testing, in: SAE Technical Papers. <https://doi.org/10.4271/860093>
- Chen, X., Li, M., 2019. Delayed Detached Eddy Simulation of Subcritical Flow past Generic Side Mirror. *J. Shanghai Jiaotong Univ.* 24, 107–112. <https://doi.org/10.1007/s12204-019-2044-z>
- Cheng, S.Y., Tsubokura, M., Nakashima, T., Okada, Y., Nouzawa, T., 2012. Numerical quantification of aerodynamic damping on pitching of vehicle-inspired bluff body. *J. Fluids Struct.* 30, 188–204. <https://doi.org/10.1016/j.jfluidstructs.2012.01.002>
- Cho, J., Kim, T.K., Kim, K.H., Yee, K., 2017. Comparative investigation on the aerodynamic effects of combined use of underbody drag reduction devices applied to real sedan. *Int. J. Automot. Technol.* 18, 959–971. <https://doi.org/10.1007/s12239-017-0094-5>
- Chode, K. K., Viswanathan, H., Chow, K., H. Reese. (2023). Investigating the Aerodynamic Drag and Noise Characteristics of a Standard Squareback Vehicle with Inclined Side-View Mirror configurations using a Hybrid Computational Aeroacoustics (CAA) Approach. *Physics of Fluids*, Accepted. Doi: 10.1063/5.0156111
- Chode, K.K., Viswanathan, H., Chow, K., 2021. Noise emitted from a generic side-view mirror with different aspect ratios and inclinations. *Phys. Fluids* 33, 084105. <https://doi.org/10.1063/5.0057166>
- Chode, K.K., Viswanathan, H., Chow, K., 2020. Numerical investigation on the salient features of flow over standard notchback configurations using scale resolving simulations. *Comput. Fluids* 210, 104666. <https://doi.org/10.1016/j.compfluid.2020.104666>
- Choi, H., Lee, J., Park, H., 2014. Aerodynamics of heavy vehicles. *Annu. Rev. Fluid Mech.* 46, 441–468. <https://doi.org/10.1146/annurev-fluid-011212-140616>
- Chu, Y.-J., Shin, Y.-S., Lee, S.-Y., 2018. Aerodynamic Analysis and Noise-Reducing Design of an Outside Rear View Mirror. *Appl. Sci.* 8, 519. <https://doi.org/10.3390/app8040519>

- Collin, C., Mack, S., Indinger, T., Mueller, J., 2016. A Numerical and Experimental Evaluation of Open Jet Wind Tunnel Interferences using the DrivAer Reference Model. *SAE Int. J. Passeng. Cars - Mech. Syst.* 9, 2016-01–1597. <https://doi.org/10.4271/2016-01-1597>
- Corallo, M., Sheridan, J., Thompson, M.C., 2015. Effect of aspect ratio on the near-wake flow structure of an Ahmed body. *J. Wind Eng. Ind. Aerodyn.* 147, 95–103. <https://doi.org/10.1016/j.jweia.2015.09.006>
- Curle, N., 1955. The influence of solid boundaries upon aerodynamic sound. *Proc. R. Soc. London. Ser. A. Math. Phys. Sci.* 231, 505–514. <https://doi.org/10.1098/rspa.1955.0191>
- Dawi, A.H., Akkermans, R.A.D., 2019. Direct noise computation of a generic vehicle model using a finite volume method. *Comput. Fluids* 191, 104243. <https://doi.org/10.1016/j.compfluid.2019.104243>
- Dawi, A.H., Akkermans, R.A.D., 2018. Spurious noise in direct noise computation with a finite volume method for automotive applications. *Int. J. Heat Fluid Flow* 72, 243–256. <https://doi.org/10.1016/j.ijheatfluidflow.2018.06.008>
- Dechitre, H., Hartmann, M., 2009. Aeroacoustics Simulation of an Automotive A-Pillar Rain Gutter, in: 4th European Automotive Simulation Conference. pp. 1–12.
- Devenport, W., Alexander, N., Glegg, S., Wang, M., 2018. The Sound of Flow Over Rigid Walls. *Annu. Rev. Fluid Mech.* 50, 435–458. <https://doi.org/10.1146/annurev-fluid-122316-045056>
- Duell, E.G., George, A.R., 1999. Experimental study of a ground vehicle body unsteady near wake. *SAE Tech. Pap.* <https://doi.org/10.4271/1999-01-0812>
- Egorov, Y., Menter, F.R., Lechner, R., Cokljat, D., 2010. The Scale-Adaptive Simulation Method for Unsteady Turbulent Flow Predictions. Part 2: Application to Complex Flows. *Flow, Turbul. Combust.* 85, 139–165. <https://doi.org/10.1007/s10494-010-9265-4>
- Ekman, P., Wieser, D., Virdung, T., Karlsson, M., 2020. Assessment of hybrid RANS-LES methods for accurate automotive aerodynamic simulations. *J. Wind Eng. Ind. Aerodyn.* 206, 104301. <https://doi.org/10.1016/j.jweia.2020.104301>
- Elliott, S.J., 1994. Active Control Of Structure-Borne Noise. *J. Sound Vib.* 177, 651–673. <https://doi.org/10.1006/jsvi.1994.1459>
- Endo, T., Himeno, R., 2002. Direct numerical simulation of turbulent flow over a compliant surface. *J. Turbul.* 3, N7. <https://doi.org/10.1088/1468-5248/3/1/007>
- Evans, D., Hartmann, M., Delfs, J., 2019. Beamforming for point force surface sources in numerical data. *J. Sound Vib.* 458, 303–319. <https://doi.org/10.1016/j.jsv.2019.05.030>
- Evstafyeva, O., Morgans, A.S., Dalla Longa, L., 2017. Simulation and feedback control of the Ahmed body flow exhibiting symmetry breaking behaviour. *J. Fluid Mech.* 817, R2. <https://doi.org/10.1017/jfm.2017.118>
- Ewert, R., Schröder, W., 2003. Acoustic perturbation equations based on flow decomposition via source filtering. *J. Comput. Phys.* 188, 365–398. [https://doi.org/10.1016/S0021-9991\(03\)00168-2](https://doi.org/10.1016/S0021-9991(03)00168-2)

- Fan, Y., Xia, C., Chu, S., Yang, Z., Cadot, O., 2020. Experimental and numerical analysis of the bi-stable turbulent wake of a rectangular flat-backed bluff body. *Phys. Fluids* 32, 105111. <https://doi.org/10.1063/5.0019794>
- Fares, E., 2006. Unsteady flow simulation of the Ahmed reference body using a lattice Boltzmann approach. *Comput. Fluids* 35, 940–950. <https://doi.org/10.1016/j.compfluid.2005.04.011>
- Ffowcs Williams, J. E., and Hawkings, D.L., 1969. Sound generation by turbulence and surfaces in arbitrary motion by J . E . Ffowcs williams and D . L . Hawking, *St. Philos. Trans. R. Soc. London. Ser. A, Math. Phys. Sci.* 264, 321–342.
- Fröhlich, J., Mellen, C.P., Rodi, W., Temmerman, L., Leschziner, M.A., 2005. Highly resolved large-eddy simulation of separated flow in a channel with streamwise periodic constrictions. *J. Fluid Mech.* 526, 19–66. <https://doi.org/10.1017/S0022112004002812>
- Fröhlich, J., von Terzi, D., 2008. Hybrid LES/RANS methods for the simulation of turbulent flows. *Prog. Aerosp. Sci.* 44, 349–377. <https://doi.org/10.1016/j.paerosci.2008.05.001>
- Fuller, J., Passmore, M.A., 2014. The importance of rear pillar geometry on fastback wake structures. *J. Wind Eng. Ind. Aerodyn.* 125, 111–120. <https://doi.org/10.1016/j.jweia.2013.11.002>
- Ganuga, R.S., Viswanathan, H., Sonar, S., Awasthi, A., 2014. Fluid-Structure Interaction Modelling of Internal Structures in a Sloshing Tank Subjected to Resonance. *Int. J. Fluid Mech. Res.* 41, 145–168. <https://doi.org/10.1615/InterJFluidMechRes.v41.i2.40>
- Gaylard, A.P., Howell, J.P., Garry, K.P., 2007. Observation of flow asymmetry over the rear of notchback vehicles. *SAE Tech. Pap.* 2007. <https://doi.org/10.4271/2007-01-0900>
- Germano, M., Piomelli, U., Moin, P., Cabot, W.H., 1991. A dynamic subgrid-scale eddy viscosity model. *Phys. Fluids A Fluid Dyn.* 3, 1760–1765. <https://doi.org/10.1063/1.857955>
- Gilhome, B.R., Saunders, J.W., Sheridan, J., 2001. Time Averaged and Unsteady Near-Wake Analysis of Cars, in: *SAE Technical Papers*. <https://doi.org/10.4271/2001-01-1040>
- Girimaji, S., Abdol-Hamid, K., 2005. Partially-Averaged Navier Stokes Model for Turbulence: Implementation and Validation, in: *43rd AIAA Aerospace Sciences Meeting and Exhibit*. American Institute of Aeronautics and Astronautics, Reston, Virginia, pp. 12887–12900. <https://doi.org/10.2514/6.2005-502>
- Girimaji, S.S., Suman, S., 2012. Partially Averaged Navier Stokes (PANS) Method for Turbulence Simulations: Theory and Practice, in: *Notes on Numerical Fluid Mechanics and Multidisciplinary Design*. pp. 29–43. https://doi.org/10.1007/978-3-642-31818-4_3
- Goetchius, G., 2011. The Future of Electric Vehicle Noise Control.
- Grahs, T., Othmer, C., 2006. Evaluation of aerodynamic noise generation: Parameter study of generic side mirror evaluating the aeroacoustic source strength, in: *European Conference on Computational Fluid Dynamics (ECCOMAS CFD 2006)*. pp. 1–14.
- Grandemange, M., Cadot, O., Courbois, A., Herbert, V., Ricot, D., Ruiz, T., Vigneron, R., 2015. A study of wake effects on the drag of Ahmed's squareback model at the industrial scale. *J. Wind Eng. Ind. Aerodyn.* 145, 282–291. <https://doi.org/10.1016/j.jweia.2015.03.004>

- Grandemange, M., Cadot, O., Gohlke, M., 2012. Reflectional symmetry breaking of the separated flow over three-dimensional bluff bodies. *Phys. Rev. E* 86, 035302. <https://doi.org/10.1103/PhysRevE.86.035302>
- Grandemange, M., Gohlke, M., Cadot, O., 2013. Turbulent wake past a three-dimensional blunt body. Part 1. Global modes and bi-stability. *J. Fluid Mech.* 722, 51–84. <https://doi.org/10.1017/jfm.2013.83>
- Gu, Z., Zong, Y., Luo, Z., Yang, Z., Jiang, C., Chen, Z., 2015. Numerical simulation of automobile side-window buffeting noise based on fluid–structure interaction. *Appl. Acoust.* 90, 126–137. <https://doi.org/10.1016/j.apacoust.2014.11.003>
- Guilmineau, E., 2008. Computational study of flow around a simplified car body. *J. Wind Eng. Ind. Aerodyn.* 96, 1207–1217. <https://doi.org/10.1016/j.jweia.2007.06.041>
- Guilmineau, E., Deng, G., Wackers, J., 2011. Numerical simulation with a DES approach for automotive flows. *J. Fluids Struct.* 27, 807–816. <https://doi.org/10.1016/j.jfluidstructs.2011.03.010>
- Guilmineau, E., Deng, G.B., Leroyer, A., Queutey, P., Visonneau, M., Wackers, J., 2018. Assessment of hybrid RANS-LES formulations for flow simulation around the Ahmed body. *Comput. Fluids* 176, 302–319. <https://doi.org/10.1016/j.compfluid.2017.01.005>
- Han, T., 1989. Computational analysis of three-dimensional turbulent flow around a bluff body in ground proximity. *AIAA J.* 27, 1213–1219. <https://doi.org/10.2514/3.10248>
- Hartmann, M., Ocker, J., Lemke, T., Mutzke, A., Schwarz, V., Tokuno, H., Toppinga, R., Unterlechner, P., Wickern, G., 2012. Wind Noise Caused by the Side-Mirror and A-Pillar of a Generic Vehicle Model, in: 18th AIAA/CEAS Aeroacoustics Conference (33rd AIAA Aeroacoustics Conference). American Institute of Aeronautics and Astronautics, Reston, Virginia, Virginia, pp. 4–6. <https://doi.org/10.2514/6.2012-2205>
- He, K., Minelli, G., Wang, J., Dong, T., Gao, G., Krajnović, S., 2021. Numerical investigation of the wake bi-stability behind a notchback Ahmed body. *J. Fluid Mech.* 926, A36. <https://doi.org/10.1017/jfm.2021.748>
- He, Y., Liu, Y., Wen, S., Yang, Z., 2021a. Separation of convective and acoustic pressure fluctuations on the front side window of DrivAer model based on pellicular mode decomposition. *Appl. Acoust.* 174, 107755. <https://doi.org/10.1016/j.apacoust.2020.107755>
- He, Y., Schröder, S., Shi, Z., Blumrich, R., Yang, Z., Wiedemann, J., 2020. Wind noise source filtering and transmission study through a side glass of DrivAer model. *Appl. Acoust.* 160, 107161. <https://doi.org/10.1016/j.apacoust.2019.107161>
- He, Y., Wen, S., Liu, Y., Yang, Z., 2021b. Wind noise source characterization and transmission study through a side glass of DrivAer model based on a hybrid DES/APE method. *Proc. Inst. Mech. Eng. Part D J. Automob. Eng.* 235, 1757–1766. <https://doi.org/10.1177/0954407020969551>
- Heft, A.I., Indinger, T., Adams, N.A., 2012. Introduction of a New Realistic Generic Car Model for Aerodynamic Investigations, in: SAE Technical Papers. <https://doi.org/10.4271/2012-01-0168>
- Helfer, M., 2005. General Aspects of Vehicle Aeroacoustics, in: In Lecture Series: Road Vehicle Aerodynamics. Von Karman Institute, Rhode-Genese, Belgium.

- Herpe, F., Vergne, S., Gaudard, E., 2012. Wavenumber-frequency analysis of the wall pressure fluctuations in the wake of a rear view mirror using a lattice Boltzmann model. *Proc. Acoust. 2012 Nantes Conf.* 1851–1856.
- Hoffman, J., Martindale, B., Arnette, S., Williams, J., Wallis, S., 2001. Effect of Test Section Configuration on Aerodynamic Drag Measurements, in: *SAE Technical Papers*. <https://doi.org/10.4271/2001-01-0631>
- Höld, R., Brenneis, A., Eberle, A., Schwarz, V., Siegert, R., 1999. Numerical simulation of aeroacoustic sound generated by generic bodies placed on a plate: Part I - Prediction of aeroacoustic sources, in: *5th AIAA/CEAS Aeroacoustics Conference and Exhibit*. American Institute of Aeronautics and Astronautics, Reston, Virginia. <https://doi.org/10.2514/6.1999-1896>
- Howard, R.J.A., Pourquie, M., 2002. Large eddy simulation of an Ahmed reference model. *J. Turbul.* 3, N12. <https://doi.org/10.1088/1468-5248/3/1/012>
- Hucho, W.H., 1998. *Road Vehicle Aerodynamics*. SAE International.
- Islam, A., Thornber, B., 2017. High-order detached-eddy simulation of external aerodynamics over an SAE notchback model. *Aeronaut. J.* 121, 1342–1367. <https://doi.org/10.1017/aer.2017.61>
- Islam, M., Decker, F., Hartmann, M., Jaeger, A., Lemke, T., Ocker, J., Schwarz, V., Ullrich, F., Crouse, B., Balasubramanian, G., Mendonca, F., 2008a. Investigations of Sunroof Buffeting in an Idealised Generic Vehicle Model - Part II: Numerical Simulations, in: *14th AIAA/CEAS Aeroacoustics Conference (29th AIAA Aeroacoustics Conference)*. American Institute of Aeronautics and Astronautics, Reston, Virginia, pp. 5–7. <https://doi.org/10.2514/6.2008-2901>
- Islam, M., Decker, F., Hartmann, M., Jaeger, A., Lemke, T., Ocker, J., Schwarz, V., Ullrich, F., Schroeder, A., Heider, A., 2008b. Investigations of Sunroof Buffeting in an Idealised Generic Vehicle Model - Part I: Experimental Results, in: *14th AIAA/CEAS Aeroacoustics Conference (29th AIAA Aeroacoustics Conference)*. American Institute of Aeronautics and Astronautics, Reston, Virginia, pp. 5–7. <https://doi.org/10.2514/6.2008-2900>
- Ito, Y., 2013. Challenges in unstructured mesh generation for practical and efficient computational fluid dynamics simulations. *Comput. Fluids* 85, 47–52. <https://doi.org/10.1016/j.compfluid.2012.09.031>
- Jadon, V., Agawane, G., Baghel, A., Balide, V., Banerjee, R., Getta, A., Viswanathan, H., Awasthi, A., 2014. An Experimental and Multiphysics Based Numerical Study to Predict Automotive Fuel Tank Sloshing Noise, in: *SAE Technical Papers*. <https://doi.org/10.4271/2014-01-0888>
- Jasak, H., Weller, H.G., Gosman, A.D., 1999. High resolution NVD differencing scheme for arbitrarily unstructured meshes. *Int. J. Numer. Methods Fluids* 31, 431–449. [https://doi.org/10.1002/\(SICI\)1097-0363\(19990930\)31:2<431::AID-FLD884>3.0.CO;2-T](https://doi.org/10.1002/(SICI)1097-0363(19990930)31:2<431::AID-FLD884>3.0.CO;2-T)
- Kabat Vel Job, A., Hartmann, M., Sesterhenn, J., 2016. Prediction of the interior noise level for automotive applications based on time-domain methods, in: *Proceedings of the INTER-NOISE 2016 - 45th International Congress and Exposition on Noise Control Engineering: Towards a Quieter Future*. pp. 5344–5354.

- Karkoulias, D.G., Tzoganis, E.D., Panagiotopoulos, A.G., Acheimastos, S.-G.D., Margaris, D.P., 2022. Computational Fluid Dynamics Study of Wing in Air Flow and Air–Solid Flow Using Three Different Meshing Techniques and Comparison with Experimental Results in Wind Tunnel. *Computation* 10, 34. <https://doi.org/10.3390/computation10030034>
- Keogh, J., Barber, T., Diasinos, S., Doig, G., 2016. The aerodynamic effects on a cornering Ahmed body. *J. Wind Eng. Ind. Aerodyn.* 154, 34–46. <https://doi.org/10.1016/j.jweia.2016.04.002>
- Khalighi, B., Zhang, S., Koromilas, C., Balkanyi, S.R., Bernal, L.P., Iaccarino, G., Moin, P., 2001. Experimental and Computational Study of Unsteady Wake Flow Behind a Bluff Body with a Drag Reduction Device, in: *SAE Technical Papers*. <https://doi.org/10.4271/2001-01-1042>
- Kim, J., Sung, H.J., 2006. Wall pressure fluctuations and flow-induced noise in a turbulent imboundary layer over a bump. *J. Fluid Mech.* 558, 79. <https://doi.org/10.1017/S002211200600989X>
- Koomullil, R., Soni, B., Singh, R., 2008. A comprehensive generalized mesh system for CFD applications. *Math. Comput. Simul.* 78, 605–617. <https://doi.org/10.1016/j.matcom.2008.04.005>
- Koomullil, R.P., Soni, B.K., 1999. Flow simulation using generalized static and dynamic grids. *AIAA J.* 37, 1551–1557. <https://doi.org/10.2514/2.655>
- Krajnović, S., Davidson, L., 2003. Numerical Study of the Flow Around a Bus-Shaped Body. *J. Fluids Eng.* 125, 500–509. <https://doi.org/10.1115/1.1567305>
- Krajnović, S., Davidson, L., 2002. Large-Eddy Simulation of the Flow Around a Bluff Body. *AIAA J.* 40, 927–936. <https://doi.org/10.2514/2.1729>
- Krajnović, S., Davidson, L., 2005a. Flow Around a Simplified Car, Part 2: Understanding the Flow. *J. Fluids Eng.* 127, 919–928. <https://doi.org/10.1115/1.1989372>
- Krajnović, S., Davidson, L., 2005b. Flow Around a Simplified Car, Part 1: Large Eddy Simulation. *J. Fluids Eng.* 127, 907–918. <https://doi.org/10.1115/1.1989371>
- Kumarasamy, S., Karbon, K., 1999. Aeroacoustics of an Automobile A-Pillar Rain Gutter: Computational and Experimental Study, in: *SAE Technical Papers*. <https://doi.org/10.4271/1999-01-1128>
- Lai, C., Zhu, S., Feng, S., Zhai, G., Tan, L., Obayashi, S., 2023. Flow characteristics and wake topology of two-seat convertibles. *Phys. Fluids* 35, 015144. <https://doi.org/10.1063/5.0134090>
- Lauder, B.E., Spalding, D.B., 1974. The numerical computation of turbulent flows. *Comput. Methods Appl. Mech. Eng.* 3, 269–289. [https://doi.org/10.1016/0045-7825\(74\)90029-2](https://doi.org/10.1016/0045-7825(74)90029-2)
- Lawson, N.J., Garry, K.P., Faucompret, N., 2007. An investigation of the flow characteristics in the bootdeck region of a scale model notchback saloon vehicle. *Proc. Inst. Mech. Eng. Part D J. Automob. Eng.* 221, 739–754. <https://doi.org/10.1243/09544070JAUTO155>
- Lee, C.Y., Cant, S., 2017. Assessment of LES Subgrid-scale Models and Investigation of Hydrodynamic Behaviour for an Axisymmetrical Bluff Body Flow. *Flow, Turbul. Combust.* 98, 155–176. <https://doi.org/10.1007/s10494-016-9751-4>

- Leonard, B.P., 1991. The ULTIMATE conservative difference scheme applied to unsteady one-dimensional advection. *Comput. Methods Appl. Mech. Eng.* 88, 17–74. [https://doi.org/10.1016/0045-7825\(91\)90232-U](https://doi.org/10.1016/0045-7825(91)90232-U)
- Leonardi, S., Orlandi, P., Smalley, R.J., Djenidi, L., Antonia, R.A., 2003. Direct numerical simulations of turbulent channel flow with transverse square bars on one wall. *J. Fluid Mech.* 491, S0022112003005500. <https://doi.org/10.1017/S0022112003005500>
- Li, C., Tang, S., Li, Y., Geng, Z., 2022. A Modified RANS Model for Drag Prediction of Practical Configuration with Riblets and Experimental Validation. *Aerospace* 9, 125. <https://doi.org/10.3390/aerospace9030125>
- Li, T., Burdisso, R., Sandu, C., 2018. Literature review of models on tire-pavement interaction noise. *J. Sound Vib.* 420, 357–445. <https://doi.org/10.1016/j.jsv.2018.01.026>
- Lighthill, M.J., 1954. On sound generated aerodynamically II. Turbulence as a source of sound. *Proc. R. Soc. London. Ser. A. Math. Phys. Sci.* 222, 1–32. <https://doi.org/10.1098/rspa.1954.0049>
- Lighthill, M.J., 1952. On sound generated aerodynamically I. General theory. *Proc. R. Soc. London. Ser. A. Math. Phys. Sci.* 211, 564–587. <https://doi.org/10.1098/rspa.1952.0060>
- Lilly, D.K., 1992. A proposed modification of the Germano subgrid-scale closure method. *Phys. Fluids A Fluid Dyn.* 4, 633–635. <https://doi.org/10.1063/1.858280>
- Lokhande, B., Sovani, S., Xu, J., 2003. Computational Aeroacoustic Analysis of a Generic Side View Mirror, in: *SAE Technical Papers*. <https://doi.org/10.4271/2003-01-1698>
- Lucas, J.-M., Cadot, O., Herbert, V., Parpais, S., Détery, J., 2017. A numerical investigation of the asymmetric wake mode of a squareback Ahmed body – effect of a base cavity. *J. Fluid Mech.* 831, 675–697. <https://doi.org/10.1017/jfm.2017.654>
- Marcum, D.L., Weatherill, N.P., 1995. A procedure for efficient generation of solution adapted unstructured grids. *Comput. Methods Appl. Mech. Eng.* 127, 259–268. [https://doi.org/10.1016/0045-7825\(95\)00836-X](https://doi.org/10.1016/0045-7825(95)00836-X)
- Menter, F., 2018. Stress-Blended Eddy Simulation (SBES)—A New Paradigm in Hybrid RANS-LES Modeling, in: *Notes on Numerical Fluid Mechanics and Multidisciplinary Design*. pp. 27–37. https://doi.org/10.1007/978-3-319-70031-1_3
- Menter, F., Hüppe, A., Matyushenko, A., Kolmogorov, D., 2021. An Overview of Hybrid RANS–LES Models Developed for Industrial CFD. *Appl. Sci.* 11, 2459. <https://doi.org/10.3390/app11062459>
- Menter, F., Kuntz, M., Bender, R., 2003. A Scale-Adaptive Simulation Model for Turbulent Flow Predictions, in: *41st Aerospace Sciences Meeting and Exhibit*. American Institute of Aeronautics and Astronautics, Reston, Virginia. <https://doi.org/10.2514/6.2003-767>
- Menter, F.R., 2015. Best Practice : Scale-Resolving Simulations in ANSYS CFD.
- Menter, F.R., 2014. Scale-Adaptive Simulation (SAS) Turbulence Modeling Unsteady RANS Based Models 1–41.
- Menter, F.R., 1994. Two-equation eddy-viscosity turbulence models for engineering applications. *AIAA J.* 32, 1598–1605. <https://doi.org/10.2514/3.12149>

- Mercker, E., 1986. A blockage correction for automotive testing in a wind tunnel with closed test section. *J. Wind Eng. Ind. Aerodyn.* 22, 149–167. [https://doi.org/10.1016/0167-6105\(86\)90080-2](https://doi.org/10.1016/0167-6105(86)90080-2)
- Minguez, M., Pasquetti, R., Serre, E., 2008. High-order large-eddy simulation of flow over the “Ahmed body” car model. *Phys. Fluids* 20. <https://doi.org/10.1063/1.2952595>
- Molisani, L.R., Burdisso, R.A., Tsihlas, D., 2003. A coupled tire structure/acoustic cavity model. *Int. J. Solids Struct.* 40, 5125–5138. [https://doi.org/10.1016/S0020-7683\(03\)00259-2](https://doi.org/10.1016/S0020-7683(03)00259-2)
- Müller, S., Becker, S., Gabriel, C., Lerch, R., Ullrich, F., 2014. Flow-Induced Airborne and Structure-Borne Noise at a Simplified Car Model, in: Dillmann, A., Heller, G., Krämer, E., Kreplin, H.-P., Nitsche, W., Rist, U. (Eds.), *Notes on Numerical Fluid Mechanics and Multidisciplinary Design*, Notes on Numerical Fluid Mechanics and Multidisciplinary Design. Springer International Publishing, Cham, pp. 353–361. https://doi.org/10.1007/978-3-319-03158-3_36
- Müller, S., Becker, S., Gabriel, C., Lerch, R., Ullrich, F., 2013. Flow-Induced Input of Sound to the Interior of a Simplified Car Model Depending on Various Setup Parameters, in: 19th AIAA/CEAS Aeroacoustics Conference. American Institute of Aeronautics and Astronautics, Reston, Virginia, p. 28. <https://doi.org/10.2514/6.2013-2029>
- Murad, N., Naser, J., Alam, F., Watkins, S., 2013. Computational fluid dynamics study of vehicle A-pillar aero-acoustics. *Appl. Acoust.* 74, 882–896. <https://doi.org/10.1016/j.apacoust.2012.12.011>
- Noack, R.W., Steinbrenner, J.P., 1995. A three-dimensional hybrid grid generation technique. 12th Comput. Fluid Dyn. Conf. 413–423. <https://doi.org/10.2514/6.1995-1684>
- Nusser, K., 2019. Investigation of the Fluid-Structure-Acoustics Interaction on a Simplified Car Model.
- Nusser, K. and Becker, S., 2021. Numerical investigation of the fluid structure acoustics interaction on a simplified car model. *Acta Acustica*, 5, p.22. <https://doi.org/10.1051/aacus/2021014>
- Nusser, K., Müller, S., Scheit, C., Oswald, M., Becker, S., 2018. Large Eddy Simulation of the Flow Around a Simplified Car Model, in: Grigoriadis, D.G.E., Geurts, B.J., Kuerten, H., Fröhlich, J., Armenio, V. (Eds.), *ERCOFTAC Series*, ERCOFTAC Series. Springer International Publishing, Cham, pp. 243–249. https://doi.org/10.1007/978-3-319-63212-4_30
- Oettle, N., Sims-Williams, D., 2017. Automotive aeroacoustics: An overview. *Proc. Inst. Mech. Eng. Part D J. Automob. Eng.* 231, 1177–1189. <https://doi.org/10.1177/0954407017695147>
- Pang, J., 2018. *Noise and Vibration Control in Automotive Bodies*, Noise and Vibration Control in Automotive Bodies, Automotive Series. Wiley. <https://doi.org/10.1002/9781119515500>
- Pavia, G., 2019. Characterisation of the Unsteady Wake of a Square-Back Road Vehicle.
- Pavia, G., Passmore, M., Sardu, C., 2018. Evolution of the bi-stable wake of a square-back automotive shape. *Exp. Fluids* 59, 1–20. <https://doi.org/10.1007/s00348-017-2473-0>

- Perry, A.K., Pavia, G., Passmore, M., 2016. Influence of short rear end tapers on the wake of a simplified square-back vehicle: wake topology and rear drag. *Exp. Fluids* 57, 1–17. <https://doi.org/10.1007/s00348-016-2260-3>
- Piomelli, U., Chasnov, J.R., 1996. Large-Eddy Simulations: Theory and Applications, in: Hallböck, M., Henningson, D.S., Johansson, A. V, Alfredsson, P.H. (Eds.), . Springer Netherlands, Dordrecht, pp. 269–336. https://doi.org/10.1007/978-94-015-8666-5_7
- Pope, S.B., 2001. Turbulent Flows. *Meas. Sci. Technol.* 12, 2020–2021. <https://doi.org/10.1088/0957-0233/12/11/705>
- Prieur, J., Rahier, G., 2001. Aeroacoustic integral methods, formulation and efficient numerical implementation. *Aerosp. Sci. Technol.* 5, 457–468. [https://doi.org/10.1016/S1270-9638\(01\)01123-3](https://doi.org/10.1016/S1270-9638(01)01123-3)
- Qatu, M.S., 2012. Recent research on vehicle noise and vibration. *Int. J. Veh. Noise Vib.* 8, 289. <https://doi.org/10.1504/IJVNV.2012.051536>
- Rao, A.N., Minelli, G., Zhang, J., Basara, B., Krajnović, S., 2018. Investigation of the near-wake flow topology of a simplified heavy vehicle using PANS simulations. *J. Wind Eng. Ind. Aerodyn.* 183, 243–272. <https://doi.org/10.1016/j.jweia.2018.09.019>
- Read, C., Viswanathan, H., 2020. An Aerodynamic Assessment of Vehicle-Side Wall Interaction using Numerical Simulations. *Int. J. Automot. Mech. Eng.* 17, 7587–7598. <https://doi.org/10.15282/ijame.17.1.2020.08.0563>
- Rodi, W., 1997. Comparison of LES and RANS calculations of the flow around bluff bodies. *J. Wind Eng. Ind. Aerodyn.* 69–71, 55–75. [https://doi.org/10.1016/S0167-6105\(97\)00147-5](https://doi.org/10.1016/S0167-6105(97)00147-5)
- Rogallo, R.S., Moin, P., 1984. Numerical Simulation of Turbulent Flows. *Annu. Rev. Fluid Mech.* 16, 99–137. <https://doi.org/10.1146/annurev.fl.16.010184.000531>
- Rouméas, M., Gilliéron, P., Kourta, A., 2009. Analysis and control of the near-wake flow over a square-back geometry. *Comput. Fluids* 38, 60–70. <https://doi.org/10.1016/j.compfluid.2008.01.009>
- Rung, T., Eschricht, D., Yan, J., Thiele, F., 2002. Sound Radiation of the Vortex Flow Past a Generic Side Mirror, in: 8th AIAA/CEAS Aeroacoustics Conference & Exhibit. American Institute of Aeronautics and Astronautics, Reston, Virginia, pp. 1–10. <https://doi.org/10.2514/6.2002-2549>
- Russell, D.A., Titlow, J.P., Bemmen, Y.-J., 1999. Acoustic monopoles, dipoles, and quadrupoles: An experiment revisited. *Am. J. Phys.* 67, 660–664. <https://doi.org/10.1119/1.19349>
- Serre, E., Minguez, M., Pasquetti, R., Guilmineau, E., Deng, G.B., Kornhaas, M., Schäfer, M., Fröhlich, J., Hinterberger, C., Rodi, W., 2013. On simulating the turbulent flow around the Ahmed body: A French–German collaborative evaluation of LES and DES. *Comput. Fluids* 78, 10–23. <https://doi.org/10.1016/j.compfluid.2011.05.017>
- Shur, M.L., Spalart, P.R., Strelets, M.K., Travin, A.K., 2008. A hybrid RANS-LES approach with delayed-DES and wall-modelled LES capabilities. *Int. J. Heat Fluid Flow* 29, 1638–1649. <https://doi.org/10.1016/j.ijheatfluidflow.2008.07.001>

- Siegert, R., Schwarz, V., Reichenberger, J., 1999. Numerical simulation of aeroacoustic sound generated by generic bodies placed on a plate. II - Prediction of radiated sound pressure, in: 5th AIAA/CEAS Aeroacoustics Conference and Exhibit. American Institute of Aeronautics and Astronautics, Reston, Virginia. <https://doi.org/10.2514/6.1999-1895>
- Sims-Williams, D., Marwood, D., Sprot, A., 2011. Links between Notchback Geometry, Aerodynamic Drag, Flow Asymmetry and Unsteady Wake Structure. *SAE Int. J. Passeng. Cars - Mech. Syst.* 4, 156–165. <https://doi.org/10.4271/2011-01-0166>
- Smith, F.T., 2012. *Aerodynamics of Road Vehicles: From Fluid Mechanics to Vehicle Engineering*. Butterworth-Heinemann.
- Smith, T.A., Klettner, C.A., 2022. Airfoil trailing-edge noise and drag reduction at a moderate Reynolds number using wavy geometries. *Phys. Fluids* 34, 117107. <https://doi.org/10.1063/5.0120124>
- SPALART, P., ALLMARAS, S., 1992. A one-equation turbulence model for aerodynamic flows, in: 30th Aerospace Sciences Meeting and Exhibit. American Institute of Aeronautics and Astronautics, Reston, Virginia, Virginia, pp. 5–21. <https://doi.org/10.2514/6.1992-439>
- Spalart, P.R., Deck, S., Shur, M.L., Squires, K.D., Strelets, M.K., Travin, A., 2006. A New Version of Detached-eddy Simulation, Resistant to Ambiguous Grid Densities. *Theor. Comput. Fluid Dyn.* 20, 181–195. <https://doi.org/10.1007/s00162-006-0015-0>
- Thompson, J.F., 1987. A general three-dimensional elliptic grid generation system on a composite block structure. *Comput. Methods Appl. Mech. Eng.* 64, 377–411. [https://doi.org/10.1016/0045-7825\(87\)90047-8](https://doi.org/10.1016/0045-7825(87)90047-8)
- Tosh, A., Caraeni, M., Caraeni, D., 2018. A Hybrid Computational Aeroacoustic Method For Low Speed Flows, in: 2018 AIAA/CEAS Aeroacoustics Conference. American Institute of Aeronautics and Astronautics, Reston, Virginia, pp. 1–20. <https://doi.org/10.2514/6.2018-4096>
- Tsubokura, M., Kobayashi, T., Nakashima, T., Nouzawa, T., Nakamura, T., Zhang, H., Onishi, K., Oshima, N., 2009. Computational visualization of unsteady flow around vehicles using high performance computing. *Comput. Fluids* 38, 981–990. <https://doi.org/10.1016/j.compfluid.2008.01.020>
- Varney, M., Passmore, M., Gaylard, A., 2017. The Effect of Passive Base Ventilation on the Aerodynamic Drag of a Generic SUV Vehicle. *SAE Int. J. Passeng. Cars - Mech. Syst.* 10, 2017-01–1548. <https://doi.org/10.4271/2017-01-1548>
- Versteeg, H., Malalasekera, W., 2007. *Introduction to Computational Fluid Dynamics, An: The Finite Volume Method*, 2nd ed. Pearson Education.
- Viswanathan, H., 2021. Aerodynamic performance of several passive vortex generator configurations on an Ahmed body subjected to yaw angles. *J. Brazilian Soc. Mech. Sci. Eng.* 43, 131. <https://doi.org/10.1007/s40430-021-02850-8>
- Volpe, R., Devinant, P., Kourta, A., 2015. Experimental characterization of the unsteady natural wake of the full-scale square back Ahmed body: flow bi-stability and spectral analysis. *Exp. Fluids* 56, 99. <https://doi.org/10.1007/s00348-015-1972-0>
- Wagner, C., Hüttl, T., Sagaut, P., 2007. *Large-Eddy Simulation for Acoustics*. Cambridge University Press. <https://doi.org/10.1017/CBO9780511546143>

- Wang, Q., Chen, X., Zhang, Y., Meng, W., 2018. Unsteady Flow Control and Wind Noise Reduction of Side-View Mirror, in: SAE Technical Papers. pp. 1–13. <https://doi.org/10.4271/2018-01-0744>
- Wang, S., Bell, J.R., Burton, D., Herbst, A.H., Sheridan, J., Thompson, M.C., 2017. The performance of different turbulence models (URANS, SAS and DES) for predicting high-speed train slipstream. *J. Wind Eng. Ind. Aerodyn.* 165, 46–57. <https://doi.org/10.1016/j.jweia.2017.03.001>
- Wang, Yanan, Hu, Z., Thompson, D., 2020. Numerical investigations on the flow over cubes with rounded corners and the noise emitted. *Comput. Fluids* 202, 104521. <https://doi.org/10.1016/j.compfluid.2020.104521>
- Wang, Yanan,; Thompson, D., Hu, Z., 2020. Numerical investigations on the flow over cuboids with different aspect ratios and the emitted noise. *Phys. Fluids* 32, 025103. <https://doi.org/10.1063/1.5131827>
- Wang, Y., Thompson, D., Hu, Z., 2019. Effect of wall proximity on the flow over a cube and the implications for the noise emitted. *Phys. Fluids* 31, 077101. <https://doi.org/10.1063/1.5096072>
- Wassen, E., Eichinger, S., Thiele, F., 2010. Simulation of Active Drag Reduction for a Square-Back Vehicle, in: Notes on Numerical Fluid Mechanics and Multidisciplinary Design. pp. 241–255. https://doi.org/10.1007/978-3-642-11735-0_16
- Watkins, S., 2010. Aerodynamic noise and its refinement in vehicles. *Veh. Noise Vib. Refinement* 219–234. <https://doi.org/10.1533/9781845698041.3.219>
- Wieser, D., Nayeri, C.N., Paschereit, C.O., 2020. Wake Structures and Surface Patterns of the DrivAer Notchback Car Model under Side Wind Conditions. *Energies* 13, 320. <https://doi.org/10.3390/en13020320>
- Wieser, D., Schmidt, H.J., Müller, S., Strangfeld, C., Nayeri, C., Paschereit, C., 2014. Experimental Comparison of the Aerodynamic Behavior of Fastback and Notchback DrivAer Models. *SAE Int. J. Passeng. Cars - Mech. Syst.* 7, 682–691. <https://doi.org/10.4271/2014-01-0613>
- Wilcox, D., 1997. Turbulence Modeling for CFD, Second edi. ed. D C W Industries.
- Witte, M., Hieke, M., Wurm, F.-H., 2019. Identification of coherent flow structures and experimental analysis of the hydroacoustic emission of a hubless propeller. *Ocean Eng.* 188, 106248. <https://doi.org/10.1016/j.oceaneng.2019.106248>
- Wolf, W.R., Azevedo, J.L.F., Lele, S.K., 2012. Convective effects and the role of quadrupole sources for aerofoil aeroacoustics. *J. Fluid Mech.* 708, 502–538. <https://doi.org/10.1017/jfm.2012.327>
- Wolmarans, J.R., Craig, K.J., 2019. One-way fluid-structure interaction of a medium-sized heliostat using scale-resolving CFD simulation. *Sol. Energy* 191, 84–99. <https://doi.org/10.1016/j.solener.2019.08.068>
- Wood, D., 2015. The Effect of Rear Geometry Changes on the Notchback Flow Field. PhD Thesis 285.

- Wood, D., Passmore, M.A., Perry, A.-K., 2014. Experimental Data for the Validation of Numerical Methods - SAE Reference Notchback Model. *SAE Int. J. Passeng. Cars - Mech. Syst.* 7, 2014-01–0590. <https://doi.org/10.4271/2014-01-0590>
- Yang, Z., Gu, Z., Tu, J., Dong, G., Wang, Y., 2014. Numerical analysis and passive control of a car side window buffeting noise based on Scale-Adaptive Simulation. *Appl. Acoust.* 79, 23–34. <https://doi.org/10.1016/j.apacoust.2013.12.006>
- Yao, H.-D.D., Davidson, L., 2018. Generation of interior cavity noise due to window vibration excited by turbulent flows past a generic side-view mirror. *Phys. Fluids* 30, 036104. <https://doi.org/10.1063/1.5008611>
- Ye, J., Xu, M., Xing, P., Cheng, Y., Meng, D., Tang, Y., Zhu, M., 2021. Investigation of aerodynamic noise reduction of exterior side view mirror based on bionic shark fin structure. *Appl. Acoust.* 182, 108188. <https://doi.org/10.1016/j.apacoust.2021.108188>
- Yokokawa, M., Itakura, K., Uno, A., Ishihara, T., Kaneda, Y., 2002. 16.4-Tflops Direct Numerical Simulation of Turbulence by a Fourier Spectral Method on the Earth Simulator, in: *ACM/IEEE SC 2002 Conference (SC'02)*. IEEE, pp. 50–50. <https://doi.org/10.1109/SC.2002.10052>
- Yu, L., Diasinos, S., Thornber, B., 2021. A fast transient solver for low-Mach number aerodynamics and aeroacoustics. *Comput. Fluids* 214, 104748. <https://doi.org/10.1016/j.compfluid.2020.104748>
- Yuan, H., Yang, Z., Li, Q., 2017. Effects of Installation Environment on Flow around Rear View Mirror. *SAE Int. J. Passeng. Cars - Mech. Syst.* 10, 2017-01–1517. <https://doi.org/10.4271/2017-01-1517>
- Yuan, H., Yang, Z., Wang, Y., Fan, Y., Fang, Y., 2020. Experimental analysis of hydrodynamic and acoustic pressure on automotive front side window. *J. Sound Vib.* 476, 115296. <https://doi.org/10.1016/j.jsv.2020.115296>
- Zore, K., Azab, M., Sasanapuri, B., Shoaib, S., Stokes, J., 2019. ANSYS scale resolving simulations of launch-vehicle. *21st AeSi Annu. CFD Symp.* 8–9.